# FUNCTIONALIZED CARBON NANOTUBE BASED POLYMER COMPOSITES AS ELECTROLYTES IN PROTON EXCHANGE MEMBRANE FUEL CELLS

**A THESIS SUBMITTED TO THE UNIVERSITY OF PUNE**
**FOR THE DEGREE OF DOCTOR OF PHILOSOPHY**
**IN**
**CHEMISTRY**

**By**
**R. KANNAN**

**Dr. K. VIJAYAMOHANAN**
**(Research Guide)**

**PHYSICAL AND MATERIALS CHEMISTRY DIVISION**
**NATIONAL CHEMICAL LABORATORY**
**PUNE – 411 008, INDIA**

**OCTOBER 2010**

# FUNCTIONALIZED CARBON NANOTUBE BASED POLYMER COMPOSITES AS ELECTROLYTES IN PROTON EXCHANGE MEMBRANE FUEL CELLS

**A THESIS SUBMITTED TO THE UNIVERSITY OF PUNE**
**FOR THE DEGREE OF DOCTOR OF PHILOSOPHY**
**IN**
**CHEMISTRY**

**By**

**R. KANNAN**

**Dr. K. VIJAYAMOHANAN**
**(Research Guide)**

**PHYSICAL AND MATERIALS CHEMISTRY DIVISION**
**NATIONAL CHEMICAL LABORATORY**
**PUNE – 411 008, INDIA**

**NOVEMBER 2010**

# FUNCTIONALIZED CARBON NANOTUBE BASED POLYMER COMPOSITES AS ELECTROLYTES IN PROTON EXCHANGE MEMBRANE FUEL CELLS

**A THESIS SUBMITTED OT THE**

**UNIVERSITY OF PUNE**

**FOR THE DEGREE OF**

**DOCTOR OF PHILOSOPHY**

**IN**

**CHEMISTRY**


**By**

**R. KANNAN**

**PHYSICAL AND MATERIALS CHEMISTRY DIVISION**

**NATIONAL CHEMICAL LABORATORY**

**PUNE – 411 008, INDIA**



**NOVEMBER 2010**

# DECLARATION

I, hereby declare that all the experiments embodies in this thesis entitled, **"FUNCTIONALIZED CARBON NANOTUBE BASED POLYMER COMPOSITES AS ELECTROLYTES IN PROTON EXCHANGE MEMBRANE FUEL CELLS"** submitted for the degree of Doctor of Philosophy in Chemistry, to the university of Pune have been carried out by me at the Physical and Materials Chemistry Division, National Chemical laboratory, Pune, 411 008, India, under the supervision of Dr. K. Vijayamohanan. The work is original and has not been submitted in part or full by me, for any degree or diploma to this or to any other University.

Date: R. Kannan

Physical and Materials Chemistry Division

National Chemical Laboratory

Pune – 411008

**Dr. K. Vijayamohanan**
**Scientist**

Physical and Materials
Chemistry Division
National Chemical Laboratory
Pune – 411 008
INDIA

Tel : 91-020-2590 2588
Res : 91-020-2587 0307
Fax : 91-020-2590 2636
Email : vk.pillai@ncl.res.in

# CERTIFICATE

This is to certify that the work incorporated in the thesis entitled, **"FUNCTIONALIZED CARBON NANOTUBE BASED POLYMER COMPOSITES AS ELECTROLYTES IN PROTON EXCHANGE MEMBRANE FUEL CELLS"** submitted by **Mr. R. Kannan,** has been carried out by him under my supervision at the Physical and Materials Chemistry Division, National Chemical Laboratory, Pune, 411 008, India. All the materials from other sources have been duly acknowledged in the thesis.

Research Guide
**(Dr. K. Vijayamohanan)**

Date :
Place : Pune

*Dedicated to my Parents, Wife, Brothers and Akila Akka*

## *Acknowledgements*

*In the voyage of my life, many people with or without knowing, have contributed significantly to help me reach this level through their constant support and encouragement. Thus, without acknowledging their effort, this thesis may not be complete.*

*I reserve the first and best part of it to my research guide Dr. K. Vijayamohanan, whose noble principles and whole hearted dedication to science has gained my unassailable respect. He has been thoroughly supportive during my stay here and his fatherly care can never find an equal match. I absolutely admire his desire to do high quality science and instilling the thirst for science in not only his students but in all whom he comes across and I wish I could imbibe some of those qualities and exercise them for the rest of my life. I learned a lot about electrochemistry under his constant guidance and I believe that the essential habits he cultivated in me such as monthly plans, weekly seminars, group meetings, yearly resolutions and daily planning will give me the confidence to start an independent scientific career. I also extend my sincere gratitude to Mrs. Manju Madam for her motherly care, blessing and constant support and Keshu for refreshing my thoughts.*

*I would like to convey my sincere thanks to Dr. U. K. Kharul for his kind time and efforts in systematically designing my experiments in his lab.*

*I would also like to convey my admiration to Dr. I.S. Mulla for all his help, support, suggestions and advice during the course of this study.*

*My special and sincere thanks go to Dr. Sreekumar whose presence helped me significantly in speeding up my work. I would like to convey my great respect to Dr. Manjusha Shelke for her kind help and support.*

*I wish to thank Dr. S. Sivaram, the Director, NCL for providing me all infrastructural facilities. I am also grateful to Dr. S. Pal, head of Physical and Materials Chemistry Division for allowing me to use all the available facilities in the division. I also would like to extend my sincere thanks to my teachers, Profs. P. Venuvanalingam, R. Jayaraman, M. Palaniyandavar, K. Panchanadeeswaran, and all my M.Sc teachers, V. Sethuraman and K. Veeramani for introducing me to the beauty of Chemistry.*

*My heartfelt gratitude to Drs. P. A. Joy, Anil Kumar, Satish Ogale, P. C. Ghosh, B. L. V. Prasad, A. Lele, Guruswamy, C. Gopinath and T. Raja for their advice and help. I am highly indebted to Dr. K. R. Patil, Mr. A. B. Gaikwad, Mr. Naren and Mr. Kethan for helping me in characterizing my samples. The timely help and friendly atmosphere created by Mr. Deepak and Mr. Punekar in the Physical Chemistry office deserves the best of my compliments. The entire library staffs for providing excellent facilities are gratefully acknowledged. Further, UGC and CSIR are gratefully acknowledged for the financial support.*

*I can never forget the help from my seniors, Drs. Nirmal, Jadabji, Niranjan, Deepali, Bhalu, Mahima and Meera for their constant support and help provided at crucial junctures. An individual thanks to all my labmates, Sathe, Joy, Beena, Vinisha, Kutta, Vishal "Sir", "Karami" Husain, "Rotlu" Ashvini, Bipin, Ranju, Nilesh, Vinayak, Rami, Rathod, Praveen, Sanjay, Mrudula, Meenu, Suga and Mandar who have helped me in all*

*possible ways during the tenure of my work at NCL. A special thanks to Dhanu and "torture" Palani for their persistent help during difficult times and for all the fun. I wish to extend my thanks to my project colleagues Subhasis, Chinmay, Aniketh, Ashish and Arun for their constant effort and enthusiasm. My CECRI friends Sahu, Manohar, Rani are greatfully acknowledged for their help.*

*I would also like to express my sincere thanks to all my divisional colleagues Nagesh, Saritha, Geethanjali, Raju, Sashi, Arpan, Sumith, Sasanka, Sekar, Sanjay, Sreeja, Mangesh,Pankaj, Govind, Jaya, Bindhu, Ravi, Deepti, Sudarsan (Roomie), Umesh, Rahul, Tuhina, Mudit, Subratho, and other divisional friends Swetha, Abba, Satish, Bhuvan, Ravi, Anumon, Rajesh, Reni, Elda, Aani, Sheetal, Sandeep, Mahesh, Sandi, Nazrul, Subangi, Mrunal, Pradnya, Harsal, Kalyani, Sahu, Atul. I also extend my thanks to NCL cricket team friends for the wonderful experience and sports friends Kamu, Kishore (Bhaiyaa), Dillu, Ambrish, Sudir, Ashish, Sridhar (President: BCCGJ), Ganya (Saa ku ka), Rao the jet, Bogesh, Aarif, Mehraj, Sachin, Ankkya, Kausal, and several other friends. A special thanks goes to my Tamil seniors Drs. Devaraj, Selvakannan, Vijayaraj, Sankars, Balki, Venkatesh, Pradeep, KT, Elango, Prathap, Eswar, Jayanthi, Sabari, "Erodu" Viji, Padma and friends Kaajha, Vijay, Selva, Suresh, Ramanujam, TMS, Lalitha, Nagaraj, Thusara, Nellai, Lenin, Edwin, Siva, Raji, Senthils, Sridar, Dhana, Ramsundar, Venkat, Pandi, Punith, John, Sivaguru, Marimuthu anna, "AC" Prabu, "Alumonji" Baskar, "Kudigara" Viji UG classmates Vinoth, Sridher, Mohana, Vino and Udhaya. My M.Sc classmates Ganga, Kiruba, Sangeetha, Sathya, Sony, Suga, Saravana, Parama, Venkatesh, Selva, Tamil, Hari, who were the motivation for me to clear the CSIR exam. I have to express all my gratitude to my dearest friends Malli, Dharma, Venki, Mogli and Suguna who were always with me during my tough times and gave me the strength to surmount it. I definitely need to acknowledge my sister Akila akka who inspired me to do Ph.D and I believe the spiritual motivation she gave will drive me towards higher accomplishments.*

*As always, it is impossible to mention everybody who made an impact on this work although there are those whose spiritual support is even more important. I find no words to express my feelings for my parents (SR Yadav, Jayam) whose moral support, love and constant encouragement have helped me to complete this journey. I wish to thank all my family members, Vasu, Regu, Mano, Bhuvaneswari, Sivasankari, Rajeswari, Priya, Isai, Senthu, Madhan, Anu, Gokul for their support. I wish to express my gratitude to Mari, Karuppaiyah, Vijay, Siva, Aruna, Ranjit, Gokul and Yasika for their encouragement. Finally, a very special appreciation is due to my wife Sangeetha for standing by me throughout my PhD and for the sleepless nights she had to have my thesis completed.*

*R. KANNAN*

"Years wrinkle the skin, but to give up enthusiasm wrinkles the Soul"

# List of Abbreviations

| Abbreviation | Expansion |
|---|---|
| **AEM** | Anion Exchange Membranes |
| **AEP** | Amino ethyl phosphoric acid |
| **CNTs** | Carbon Nanotubes |
| **CV** | Cyclic Voltammetry |
| **CL** | Catalyst Layer |
| **CHP** | Combined Heat and Power |
| **DWCNT** | Double Walled Carbon Nanotubes |
| **DOE** | Department of Energy |
| **DAB** | Diaminobenzidine |
| **EDX or EDAX** | Energy Dispersive X-ray Analysis |
| **EDLC** | Electrical Double layer Capacitors |
| **EC** | Electrochemical Capacitors |
| **FT-IR** | Fourier Transform Infra Red spectrascopy |
| **GC** | Glassy carbon |
| **GDL** | Gas Diffusion Layer |
| **HOR** | Hydrogen Oxidation Reaction |
| **ICE** | Internal Combustion Engines |
| **K-L** | Koutecky-Levich |
| **LSV** | Linear Sweep Voltammetry |
| **LIB** | Li ion Batteries |
| **MWCNT** | Multi Walled Carbon Nanotubes |
| **MW** | Microwave |

| | |
|---|---|
| **MEMs** | Microelectromechanical devices |
| **MEA** | Membrane Electrode Assembly |
| **NasM** | Nafion/Sulfonated MWCNT composite |
| **NapM** | Nafion/pristine MWCNT composite |
| **NMR** | Nuclear Magnetic Resonance |
| **N-CNTs** | Nitrogen doped CNTs |
| **ORR** | Oxygen Reduction Reaction |
| **OCV or OCP** | Open Circuit Potential |
| **PEM** | Polymer Electrolyte Membrane |
| **PtC or Pt/C** | Platinized Carbon |
| **PPA** | Polyphosphoric acid |
| **PBpNT** | Polybenzimidazole/phosphonated MWCNT composite |
| **PBNT** | Polybenzimidazole/pristine MWCNT composite |
| **PEMFC** | Polymer Electrolyte Membrane Fuel Cells |
| **P-MWCNT** | Phosphonated Multi Walled Carbon Nanotubes |
| **PBI** | Polybenzimidazole |
| **PTFE** | Polytetrafluroethane |
| **RDE** | Rotating Disc Electrode |
| **RRDE** | Rotating Ring Disc Electrode |
| **$RuO_2C$ or $RuO_2/C$** | Ruthenium oxide Carbon |
| **SECM** | Scanning Electrochemical Microscope |
| **SPE** | Solid Polymer Electrolyte |
| **SWCNT** | Single Walled Carbon Nanotubes |
| **SEM** | Scanning Electron Microscope |

| | |
|---|---|
| **S-MWCNT** | Sulfonated Multi Walled Carbon Nanotubes |
| **TEM** | Transmission Electron microscope |
| **TGA** | Thermo Gravimetric Analysis |
| **XRD** | X-ray Diffraction |
| **YSZ** | Yittria Stabilized Zirconia |

# Table of Contents

## Chapter 1

# Chapter 1

## Applications of Carbon Nanotubes in Polymer Electrolyte Membrane Fuel Cells

This chapter gives a brief review of current energy scenario and the different energy generation and conversion technologies. An elaboration of the advantages of electrochemical energy conversion devices over conventional internal combustion engines is followed by a brief study on fuel cells with special attention on PEMFCs. A comprehensive analysis on applications of carbon nanotubes in improving the characteristic features of different PEMFC components has also been provided along with the need for functionalizing CNTs and different functionalizing strategies. A general introduction of current polymer electrolyte membranes available for electrolyte applications and their drawbacks are discussed. Finally, the objectives of the present thesis are discussed with this perspective along with main limitations of the overall investigations at the end.

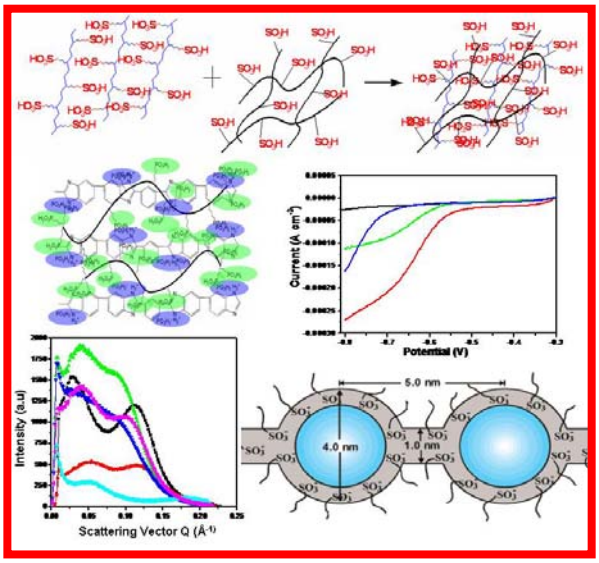


* A part of the work discussed in this chapter has been published in *Journal of Indian Institute of Science* **2009,** 89, 425.

## 1.1. Introduction

Production of affordable and clean energy for the future needs is one of the biggest challenges facing mankind. Currently the majority of energy requirements are obtained from fossil fuels [1-4]. However, the supplies are finite and could last only for a specified period depending on the nature of resources. At current consumption rate, only coal will perhaps remain for approximately 150 years while oil and natural gas are expected to vanish in 50 years [5-8]. The other forms of energy are nuclear, wind, hydrothermal, biomass, solar and geothermal where each has its own advantages and disadvantages based on the geographical locations of the country and its habitants. Among the different energy sources, solar energy presents one truly widespread and clean case where, despite being in its developmental stage, only 0.02 % of available resource is sufficient to replace fossil fuels and nuclear power together from the energy sector [9-10]. However, due to the diffuse nature of solar energy, it demands a larger area to attain considerable energy density, and is thus not suitable for use as such in mobile and portable applications. Further, the huge requirement for landscape necessarily puts this technology in to rural places from where the electricity has to be transported in grids that results in further energy loss. On the other hand, in today's scenario, the use of fossil fuels for meeting our energy needs cannot be ruled out due to the lack of other energy resources. However, it poses severe environmental concern due to the emission of green house gases ($CO_2$). This fact is exacerbated by the low conversion efficiency (25-40 %) of current internal combustion engines (ICEs) whose efficiency is controlled by the Carnot cycle. While Carnot cycle efficiency can reach much higher values in an ideal world, only 25 – 40 % is achievable under practical conditions [11]. The significance of this problem can easily

be understood from the sharp rise of $CO_2$ levels in the atmosphere from the 280 ppm of pre-industrial era, to 387 ppm in 2007 suggesting a 36 % increase from 1750s [12]. More importantly, while it took 215 years for initial 50 % of this increase in $CO_2$ content, it only took 33 years for the next 50 % and this rate of increase is only expected to grow further as observed from the Keeling curves [13-14]. Thus a clean energy conversion and/or storage device with environmental friendliness and higher practical efficiency (appreciably around 70 % at least) is an urgent need for sustainable development. In this respect, electrochemical energy conversion and storage devices due to their intrinsic ability to convert chemical energy directly in to electrical energy offer a unique opportunity to tackle many of these challenges in terms of innovative materials, processes and devices.

### 1.2. Electrochemical Power Sources

Electrochemical power sources are devices that convert the chemical energy stored in chemicals (or fuels) directly into electricity. Major electrochemical energy conversion and storage devices that are considered for the future energy needs are batteries, fuel cells and supercapacitors. While all these three technologies have different, material-dependant, reactions for storage and conversion, the basic energy providing steps take place at the electrode electrolyte interface as the case with any electrochemical system. Scheme 1.1 shows the major classification of electrochemical power sources with the exception of fuel cells which are postponed for a later discussion. Apart from the above categories, there are also overlapping systems such as metal air batteries where a battery electrode is combined with a fuel cell electrode (i.e., half-cell

reaction) to realise benefits of both the systems as illustrated by Metal-air rechargeable batteries using Zn(or Fe) as the anode and air as the cathode [15-16].

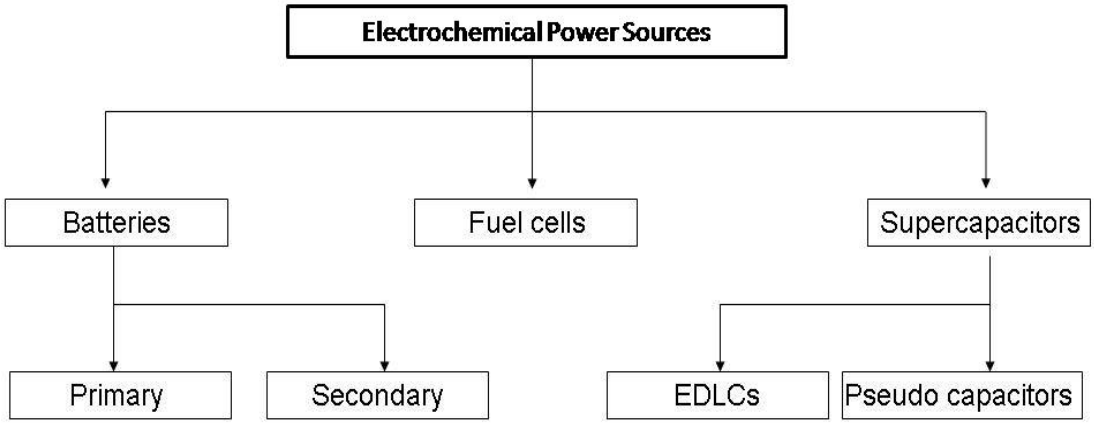


**Scheme 1.1.** Three types of electrochemical energy conversion and storage devices and their basic classification.

### 1.2.1. Batteries

A battery is an electrochemical device that converts the free energy stored in the reactants directly to electricity. The term battery was first coined by Benjamin Franklin to describe an array of charged glass plates in 1748. However, the practical method for the generation of electricity was first demonstrated by Alessandro Volta in the 1800 whose experimental set up included two metal plates separated by pieces of cardboard soaked in brine and is famously called as wet cell battery [17]. Batteries can be classified mainly in to two types based on their ability for multiple usages. Primary batteries use irreversible redox reactions for the energy delivery and hence are generally for one time use (disposable). Common types of primary batteries include Zinc - copper oxide, Zinc - mercuric oxide, Zinc - silver oxide, Zinc - $MnO_2$, Li –$MnO_2$, Li-$SOCl_2$ and Li-$SO_2$ batteries [17].

Secondary batteries, on the other hand, use reversible reactions which enable them to reuse after utilizing the chemical energy stored in it completely by means of

external charging. The oldest form of rechargeable battery is the lead-acid battery developed by Gaston Planté in 1859. The low manufacturing cost and established recycling processes make it one of the most convenient battery systems available even today. Other rechargeable batteries include Ni-Cd, Ni-Zn, Nickel Metal hydride and Li ion batteries (LIB) [18]. LIBs technology with its higher energy density and lighter weight becomes the choice of portable electronic devices. LIBs normally use a lithiated carbon or graphite as anode, lithium cobalt oxide as the cathode and an organic electrolyte of $LiPF_6$ with ethylene/propylene carbonate as the electrolyte. Li ion polymer batteries are also reported where a suitable Li salt is held in a solid polymer matrix such as polyethylene oxide or polyacrylonytrile as the electrolyte[19].

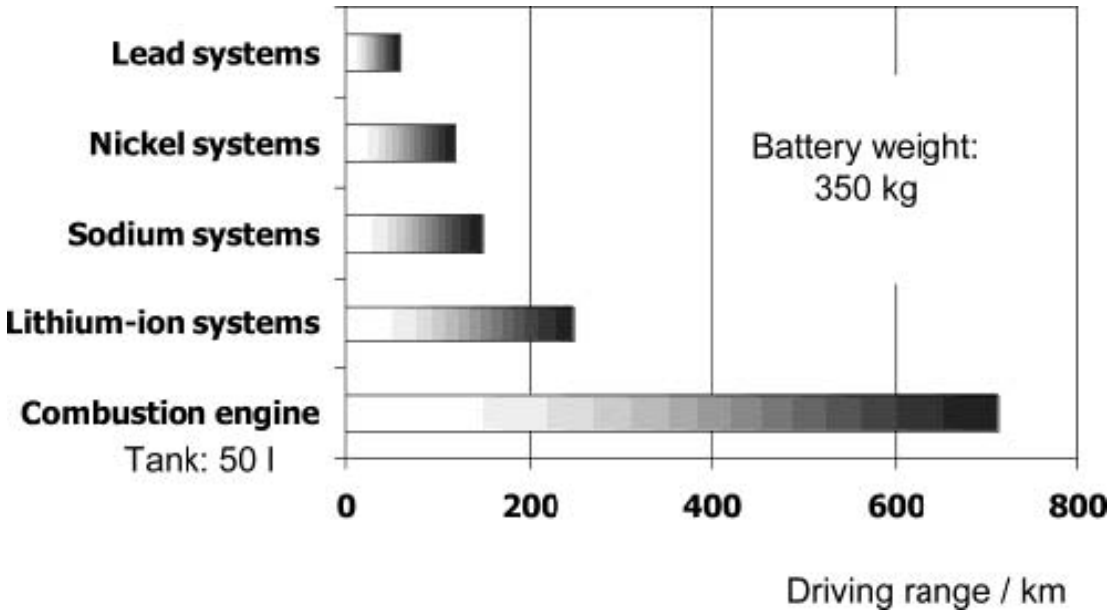


**Figure 1.1.** Comparison of the driving ranges for a vehicle powered by various battery systems or a gasoline-powered combustion engine. (Adapted from ref. 20)

However, the cost and safety related issues are still to be sorted out for widespread LIB applications. Further, the different electrode materials that are being used in batteries have comparatively low energy density than that of many fuels such

as hydrogen, gasoline and natural gas. This limits the use of batteries in applications where sustained operation for longer periods is necessary. For example, a comparison of driving ranges of some battery powered cars with combustion engines (Figure 1.1) clearly demonstrates that why batteries alone can not be considered for automobile applications [20].

### 1.2.2. Supercapacitors

Supercapacitors are electrochemical devices which are ideal for rapid storage and retrieval and they can be generally categorized into two classes, based on the type of electrode materials and also the associated charge storage mechanism, as electrical double layer capacitors (EDLCs) and pseudocapacitors [21-23]. Hybrids of EDLCs and faradaic pseudocapacitors have also been reported as good candidates for certain applications [24-25]. The higher capacitance provided by these electro-chemical capacitors (ECs) is mainly due to the enhanced surface area and adsorption features of the electroactive materials selected from many types of conducting materials such as activated carbon, graphene, carbon nanotubes, nanocomposite papers, carbon aerogels, conducting polymers and certain selected transition metal oxides [26-27]. Among different transition metal oxides, hydrous ruthenium oxide is considered as one of the best candidates for ECs, owing to its unique features, like high charge storage capacity, superior energy/power density, excellent stability and very high conductivity [28-30]. However, there are remarkable results with other transition metal oxides such as $Co_3O_4$ and $LiCoO_2$ and some conducting polymer hybrids for supercapacitor applications although their durability needs to be demonstrated further [31-32].

Most of the present supercapacitors use liquid electrolytes like aqueous sulphuric acid, potassium hydroxide, disodium sulphate or certain organic liquids with dissolved salts like tetrabutylammonium tetrafluoroborate, $LiClO_4$ and more recently ionic liquids such as ethyl-methylimmidazolium-bis(trifluoromethane-sulfonyl)imide [33-38]. Solid polymer electrolytes (SPE) have also been reported for supercapacitor application due to their unique advantages such as simpler design, hermetic sealing and flexibility. However, due to their inability to penetrate the catalyst layer and lower ionic conductivity; SPEs generally give lower specific capacitance in comparison with liquid electrolytes [39-40].

### 1.2.3. Fuel Cells

Fuel cells are electrochemical devices that convert the chemical energy stored in a fuel directly to electrical energy by sustaining redox reactions at the cathode and anode respectively separated by an electrolyte. The electrode reactions do take place at the three phase interface, (more specifically on the surface of electrocatalyst), leaving ions to pass through the electrolyte and electrons through the external circuit. Unlike batteries, fuel cells can operate continuously as long as the necessary reactant, fuel and oxidant, flows are maintained. By stacking hundreds of such single cells, known as membrane-electrode assemblies (MEAs) in a modular form, fuel cell power plants can be erected to provide electricity for a number of applications such as electric vehicles, large grid connected utility power plants for stationary and portable power applications (e.g. micro fuel cells) [41].

Among the different electrochemical energy conversion devices, supercapacitors offer very high cycle life and power density but poor energy density [20]. On the other hand, batteries and fuel cells offer higher energy density but lower

power density. Figure 1.2 presents a simplified Ragone plot for the energy storage domains of various electrochemical energy conversion systems compared to internal combustion engines (ICE), turbines and conventional capacitors. It is clear that all these electrochemical energy conversion devises are inferior to the ICEs and only a hybrid devise comprising fuel cells and/or batteries with supercapacitors can provide energy and power densities that are comparable to that of ICEs.

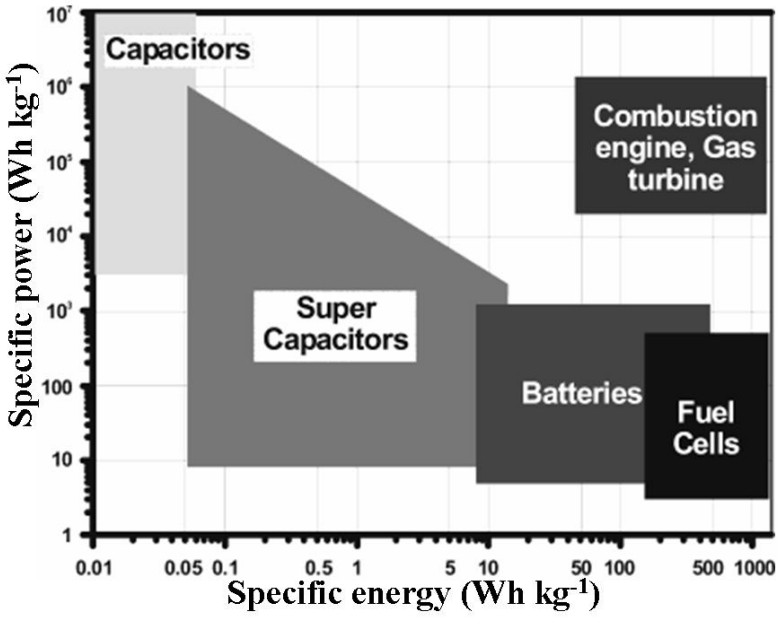


**Figure 1.2.** Simplified Ragone plot of the energy storage devices for the various electrochemical energy conversion systems compared to internal combustion engines, turbines and conventional capacitors (Adopted after Ref. 20).

### 1.2.3.1. Advantages of Fuel Cells

Despite the electrochemical similarities between fuel cells and batteries, batteries have limited space for reactant storage and hence needs to get recharged quite often for practical applications. For example, in fuel cells the reactants are continuously supplied externally which make them an ideal choice for applications that require the sustained delivery of power unlike that of batteries. Further, due to the external supply

of fuel cells, filling up (recharging or more correctly replacing the feed) can be much faster than that of batteries. Also, fuel cells and batteries are not limited by the Carnot efficiency and hence have higher practical efficiency than the internal combustion engines (ICEs). However, many types of batteries have disposal and recyclability issues and hence special efforts are being made in recent times to make greener batteries. Fuel cells normally do not have any moving parts which reduce the wear and tear of their components. The only byproduct when pure hydrogen is used as the fuel is water, thus making them environment-friendly. Due to these above mentioned advantages, different types of fuel cells using innovative materials are under intense research and development for future energy applications.

#### 1.2.3.2. Classification of Fuel Cells

Fuel cells can be classified by different parameters which include the nature of fuels used, temperature of operation and on the basis of electrolytes used. Among them the most common is the basis of electrolytes used in the fuel cell that classifies them mainly into five categories namely; solid oxide fuel cells (SOFC), molten carbonate fuel cells (MOFC), phosphoric acid fuel cells (PAFC), polymer electrolyte membrane fuel cells (PEMFC) and alkaline fuel cells (AFC). Accordingly, Table 1.1 shows different types of fuel cells, their operating temperatures, type of electrochemical reactions involved, electrolytes and the mobile ions. Among the different types of fuel cells, PEMFCs are considered as the most promising candidates for the stationary and mobile applications due to many associated advantages such as low temperature of operation, simpler start ups and easy handling.

**Table 1.1:** Different types of fuel cells, their electrolytes, electrochemical reaction and the mobile ions in them.

| Fuel cell type | Electrolyte | Anode reaction | Cathode reaction | Mobile ion |
|---|---|---|---|---|
| SOFC (500 – 1000 °C) | YSZ - ceramics | $H_2 + O^{2-} \rightarrow H_2O + 2e^-$ | $O_2 + 4e^- \rightarrow 2O^{2-}$ | $O^{2-}$ |
| MCFC (650 °C) | Molten carbonate salts | $H_2 + CO_3^{2-} \rightarrow H_2O + CO_2 + 2e^-$ | $\frac{1}{2}O_2 + CO_2 + 2e^- \rightarrow CO_3^{2-}$ | $CO_3^{2-}$ |
| PAFC (200 °C) | Phosphoric acid | $H_2 \rightarrow 2H^+ + 2e^-$ | $\frac{1}{2}O_2 + 2H^+ + 2e^- \rightarrow H_2O$ | $H^+$ |
| PEMFC (0 – 200 °C) | Polymer electrolyte membrane | $H_2 \rightarrow 2H^+ + 2e^-$ | $\frac{1}{2}O_2 + 2H^+ + 2e^- \rightarrow H_2O$ | $H^+$ |
| AFC (70 °C) | Aqueous alkaline solution in porous media | $H_2 + 2OH^- \rightarrow 2H_2O + 2e^-$ | $\frac{1}{2}O_2 + H_2O + 2e^- \rightarrow 2OH^-$ | $OH^-$ |
| DMFC (0-100 °C) | Polymer electrolyte membrane | $CH_3OH + H_2 \rightarrow CO_2 + 6H^+ + 6e^-$ | $\frac{1}{2}O_2 + 2H^+ + 2e^- \rightarrow H_2O$ | $H^+$ |
| DBFC | Polymer electrolyte membrane | $NaBH_4 + 8OH^- \rightarrow NaBO_2 + 6H_2O + 8e^-$ | $2O_2 + 4H_2O + 8e^- \rightarrow 8OH^-$ | $OH^-$ |

#### 1.2.3.2.1. Solid Oxide Fuel Cells (SOFCs)

SOFC typically operates in the temperature range of 650 – 1000 °C, using porous ceramic electrodes, interposed between a solid electrolyte that can conduct oxide ($O^{2-}$) ions or protons. Due to the high temperature operation, noble metal catalysts are not required to catalyze the electrode reactions. However, it necessitates that all the three key components i.e., cathode, anode and electrolyte should have more or less similar thermal expansion coefficients to be compatible with each other. SOFC stacks can be fabricated in tubular or planar form although anode supported planar configuration

has received more attention recently for power generation. Direct use of hydrocarbon (with out any need for hydrogen generation using external reformers) is an attractive feature and combined heat and power efficiency (cogeneration) could be as high as 80 %. There are many material related challenges involving anode (Ni/Yttria stabilized Zirconia,YSZ), cathode ($Sr_xLa_{1-x}MnO_{3-\delta}$), electrolyte ($Y_2O_3$-$ZrO_2$) and the interconnect ($LaCrO_3$) for making these commercial and the recent trend is to develop materials for SOFCs operating at intermediate temperatures especially as microfuel cells often on Si chips, using micro-electro-mechanical systems (MEMS) technology [42,43].

#### 1.2.3.2.2. Molten Carbonate Fuel Cells (MCFCs)

These fuel cells operate at relatively high temperatures (600-650°C) allowing them to generate power using a variety of both direct as well as reformed hydrocarbons. The operation of an MCFC is based on the shuttle action provided by carbonate ions. The higher operating temperature of MCFCs provides an opportunity for achieving higher overall system efficiencies and greater flexibility in the use of available fuels. Several MCFCs have been developed for natural gas and coal based power plants for electrical utility, industrial and military applications in the past. On the other hand, the higher operating temperature places severe demand on the corrosion stability and life of fuel cell components and consequently these R&D activities are slowly declining. The electrolyte in this fuel cell is usually a combination of alkali (Na, K, Li) carbonates retained in a ceramic matrix made of $LiAlO_2$ [44]. At the high operating temperature of this fuel cell nickel is an adequate electrocatalyst for the anode and cathode [45-46].

#### 1.2.3.2.3. Alkaline Fuel Cells (AFCs)

Major developments in the area of AFCs have been carried out by Francis Bacon in the 1930s and later by many other groups. The AFCs were adopted as the primary power source on the NASA space flights throughout the 1960s and 1970s [47]. A single AFC consists of two porous electrodes with liquid KOH electrolyte between them. Standard AFC stacks use a Pt loading of 0.3 mg $cm^{-2}$. However, a major constraint in the AFC operation is the requirement for low $CO_2$ concentrations in the feed oxidant stream because in the presence of $CO_2$, carbonates were formed and precipitated. To circumvent this problem, electrolyte circulation has been proposed and under rigorous investigation due to the added advantages of water and heat management in the fuel cell system [48]. AFCs normally operate at 50 to 70 °C which can be easily achieved even in cold storage conditions.

#### 1.2.3.2.4. Phosphoric Acid Fuel Cells (PAFCs)

Phosphoric acid fuel cells (PAFC) were the first fuel cells to cross the commercial threshold [49]. As the name implies, these fuel cells use liquid phosphoric acid as the electrolyte. The electrodes are made of carbon paper coated with a finely-dispersed platinum catalyst. Due to the higher operating temperatures, 150-200 °C, PAFCs have higher CO tolerance. Operating at 200 °C, PAFCs convert fuel in to electric energy with about 40 % efficiency. Recovery of the waste heat can raise the overall efficiency to more than 80 %. However, slow start up due to higher temperature operation and high cost due to the usage of Pt as the electrocatalyst are major barriers facing the PAFC technology [50].

#### 1.2.3.2.5. Direct Borohydride Fuel Cells (DBFCs)

The DBFCs were first proposed by Indig and Snyder in 1962. In a DBFC, an alkaline solution of $NaBH_4$ is fed to the anode, which is oxidized to $[B(OH)_4]^-$ delivering electrical energy [51-54]. The theoretical open-circuit voltage for the DBFC, with oxygen as the oxidant, is 1.64 V and this can reach up to 3.02 V interestingly, if hydrogen peroxide is used as the oxidant. Further, the byproduct borax can be hydrogenated back to borohydride by several techniques to provide recyclability. A major drawback with this technology is the possible fuel crossover through the polymer electrolyte membrane that would reduce the over all fuel cell efficiency due to mixed potential and commercial viability except perhaps for strategic applications.

#### 1.2.3.2.6. Direct Methanol Fuel Cells (DMFCs)

DMFC is a promising candidate for portable power sources because methanol is relatively cheap, readily available and soluble in aqueous electrolytes and has a high calorific value. However, the necessity to use Pt based catalysts increases the system cost and restricts the commercialization. Further the electro oxidation of methanol and associated CO poisoning poses severe restriction in the life time of the catalyst and many catalyst systems are being attempted for methanol oxidation [55]. The fuel cross over is another important issue because it not only reduces the systems operating potential but also poisons the cathode Pt catalyst. Recently, methanol powered fuel cells were demonstrated to Power Telecommunications Installation at Mobile World Congress in Barcelona conducted by Motorola [56-57]. Use of methanol in micro fuel cells is another interesting area due to their promise especially in portable

applications. Many reports are available on the use of Si chips based direct methanol micro fuel cells [58-60].

### 1.3. Polymer Electrolyte Membrane Fuel Cells (PEMFCs)

PEMFCs utilize a solid polymer electrolyte membrane (hence PEM, also meaning proton exchange membrane) to transport protons from anode to cathode and restrict electrons from directly going to cathode from anode. PEMFCs operate normally in the temperature range of 30 – 100 °C under humidified environment although PEMs that can operate upto 200 °C are also available. The easy start up and flexible design has attracted interests in both stationary and portable applications [4, 61, 62]. In fact, it represents one potential case for reducing the green house gas emission from a renewable energy point of view especially if hydrogen is produced by solar technologies without any carbon foot print [63]. PEMFCs also have higher practical efficiencies over commercial combustion engines especially if combined heat-power generation is targeted [64].

#### 1.3.1. Electrode reactions in PEMFC operation

The basic electrochemical reactions involved in a PEMFC are

At the anode: $H_2 \rightarrow 2H^+ + 2e^-$ $E^o = 0.0$ V

At the cathode: $\frac{1}{2}O_2 + 2H^+ + 2e^- \rightarrow H_2O$ $E^o = 1.23$ V

Overall: $H_2 + \frac{1}{2}O_2 \rightarrow H_2O$ $E^o = 1.23$ V

A schematic representation of PEMFCs is given in Figure 1.3. A state of the art PEMFC accordingly, has five critical components, 1) Pt electrocatalyst, 2) Catalyst

support carbon, 3) Gas diffusion layers or backing layers, 4) Bipolar plates, and 5) Polymer electrolyte membranes. For the successful operation of PEMFCs, the reactant $H_2$ and $O_2$ must reach the catalyst site where the electrochemical reactions take place and the product water has to be expelled from the catalyst site to prevent water clogging and better access of reactant gases to the electrocatalyst. Similarly, the generated protons at the electrocatalyst sites must reach the cathode through PEM while the electrons need to reach the cathode through an external circuit, where it does the useful work, to react with oxygen and protons to form water. Hence the effective formation of triple phase boundary (reactant gases, electrocatalyst and electrolyte membrane) is an important criteria for successful PEMFC operation.

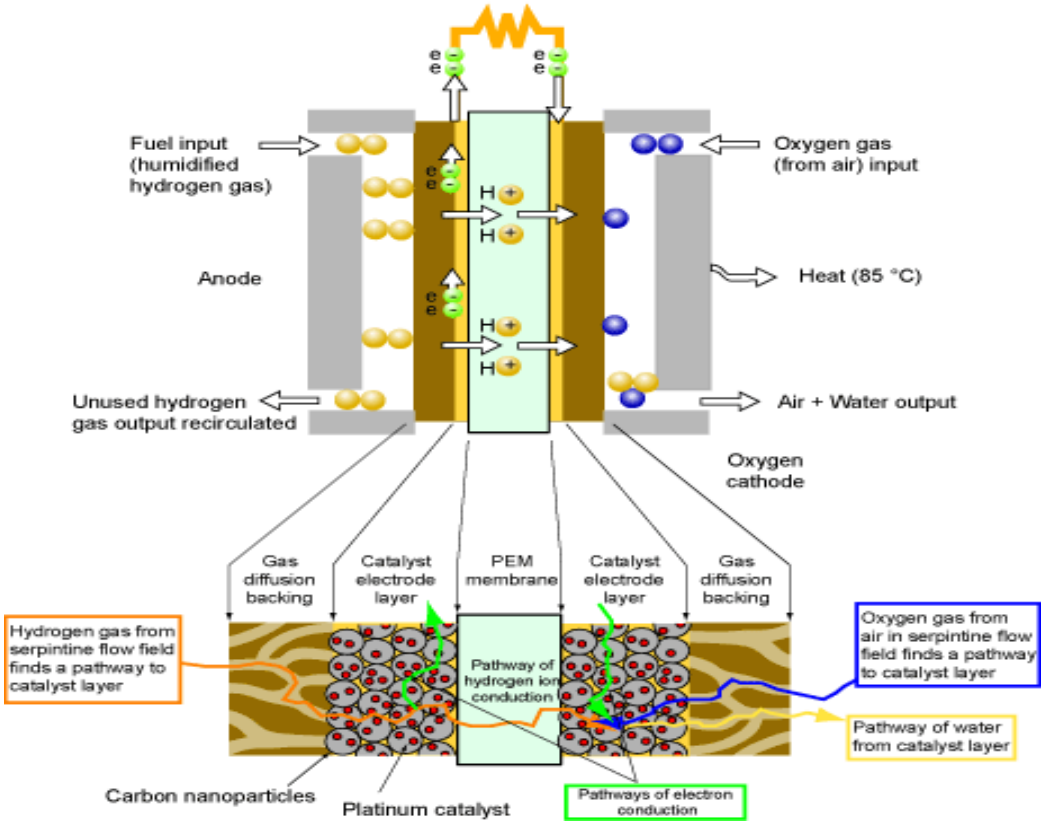


**Figure 1.3.** Schematic representation of various PEMFC components and their operation.

### 1.3.2. Barriers for PEMFCs commercialization

Despite many advantages, PEMFCs still have many challenges owing to the availability of critical materials and processes to effectively address the lack of commercialization aspects [65-66]. For example, the use of Pt as electrocatalyst, graphite bipolar plate and perfluoro sulfonic acid (PFSA) membranes makes the system very expensive, preventing its commercial applications. For example, the state of the art PEMFC stacks use a Pt loading of 0.3 mg $cm^{-2}$ which is too expensive for commercialization while American Department of Energy (DOE) target for 2015 lies at 0.03 mg $cm^{-2}$ [67-68]. Further, the use of PFSA membranes limits the operating temperature below 100 °C that necessitates the use of ultrapure hydrogen as the fuel which further increases the system cost. A cost analysis of different PEMFC components reveals that the membrane electrode assembly (MEA), comprising Pt and PEM, accounts for almost 76 % of the systems cost (Figure 1.4) [69]. A further breakdown of MEA cost contribution reveals that Pt electrocatalyst contributes to approximately 67 % while PEMs contribute a significant 25 % in the total cost analysis. This amounts to a total contribution of 18 % in the cost of PEMFCs.

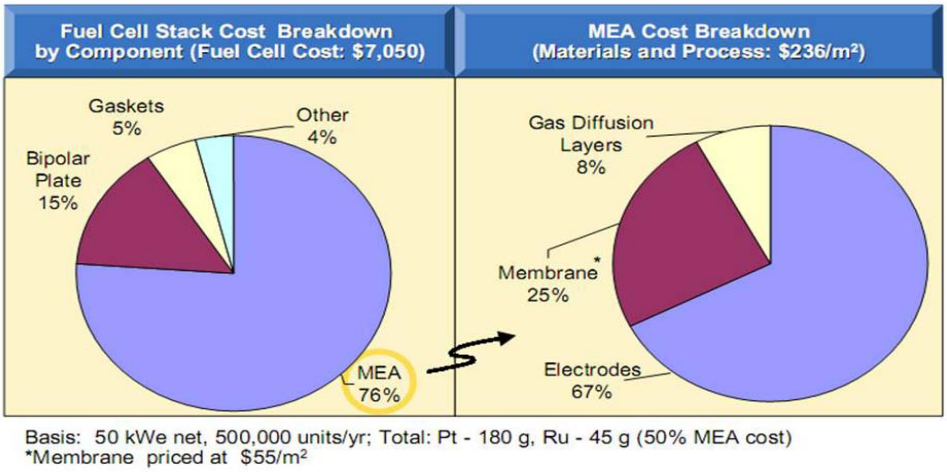


**Figure 1.4.** Cost analysis of PEMFC stack and MEAs (Adapted from ref. 69)

Further, the PFSA based PEMs have many drawbacks such as 1) dependence on water for conductivity, 2) high methanol permeability, 3) a tendency to disintegrate in the presence of hydroxyl radicals, an intermediate in the cathode reaction and 4) moderate mechanical and chemical stability. The use of carbon as the catalyst support and Pt as the electrocatalyst induce durability related issues since Vulcan XC-72 carbon materials are reported to corrode after 150 h of operation [70]. Similarly, other components that are used in fuel cells such as bipolar plates also have many restrictions related to fragility and therefore to realize a commercially feasible fuel cell many of these limitations should be surmounted.

### 1.4. Importance of Nanotechnology

Nanotechnology offers many potential advantages in a vast number of fields such as biomedicine, nanoelectronics and energy research. Generally nanotechnology deals with materials between 1 to 50 nm in at least one dimension and involves developing materials or devices with unique size and shape dependant features. One of the greatest advantages of nanomaterials is the ability to control their electronic, optical and other characteristic properties through manipulation of their size, shape and topology [71]. For example, Pt nanowires and Y- junction platinum nano-structures are demonstrated to have better catalytic activity towards the ethanol and formic acid oxidation in fuel cells than that of simple nanoparticles, which indeed are much better than Pt bulk particles [72].

Further, the increased surface area helps in decreasing the material requirements especially in many fuel cell applications. For example, the amount of Pt loading in the catalyst layer at the early stages of PEMFC development in 1960 was a

staggering 20 to 30 mg $cm^{-2}$. However, the introduction of nanotechnology effectively has reduced the Pt amount in the catalyst layer to many folds and the current state of the art fuel cells use less than 0.5 mg $cm^{-2}$ of Pt although a total elimination of Pt has been indicated [67,73]. Among the different nanostructured materials, one such material which seems to be playing a crucial role in almost all fields is carbon nanotubes.

### 1.5. Carbon nanotubes

Since the pioneering work by Iijima in 1991, carbon nanotubes (CNTs) have become the pinnacle of recent research among different carbonaceous materials due to their distinct characteristics such as inertness under various chemical environments, highest young's modulus, electrical conductivity, high surface area, light weight and easy interfacing capability with many inorganic and organic compounds [74-78]. For example, CNTs pose higher electrical conductivity than copper, higher mechanical strength than stainless steel and higher thermal conductivity than diamond [79]. Carbon nanotubes can be broadly classified in to two types, single-walled and multi-walled carbon nanotubes with reports available on even double-walled nanotubes [80-83]. Carbon nanotubes are considered as analogous to fullerenes due to the similarities in the electronic structure. Moreover, many recent reports have clearly illustrated that the unique electronic structure of CNTs helps in enhancing the catalytic activity of the supported metal in addition to providing mechanical integrity [84-87]. Due to these promising and special properties, CNTs have found wide range of applications such as nanoelectronics, [88] molecular switches, [89, 90] nanotransistors, [91] sensing, [92] gas storage, [93] field emission devices, [94-98] catalyst supports,[99] probes for

scanning probe microscopy, [100] batteries, [101-102] supercapacitors, [103-104] actuators, [105-106] and fuel cells mainly due to their interesting mechanical and electrical properties. However, there are many challenges which revolve around the chemical functionalization of carbon nanotubes to attach specific functional groups to prepare tailor made application oriented hybrid materials that would fulfil many requirements of modern day technologies [76].

### 1.5.1. Need for the Functionalization of CNTs

One of the revealing features of carbon nanotube is its unique composition, where graphene sheets are rolled up in to cylindrical bundles enabling the arrangement of hexagonal rings along the tubular axis suitable for functionalization for specific applications. Carbon nanotubes with defects or surface functional groups can be used in many applications depending on the kind of modification and atoms or molecules that are attached to it. For example, Au, $TiO_2$ and $SiO_2$ nanoparticles covalently bound to CNTs are expected to find interesting applications in field-effect transistors, sensors and solar cells [107-108]. Similarly after special functionalization treatment, CNTs have been reported to reveal more than 100000 turn over numbers for the $H_2$ evolution reaction in aqueous sulphuric acid with very low overvoltage [109]. Different functional groups such as carboxylic acid, sulfonic acid, phosphonic acid and basic groups like hydroxy moieties, amines, polymers, DNA and proteins can be attached on the CNT surface through careful chemical strategies, each having their own advantages for specific applications.

Hence, it is imperative to understand the mechanism of functionalization of carbon nanotubes since there are myriad ways to control the extent of

functionalization. Functionalization of carbon nanotube can be classified based either on the mode of attachment or on the site of attachment. For example, depending upon the mode of attachment, it is broadly classified in to three categories; 1. Covalent functionalization, 2. Non-covalent functionalization, and 3. Inner cavity filling [76]. Electrochemical functionalization is another important method which controls the extent of functionalization directly by means of applied voltage and current. Further, based on the site of attachment it can be classified in to two further categories such as sidewall functionalization and tip/defect site functionalization. A schematic representation of different modes of functionalization and the classification based on the site of attachment is given in Scheme 1.2. After functionalization, carbon nanotubes show dramatic changes in their properties from that of the pristine nanotubes, and hence they are some times called as meta nanotubes [110].

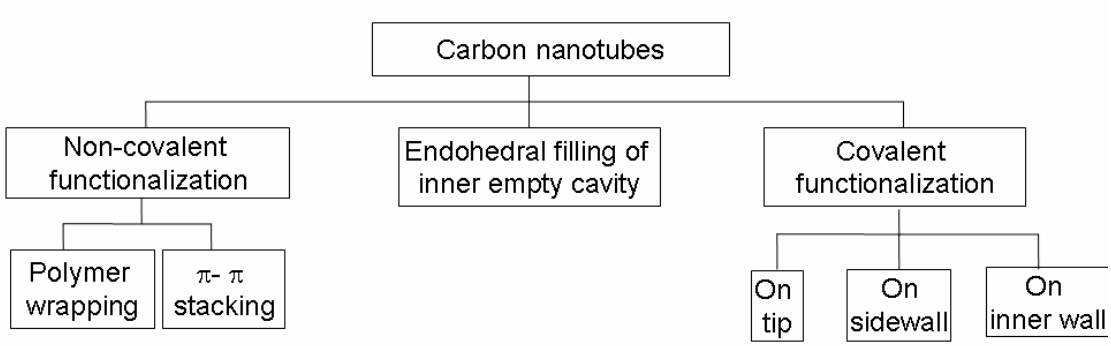


**Scheme 1.2.** Schematic representation of different functionalization protocols based on the mode of functionalization and on the site of attachment.

### 1.5.2. Functionalization Strategies for CNTs

Although single walled carbon nanotubes are mainly considered for all chemical transformations, double walled, multiwalled carbon nanotubes and graphene could as well be used for similar functionalization approaches except for some important

changes in their band structure. [111-112] General methodologies used for functionalizing carbon nanotubes with various functional groups are given in Figure 1.5, where it can be easily seen that any given molecule can be attached on to carbon nanotubes by adopting at least any one of the techniques for functionalization. For example, carbon nanotubes can be attached with functional groups such as carboxylic acids, hydroxyl groups, amine, fluorine, aromatic molecules, semiconducting quantum dots, biomolecules such as proteins and amino acids.

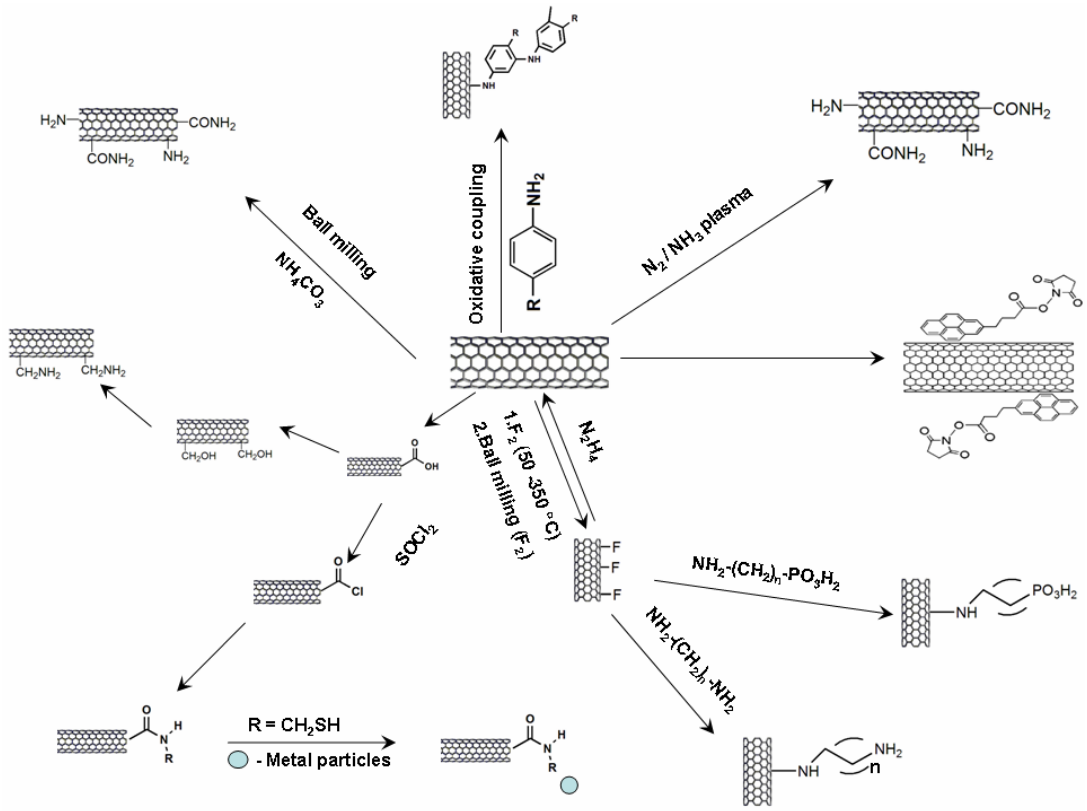


**Figure 1.5.** Various methodologies of functionalization of carbon nanotubes with different reagents.

### 1.5.2.1. Non-covalent Functionalization

Non-covalent functionalization normally involves the wrapping of high molecular weight species such as polymers, DNA and proteins on the CNT surface thereby

disrupting the hydrophobic interface with water. Further, it also interrupts the inter-tubular interactions in a tubular aggregate thus individualizing the nanotube. For example, SWCNT has been attached with protein molecules by noncovalent interactions of pyrenebutanoic acid. One of the main advantages associated with non-covalent functionalization is the preservation of $sp^2$ network in CNTs which is the key for its unique electronic and electrical properties. Non-covalent attachment mainly happens through the π-π stacking of the aromatic rings of CNTs with incoming aromatic systems such as pyrene, naphthalene etc., to which further chemical modifications are required to generate desired functional groups. However, noncovalent functionalization suffers from limitations such as the difficulty of controlling the degree of functionalization and its delicate nature due to the week interaction between the CNT and the aromatic attaching groups (thus not robust) as required for some applications.

#### 1.5.2.2. Covalent Functionalization

Covalent functionalization, on the other hand, provides a better methodology to attach application specific functional groups on to the carbon nanotube surface thereby improving the nanotube processability and dispersing ability in different solvents. Further the possibility to vary the level of covalent attachment provides a unique means to tune the CNT properties which is not possible with non covalent attachment. Covalent modification of carbon nanotube surface normally is carried out through two methods. First one involves the carbon nanotube surface oxidation through strong oxidizing agents such as refluxing in $HNO_3$ to create carboxylic acid moieties. Further, the sites for the functionalization can be controlled by varying the oxidation conditions. For instance, milder oxidizing conditions specifically attack the carbon

nanotube tips and defect sites to leave the sidewall unaffected, thus important for molecular wires and transistors based applications while strong oxidizing reagents attack both sidewalls and tips there by making the functionalized carbon nanotubes suitable for composite making. This carboxylic acid groups are further modified to incorporate specific functionalities ranging in a wide variety such as biomolecules and semiconductor quantum dots by chemical conversions.

#### 1.5.2.3. Electrochemical Functionalization

Electrochemical attachment of functional groups on the sidewalls is another attractive way for the chemical modification of carbon nanotubes. An array of compounds has been attached on the sidewalls of carbon nanotubes by electrochemical reduction of aryl diazonium salts [113-114]. The electrochemical approach is highly desired for modification because the extent of reaction can be directly adjusted by an applied potential or current.

Recently, microwave associated synthesis of functionalized carbon nanotubes has also been reported as a viable technique due to the reduced time of reaction and increased functionalization [115]. However, since a large amount of localized energy is used in a short time scale, microwave method can have undesirable side effects such as chopping of CNTs, uncontrolled defect generation and contamination due to the presence of a dipolar liquid. Ability to scale up for industrial application is also a serious limitation of microwave methodology.

#### 1.5.2.4. Sidewall Functionalization

Sidewall functionalization of CNTs can be carried out through many methods out of which, mainly two are most popular to adopt. First, fluorinated CNTs, prepared by

treating CNTs with $F_2$/Ar mixture at temperatures ranging from 150 °C to 350 °C, are treated with various compounds in pyridine medium at 120 °C to obtain specific functional groups attached directly without the amide linkage on the sidewalls of CNTs [116-118]. The general procedure for various group functionalizations on F-CNTs is given in Figure 1.5, where various modes for sidewall functionalization are presented. Second, electrochemical oxidation and reduction of amines in the presence of carbon nanotubes result in sidewall functionalization through a radical induced mechanism for attacking the double bonds in the CNTs. Further, electrochemical attachment can also be used to form a monolayer of functional groups by varying the duration of the reaction.

#### 1.5.2.5. Tip and Defect site Functionalization

Tips and defect site functionalization of carbon nanotubes is achieved mainly by acid treatment which opens up the tips by creating carboxylic acid groups at the tube openings along with creating some defects on the sidewalls. The level of carboxylic acid creation on the surface of carbon nanotubes can be varied by controlling the reagents used for the functionalization. After this, there are three major modes for attaching different functional groups on the carboxylic sites;

1. Reaction with thionyl chloride creates acyl chloride which can be readily converted to amides when reacted with amines [119-120].
2. Reaction with oxalyl chloride is also known to create acyl chloride moieties that are converted in to amide groups for attaching long chain organic molecules with high solubility in organic solvents such as $CHCl_3$ and $CS_2$ [121].

3. Reaction with carbodiimides creates a temporary intermediate which upon exposure to amines form the amide linkage.

However, the use of thionyl chloride route produces more individual nanotubes in comparison with carbodiimide route [122]. After attaching the desired functional groups on to carbon nanotubes by varying the chain end functional groups, we can prepare application oriented carbon nanotubes. For example, ethylendiamine gives amine end groups which in turn can be used to bind proteins, amino acids and nucleic acids while the use of aminoethyl phosphonic acid helps to bind $TiO_2$.

Both tip and sidewall functionalization have their own merits as tip functionalization ensures that the electronic properties of carbon nanotube remain intact. This is specially helpful in molecular electronics while sidewall functionalization often reduces the electronic conductivity which is more suitable for composite making with polymers especially where the electrical conductivity is not desired. Thus, there are plenty of methods to functionalize carbon nanotubes to acquire the optimum level of performance. CNTs, functionalized or pristine, have been used in many applications and polymer electrolyte membrane fuel cell (PEMFCs) is one among them holding the key for future energy demands. CNTs play critical roles in making different components of PEMFCs to improve their performance.

### 1.6. Application of CNTs in PEMFC Components

CNTs have made a positive impact in almost all the five critical components of PEMFCs in bringing down the cost and improve the durability of fuel cells. For instance, the electrical conductivity and its unique electronic structure can improve

the electron transport from the catalyst to bipolar plate while its higher mechanical stability would improve the graphite based bipolar plates strength.

### 1.6.1. Electrocatalysis: Nitrogen doped CNTs toward ORR

Electrochemical reduction of oxygen is one of the key parameters restricting the performance of PEMFCs. Many different catalyst systems including Pt based alloys, Non noble metal catalyst systems including metallophorphyrins have been studied for oxygen reduction reaction (ORR) applications [123]. Even though Pt is used as the benchmark catalyst for ORR, it has to be eliminated from the catalyst layer considering the very low abundance of Pt on the earth crust ($3.7x10^{-6}$ %) and its fluctuating cost [124]. Interestingly, Nitrogen doped CNTs (N-CNTs) tend to give an option here although at present, it offers only a partial solution to eliminate Pt [125-126]. For example, vertically aligned CNTs containing nitrogen show better ORR catalytic activity than that of Pt as proved by the cyclic voltammetry and rotating ring disc electrode (RRDE) experiments. Despite the fact that these results are in alkaline medium, the possibility of N-CNTs to replace Pt as an electrocatalyst for the sluggish cathode ORR has profound implications in making Pt free MEAs for PEMFC with out any change in performance using nanotechnology. Further, N-CNTs are also reported to be better support materials for Pt electrocatalysts on the cathode and anode of PEMFCs where, some of the degradation issues can be prevented due to the robust mechanical properties of CNTs [127]. More promising results on Nitrogen and Boron doped CNTs are expected to revolutionize this area in the near future.

### 1.6.2. Support Material for Electrocatalysts

Poor kinetics of ORR sustained at the cathode of MEAs typically necessitates the use of higher Pt content in comparison with that in the anode. However, in many cases the

use of CNTs has been shown to be profitable in terms of providing a better exchange current density towards ORR without causing any detrimental mechanical behaviour as a support for the electrocatalyst [84, 128]. For example, Yan *et al.,* have carried out pioneering work on the use of CNTs in PEMFC electrodes especially in the cathode to improve Pt utilization [70, 129-131]. Their initial study of depositing 4 nm Pt nanoparticles on CNTs has shown improved current and power density in all the regions (i.e., activation, ohmic and mass transport regions), presumably due to the intrinsic properties of CNTs to increase the oxygen reduction kinetics. This is in accordance with the findings of Britto *et al*, where CNT/metal electrodes show higher exchange current density than that on other metal/C based electrodes [84]. Enhanced mass transport is also anticipated to be beneficial in the case of CNT based electrodes coupled with reduced ohmic loss, which is acceptable while comparing the electrical conductivity of CNTs, graphitic powders and other forms of conducting carbon. This has resulted in the enhanced Pt utilization of 58 % against 34 % of carbon based electrodes under favourable conditions. However, water clogging remains as a critical problem in the cathode which severely restricts the performance of PEMFC under high humidity conditions [130].

Carbon nanotubes are generally hydrophobic in nature, which helps in controlling the gas diffusion properties. More specifically, oriented CNTs are shown to have increased hydrophobicity than that of disordered CNTs. Further the electronic conductivity is higher along the tubes than across the tube and along with increased gas permeability, this is expected to help in achieving better mass transport conditions [132-133]. Considering all these benefits associated with oriented CNTs Yan et al., have developed a unique method to orient the CNTs by a filtration method followed

by transfer to the membrane (Figure 1.6). In this method, the surface of CNTs are introduced with functional groups such as –COOH by refluxing with Conc.$HNO_3$/$H_2SO_4$ mixture followed by *in situ* chemical reduction of the Pt precursor on them for the proper anchoring on the CNT surface. Subsequent to the chemical reactions, the functionalized CNTs are filtered through a hydrophobic nylon membrane with precisely controlled pore size/distribution in CNTs standing up with

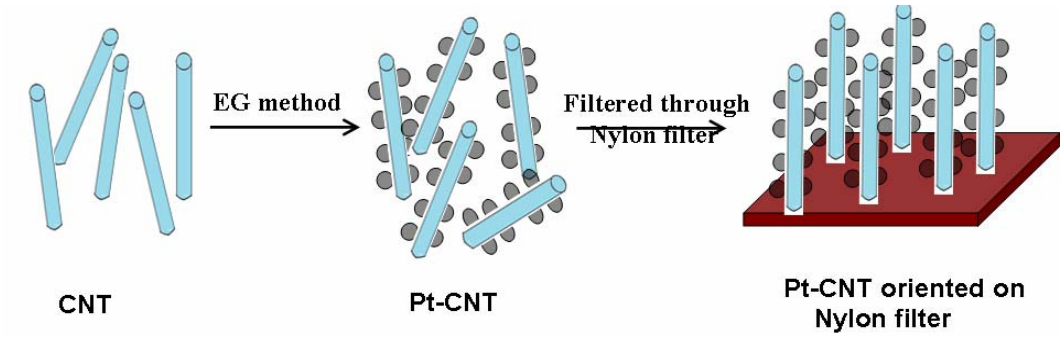


**Figure 1.6.** Scheme for the preparation of oriented Pt/CNT film based MEAs using acid functionalized CNTs deposited with Pt nanoparticles.

the preferred orientation and length. The use of this type of oriented CNTs results in better fuel cell performance than that of randomly aligned CNT based electrodes and Pt/C based electrodes. Table 1.2 illustrates the use of CNTs to enhance the fuel cell performance compared to that of commercial Pt/C catalysts.

One of the reasons for the poor durability of a fuel cell stack is the corrosion of carbon support under the operating conditions of the cathode especially due to the production of hydrogen peroxide as an intermediate. Peroxide generation has several deleterious effects (including damage of the Nafion electrolyte membrane) and several studies have established beyond doubt that Pt nanoparticles are expected to double in size with an operation time of around 200 h. In this regard, the use of CNTs

**Table 1.2.** Increased performance of fuel cells by using CNTs in the cathode catalyst layer; data in the parenthesis represents the dispersion in particle size of the Pt catalyst.

| S. No | Particle size (nm) | Pt Utilization (%) | Surface oxidation | Current density at 0.8 V (mA $cm^{-2}$) | Reference |
|---|---|---|---|---|---|
| 1. | 4 (2-10 ) Pt/CNT | 58 | Yes | 153 | *132* |
| 2. | 2.5 E-TEC* | 34 | --- | 98 | |
| 3. | 2.8 (2-5) Oriented Pt/CNT | --- | Yes | 220 | *133* |

* - E-TEC is the commercial Pt/C catalyst.

which is known for their chemical inertness and remarkable mechanical strength can increase the endurance of a fuel cell MEA. More specifically, an attempt to prove the durability of CNTs carried out by a potentiostatic treatment for 168 h for Pt supported on CNTs and Vulcan XC-72 reveals that CNTs have lesser surface oxides than that of Vulcan XC-72, concomitantly demonstrating 30 % lower corrosion rates [70]. This is well supported by the histograms of Pt size distribution which confirms that the average particle size of 2.5 nm becomes 4.8 nm after 168 h of operation while those Pt nanoparticles supported on CNTs show a slight increase in particle size despite majority of the particles remaining at 2.5 nm [70]. Further, after this prolonged oxidation treatment these Pt/CNTs show considerable ORR catalytic activity while Pt/C samples show a drastic decrease in the onset potential of ORR (~120 mV).

A more recent work by Lin et al., has demonstrated how to reduce the cost of the fuel cell by reducing the particle size as well as increasing the Pt distribution by a wet chemical modification route (Figure 1.7) [134]. By this method Pt nanoparticles of 1-3 nm are stabilized at the same time maintaining a uniform Pt distribution due to

the anchoring groups present on the CNTs surface. Interestingly, fuel cell polarization plot with this catalyst shows a power density of 1100 mW $cm^{-2}$ against 800 mW $cm^{-2}$ for a commercial catalyst. Further, the activation loss at 50 mA $cm^{-2}$ is only 50 mV from the open circuit voltage (OCV) for this surface modified process compared to that of 150 mV for unmodified CNTs. However, with carbon black it is much higher, which signifies the more efficient use of CNTs in the catalyst layer of PEMFCs.

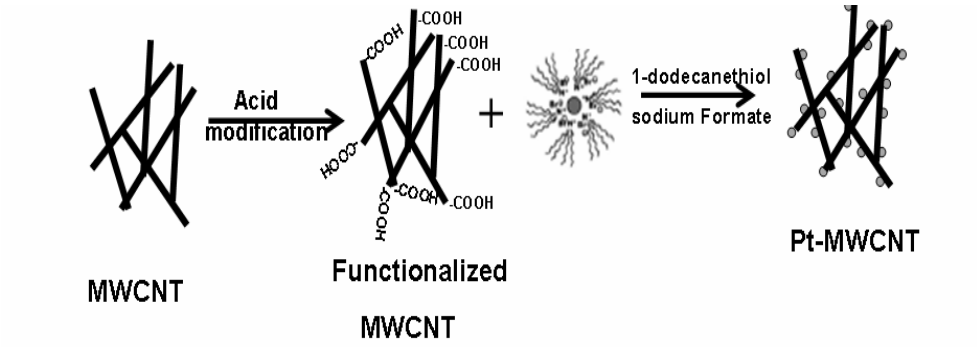


**Figure 1.7.** Scheme for the surface modification of MWCNTs and Pt nanoparticles deposition. (Adapted from ref. 134)

A large number of reports are available on preparing CNT based electrodes especially to increase the Pt utilization by means of using different experimental conditions such as chemical reduction in a formaldehyde bath, and electrochemical deposition of Pt on CNTs. Growing CNTs directly on carbon paper support in order to reduce the ohmic resistance and the modification of the reduction method to prepare smaller nanoparticles with a more narrow size distribution have also been reported as an interesting alternative for Vulcan XC-72 based electrodes demonstrating that the performance could be better although durability and chemical stability aspects of these need to be rigorously evaluated [135-143].

Compared to the vast number of reports available on cathode support materials, only a few reports exist for anode supports mainly due the highly facile nature of the

hydrogen oxidation reaction. However, the actual challenge in the anode is to obtain sustained performance using the reformed $H_2$ having variable CO content. In this regard, catalyst systems (e.g., Pt-Ru) that show good catalytic activity towards methanol oxidation reaction are expected to have a better tolerance for CO and substantial efforts are rendered towards improving the support-metal interaction. Since stronger metal-support interactions would help the electron transfer between the metal and support during electrochemical reactions, the Pt nanoparticles deposited on CNTs tend to have increased catalytic activity than that of unsupported metal due to the unique electronic structure. Interesting improvements have been observed for methanol oxidation on Pt surfaces with and without the presence of CNTs like significant enhancement in current density (50-60 mA $cm^{-2}$) for Pt/CNT electrode compared that of unsupported Pt (6 mA $cm^{-2}$). While this enhancement can have contributions from the increased surface area, the kinetic aspects demonstrate an unambiguous improvement in the catalytic activity of Pt that is supported on CNTs. The onset potential of methanol oxidation is shifted in case of Pt/CNT electrode associated with enhancement of the anodic current. A similar shift observed with Pt-Ru alloy system is attributed to the reduced work function of Ru ($\Phi_{Ru}$=4.52 eV) in comparison with that of Pt ($\Phi_{Pt}$=5.36 eV). Hence the shift observed in CNT/Pt can be ascribed to the reduced work function of CNT (($\Phi_{CNT}$=5 eV) [144-150]. In another report, Wu *et al* have shown a remarkable enhancement in CO tolerance of Pt when supported on SWCNTs and MWCNTs over E-TEK Pt/C catalyst, a commercial sample often used by fuel cell companies. The peak potential for CO stripping are observed at 0.75 V, 0.78 V and 0.82 V respectively for corresponding Pt/SWCNT, Pt/MWCNT and E-TEK Pt/C catalysts suggesting an easy removal of the adsorbed

CO at a much lower onset potential. This could help in achieving better performance even with increased CO level in the hydrogen stream without going for higher temperatures.

### 1.6.3. Gas Diffusion Layer (GDL)

Gas diffusion layer (GDL) plays an important role in the distribution of fuel and oxidant gases across the catalyst layer, efficient water management and transport of electrons from the catalyst layer to the bipolar plate. Normally, GDLs are prepared by applying a mixture of Vulcan XC-72 carbon and PTFE on carbon paper or cloth followed by backing at 350 °C. However, it is desirable to have higher electrical conductivity and higher hydrophobicity to facilitate better water management and electron transport. Thus, bucky papers, a kind of paper made up of CNTs are used instead of carbon cloth or paper, where the increased conductivity helps in transferring the electrons from the catalyst layer to the bipolar plate [151-154]. When Pt nanoparticles are attached directly on the bucky paper, an electrochemical surface area of ~40 $m^2$ $g^{-1}$ was obtained. Further, the higher hydrophobicity of CNTs results in expelling water (product) at an easier rate than in the case of carbon black. Carbon papers and mats made up of CNTs are also reported for GDL application although their integrity needs to be evaluated for sustained stability during their long term use.

### 1.6.4. Bipolar Plates

The current graphite based state-of-art bipolar plates in PEMFCs face severe concerns mainly due to their higher weight, fragility, brittleness and volume. While they have desirable electrical, thermal and chemical properties, their inadequate mechanical properties are another concern that requires alternative options such as metallic alloys

and conducting polymer based composites. Conducting polymer based composites provide a promising option, but needs higher level of carbon fillers (>50 vol.%) to achieve the required electrical and thermal conductivity. This also results in several manufacturing and processing related issues. However, carbon nanotubes offer significant advantages due to their high electrical properties and ability to form composites with conducting polymers [155-158]. For example, carbon nanotube composites with polyethylene terephthalate (PET)/polyvinylidene fluoride (PVDF) blend result in continuous conductive path provided by the CNTs while the PVDF phase offers crack bridging and PET/PVDF interface provides crack deflection for the composite. Due to this combination, the CNT-PET/PVDF composite has better electrical conductivity, strength and elongation and is considered as one of the promising materials for bipolar plate applications [158]. Recently, graphite-phenol formaldehyde resin shows improved bend strength that is necessary for bipolar plate applications. Similarly, CNT/reinforced vinyl ester nanocomposite is shown to have bulk (in- plane) electrical conductivity higher than 100 $Scm^{-1}$, the benchmark for good bipolar plates [155]. Composite of low crystalline polypropylene with CNTs shows electrical conductivity more than 100 $Scm^{-1}$ along with improved mechanical stability and lower thermal expansion [156]. Thus CNTs have helped in improving the desired features of conducting polymer composites toward bipolar plate applications.

While bipolar plates based on graphitic material remains the main focus for PEMFC applications, further cost reduction and increase of power density is beneficial and bipolar plates based on metals offer a high potential to reduce costs and enhance power density (much thinner bipolar plates). However, it is well known that corrosion-resistant metals such as stainless steel form passive surface layers with

intrinsically higher ohmic resistance under PEM fuel cell operating conditions. The direct use of these materials leads to a voltage drop in the fuel cell. In order to reduce the contact resistance of the metallic bipolar plates, various types of coatings and surface treatments have been applied to these metallic plates [159]. Among the different materials, stainless steel 316L is the material of choice for the bipolar plates application and recently Ti, Cr nitride ($(Ti,Cr)n_x$) powders have been tested for coating applications [160-161].

### 1.6.5. Composite Electrolytes

Solid polymer electrolyte membrane is one of the key materials that restrict the performance as well as the cost of the PEMFCs, as electrolyte is an integral component of the MEAs with critical functions. For a successful PEM a candidate membrane should have

- High proton conductivity (> 0.05 S $cm^{-1}$)
- Lower permeability towards reactant gases (< 8 x $10^4$ $cm^3$ cm $m^{-2}s^{-1}$ kPa) [162]
- Low electronic conductivity (< 2 x $10^5$ Ωcm) [163]
- Zero or less reliability on water for proton conductivity
- Wide range of operating temperature (0 to 200 °C)
- High mechanical stability
- Good chemical stability under the highly corrosive environments
- Higher durability and
- Low cost.

A large number of polymer membranes, inorganic solid acids and their hybrids have been proposed for this application. However, two most studied polymers in this

respect are Nafion and phosphoric acid doped polybenzimidazole. Carbon nanotubes for long have not been tried for electrolyte applications fearing the possible electronic conductivity that could arise from them. Initially Nafion has been used as a dispersing agent for making carbon nanotube solutions [164-165]. Even Nafion CNT composite electrodes have also been used for PEMFC electrode fabrication [138]. However, of late they have been attempted in different applications such as actuators with Nafion membranes with considerable success. For example, Nafion carbon nanotube composites with SWCNTs (weight percent ranging from 0.1 to 18 %) have been demonstrated to show better actuator properties than metal nanoparticles incorporated Nafion membranes [166]. This sparked a change in the approach and several CNT polymer composites have been reported for various applications [167-169]. The addition of CNTs can be expected to give increased mechanical robustness and integrity as CNTs are well known for their highest Young's modulus. For instance, Liu *et al*, studied the impact of CNTs on the electrolytic behaviour of Nafion membranes upon reinforcement to observe several improved features [168]. However, the fabrication of composite membranes of CNTs and Nafion at 1:99 wt% after ball-milling and solution casting shows similar performance to that of pure Nafion membrane in terms of proton conductivity, despite with significantly less dimensional change for the case of CNT reinforced composite membranes. Similarly, Thomassin *et al* have used melt extrusion to incorporate the CNTs on to Nafion membrane to observe reduced methanol permeability to about 60 % along with an unusual increase in the Young's modulus up to 140-160 % in comparison to that of commercial Nafion membranes [169].

On the other hand, PBI membranes have also been used as a dispersing agent for carbon nanotubes owing to their ability to interact with carbon nanotubes through π-π interaction as illustrated by the use of PBI membranes with a small addition of SWCNT (0.06 wt%) to display 50 % improved mechanical stability [170]. Even *in situ* polymerization of PBI with functionalized carbon fibres with carboxyl, hydroxyl and amine groups have also been attempted that resulted in significant stability improvement [171]. Further, sulfonated poly[bis(benzimidazobenzisoquinolinones)] in combination with carbon nanotubes have shown good proton conduction [172-173]. However, many of these studies are focused on mechanical properties and their application as thermally stable materials for aerospace applications and the possibility of using CNTs to improve their proton conductivity is largely unexplored.

So despite being attempted as additives in both Nafion and PBI based polymer membranes, why carbon nanotube could not make a significant breakthrough in terms of fuel cell performance? Further, although there are many reviews explaining the advantages of a composite between the CNT and polymer electrolyte, there are several challenges in preventing phase segregation due to lack of knowledge in the use of properly functionalized carbon nanotubes for making composite membranes for electrolyte applications [174-176]. This is basically because CNTs so far have been considered only as an additive to improve mechanical stability and the possibility of using CNTs to overcome the barriers for improved proton conduction has been by and large ignored.

### 1.7. Proton Conducting Membranes in PEMFCs

Many types of ionically conducting polymers are currently under investigation for the electrolyte applications in PEMFCs such as perfluorosulfonic acid membranes

(Nafion), phosphoric acid doped polybenzimidazole membranes, sulfonated polyetherether ketones poly-2-vinylpyridine (P2VP), polyvinylimidazoline and protic ionic liquids. Among them, Nafion and polybenzimidazole membranes are considered as some of the popular choices for PEMFCs operating below and above 100 °C respectively, both having their own advantages and disadvantages [177-181]. Hence we shall have a closer look at these two membranes, especially their structure and properties which make them unique before discussing about the objective of the present thesis.

### 1.7.1. Perfluoro Sulfonic Acid Membranes

#### 1.7.1.1. Nafion: Structure and Mechanism of Proton Conduction

Nafion ionomers are developed and produced by the E. I. DuPont Company. Nafion membranes initially were used in chlor alkali industries for the mass production of NaOH, KOH and $Cl_2$ along with many other proposed applications such as electrochemical energy storage systems, water electrolyzers, Donnan dialysis cells, electrochromic devices, ion selective electrodes and sensors [182-183]. These materials are generated by copolymerization of a perfluorinated vinyl ether comonomer with tetrafluoroethylene (TFE), resulting in polytetrafluoroethylene backbone with vinyl ether side chains ending with sulfonic acid group. The structure of Nafion membrane in the acid form is given below (Scheme 1.3).

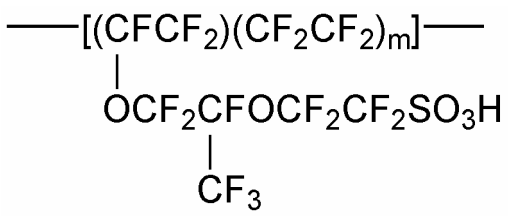

**Scheme 1. 3**. Chemical structure of Nafion resulting from the copolymerization of perfluorinated vinyl ether comonomer with tetrafluoroethylene (TFE).

The hydrophobic backbone along with a hydrophilic side chain offers a unique structure where, Nafion membranes in combination with water can conduct protons and low molecular weight cations, such as $Li^+$ and $Na^+$. Nafion form hydrophilic clusters between side chain sulfonic acid groups and water molecules with an approximate ratio of 70:1000 [182,184]. These clusters, with an average diameter of 4 nm, are interconnected by channels of 1 nm size (Figure 1. 8). It is the distribution and interconnection of these hydrophilic domains that helps in achieving good proton conductivity. Hence, the amount of sulfonic acid and water plays a crucial role and a deficiency in any one of them means a dramatic drop in proton conductivity.

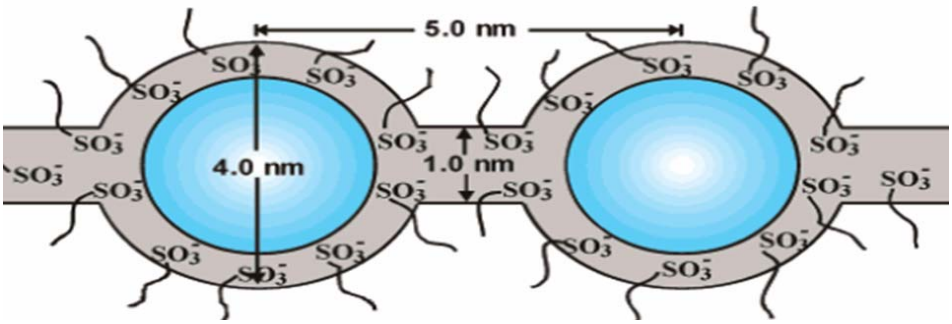


**Figure 1.8.** Cluster-network model for the morphology of hydrated Nafion explaining the proton conductivity.

### 1.7.1.2. Drawbacks of Nafion Membranes

Nafion membranes have been the focus of immense research for the past two decades due to its significant role as an electrolyte in PEMFC. However, despite several attractive features as discussed earlier, they still pose many challenges that need to be overcome. For example,

1. Their proton conductivity relies critically on the water content of the membrane.

2. The dependence on water for its proton conductivity restricts their operating temperature to virtually less than 100 °C.
3. Low operating temperatures necessitate the use of Pt and ultra pure hydrogen as the fuel that increases the system cost significantly.
4. Moderate chemical and mechanical stability.
5. A tendency to disintegrate in the presence of hydroxyl radicals, an intermediate in the cathode reaction.
6. High methanol and hydrogen permeability.

Efforts on solving these problems mainly include the addition of hygroscopic inorganic, organic fillers that would capture the moisture efficiently even at high temperatures or blending with structurally similar ionomers thus keeping the water content of the membrane intact. On the other hand, attempts on increasing the mechanical stability included addition of cross linking molecules and carbon nanotubes at very low concentrations. However, both these methods result in decreased net sulfonic acid content in the composite membranes, thus effectively reducing the overall proton conductivity.

### 1.7.2. PEMs for High Temperature PEMFCs

#### 1.7.2.1. Polybenzimidazole Membranes: Structure and Proton Conductivity

PBI was originally developed for flame retardation due to its very high thermal stability and oxidation resistance. At Case Western University, the development of PBI as proton conducting membrane was initially carried out by doping with sulfonic acid and then with phosphoric acid. Phosphoric acid in PBI has two functions, first as a proton conductor and more significantly as a proton conducting medium.

Phosphoric acid doped polybenzimidazole membranes represent one of the emerging proton conducting membrane for the electrolyte applications in fuel cells that would operate in the range of 120 - 200 °C [185-189]. Working at higher temperatures (like 150 °C) is extremely critical to prevent CO poisoning of the Pt electrocatalyst (either present inadvertently in the hydrogen feed from a reformer or generated as an intermediate during the oxidation of fuels like methanol and ethanol) apart from the improved kinetics and higher efficiency. Further, PBI membranes do not rely on water for its proton conductivity thus simplifying the balance of plant components greatly.

PBI membranes when made to contact with phosphoric acid adsorbs it by both chemical and physical means. The chemisorption results in 2 mol of phosphoric acid per repeat unit of PBI while physisorption results in phosphoric acid uptake as high as 10 mol per repeat unit (Scheme 1.4). It is the presence and distribution of these phosphoric acid in the PBI matrix which makes them a good proton conductor at

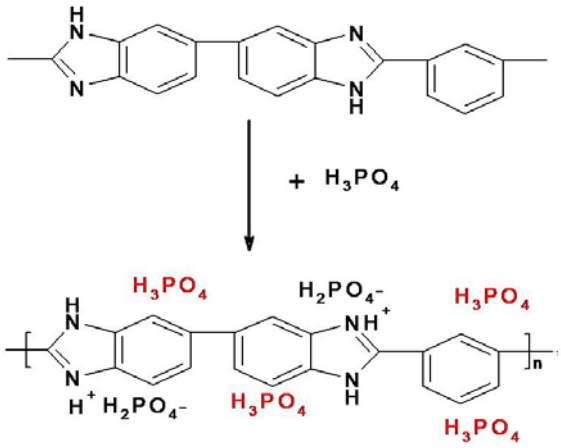


**Scheme 1.4.** Interaction of phosphoric acid with PBI; phosphoric acid in red colour indicates the physically adsorbed phosphoric acid while in black represents the chemically bound phosphoric acid.

temperatures above 100 °C. Proton transport in $H_3PO_4$ doped PBI is mainly through two modes; the rapid exchange of proton via hydrogen bonds between phosphate, N-

heterocycles of PBI (Grotthus type) and through the self-diffusion of phosphate ions. While the chemisorbed 2 % phosphoric acid alone cannot provide proton conductivity, higher phosphoric acid content due to physorption results in mechanically poor membranes and lack durability under fuel cell operating conditions [190-191]. Hence an optimum level of physisorbed phosphoric acid should be maintained to keep the membrane integrity intact.

#### 1.7.2.2. Drawbacks of Polybenzimidazole Membranes

Despite the advantages of $H_3PO_4$ doped PBI membrane such as increased reaction kinetics, higher CO tolerance, easy water management and lesser balance of plant components, PBI membranes also face severe challenges in terms of

1. Poor proton conductivity (< 0.06 S $cm^{-1}$ at 200 °C)

   The proton conductivity of phosphoric acid doped PBI membranes are normally in the range of 0.01 $Scm^{-1}$ which is one order of magnitude lesser than that of Nafion based PEMs at room temperature.

2. Durability mainly due to phosphoric acid leaching (40,000 h)

   The durability is a serious issue in phosphoric acid doped PBI membranes mainly due to the leaching out of physically adsorbed phosphoric acid (free) that reduces the proton conductivity of the membrane thereby reducing the performance of the fuel cell stack.

3. Mechanical stability

   The mechanical strength of these membranes gets reduced by the adsorption of phosphoric acid due to the swelling of polymer matrix. On the other hand, lower phosphoric acid uptake results in poor proton conductivity.

Attempts to increase the proton conductivity of PBI membranes include the addition of inorganic and organic fillers containing phosphate molecules resulted in proton conductivity improvement but hampered the mechanical stability [192-196]. On the other hand, the cross linkers added to improve the mechanical stability resulted in a sacrifice in proton conductivity [197-199].

### 1.8. Other Ion Conducting Polymer Electrolytes

Apart from the proton conducting polymer electrolyte membranes, there are also other ions, such as $Li^+$, $Na^+$ and hydroxyl conducting PEMs that are being developed due to many advantages associated with solid PEMs over their liquid counterparts such as easy handling, removal of leakage problems, improved safety and flexibility. For example, crystalline complexes formed between alkali metal salts and poly(ethylene oxide) are capable of demonstrating significant $Li^+$ conductivity which highlight possible applications in LIB electrolytes. Various Li ion conducting PEMs including $LiClO_4$-polyacrylonitrile and poly(vinylidene fluoride) have been reported [200-202]. Solid-state polymer–silicate nanocomposite electrolytes based on an amorphous polymer poly[$(oxyethylene)_8$ methacrylate], POEM, and lithium montmorillonite clay have also been tested as ‘salt-free’ electrolytes in lithium polymer batteries [203].

Hydroxide anion conducting polymer membranes also termed as anion exchange membranes (AEMs) are another interesting variety of ion conducting PEMs that recently started gaining more interest towards alkaline fuel cells, and electrolyzers. Several types of polymers, such as poly(2,6-dimethyl-1,4-phenylene oxide) (PPO), copolymer of chloromethylstyrene and divinylbenzene, PVDF-vinyl-benzyl chloride, and poly(vinyl alcohol) poly(1,3-diethyl-1, 1-vinyl imidazolium

bromide) have been used for the preparation of anion-exchange membranes [204-206]. The preparation procedure for AEMs based on poly(vinyl alcohol) (PVA) and copolymer of poly(acrylonitrile (PAN)-dimethylamino ethylmethacrylate) (DMAEMA) with strongly basic quaternary ammonium in aqueous media has also been reported [207]. These studies reveal that different ion conducting PEMs including proton are being developed for future energy needs and a breakthrough in any of these materials might open up the electrochemical power systems with improved efficiency.

## 1.9. Conclusions

PEMFC offers a clean and efficient technology for the energy conversion to fulfil the future energy needs. However, currently the technology is too expensive and also the durability of some of its components needs to be further validated. Carbon nanotubes play a critical role in almost all the parts of PEMFCs. While most of those applications are based on their electrical conductivity, the same electrical properties restrict their use in electrolyte applications which needs to be tailored to suit specific applications. However, the ability to functionalize the carbon nanotubes with specific functional groups on its surface not only reduces their electronic conductivity but also make them suitable for composites with electrolyte membranes. While, both Nafion and polybenzimidazole membranes are considered as promising candidates for PEMFC electrolyte applications, a major development in terms of enhanced proton conductivity, improved mechanical stability and durability is an urgent need to take the technology a step closer towards commercialization. Currently used techniques to overcome this challenge either increase the proton conductivity or mechanical

stability separately by sacrificing the other and hence a simultaneous increase is essential to achieve success in solving some of these issues.

### 1.10. Objective of the Present Thesis

The above critical review of current research activities on CNT functionalization gives an opportunity to understand how CNT functionalization can help to overcome the problems faced by PEMFCs. CNTs in fact are used to make composites for PEM applications. However, without any surface functional groups the proton conductivity observed would be always lower than that of the pristine membranes. Hence functionalized CNTs in this respect offer several unique advantages as these tailor made surface functional groups would improve the intensity/concentration of surface functional groups as well as the mechanical stability.

This thesis deals with Nafion and polybenzimidazole membranes as candidates by a strategic approach to increase their mechanical stability and proton conductivity simultaneously, using selectively functionalized carbon nanotubes. The objectives of the present thesis are thus formulated as follows:

- Preparation of application-specific functionalized carbon nanotubes i.e., sulfonated MWCNTs (S-MWCNTs) and phosphonated MWCNTs (P-MWCNTs) with higher solubility in polar solvents.
- Characterization of these functionalized CNTs and their ORR catalytic activity.
- Preparation of polybenzimidazole P-MWCNT (PBpNT) composite membranes and their physicochemical characterization.

- Evaluation of the PBpNT composite membranes as PEMs in actual PEMFC operating conditions.
- Preparation of Nafion S-MWCNT (NasM) composite membranes and their physicochemical characterization.
- Evaluation of the NasM composite membranes as PEMs in actual PEMFC operating conditions.
- Evaluation of these composite membranes as electrolytes in all solid-state supercapacitors.

### 1.11. Organization of the Present Thesis

Studies in this thesis address the aforementioned problems associated with PEMFCs by using selectively functionalized carbon nanotubes. After a brief review on CNTs, CNT functionalization and their role in improving the characteristic features of the different components of PEMFCs in Chapter I, Chapter II deals with the preparation of MEA for PBI based fuel cells since there is not much report on the preparation and optimization of parameters despite the importance in working at high temperatures. We have selected 7 critical parameters such as, catalyst loading, binder loading in catalyst layer and gas diffusion layer, amount of carbon in GDL, hot pressing temperature, pressure and time, which play a vital role in the outcome of MEA performance. A $2^{7-3}$ fractional factorial optimization study has been carried out to optimize the MEA fabrication strategy for high temperature fuel cells. An overall 32 MEAs made as per the design and the results are being analyzed through YATE's algorithm. Based on the results and analysis 6 more MEAs were prepared to optimize

the fabrication condition. SEM images were used to analyze the morphological change in the electrodes.

Chapter III illustrates the preparation and characteristics of functionalized carbon nanotubes and their catalytic activity towards ORR. CNTs have been characterized through scanning electron microscopy (SEM), X-ray photoelectron spectroscopy and (XPS) measurements. The role of functionalization in attaining catalytic activity along with the importance of proper ionomer binder in the catalyst layer to understand the kinetics is also discussed through cyclic voltammetry (CV) and linear sweep voltammetry (LSV) with rotating disc electrode (RDE) measurements.

Chapter IV describes the synthesis of phosphonic acid functionalized carbon nanotubes using aminoethyl phosphonic acid (AEP) as the precursor for phosphonate groups and their composite fabrication with polybenzimidazole membranes. The mode of bonding between amino ethyl phosphonic acid and carbon nanotube has been confirmed with $^{1}H$ and $^{31}P$ NMR which gives evidence for amide linkage between CNT and AEP. The proton conductivity of the composite membrane was analyzed through temperature dependant impedance measurements and mechanical stability was evaluated through stress-strain plots. Arrhenius plots reveal a slight change in the activation energy revealing a change in the mechanism of proton transport. Actual fuel cell experiments revealed improved performance with increasing level of P-MWCNT up to 1 wt% loading followed by drop in performance. *In situ* MEA impedance and solid-state cyclic voltammetry results were discussed to emphasize the role of CNTs in improving the electrode-electrolyte interface. TGA, TEM and SEM were used to analyze the morphology of the composite membrane and CNT

dispersion in the polymer matrix coupled with small angle X-ray scattering (SAXS) results.

Chapter V describes the preparation of sulfonated carbon nanotubes and their composite with Nafion based membranes and their characterization. The composite membrane is shown to have improved proton conductivity than that of the commercial Nafion membranes with similar thickness by impedance measurements at various temperatures in the frequency range of 1 MHz to 1 Hz. The reason for the improved proton conductivity is observed to be the increased hydrophilic domain size of the composite membranes due to the sulfonic acid present on the side walls of carbon nanotubes as inferred from SAXS measurements. SEM, TEM and thermo gravimetric data are discussed to prove the membrane superiority over commercial membranes despite using solution casting method against the industrial extrusion of commercial membranes. Mechanical stability experiments revealed improved yield strength and break at rupture for the composite membrane than that of recast Nafion membranes. Fuel cell polarization studies, MEA *in situ* impedance, solid-state cyclic voltammetry data are also presented to outline the improvement in fuel cell performance. These data synchronize with each other to reveal the role of sulfonated carbon nanotube Nafion composite membranes in improving the performance by providing increased hydrophilic domains for proton transport along with better electrode-electrolyte interface achieved by CNTs present in the composite membrane.

Chapter VI describes the miscellaneous applications of NasM and PBpNT composite membranes as the solid polymer electrolyte in an all-solid-state supercapacitor with state-of-the-art $RuO_2$ as the electrode material. Supercapacitors

made with the composite membrane show increased storage capacity due to the improved interface between the composite and electrode.

The summary of all the major conclusions of the present study with respect to preparation, characterization, properties and potential applications of these nanocomposite membranes are given in Chapter VII, clearly indicating the advantages of functionalized carbon nanotubes in the fabrication of nanocomposite membranes for different applications. One of the unique observations is the ability to tune the hydrophilic domain size of the Nafion based composite membranes by varying the CNT content which offers an attractive option to manipulate the proton conductivity and mechanical stability. Further, the difference in optimum level of CNT loading for the Nafion and PBI based composites can be explained on the basis of amount of expansion after inhaling the water and phosphoric acid respectively. This chapter also outlines some of the limitations of this methodology in improving the properties of parent polymer electrolyte membranes along with future prospects.

## 1.12. References

**[1]** Karunadasa, H. I.; Chang, C. J.; Long, J. R. *Nature* **464,** 2010, 1329.

**[2]** Tollefson, J. *Nature* **464,** 2010, 1262.

**[3]** Lewis, N.S.; Nocera. D.G. Powering the Planet: Chemical challenges in solar energy utilization; *Proc. Natl Acad. Sci.* USA **2006,** 103, 15729.

**[4]** Dresselhaus, M. S.; Thomas, I. L. *Nature* **2001,** 414, 332.

**[5]** http://www.eia.doe.gov/pub/international/iealf/table14.xls accessed on **20th September, 2010.**

**[6]** http://www.eia.doe.gov/emeu/international/RecentPetroleumConsumptionBarrelsperDay.xls accessed on **20th September, 2010.**

**[7]** http://www.eia.doe.gov/pub/international/iealf/table13.xls accessed on **20th September, 2010.**

**[8]** http://en.wikipedia.org/wiki/Fossil_fuel#cite_note-14 accessed on **20th September, 2010.**

**[9]** Pagliaro, M.; Palmisano, G.; Cirminna, R. *Flexible Solar Cells;* Wiley-VCH **2008.**

**[10]** Das, B. K. *Photovoltaic Materials and Devices;* Wiley Eastern Ltd, **1985.**

**[11]** Zhao, T. S.; Kreuer, K-D.; Nguyen, T. V. *Advances in fuel Cells, Volume 1*, Elsevier **2007,** Chapter 1.

**[12]** http://www.epa.gov/climatechange/endangerment.html accessed on **20th September, 2010.**

**[13]** http://cdiac.ornl.gov/trends/co2/graphics/mlo145e_thrudc04.pdf accessed on **20th September, 2010.**

**[14]** http://en.wikipedia.org/wiki/Keeling_Curve#cite_ref-bbc_0-0 accessed on **20th September, 2010.**

**[15]** Smedley, S. I.; Zhang, X. G. *J. Power Sources*, **2007,** 165, 897.

**[16]** Sapkota, P.; Kim, H. *J. Industrial and Engineering Chemistry*, **2010,** 16, 39.

**[17]** Heise, G. W.; Cahoon, N. C. *The Primary Battery*, John Wiley & sons, Inc. **1971.**

**[18]** Nunez, M.Ed. *Electrochemical studies in batteries;* Nova Science publishers **2005.**

**[19]** Yamasaki, Mikiya (Sumoto, JP) **2003,** United States Sanyo Electric Co., Ltd. (Moriguchi, JP) 6623891

**[20]** Winter. M.; Brodd. R. J. *Chem. Rev*. **2004,** 104, 4245.

**[21]** Conway, B. E. *Electrochemical Supercapacitors: Scientific Fundamentals and Technological Applications;* 2nd edn. Kluwer Academic Publisher, New York. **1999**

**[22]** Lin, C.; Ritter, J.A.; Popov, B. N. *J. Electrochem. Soc.,* **1998,**145, 4097

**[23]** Burke, A. *J. Power Sources* **2000,** 91, 37.

**[24]** Frackowiak, E.; Beguin, F. *Carbon* **2001,**40, 1775

**[25]** Reddy, A.; Ramaprabhu, S. *J. Phys. Chem. C* **2007,** 111, 7727.

**[26]** Pushparaj, V.L.; Shaijumon, M. M.; Kumar, A.; Saravanababu, M.; Ci, L. J.; Vajtai, R.; Nalamasu, O.; Ajayan, P. M. *PNAS* **2007,**104, 13574

**[27]** Sivaraman, P.; Rath, S. K.; Hande, V. R.; Thakur, A. P.; Patri, M.; Samui, A. B. *Synth. Metals* **2006,** 156, 1057.

**[28]** Kim, H.; Popov, B. N. *J. Power Sources* **2002,**104, 52.

**[29]** Zheng, J.P.; Jow, T. R.; *J. Electrochem. Soc.* **1995,** L6, 142.

**[30]** Sarangapani, S.; Tilak, B. V.; Chen, C. P. *J. Electrochem. Soc.* **1996,** 143, 791.

**[31]** Cui, L.; Li, J.; Zhang, X.G. *Journal of Applied Electrochemistry* **2009,** 10, 1871.

**[32]** Yan, J.; Wei, T.; Qaio, W.; Zhao, Q.; Zhang, L.; Fan, Z. *Electrochim. Acta.,* **2010,** 55, 6973.

**[33]** Du, X.; Wang, C.; Chen, M.; Jiao, Y.; Wang, J. *J. Phys. Chem. C* **2009,** 113, 2643**.**

**[34]** Athouël, L.; Moser, F.; Dugas, R.; Crosnier, O.; Be´langer, D.; Brousse, T. *J. Phys. Chem. C,* **2008,** 112, 7270**.**

**[35]** Placin, F.; Desvergne, J. P.; Lasse`gues, J. C. *Chem. Mater.* **2001,** 13, 117**.**

**[36]** Largeot, C.; Portet, C.; Chmiola, J.; Taberna, P. L.; Gogotsi, Y.; Simon, P. *J. Am. Chem. Soc.* **2008,** 130, 2730**.**

**[37]** Frackowiak, E.; Lota, G.; Pernak, J. *Appl. Phys. Lett.* **2005,** 86, 164104**.**

**[38]** Lufrano, F.; Staiti, P. *Electrochim. Acta,* **2004,** 49, 2683**.**

**[39]** Osaka, T.; Liu, X.; Nojima, M.; Momma, T. *J. Electrochem. Soc.* **1999,** 146, 1724.

**[40]** Park, K. W.; Ahn, H. J.; Sung, Y. E. *J. Power Sources* **2002,** 109, 500**.**

**[41]** Viswanathan, B.; Scibioh, M. A. *Fuel Cells: Principles and Applications.* University Press, India, **2006.**

**[42]** Litzelman, S. J.; Hertz, J. L.; Jung, W.; Tuller, H. L. *Fuel Cells,* **2008,** 8, 294.

**[43]** Lai, B. K.; Xiong, H.; Tsuchiya, N.; Johnson, A. C.; Ramanathan, S. *Fuel Cells,* **2009,** 9, 699.

**[44]** Marianowski, L. G.; Camara, E. H.; Maru, H. C. *U.S. Patent* 4079171, **1977**.

**[45]** Berger, R. J.; Doesburg, E. B. M.; van Ommen, J. G.; Ross, J. R. H. *Applied Catalysis A: General,* **1996,** 143, 343.

**[46]** Cavaiaro, S.; Mondello, N.; Freni, S. *J. Power Sources,* **2001,** 102, 198.

**[47]** Kordesh, K.; Simader, G.R. *Chem. Rev.* **1995,** 95, 191.

**[48]** Kordesh, K. Power Sources for Electric Vehicles. Modern Aspects of Electrochemistry, Plenum Press, New York, 10, 339-443, **1975**.

[49] http://www.energy.ca.gov/pier/conferences+seminars/2006-05-31_fuel_cell_workshop/presentations/2006-05-31_BINDER.PDF accessed on **20th September, 2010.**

**[50]** Viswanathan, B.; Scibioh, M. A. *Fuel Cells: Principles and Applications.* University Press, India, **2006.** Chapter 4

**[51]** Kiran, V.; Ravikumar, T.; Kalyanasundaram, N. T.; Krishnamurty, S.; Shukla, A. K.; Sampath, S. *J. Electrochem. Soc.*, **2010,** 157, B1201.

**[52]** Dilimon, V. S.; Venkata Narayanan, N. S.; Sampath, S. *Electrochim. Acta*, **2010,** 55, 5930.

**[53]** Wee, J. H. *J. Power Sources*, **2006,** 155, 329.

**[54]** Raman, R. K.; Choudhury, N. A.; Shukla, A. K. *Electrochemical Solid-State Letters*, **2004, 7**, A488.

**[55]** Pandikumar, A.; Murugesan, S.; Ramaraj, R. *Applied Materials & Interfaces,* **2010,** 2, 1912.

**[56]** *Fuel cell bulletin*, **2008,** 2008, 4.

**[57]** http://www.fuelcellmarkets.com/idatech/news_and_information/3,1,599,1,26831.html accessed on **20th September, 2010.**

**[58]** Kamarudin, S. K.; Daud, W. R. W.; Ho, S. L.; Hasran, U. A. *J. Power Sources,* **2007,** 163, 743.

**[59]** Yen, T. J.; Fang, N.; Zhang, X.; Lu, G. Q.; Wang, C. Y. *Applied physics Letters,* **2003,** 83, 4056.

**[60]** Chu, K. L.; Gold, S.; Subramanian, V.; Lu, C.; Shannon, M. A.; Masel, r. i. *J. Micromechanical Systems,* **2006,** 15, 671.

**[61]** Steele, B. C. H.; Heinzel, A. *Nature* **2001,** 414, 345.

**[62]** Mallouk, T. E. *Nature* **1990,** 343, 515.

**[63]** Schlapbach, L. *Nature* **2009,** 460, 809

**[64]** Kunze, J.; Stimming, U. *Angew. Chem. Int. Ed.* **2009,** 48, 9230.

**[65]** Metha, V.; Cooper, J. S. *J. Power Sources,* **2003,** 114, 32.

**[66]** Litster, S.; McLean, G. *J. Power Sources,* **2004,** 130, 61.

**[67]** Mock, P.; Schmid, S. A. *J. Power Sources,* **2009,** 190, 133.

**[68]** Kjelstrup, S.; Coppens, M. O.; Pharoah, J. G.; Pfeifer, P. *Energy Fuels,* DOI:10.1021/ef100610.

**[69]** http://www.fuelcells.org/info/library/ADLCostModel.pdf accessed on **20th September, 2010.**

**[70]** Wang, X.; Li, W.; Chen, Z.; Waje, M.; Yan, Y. *J. Power Sources,* **2006,** 158, 154.

**[71]** Kilina, S. V.; Habenicht, B. F. Excitonic and Vibrational Dynamics in Nanotechnology. Quantum dots Vs Nanotubes. Pan Stanford Publishing Pte. Ltd. **2009.**

**[72]** Mahima, S.; Pillai, V. K. *J. Mater. Chem.* **2008,** 18, 5858.

**[73]** Borup, R.; Meyers, J.; Pivovar, B.; Kim, Y. S.; Mukundan, R.; Garland, N.; Myers, D.; Wilson, M.; Garzon, F.; Wood, D.; Zelenay, P.; More, K.; Stroh, K.; Zawodzinski, T.; Wilson, M.; *et al Chem. Rev.* **2007,** 107, 3904.

**[74]** Iijima, S. *Nature* **1991,** 354, 56.

**[75]** Rao, C.N.R.; Govindaraj, A. *Nanotubes and Nanowires,* Royal society of Chemistry, **2005**.

**[76]** Tasis, D.; Tagmatarchis, N.; Bianco, A.; Prato, M. *Chem. Rev*. **2006**, 106, 1105

**[77]** Sun, Y. P.; Fu, K.; Lin, Y.; Huang, W. *Acc. Chem. Res.* **2002,** 35, 1096.

**[78]** Rao, C. N. R.; Satishkumar, B. C.; Govindaraj, A.; Nath, M. *ChemPhysChem* **2001**, 2, 78.

**[79]** Eder, D. *Chem. Rev.* **2010,** 110, 1348.

**[80]** Liu, K.; Wang, W.; Xu, Z.; Bai, X.; Wang, E.; Yao, Y.; Zhang, J.; Liu, Z. *J. Am. Chem. Soc.* **2009,** 131, 62.

**[81]** Kim, Y. A.; Muramatsu, H.; Hayashi, T.; Endo, M.; Terrones, M.; Dresselhaus, M. S. *Chem. Phys. Lett.* **2004**, *398*, 87.

**[82]** Peng, B.; Locascio, M.; Zapol, P.; Li, S.; Mielke, S. L.; Schatz, G. C.; Espinosa, H. D. *Nat. Nanotechnol.* **2008**, *3*, 626.

**[83]** Brozena, A. H.; Moskowitz, J.; Shao, B.; Deng, S.; Liao, H.; Gaskell, K. J.; Wang, Y. *J. Am. Chem. Soc.*, **2010,** 132, 3932.

**[84]** Britto, P. J.; Santhanam, K. S. V.; Rubio, A.; Allonso, J. A; Ajayan, P. M. *Advanced Materials* **1999,** 11, 154.

**[85]** Wu, G.; Xu, B. Q. *J. Power Sources* **2007,** 174, 148.

**[86]** Tang, Z; Poh, C. K.; Lee, K. K.; Tian, Z.; Chua, D. H. C.; Lin, J. *J. Power Sources* **2010,** 195, 155.

**[87]** Chen, X.; Eckhard, K.; Zhou, M.; Bron, M.; Schumann, W. *Anal. Chem.* **2009,** 81 7597.

**[88]** Li, J.; Papadopoulos, C.; Xu, J. *Nature* **1999,** 402, 253.

**[89]** Tans, S. J.; Verschueren, A. R. M.; Dekker, C. *Nature,* **1998,** 393, 49.

**[90]** Diehl, M. R.; Steuerman, D. W.; Tseng, H. R.; Vignon, S. A.; Star, A.; Celestre, P. C.; Stoddart, J. F.; Heath, J. R. *ChemPhysChem,* **2003,** 4, 1335.

**[91]** Javey, A.; Guo, J.; Wang, Q.; Lundstorm, M.; Dai, H. *Nature,* **2003,** 424, 654.

**[92]** Penza, M.; Antolini, F.; Antisari, M. V. *Sensor Actuators B: Chem* **2004,** 100, 47

**[93]** Liu, C.; Fan, Y. Y.; Cong, H. T.; Cheng, H. M.; Dresselhaus, M. S. *Science,* **1999,** 286, 1127.

**[94]** Rajalakshmi, N.; Dhathathreyan, K. S.; Govindaraj, A.; Satishkumar, B. C. *Electrochim.Acta*, **2000,** 45, 4511.

**[95]** Nutzenadel, C.; Zuttel, D.; Schlapbach, L. *Electrochemical Solid-State Letters*, **1999,** 2, 30.

**[96]** Zuttel, A.; Sudan, P.; Mauron, P.; Kiyobayashi, T.; Emmenegger, C.; Schlapbach, L. *Int. J. Hydrogen Energy*, **2002,** 27, 203.

**[97]** Barisci, J. N.; Wallace, G. G.; Baughman, R. H. *J. Electroanal. Chem.*, **2000,** 488, 92.

**[98]** Luxembourg, D.; Flamant, G.; Guillot, A.; Laplaze, D. *Mater Sci Eng: B* **2004,** 108, 114.

**[99]** Planeix, J. M.; Coustel, N.; Coq, B.; Brotons, V.; Kumbhar, P. S.; Dutartre, R.; Bernier, P. Ajayan, P. M. *J. Am. Chem. Soc*, **1994,** 116, 7935.

**[100]** Dai, H.; Hafner, J. H.; Rinzler, A. G.; Colbert, D. T.; Smalley, R. *Nature* **1996,** 384, 147.

**[101]** Gao, B.; Kleinhammes, A.; Tang, X. P.; Bower, C.; Fleming, L.; Wu, Y.; Zhou, O. *Chem. Phys. Lett.*, **1999,** 307, 153.

**[102]** Zhao, J.; Buldum, A.; Han, J.; Lu, J. P. *Phys. Rev. Lett.,* **2000,** 85, 1706.

**[103]** Frackowiak, E.; Jurewicz, K.; Delpeux, S.; Beguin, F. *J. Power Sources,* **2001,** 97, 822.

**[104]** Frackowiak, E.; Beguin, F. *Carbon,* **2001,** 39, 937.

**[105]** Baughman, R. H.; Cui, C.; Zakhidov, A. A.; Iqbal, Z.; Barisci, J. N.; Spinks, G. M.; Wallace, G. G.; Mazzoldi, A.; Rossi, D. D.; Rinzler, A. G.; Jaschinski, O.; Roth, S.; Kertesz, M.; *Science,* **1999,** 284, 1340.

**[106]** Landi, B. J.; Raffaelle, R. P.; Heben, M. J.; Alleman, J. L.; vanDerveer, W.; Gennett, T. *Nano Letters,* **2002,** 2, 1329.

**[107]** Sainsbury, T.; Fitzmaurice, D. *Chem Mater.* **2004**, 16, 3780.

**[108]** Ellis, A.V.; Vijayamohanan, K.; Goswami, R.; Chakrapani, N.; Ramanathan, L. S.; Ajayan, P. M.; Ramanath, G. *Nano Lett* **2003,** 3, 279.

**[109]** Goff, A. L.; Artero, V.; Jousselme, B.; Tran, P. D.; Guillet, N.; Metaye, R.; Fihri, A.; Palacin, S.; Fontecave, M. *Science* **2009,** 326, 1384.

**[110]** M. Monthioux, E. Flahaut, *Materials Science and Engineering: C* **2007,** 27, 1096.

**[111]** Pumera, M. *Chem. Eur. J.* **2009,** 15, 4970.

**[112]** Dumitrescu, I.; Unwin, P. R.; Macpherson, J. V. *Chem. Commun,* **2009,** 6886

**[113]** Bahr, J. L.; Yang, J.; Kosynkin, D. V.; Bronikowski, M. J.; Smalley, R. E.; Tour, J. M.; *J. Am. Chem. Soc.* **2001**, 123, 6536.

**[114]** Kooi, S. E.; Schlecht, U.; Burghard, M.; Kern, K.; *Angew. Chem. Int. Ed.* **2002,** 41, 1353.

**[115]** Wang, Y.; Iqbal, Z.; Mitra, S. *Carbon* **2005,** 43, 1015.

**[116]** Mickeson, E. T.; Huffman, C. B.; Rinzler, A. G.; Smalley, R. E.; Hauge, R. H.; Margrave, J. L. *Chem. Phys. Lett.* **1998,** 296, 188.

**[117]** Zhang, L.; Kiny, V. U.; Peng, H.; Zhu, J. M.; Lobo, R. F.; Margrave, J. L.; Khabashesku, V. N. *Chem. Mater.* **2004,** 16, 2055.

**[118]** Oki, A.; Adams, L.; Khabashesku, V.; Edigin, Y.; Biney, P.; Luo, Z. *Materials Letters,* **2008,** 62,918.

**[119]** Santhosh, P.; Gopalan. A.; Lee. K. L. *Journal of Catalysis* **2006,** 238, 177.

**[120]** Shen, M.; Wang, S. H.; Shi, X.; Chen, X.; Huang, Q.; Petersen, E. J.; Pinto, R. A.; Baker Jr, J. R.; Weber Jr, W. J.; *J. Phys. Chem. C.* **2009,** 113, 3150.

**[121]** Kakade, B.; Patil, S.; Sathe, S.; Gokhale, S.; Pillai, V. *J. Chem. Sci.* **2008,** 120, 599.

**[122]** Shen, M.; Wang, S. H.; Shi, X.; Chen, X.; Huang, Q.; Petersen, E. J.; Pinto, R. A.; Baker Jr, J. R.; Weber Jr, W. J.; *J. Phys. Chem. C.* **2009,** 113, 3150.

**[123]** Gewirth, A. A.; Thorum, M. S. *Inorg. Chem.* **2010,** 49, 3557.

**[124]** http://www.platinum.matthey.com/pgm-prices/price-charts/ accessed on **20th September, 2010.**

**[125]** Gong, K.; Du, F.; Xia, Z.; Durstock, M.; Dai, L. *Science* **2009,** 323 760.

**[126]** Tang, Y.; Allen, B. L.; Kauffman, D. R.; Star, A. *J. Am. Chem. Soc.* **2009,** 131, 13200.

**[127]** Du, H. Y.; Wang, C. H.; Hsu, H. C.; Chang, S. T.; Chen, U. S.; Yen, S. C.; Chen, L. C.; Shih, H. C.; Chen, K. H. *Diamond & Related Materials* **2008,** 17, 535.

**[128]** Sun, X.; Li, R.; Villers, D.; Dodelet, J. P.; Désilets, S. *Chemical Physics Letters* **2003,** 379, 99.

**[129]** Wang, X.; Waje, M.; Yan, Y. *Electrochemical and Solid-State Letters,* **2005,** 8, A42.

**[130]** Li, W.; Wang, X.; Chen, Z.; Waje, M.; Yan, Y.; *Langmuir,* **2005,** 21 9386.

**[131]** Wang, C.; Waje, M.; Wang, X.; Tang, J. M.; Haddon, R. C.; Yan, Y. *Nano Letters,* **2004,** 4, 345.

**[132]** Frank, S.; Poncharal, P.; Wang, Z. L.; de Heer, W. A. *Science* **1998,** 280, 1744.

**[133]** Liang, W.; Bockrath, M.; Bozovic, D.; Hafner, J. H.; Tinkham, M.; Park, H. *Nature,* **2001**, 411, 665.

**[134]** Lin, J. F.; Kamavaram, V.; Kannan, A. M. *J. Power Sources*, **2010,** 195 466.

**[135]** Kannan, A. M.; Kanagala, P.; Veedu, V. *J. Power Sources* **2009,** 192, 297.

**[136]** Huang, J. E.; Guo, D. J.; Yao, Y. G.; Li, H. L. *J. Electroanalytical Chemistry* **2005,** 577, 93.

**[137]** Li, W.; liang, C.; Zhou, W.; Qiu, J.; Zhou, Z.; Sun, G.; Xin, Q. *J. Phys. Chem. B* **2003,** 107, 6292.

**[138]** Girishkumar, G.; Vinodgopal, K.; Kamat, P. V. *J. Phys. Chem. B,* **2004,** 208 19960.

**[139]** Reddy, A. L. M.; Ramaprabhu, S. *J. Phys. Chem. C,* **2007,** 111 16138.

**[140]** Wang, J.; Yin, G.; Liu, H.; Li, R.; Flemming, R. L.; Sun, X. *J. Power Sources,* **2009,** 194, 668.

**[141]** Rajalashmi, N.; Ryu, H.; Shaijumon, M. M.; Ramaprabhu, S. *J. Power Sources,* **2005,** 140, 250.

**[142]** Villers, D.; Sun, S. H.; Serventi, A. M.; Dodelet, J. P.; Désilets, S. *J. Phys. Chem. B,* **2006,** 110, 25916.

**[143]** Li, X.; Hsing, I. M. *Electrochim. Acta* **2006,** 51, 5250.

**[144]** Wu, G.; Xu, B. Q. *J. Power Sources,* **2007,** 174, 148.

**[145]** Girishkumar, G.; Rettker, M.; Underhille, R.; Binz, D.; Vinodgopal, K.; Mcginn, P.; Kamat, P. *Langmuir*, **2005,** 21, 8487.

**[146]** Du, C. Y.; Zhao, T. S.; Liang, Z. X. *J. Power Sources,* **2008,** 176, 9.

**[147]** Wu, P.; Li, B.; Du, H.; Gan, L.; Kang, F.; Zeng, Y. *J. Power Sources,* **2008,** 184, 381.

**[148]** Choi, H. C.; Shim, M.; Bangsaruntip, S.; Dai, H. *J. Am. Chem. Soc.* **2002,** 124, 9058.

**[149]** Kazaoui, S.; Minami, N.; Matsuda, N.; Kataura, H.; Achiba, Y. *Appl. Phys. Lett.* **2001,** 78, 3433.

**[150]** Suzuki, S.; Bower, C.; Watanabe, Y. *Appl. Phys. Lett.* **2000,** 76, 4007.

**[151]** Tsai, M.C.; Yeh, T. K.; Chen, C. Y.; Tsai, C. H. *Electrochemistry Communications,* **2007,** 9, 2299.

**[152]** Zhu ,W.; Ku, D.; Zheng, J. P.; Liang, Z.; Wang, B.; Zhang. C.; Walsh, G.; *Electrochem. Acta,* **2010,** 55, 2555.

**[153]** Jeng, K. T.; Chien, C. C.; Hsu, N. Y.; Huang, W. M. Chiou, S. D.; Lin, S. H. *J. Power Sources*, **2007,** 164, 33.

**[154]** Petrik, L.; Ndungu, P.; Iwuoha, E. *Nanoscale Res Lett,* **2010,** 5, 38.

**[155]** Liao, S. H.; Hung, C.Zhu, H.; Ma, C. M. Yen, C. Y.; Lin, Y. F.; Weng, C. C. *J. Power Sources*, **2008,** 176, 175.

**[156]** Liao, S. H.; Yen, C. Y.; Weng, C. C.; Lin, Y. F.; Ma, C.C. M.; Yang, C. H.; Tsai, M. C.; Yen, M. Y.; Hsiao, M. C.; Lee, S. J.; Xie, X. F.; Hsiao, Y. H. *J. Power Sources*, **2008,** 185, 1225.

**[157]** Yin, Q.; Sun, K. N.; Li, A. J.; Shao, L.; Liu, S. M. Sun, C. *J. Power Sources,* **2008,** 175, 861.

**[158]** Wu, M.; Shaw, L. L. *J. Power Sources*, **2004,** 136, 37.

**[159]** Hermann, A.; Chaudhuri, T.; Spagnol, P. *Int. J. Hydrogen Energy*, **2005,** 30, 1297.

**[160]** Wind, J.; Spah, R.; Kaiser, W.; Böhm, G. *J. Power Sources,* **2002,** 105, 256.

**[161]** Choi, H. S.; Han, D. h. Hong, W. H.; Lee, J. J. *J. Power Sources*, **2009,** 189, 966.

**[162]** Wieser, S. *Fuel Cells,* **2004,** 4, 245.

**[163]** Springer, T. E.; Wilson, M. S.; Gottesfeld, S. *J. Electrochem. Soc.*, **1993,** 140, 3513.

**[164]** Lee, J. H.; Paik, U.; Choi, J. Y.; Kim, K. K.; Yoon, S. M.; Lee, J.; Kim, B. K.; Kim, J. M.; Park, M. H.; Yang, C. W.; An, K. H. Lee, Y. H. *J. Phys. Chem. C.* **2007,** 111, 2477.

**[165]** Engtrakul, C.; Davis, M. F.; Gennett, T.; Dillon, A. C.; Jones, K. M.; Heben, M. J. *J. Am. Chem. Soc.* **2005**, *127*, 17548.

**[166]** Landi, B. J.; Raffaelle, R. P.; Heben, M. J.; Alleman, J. L.; VanDerveer, W.; Gennett, T. *Nano Lett,* **2002,** 2, 1329.

**[167]** Liu, Y. H.; Yi, B.; Shao, Z. G.; Xing, D.; Zhang, H. *Electrochemical and Solid-State Letters,* **2006,** 9, A356.

**[168]** Liu, Y. H.; Yi, B.; Shao, Z. G.; Wang, L.; Xing, D.; Zhang, H. *J. Power Sources* **2007,** 163, 807.

**[169]** Thomassin, J. M.; Kollar, J.; Caldarela, G.; Germain, A.; Jérôme, R.; Detrembleur, C. *J. Membr. Sci.* **2007,** 303, 252.

**[170]** Okamoto, M.; Fujigaya, T.; Nakashima, N. *Adv. Funct. Mater.* **2008,** 18, 1776.

**[171]** Lu, Y.; Chen, J.; Cui, H.; Zhou, H. *Composites Science and Technology* **2008,** 68, 3278.

**[172]** Shao, H.; Shi, Z.; Fang, J.; Yin, J. *Polymer,* **2009,** 50, 5987.

**[173]** Li, N. Zhang, F.; Wang, J.; Li, S.; Zhang, S. *Polymer,* **2009,** 50, 3600.

**[174]** Ajayan, P. M.; Schadler, L. S.; Giannaris, C.; Rubio, A. *Adv. Mater*. **2000,** 12, 750.

**[175]** Kymakis, E.; Alexandou, I.; Amaratunga, G. A. J. *Synthetic Metals,* **2002,** 127, 59.

**[176]** Coleman, J. N.; Khan, U.; Blau, W. J.; Gunko, Y. K. *Carbon,* **2006,** 44, 1624.

**[177]** ) Narayanan, S. R.; Yen, S. P.; Greenbaum, S. G. *J. Phys. Chem. B.* **2006,** 110, 3942

**[178]** Lin, B.; Cheng, S.; Qiu, L.; Tan, F.; Shan, S.; Lu, J. *Chem. Mater.*, **2010,** 22, 1807.

**[179]** Suryani, liu, T. L. *J. Membr. Sci.* **2009,** 121.

**[180]** Tsang, E. M. W.; Zhang, Z.; Shi, Z.; Soboleva, T.; Holdcraft, S. *J. Am. Chem. Soc.*, **2007,** 129, 15106.

**[181]** Yang, Y.; Holdcraft, S. *Fuel Cells,* **2005,** 5, 171.

**[182]** Mauritz, K. A.; Moore, R. B. *Chem. Rev.* **2004,** 104, 4535.

**[183]** Rohr, K. S.; Chen, Q. *Nature Materials* **2008,** 7, 75.

**[184]** Kreuer, K.D.; Paddison, S.J.; Spohr, E.; Schuster, M. *Chem. Rev.*, **2004,** 104, 4637.

**[185]** Wainright, J.S.; Wang, J.T.; Weng, D.; Savinell, R.F.; Litt, M. *J. Electrochem. Soc.*, **1995,** 142, L121.

**[186]** Kerres, J.A. *J. Membr. Sci.* **2001,** 185, 3.

**[187]** Kreuer, K.D.; Paddison, S.J.; Spohr, E.; Schuster, M. *Chem. Rev.*, **2004,** 104, 4637.

**[188]** Mustarelli, P.; Quartarone, E.; Grandi, S.; Carollo, A. Magistris, A. *Adv. Mater*, **2008,** 20, 1339.

**[189]** Li, Q.; He, R.; Jensen, J.O.; Bjerrum, N.J. *Chem. Mater.*, **2003,** 15, 4896.

**[190]** Pu, H.; Meyer, W. H.; Wegner, G. *J. Polym. Sci., Part B: Polym. Phys.* **2002**, *40*, 663.

**[191]** Weng, D. Ph.D. Thesis, Case Western Reserve University, Cleveland, OH (**1996**).

**[192]** Quartarone, E.; Mustarelli, P.; Carollo, A.; Grandi, S.; Magistris, A.; Gelbaldi, C. *Fuel Cells* **2009,** 09, 231.

**[193]** Hasiotis, C.; Qingfeng, L.; Deimede, V.; Kallitsis, J.K.; Kontoyannis, C.G.; Bjerrum, N.J. *J. Electrochem. Soc.*, **2001,** 148, A513.

**[194]** He, R.; Li, Q.; Xiao, G.; Bjerrum, N.J. *J. Membr. Sci.*, **2003,** 226, 169.

**[195]** Jang, M. Y.; Yamazaki, Y. *J. Power Sources*, **2005,** 139, 2.

**[196]** Chuang, S.W.; Hsu, S.L.C.; Hsu, C.L.; *J. Power Sources*, **2007,** 168, 172.

**[197]** Li, Q.; Pan, C.; Jensen, J.O.; Noye, P.; Bjerrum, N.J. *Chem. Mater.* **2007,** 19, 350.

**[198]** Lu, Y.; Chen, J.; Cui, H.; Zhou, H. *Composites Science and Technology,***2008,** 68, 3278.

**[199]** Xu, H.; Chen, K.; Guo, X.; Fang, J.; Yin, J. *J. Membr. Sci.*, **2007,** 288, 255.

**[200]** Song, J. Y.; Wang, Y. Y.; Wan, C. C. *J. Power Sources*, **1999,** 77, 183.

**[201]** Jankova, K.; Jannasch, P.; Hvilsted, S. *J. Materials Chemistry*, **2004,** 14, 2902.

**[202]** Meyer, W. H. *Adv. Mater.*,**1998,** 10, 439.

**[203]** Kurian, M.; Galvin, M. E. Trapa, P.E.; Sadoway, D. R.; Mayes, A.M. *Electrochimica Acta* **2005,** 50, 2125.

**[204]** Xu, T.; Liu, Z.; Li, Y.; Yang, W. J. Membr. Sci. **2008**, 320, 232.

**[205]** Tang, B.; Wu, P.; Siesler, H. W. J. Phys. Chem. B **2008**, 112, 2880.

**[206]** Tzanetakis, N.; Varcoe, J.; Slade, R. S.; Scott, K. *Electrochem. Commun.* **2003**, 5, 115.

**[207]** Kumar, M.; Singh, S.; Shahi, V. K. *J. Phys. Chem. B.* **2010,** 114, 198.

# Chapter 2

## A $2^{7-3}$ Fractional Factorial Optimization of Polybenzimidazole based Membrane – Electrode Assembly for $H_2/O_2$ Fuel Cell Stacks

This chapter describes the usefulness of a statistical optimization method like fractional factorial design to obtain consistent and reproducible behavior of a membrane-electrode-assembly (MEA) based on a phosphoric acid doped polybenzimidazole (PBI) membrane. This allows reliable performance for a hydrogen - oxygen fuel cell to operate above 150 °C with many intrinsic benefits. Different parameters involved during the MEA fabrication including catalyst loading, amount of binder, processing conditions like temperature and compaction load and also the amount of carbon in the gas diffusion layers (GDL) have been systematically varied according to a $2^{7-3}$ fractional factorial design and the data thus obtained have been analyzed using Yates's algorithm. The mean effects estimated in this way suggest crucial role played by carbon loading in the gas diffusion layer, hot compaction temperature and the binder to catalyst ratio in the catalyst layer for enabling continuous performance. These statistically designed electrodes provide a maximum current density of 1800 mA $cm^{-2}$ and a power density of 280 mW $cm^{-2}$ at 0.35 V, operating at 160 °C using hydrogen and pure oxygen under ambient pressure.

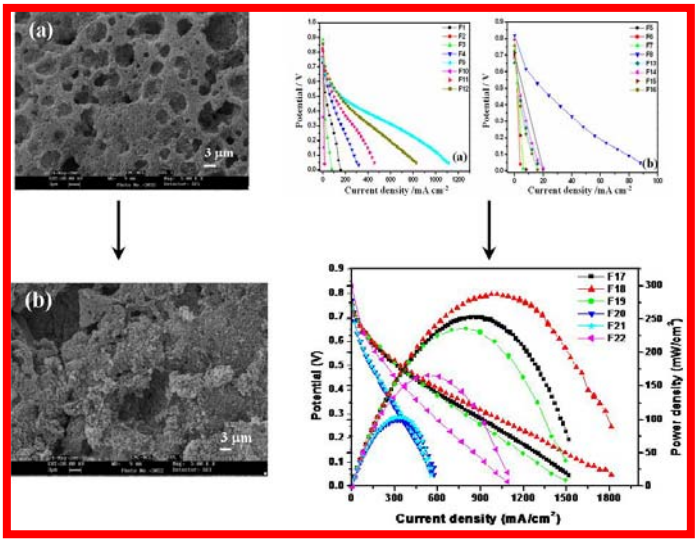


A part of the work discussed in this chapter has been published in *J. Appl. Electrochem* **2008,** 38, 583.

## 2.1. Introduction

Polymer electrolyte membrane fuel cells (PEMFCs) functioning above 120 °C have attracted much attention recently because of their improved efficiency and also for their higher tolerance towards CO, especially if the hydrogen source is from a reformer [1-2]. The performance of widely used perfluorosulphonic acid polymer electrolyte membranes (Nafion®) in fuel cells depends critically on water for their ionic conduction, thus restricting their operating temperatures less then 100 °C. Further, water management at these temperatures is difficult as it increases the system complexity and flooding of cathode by product water is one of the common problems associated with low temperature fuel cells [3-8]. Extensive efforts have been expended recently to develop membranes that can operate at temperatures more than 100 °C [9-34]. Among various type of alternative membranes, phosphoric acid doped polybenzimidazole membranes is one of the most attractive candidates to work at temperatures above 120 °C mainly owing to its higher thermal stability, good proton conductivity when doped with $H_3PO_4$, zero water electro-osmotic drag, invariance of proton conductivity with humidity and hence lesser balance of plant components and finally better combined heat and power (CHP) generation [35-46]. One of the important benefits associated with this membrane includes increased tolerance for CO poisoning at higher operating temperatures (>150 °C) along with improved kinetics towards ORR [47-49]. For example, a tolerance level of 3 % CO in hydrogen is observed at 200 °C with performance comparable to that of pure hydrogen while only 100 ppm level of CO is sufficient to reduce the fuel cell performance at 80 °C [50-52]. This is especially significant for $H_2/O_2$ fuel cells operating with reformed

hydrogen as the fuel, since a complete removal of CO will increase the cost of both hydrogen fuel and electrical energy.

Several groups around the world have devoted attention on PBI membrane and almost all the efforts have been focused on either to improve the membrane behavior along with enhanced ionic conductivity or to increase their mechanical and chemical stability [10-46, 53-56]. However, surprisingly only very few efforts have been expended on the fabrication of membrane electrode assembly (MEA) for PBI based fuel cells, which indeed is, one of the critical processes in fabricating fuel cell stacks. This is in direct contrast to the case of Nafion based MEAs, where the impact of each and every parameter has been well studied during the last two decades [57-62]. For example, Hydrophobic and hydrophilic electrodes have inherent problems in proton/gas transport caused by the properties of binder material (PTFE or Nafion) in catalyst layer (CL) and a novel cathode with dual-bonded CL (hydrophilic/hydrophobic) has been designed and evaluated [63]. The effect of catalyst ink preparation method has been studied by Lobato et al using acetone and dimethylacetamide as solvents [64]. A rather detailed study on the impact of PBI binder in the catalyst layer of anode and cathode has been carried out in tandem with different platinum to carbon ratio by Seland et al [65]. Nevertheless, the role of other parameters like compaction temperature, pressure and amount of carbon in the gas diffusion layer (GDL) has not been studied systematically. This is especially significant since a minor variation in one of these factors can cause a dramatic change in the performance of MEA and hence a thorough study on these parameters for PBI based PEMFCs is essential to ensure the optimum conditions for preparation of MEA [66]. Hence, we have attempted to analyze the impact of 7 critical parameters that we

choose from our earlier experience with PEMFC operations (screening experiments) and analyzed through fractional factorial optimization methods.

### 2.1.1. Factorial Optimization

While the optimization of these parameters is of paramount importance, it requires huge labor and time for a systematic design. Factorial experiments are one of the most efficient designs when multiple parameters interact significantly among themselves and when they have a complimentary impact on each other [67-71]. Further, factorial experiments can point the way to the choice of conditions outside those originally selected by means of which a greater response of the required parameter can be achieved using the “method of steepest ascent”. Still, one big drawback with factorial design is that, the total number of experiments goes up sharply with the number of factors, thus requiring too much of time and resources for optimization. The classical design of experiments also includes too many replications.

The use of fractional factorial experiments can greatly reduce this number of experiments facilitating a quicker realization through the path of steepest ascent. The principle of fractional factorial experiment is that when the higher order effects of two or more combination of experiments are the same, they cannot be distinguished from one another, and hence they can be aliased, thus reducing the total number of experiments. Fractional factorial experiments can be used in experiments involving 4 or more parameters and with increasing number of parameters, the number of experiments to be carried out reduces in comparison to the original set of experiments.

As discussed in Chapter 1, the focus of this thesis is to show the application of functionalized MWCNTs in improving the proton conductivity and mechanical

stability simultaneously. However, it is imperative to know the role of other parameters in determining the fuel cell performance so that their impact can be excluded from the analysis of membrane effects. Accordingly in this chapter, we describe a $2^{7-3}$ fractional factorial design of a PBI based MEA fabrication by analyzing the effect of different parameters such as compaction temperature, pressure, amount of carbon, catalyst and binder in the electrode. The mean effect of each of these parameters as well as their mutual interactions have been analyzed with rigorous error variation (analysis of variance) through Yate's algorithm and the final optimized design has been accomplished based on the path of steepest ascent. The results obtained in the polarization measurements carried out using these optimally designed MEAs at 160 °C under ambient pressure using pure $H_2$ and $O_2$ are presented and examined also through morphological analysis.

## 2.2. Experimental Aspects

### 2.2.1. Membrane Fabrication

Polybenzimidazole (PBI) was synthesized from diaminobenzidine (DAB) and isophthalic acid (IPA, AR Grade) using polyphosphoric acid as a solvent at 200 °C for 20 hours as reported by Iwakura et al [72]. The inherent viscosity of the polymer was 1.2 dl $g^{-1}$ in conc. $H_2SO_4$ (concentration: 0.2 g $dL^{-1}$). The dense membrane was prepared by solution casting method. Typically a 3 % PBI solution in N,N-dimethylacetamide was heated to 80-90 °C and kept for 16 h under dry conditions. The film was subsequently peeled off and treated with water at 60 °C for a week and was then dried under vacuum at 100 °C for 2 days before doping. The membrane was

dipped in 88 % $H_3PO_4$ solution for 72 h and then vacuum dried at 100 °C for 2 days. The $H_3PO_4$ uptake was estimated to be ~13 moles per repeating unit, gravimetrically.

### 2.2.2. Fractional Factorial Design

The seven parameters selected for the fractional factorial design, based on the preliminary screening experiments, along with their normal range are given in Table 2.1. These were selected based on literature reports for Nafion based membranes and

**Table 2.1.** Parameters considered for the $2^{7-3}$ fractional factorial optimization along with their range and treatment code.

| Parameter code | Parameter | Levels | |
|---|---|---|---|
| | | High | Low |
| A | Amount of binder in the catalyst layer | 1 mg/cm$^2$ | 0.2 mg/cm$^2$ |
| B | Electrocatalyst loading | 1 mg/cm$^2$ | 0.1 mg/cm$^2$ |
| C | Amount of carbon in the gas diffusion layer | 5 mg/cm$^2$ | 2 mg/cm$^2$ |
| D | Hot Compaction time | 10 minutes | 1 minute |
| E | Compaction temperature | 150 $^oC$ | 100 $^oC$ |
| F | Hot Compaction load | 0.2 tons/cm$^2$ | 0.04 ton/cm$^2$ |
| G | Amount of PTFE in the gas diffusion layer | 1 mg/cm$^2$ | 0.1 mg/cm$^2$ |

on our previous experience with PBI based membranes. Since 128 experiments were required for completing a $2^7$ factorial optimization study, we decided to carry out a $2^{7-3}$ fractional factorial optimization design, in order to avoid unnecessary wastage of time and resources. The design of 16 experiments with the combination of different

parameters from A to G for a $2^{7-3}$ fractional factorial algorithm is given in Table 2.2. First column of the table gives the experiment code while the last column suggests the corresponding treatment combination of that experiment.

**Table 2.2.** Various treatment combinations corresponding to the Fractional Factorial design of $2^{7-3}$ experiments.

| Exp code | A ($mg/cm^2$) | B ($mg/cm^2$) | C ($mg/cm^2$) | D (min) | E ($^oC$) | F ($ton/cm^2$) | G ($mg/cm^2$) | Treatment combination |
|---|---|---|---|---|---|---|---|---|
| F1 | 0.2 | 0.1 | 2 | 1 | 100 | 0.04 | 0.1 | 1 |
| F2 | 1 | 0.1 | 2 | 1 | 150 | 0.2 | 1 | aefg |
| F3 | 0.2 | 1 | 2 | 1 | 150 | 0.2 | 0.1 | bef |
| F4 | 1 | 1 | 2 | 1 | 100 | 0.04 | 1 | abg |
| F5 | 0.2 | 0.1 | 5 | 1 | 150 | 0.04 | 1 | ceg |
| F6 | 1 | 0.1 | 5 | 1 | 100 | 0.2 | 0.1 | acf |
| F7 | 0.2 | 1 | 5 | 1 | 100 | 0.2 | 1 | bcfg |
| F8 | 1 | 1 | 5 | 1 | 150 | 0.04 | 0.1 | abce |
| F9 | 0.2 | 0.1 | 2 | 10 | 100 | 0.2 | 0.1 | df |
| F10 | 1 | 0.1 | 2 | 10 | 150 | 0.04 | 0.1 | ade |
| F11 | 0.2 | 1 | 2 | 10 | 150 | 0.04 | 1 | bdeg |
| F12 | 1 | 1 | 2 | 10 | 100 | 0.2 | 0.1 | abdf |
| F13 | 0.2 | 0.1 | 5 | 10 | 150 | 0.2 | 0.1 | cdef |
| F14 | 1 | 0.1 | 5 | 10 | 100 | 0.2 | 0.1 | acdg |
| F15 | 0.2 | 1 | 5 | 10 | 100 | 0.04 | 0.1 | bcd |
| F16 | 1 | 1 | 5 | 10 | 150 | 0.2 | 1 | abcdefg |

### 2.2.3. Fabrication of MEA

Two carbon cloths of size 5x5 $cm^2$ were made hydrophobic by imbibing them in 15 % teflon (PTFE) emulsion (Fuel cell stores Inc), followed by air drying for 30 minutes. They were further heat treated at 350 °C for 5 h to adhere the PTFE intimately with

the carbon cloth. Carbon ink was made by combining appropriate amount of Vulcan XC-72 carbon (Cabot Corporation) with PTFE emulsion in cyclohexane and ultrasonically mixing for 30 minutes. The carbon ink was brushed on the carbon cloths till it reached the desired loading levels. The loading levels were double in the membrane facing side of the carbon cloth. These carbon cloths were cold pressed at 0.02 tons per $cm^2$ for 1 min and then kept in a furnace at 350 $^oC$ for 30 min.

Catalyst ink was prepared by adding 20 % Pt/C and 1 % PBI solution in dimethylacetamide. This mixture was ultrasonicated for 30 minutes and the resulting ink was brushed on the surface of the GDL in a hot plate until the desired loading was reached. On top of the catalyst layer a thin layer of PBI solution was given and the resulting electrodes were dried and hot pressed uni-axially with the $H_3PO_4$ doped PBI membrane. This MEA was kept in a desiccator for one day in order for the catalyst layer to get saturated with the excess $H_3PO_4$ present in the membrane. SEM images were taken for four different combinations of carbon and PTFE and for the optimized design (Leica Stereoscan 440 model EDAX system). All the GDLs prepared in this study were basically comprised of four combinations designated as GDL 1 to 4. The combinations of GDL 1 to 4 were as follows. GDL 1: 2 mg $cm^{-2}$ carbon and 0.1 mg $cm^{-2}$ PTFE, GDL 2: 2 mg $cm^{-2}$ carbon and 1 mg $cm^{-2}$ PTFE, GDL 3: 5 mg $cm^{-2}$ carbon and 0.1 mg $cm^{-2}$ PTFE, GDL 4: 5 mg $cm^{-2}$ carbon and 1 mg $cm^{-2}$ PTFE. The combination of GDL 5 was that of the optimized design.

### 2.2.4. Fuel Cell Testing

All the MEAs were tested on an Arbin fuel cell test station (Model: Arbin-001 MITS Pro-FCTS 5.0-FCTS) under non-humidified conditions. Prior to the testing, the MEAs

were conditioned by monitoring the open circuit potential (OCV) for 30 minutes to ensure its stability at constant temperature (160 $^{o}$C) and subsequently conditioned at 0.2 V for 30 minutes after which polarization measurements were carried out. A pin type flow field (figure 2.1) was used and $H_2$ and $O_2$ flow rates were maintained constant at 1 standard liter per minute (slpm). The cells were operated at 160 $^{o}$C through a pair of external electrical heating elements.

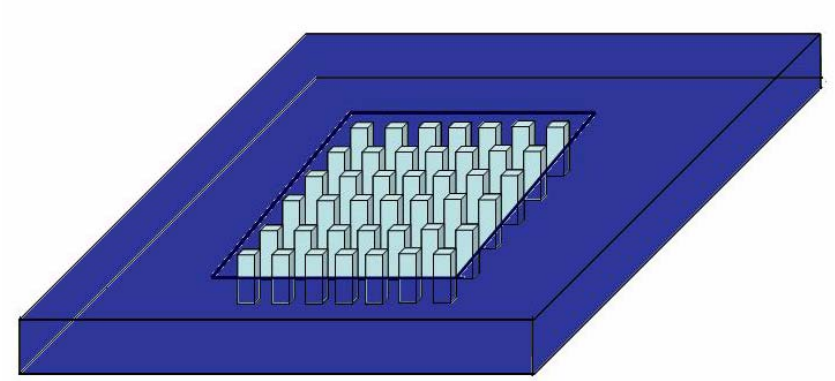

**Figure 2.1.** Schematic representation of pin type flow field used for the factorial optimization explained in this chapter.

## 2.3. Results and Discussion

### 2.3.1. Polarization Studies

Figure 2.1 shows the Polarization plot obtained for all the MEAs as per the $2^{7-3}$ design and a dramatic change in performance from 4 mA cm$^{-2}$ to 1100 mA cm$^{-2}$ due to the variations in the fabrication conditions can be clearly observed. The maximum current density in each experiment is considered as the main response for calculating the mean effects as given in the third column of Table 2.3. From Figure 2.2 and Table 2.3, it is clear that F9 gives the maximum current density of 1100 mA cm$^{-2}$ where the carbon loading is only 2 mg cm$^{-2}$. Similarly, MEAs with less carbon loading (2 mg

$cm^{-2)}$ give better performance compared to that of MEAs with higher carbon loading (5 mg $cm^{-2}$) considering equal level of all other parameters. The maximum current density obtained with higher carbon loading is 87 mA $cm^{-2}$, which is far less compared to that of MEAs with lower carbon loading. Even though other parameters in the fabrication are also varied during those experiments, a close inspection reveals the critical role of the amount of carbon in the diffusion layer than that of all other parameters. This could be due to the blocking of the gas transport by the excess carbon present in the GDL, preventing them to reach the catalyst layer at the electrode electrolyte interface.

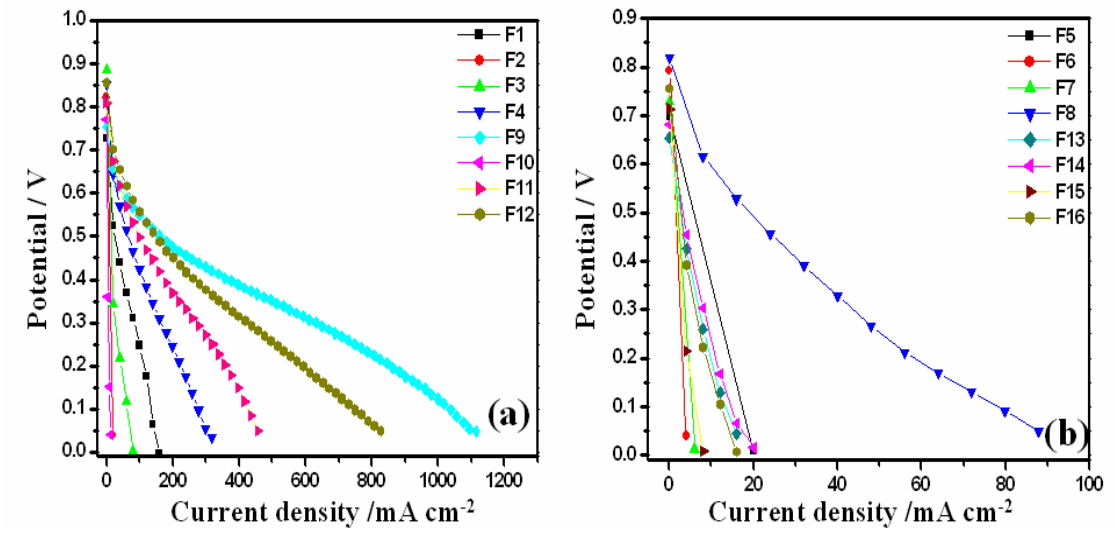


**Figure 2.2.** Polarization plots obtained during the fractional factorial optimization experiments. The cells were operated at 160 $^{o}$C with Pure $H_2$ and $O_2$ as fuel and oxidant; the details of the experiment combinations from F1 to F16 are given in Table 2.2.

### 2.3.2. SEM Analysis

To confirm the exact role of carbon in the GDL in determining the performance of electrodes, SEM images of the GDLs at different resolutions as shown in Figures 2.3 and 2.4 respectively are very helpful. It can be seen from the low resolution SEM

images (Figure 2.3) that in GDL 1 and 2, where the carbon loading is less, the morphology of the bare carbon cloth is observable even after brushing carbon to prepare the gas diffusion layer, while in GDL 3 and 4, only a uniform and dense layer of carbon can be seen.

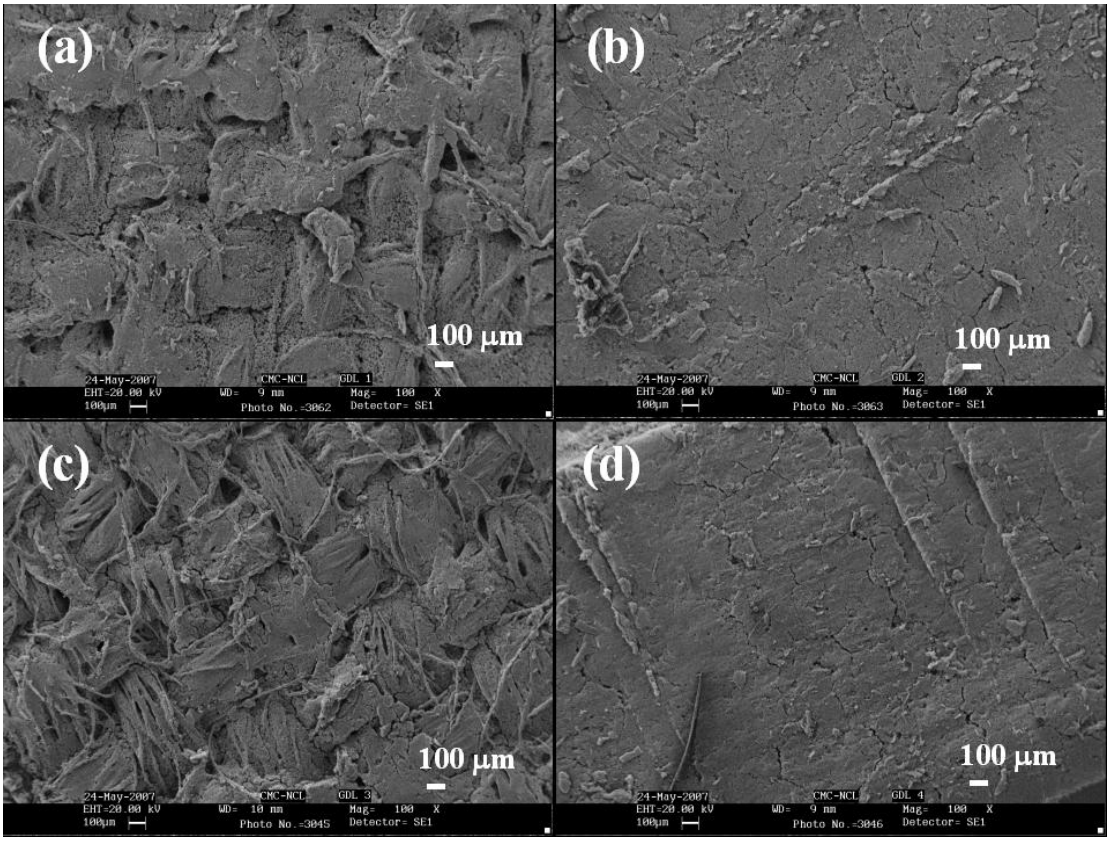


**Figure 2.3.** SEM images of (a) GDL 1, (b) GDL 3, (c) GDL 2, (d) GDL 4; GDL 1 to 4 are made with different carbon and binder ratio according to the factorial design and the details are given in experimental section.

Further, in Figure 2.4, we can see the micro pores in GDL 1, but in GDL 3 and 4, it is hardly observed because of the high content of carbon, which reduces the porosity. However, these micro pores are not seen in GDL 2 even though the carbon loading is less. This can be attributed to the high content of PTFE that binds the carbon together leading to a layered sheet like structure with less number of pores. All

the above mentioned factors together justify the higher current density obtained with F9, where the GDL composition is that of GDL 1.

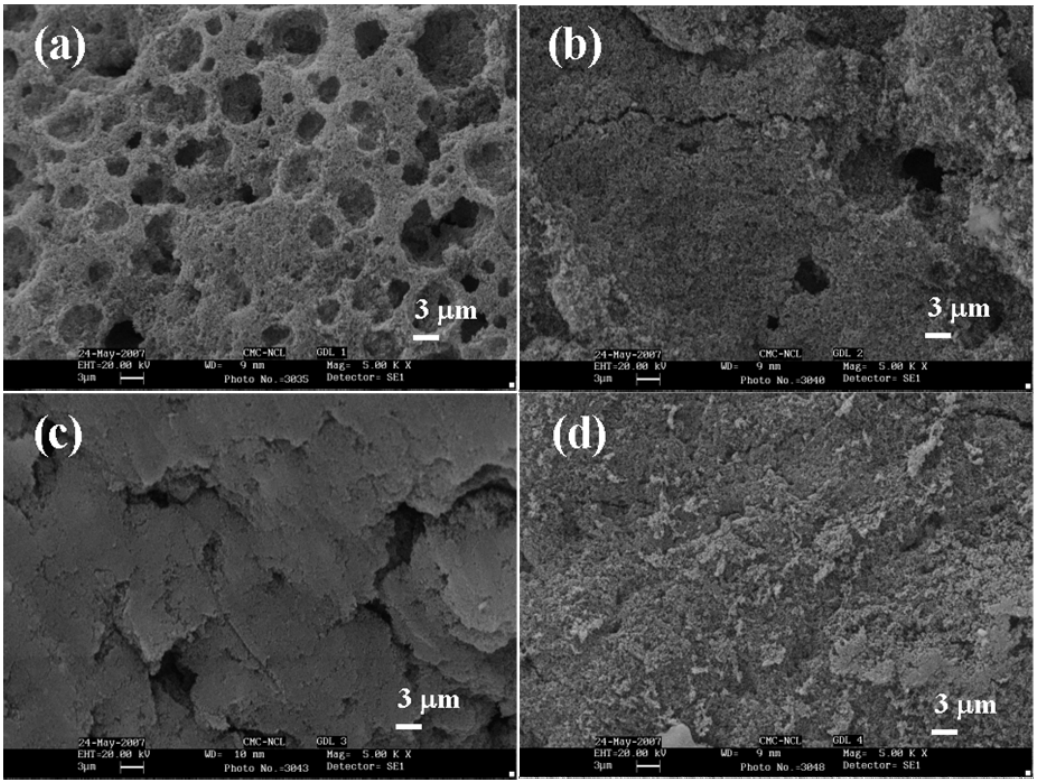


**Figure 2.4.** Magnified SEM images of (a) GDL1, (b) GDL 3, (c) GDL 2, (d) GDL 4; GDL 1 to 4 are made with different carbon to binder ratio according to the factorial design and the details are given in experimental section.

Another factor that shows a significant impact on the performance of the MEA is compaction temperature. The maximum current density values are obtained with lower compaction temperature, perhaps due to the fact that pressing the membranes at higher temperature causes the membrane to loose its mechanical stability, concomitantly leading to the leaching out of additional $H_3PO_4$ from the membrane, with plausible physical damage. This could be further confirmed by carrying out separate experiments by hot pressing the membranes at 100 and 150 $^oC$ respectively at a pressure of 0.12 tons per $cm^2$ for 5 min to show a corresponding weight loss of 8 %

**Table 2.3.** Yate's analysis on the current density values for the treatment combinations from the $2^{7-3}$ experiments and the mean effect values along with the corresponding factor combinations.

| Exp code | Treatment | Response (CD mA/cm2) | Analysis | | | | Mean Effect | Factor |
|---|---|---|---|---|---|---|---|---|
| | | | I | II | III | IV | | |
| F1 | [1] | 160 | 180 | 577 | 707.7 | 3310.7 | 51.72969 | Mean total |
| F2 | aefg | 20 | 397 | 130.7 | 2603 | -599.3 | -9.364063 | A |
| F3 | bef | 80 | 23 | 2544 | 149.7 | 608.7 | 9.510938 | B |
| F4 | abg | 317 | 107.7 | 59 | -749 | 1878.7 | 29.35469 | AB |
| F5 | ceg | 19 | 1112 | 97 | 301.7 | -2931.3 | -45.80156 | C |
| F 6 | acf | 4 | 1432 | 52.7 | 307 | 726.7 | 11.35469 | DG |
| F7 | bcfg | 20 | 36 | -760 | 459.7 | -465.3 | -7.270313 | FG |
| F8 | abce | 87.7 | 23 | 11 | 1419 | -1707.3 | -26.67656 | E |
| F9 | df | 1100 | -140 | 217 | -446.3 | 1895.3 | 29.61406 | D |
| F10 | ade | 12 | 237 | 84.7 | -2485 | -898.7 | -14.04219 | AD |
| F11 | bdeg | 552 | -15 | 320 | -44.3 | 5.3 | 0.082813 | BD |
| F12 | abdf | 880 | 67.7 | -13 | 771 | 959.3 | 14.98906 | F |
| F13 | cdef | 16 | -1088 | 377 | -132.3 | -2038.7 | -31.85469 | AG |
| F14 | acdg | 20 | 328 | 82.7 | -333 | 815.3 | 12.73906 | G |
| F15 | bcd | 8 | 4 | 1416 | -294.3 | -200.7 | -3.135938 | DFG |
| F16 | abcdefg | 15 | 7 | 3 | -1413 | -1118.7 | -17.47969 | DE |

and 13 % respectively. Hence, the significant leaching out of phosphoric acid at 150 $^{o}$C could be attributed as the primary reason behind the poor performance of MEAs with higher compaction temperatures. The remaining parameters also play crucial role on the performance of fuel cells, although their effects are not as apparent as that of carbon loading and compaction temperature. Since Yate's algorithm helps to find the

relative impact of each parameter quantitatively on the performances of MEAs in a systematic manner, all the mean effects estimated accordingly are shown in Table. 2.3.

### 2.3.3. YATEs' Analysis

Yates devised a simple technique for estimating the mean effects and determining the sums of squares in a $2^{k-p}$ fractional factorial design and accordingly Table 2.3 is built based on this strategy. For example, consider the column 3 (response) of Table 2.3. The treatment combinations are written down in standard order and this column contains the observations of each experiment. The first half of the column (I) is obtained by adding the responses in adjacent pairs. The second half is obtained by changing the sign of the first entry in each of the pairs in the response column and adding the adjacent pairs. Column (II) is obtained from column (I) just as column (I) is obtained from the response column and in a similar fashion column (III) and (IV) also obtained from (II) and (III) respectively. In general for a $2^{k-p}$ design, k-p times the analysis is to be carried out and the mean effect values are to be calculated from this column.

Each mean effect value in Table 2.3 has a sign signifying the need for either increasing (positive sign) or decreasing (negative sign) the particular parameter from the mid range to achieve the optimum as per the method of steepest ascent. For example, the amount of carbon in the gas diffusion layer has to be decreased from its midpoint (-45.8) while the amount of catalyst in the catalyst layer has to be increased from its average (9.5), indicating the constructive impact of both these parameters on the fuel cell performance.

### 2.3.4. Optimization Experiments

In order to optimize all the parameters and to follow the path of steepest ascent, the experimental variable with maximum mean effect has to be identified first and for our case this is the amount of carbon loading on the GDL (-45.8). For further optimization, it is feasible to consider a decrease in the carbon loading in 0.25 $mgcm^{-2}$ steps from the average value (one-fifth of the range of carbon loadings). Hence, six further experiments have been designed for locating the global maximum for the MEA fabrication and accordingly the required step change for all other parameters have also been calculated. This final design of such six experiments to accomplish the maximum performance of our PBI based MEA accordingly, is given in Table 2.4.

**Table 2.4.** Optimization design based on the results obtained in the $2^{7-3}$ fractional factorial experiments.

| **Experiments** | A ($mg/cm^2$) | B ($mg/cm^2$) | C ($mg/cm^2$) | D (min) | E ($^oC$) | F ($ton/cm^2$) | G ($mg/cm^2$) |
|---|---|---|---|---|---|---|---|
| F17 | 0.6 | 0.55 | 3.25 | 5.5 | 125 | 0.12 | 0.55 |
| F18 | 0.567 | 0.587 | 3 | 6.66 | 119.18 | 0.13 | 0.6 |
| F19 | 0.534 | 0.624 | 2.75 | 7.82 | 113.34 | 0.14 | 0.65 |
| F20 | 0.501 | 0.661 | 2.5 | 8.98 | 107.5 | 0.151 | 0.7 |
| F21 | 0.468 | 0.698 | 2.25 | 10.14 | 101.66 | 0.162 | 0.75 |
| F22 | 0.435 | 0.735 | 2 | 11.3 | 95.82 | 0.172 | 0.8 |

Figure 2.5 shows the polarization plots for MEAs specially designed as per the final optimization plan of F17 to F22 (Table 2.4). Interestingly, F18 gives the best performance of 1800 mA $cm^{-2}$ as maximum current density, compared to all other

treatment combinations although the preliminary design could provide a maximum current density of only 1100 mA $cm^{-2}$. The SEM image of the GDL of F18 (GDL 5) helps to rationalize this performance with the electrode morphology (Figure 2.6) since GDL 5 surface reveals much reduced pore size and density in comparison with GDL 1. This presumably helps to keep the catalyst layer in tact on the side of the membrane, thus preventing the catalyst particles from crossing the GDL. This, in turn, ensures the maximum efficient utilization of the catalyst particles contributing to

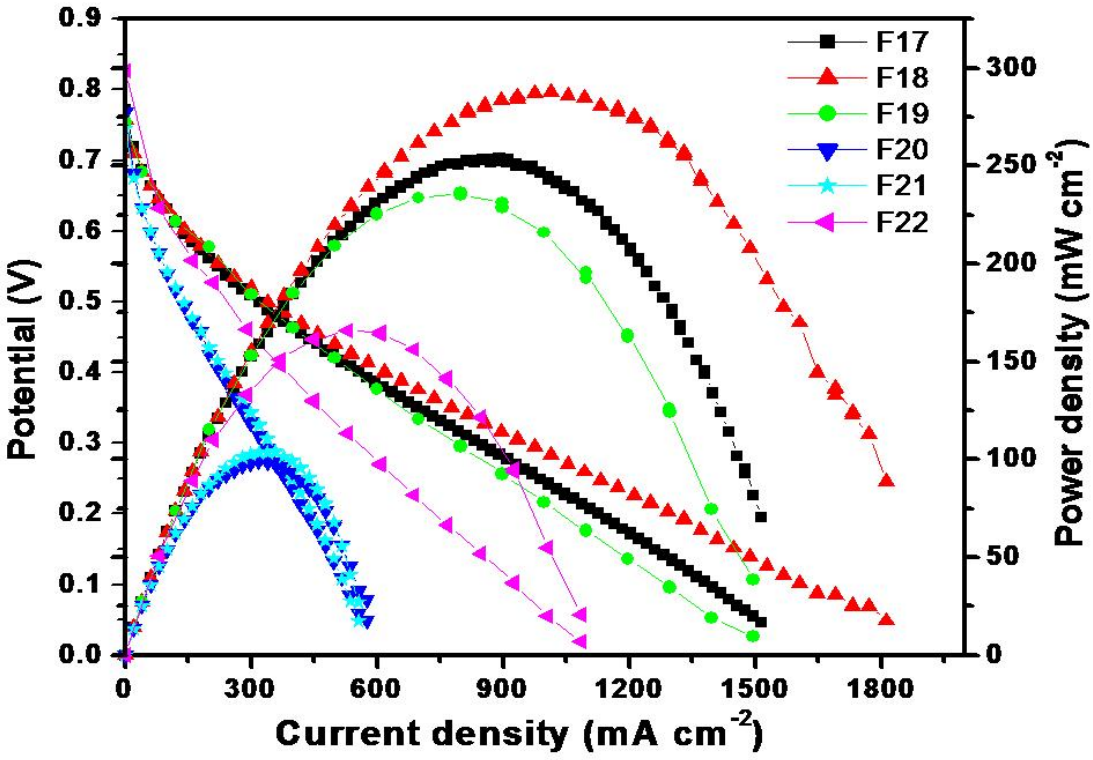


**Figure 2.5.** Polarization plot of the optimization design experiments from F17 to F22. The details of the combinations are given in Table 2.4.

enhanced performance of the fuel cell. However, the performance decreases further (F19 to F22) regardless of the small increment in F22 indicating the likelihood of global maximum, close to the combination represented by F18. From these results it can be surmised that 1:1 catalyst to the binder ratio, hot compaction temperature of

~120 $^{o}$C, and hot pressing time of 6.66 min with a hot compaction load of 0.13 ton cm$^{-2}$ represent the best combination to obtain maximum performance of these PBI based MEAs at 160 $^{o}$C. The reproducibility of performance has been confirmed by fabricating a total of five identical MEAs with the above optimum parameters and their estimated standard variation in performance is 4 %.

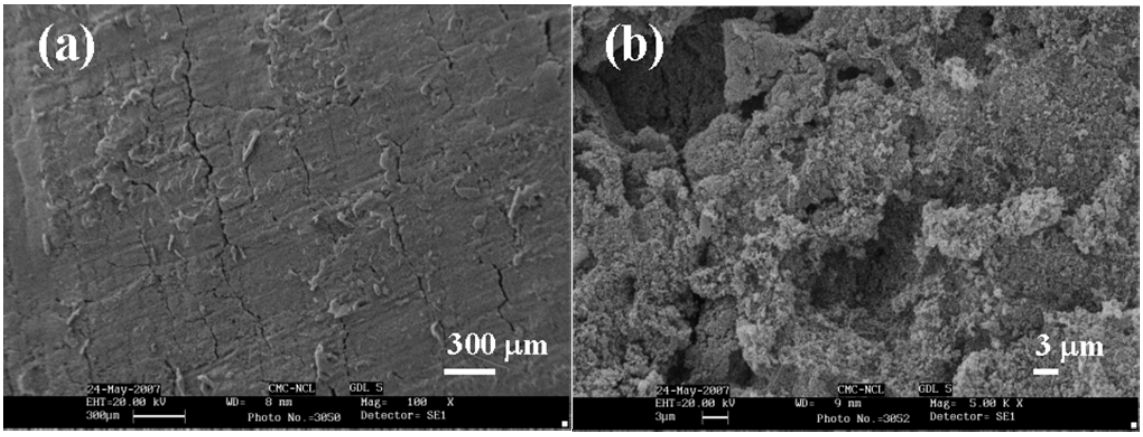


**Figure 2.6.** SEM images of optimized design F18 at two different magnifications (a) 100 K (b) 5000 K.

Although the $2^{7-3}$ fractional factorial experiments have been successful in locating the global maximum with the help of 16 experiments and as per the design the final 6 experiments has enabled confirmation, there are few limitations. A countless number of factors can contribute to the performance of a fuel cell, while we have tested only the most important few among them. For example, the operating conditions and inlet gas flow rates can also alter the performance, which have not been considered in our study. Further, there are several membranes that are being used for high temperature applications under the generic name of PBI and some of the properties might differ for each of them [57, 73]. Despite these limitations, the importance of this kind of fractional factorial study for MEA fabrication could be

reflected by the performance enhancement (about 160%), which undoubtedly suggests the usefulness of these technique for fuel cell researchers.

## 2.4. Conclusions

We have used a $2^{7-3}$ fractional factorial optimization for the MEA fabrication of PBI based fuel cells to accomplish a maximum current density and power density of 1800 mA $cm^{-2}$ and 280 mW $cm^{-2}$ respectively for a continuous operation at 160 °C. The impact of key variables like the amount of carbon in the gas diffusion layer and the electrocatalyst loading has been quantitatively analyzed using their mean effect values and a judicious analysis of their interactions has enabled to accomplish the global optimum by design. The same statistical design could be utilized also for analyzing MEA life or membrane durability as output parameters. Thus, in this chapter, we have accomplished an optimum combination MEA fabrication parameters for PBI based fuel cells which would help in analyzing the properties of PBI-functionalized MWCNT composite membranes.

## 2.5. References

**[1]** Steel, B. C. H.; Heinze, A. *Nature* **2001,** 414, 345.

**[2]** Dresselhaus, M. S.; Thomas, I. L. *Nature* **2001,** 414, 332.

**[3]** Wilikinson, D. P.; Voss, H. H.; Prater, K. *J. Power Sources* **1994,** 49, 117.

**[4]** Mosdale, R.; Srinivasan, S. *Electrochimica Acta* **1995,** 40, 413.

**[5]** Zawodzinski, T. A.; Davey, J.; Valerio, J.; Gottesfeld, S. *Electrochim.Acta* **1995,** 40, 297.

**[6]** van Nguyen, T.; Knobbe, M. W. *J. Power Sources* **2003,** 114, 70.

**[7]** van Bussel, H. P. L. H.; Koene, F. G. H.; Mallant, R. K. A. M. *J. Power Sources* **1998,** 71, 218.

**[8]** Ren, X.; Henderson, W.; Gottesfeld, S. *J. Electrochem. Soc.* **1997,** 144, L267.

**[9]** Narayanan, S. R.; Yen, S. P.; Liu, L.; Greenbaum, S.G. *J. Phys. Chem. B.* **2006,** 110, 3942.

**[10]** Li, Q.; He, R.; Jensen, J. O.; Bjerrum, N. J. *Fuel Cells* **2004,** 4, 147.

**[11]** He, R.; Li, Q.; Bach, A.; Jensen, J. O.; Bjerrum, N. J. *J. Membr. Sci.* **2006,** 277, 38.

**[12]** Wang, J. T.; Savinell, R. F.; Wainright, J.; Litt, M.; Yu, H. *Electrochim. Acta* **1996,** 41, 193.

**[13]** Kongstein, O. E.; Berning, T.; Børresen, B.; Seland, F.; Tunold, R. *Energy* **2007,** 32, 418.

**[14]** Li, Q.; He, R.; Berg, R. W.; Hjuler, H. A.; Bjerrum, N. J. *Solid State Ionics* **2004,** 168, 177.

**[15]** Gieselman, M. B.; Reynolds, J. R. *Macromolecules* **1993,** 26, 5633.

**[16]** Wainright, J. S.; Wang, J. T.; Weng, D.; Savinell, R. F.; Litt, M. *J. Electrochem. Soc.* **1995,** 142, L121.

**[17]** Staiti, P.; Lufrano, F.; Aricò, A. S.; Passalacqua, E.; Antonucci, V. *J. Membr. Sci.* **2001,** 188, 71.

**[18]** Fontanella, J. J.; Wintersgill, M. C.; Wainright, J. S.; Savinell, R. F.; Litt, M. *Electrochim. Acta* **1998,** 43, 1289.

**[19]** Kawahara, M.; Morita, J.; Rikukawa, M.; Sanui, K.; Ogata, N. *Electrochim. Acta* **2000,** 45, 1395.

**[20]** Kerres, J. A. *J. Membr. Sci.* **2001,** 185, 3.

**[21]** Jalani, N. H.; Ramani, M.; Ohlsson, K.; Buelte, S.; Pacifico, G.; Pollard, R.; Staudt, R.; Datta, R. *J. Power Sources* **2006,** 160, 1096

**[22]** Carollo, A.; Quartarone, E.; Tomasi, C.; Mustarelli, P.; Belotti, F.; Magistris, A.; Maestroni, F.; Parachini, M.; Garlaschelli, L.; Roghetti, P. P, *J. Power Sources* **2006,** 160, 175.

**[23]** Xiao, G.; Li, Q.; Hjuler, H. A.; Berg, R. W.; Bjerrum, N. J. *J. Electrochem. Soc.* **1995,** 142, 2890.

**[24]** Xing, B.; Savadogo, O. *J. New Mater. Electrochem. Syst.* **2000,** 3, 345.

**[25]** Pu, H.; Meyer, W. H.; Wegner, G. *J. Polym. Sci., Part B, Polym. Phys.* **2002,** 40, 663.

**[26]** Bouchet, R. ; Siebert, E. *Solid State Ionics* **1999,** 118, 287.

**[27]** Ma, Y. L. ; Wainright, J. S. ; Litt, M. H.; Savinell, R.F. *J. Electrochem. Soc.* **2004,** 151, A8.

**[28]** Li, Q.; Hjuler, H. A.; Bjerrum, N. J. *J. Appl. Electrochem.* **2001,** 31, 773.

**[29]** Lobato, J.; Canizares, P.; Rodrigo, M. A.; Linares, J. J.; Manjavacas, G. *J. Membr. Sci.* **2006,** 280, 351.

**[30]** Li, Q.; He, R.; Gao, J.A.; Jensen, J. O.; Bjerrum, N. J. *J. Electrochem. Soc.* **2003,** 150, A1599.

**[31]** Weng, D.; Wainright, J. S.; Landau, U.; Savinell, R. F. *J. Electrochem. Soc.* **1996,** 143, 1260.

**[32]** Xiao, L.; Zhang, H.; Jana, T.; Scanlon, E.; Chen, R.; Choe, E. W.; Ramanathan, L. S.; Yu, S.; Benicewicz, B. C. *Fuel Cells* **2005,** 5, 287.

**[33]** Saegusa, Y.; Horikiri, M.; Nakamura. S. *Macromol. Chem. Phys.* **1997,** 198, 619.

**[34]** Chiang, S. W.; Hsu, S. L. C. *J. Polym. Sci., Part A: Polym. Chem.* **2006,** 44, 4508.

**[35]** Ma, Y. L.; Wainright, J. S.; Litt, M. H.; Savinell, R. F. *J. Electrochem. Soc.* **2004,** 151, A8.

**[36]** Gottesfeld, S.; Pafford, J. *J. Electrochem. Soc.* **1988,** 135, 2651.

**[37]** Li, Q.; He, R.; Gao, J. A.; Jensen, J. O.; Bjerrum, N. J. *J. Electrochem. Soc.* **2003,** 150, A1599

**[38]** Chu, H. S.; Wang, C. P.; Liao, W. C.;, Yan, W. M. *J. Power Sources* **2006,** 159, 1071.

**[39]** Wang, C. P.; Chu, H, S. *J. Power Sources* **2006,** 159, 1025.

**[40]** Bhatia, K. K.; Wang, C. Y. *Electrochim.Acta* **2004,** 49, 2333.

**[41]** Xu, H.; Song, Y; Kunz, H. R.; Fenton, J. M. *J. Power Sources* **2006,** 159, 979.

**[42]** Krishnan, P.; Park, J. S.; Kim, C. S. *J. Power Sources* **2006,** 159, 817.

**[43]** Cheng, X.; Shi, Z.; Glass, N.; Zhang, L.; Zhang, J.; Song, D.; Liu, Z. S.; Wang, H.; Shen, J. *J. Power Sources* **2007,** 165, 739 (and references therein).

**[44]** Uchida, H.; Izumi, K.; Watanabe, M. *J. Phys. Chem. B* **2006,** 110, 21924.

**[45]** Holladay, J. D.; Wainright, J. S.; Jones, E. O.; Gano, S. R. *J. Power Sources* **2004,** 130, 111.

**[46]** Springer, T. E.; Rockward, T.; Zawodzinski, T. A.; Gottesfeld, S. *J.Electrochem. Soc.* **2001,** 148, A11.

**[47]** Zhang, J.; Sasaki, K.; Sutter, E.; Adzic, R. R. *Science* **2007,** 315, 220.

**[48]** Stamenkovic, V. R.; Fowler, B.; Mun, B. S.; Wang, G.; Ross, P. N.; Lucas, C. A.; Markovic, N. M. *Science* **2007,** 315, 493.

**[49]** Bashyam, R.; Zelanay, P. *Nature,* **2006,** 443, 63.

**[50]** Li, Q.; Pan, C.; Jensen, J. O.; Noyé, P.; Bjerrum, N. J. *Chem. Mater*. **2007,** 19, 350.

**[51]** Garcia, A. C.; Paganin, V. A.; Ticianelli, E. A. *Electrochimica Acta,* **2008,** 53, 4309.

**[52]** Jiang, R.; kunz, H. R.; Fenton, J. M. *Electrochim. Acta,* **2006,** 51, 5596.

**[53]** Staiti, P.; Minutoli, M. *J. Power Sources* **2001,** 94, 9.

**[54]** Lobato, J.; Cañizares, P.; Rodrigo, M. A.; Linares, J. J. *Electrochim. Acta* **2007,** 52, 3910.

**[55]** He, R.; Li, Q.; Xiao, G.; Bjerrum, N. J. *J. Membr. Sci*. **2003,** 226, 169.

**[56]** Hasiotis, C.; Deimede, V.; Kontoyannis, C. *Electrochim. Acta* **2001,** 46, 2401.

**[57]** Metha, V.; Cooper, J. S. *J. Power Sources* **2003,** 114, 32.

**[58]** Litster, S.; Mclean, G. *J. Power Sources* **2004,** 130, 61.

**[59]** Park, C. H.; Scibioh, A.; Kim, H. J.; Oh, I. H.; Hong, S. A.; Ha, H. Y. *J. Power Sources,* **2006,** 162, 1023.

**[60]** Komoda, Y.; Okabayashi, K.; Nishimura, H.; Himomitsu, M.; Oboshi, T.; Usui, H. *J. Power Sources*, **2009,** 193, 488.

**[61]** Velayutham, G.; Dhathathreyan, K. S.; Rajalakshmi, N.; Raman, D. S. *J. Power Sources,* **2009,** 191, 10.

**[62]** Liu, Y.; Ji, C.; Gu, W.; Baker, D. R.; Jorne, J.; Gasteiger, H. A. *J. Electrochem. Soc.*, **2010,** 157, B1154.

**[63]** Zhang, X.; Shi, P. *Electrochem Commun,* **2006,** 8, 1615.

**[64]** Lobato, J.; Rodrigo, M. A.; Linares, J. J.; Scott, K. *J. Power Sources* **2006,** 157, 284.

**[65]** Seland, F.; Berning, T.; Børresen, B.; Tunold, R. *J. Power Sources* **2006,** 160, 27.

**[66]** Williams, J.; Krinke, A. Design of Experiment. Fuel Cell Project, Spring 2005 Available via http://faculty.washington.edu/cooperjs/Education/Fuel%20cell%20class/Fuel%20cell%20reports/SP05%20Design%20of%20Experiments.pdf accessed on **20th September, 2010.**

**[67]** Duckworth, W. E. **1968** Statistical Techniques in Technological Research, Methuen, London.

**[68]** Montgomery, D. C. **1976** Design and Analysis of Experiments, John Wiley and Sons Inc, New York.

**[69]** Grujicic, M.; Chittajallu, K. M. *Applied Surface Science* **2004,** 227, 56.

**[70]** Chaudhary, V. A.; Mulla, I. S.; Sainkar, S. R.; Mandale, A. B.; Vijayamohanan, K. *Sensors and Actuators* **2000,** 79, 224.

**[71]** Kannan, A. M.; Shukla, A. K. Hamnett, A. *J. Appl. Electrochem.* **2005,** 18, 149.

**[72]** Iwakura, Y. ; Uno, K. ; Imai, Y. *J. Polym. Sci., Part A.* **1964,** 2, 2605.

**[73]** Li, Q.; He, R.; Jensen, J.O.; Bjerrum, N.J. *Chem. Mater.*, **2003,** 15, 4896.

# Chapter 3

## Electrocatalytic Activity of Functionalized Carbon Nanotubes and its Composites towards ORR in Different Electrolytes

The present chapter demonstrates the electrocatalytic activity of functionalized carbon nanotubes towards oxygen reduction reaction (ORR) in different electrolytes. Sulphonated MWCNTs show significant ORR catalytic activity in comparison with pristine MWCNTs. The reason for this improved ORR catalytic activity is attributed to the higher exposure of edge planes in the functionalized MWCNTs than that of the pristine MWCNTs. Further, a possible creation of density of states near the Fermi level which, at higher degree of functionalization, form an impurity band that would help to improve the ORR activity of MWCNTs. Interestingly, the surface confined nature of the redox peak observed in MWCNTs corresponding to the functional groups is verified by linear sweep voltammetry measurements at different rotation rates. The role of different electrolytes in facilitating the mass transport of oxygen is also analyzed using PBI and Nafion ionomer binders in sulphuric acid and phosphoric acid medium respectively. Higher viscosity, lower oxygen solubility and variable diffusion coefficient in phosphoric acid are some of the plausible parameters making the transport of oxygen difficult in the presence of ionomer binders and hence limiting current values could not be observed in phosphoric acid electrolyte.

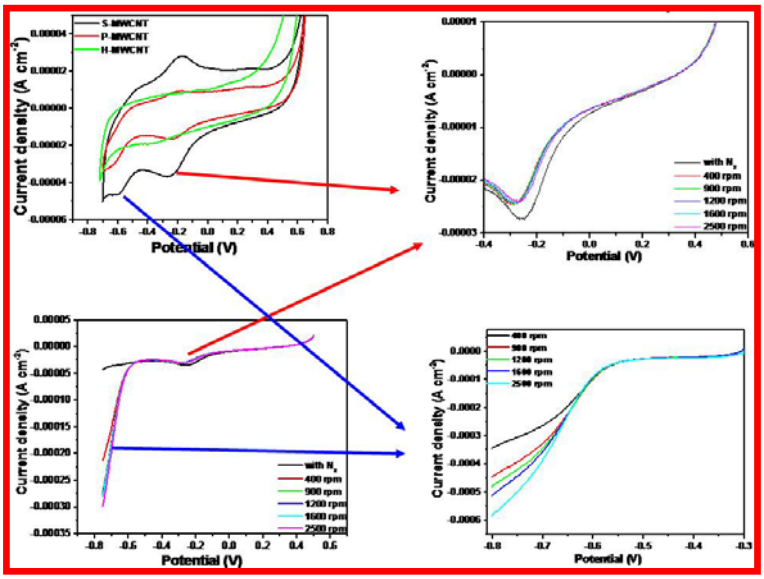


*A part of the work discussed in this chapter has been communicated to the *J. Phys. Chem. C*

## 3.1. Introduction

The performance of polymer electrolyte membrane fuel cells (PEMFCs) is mainly hindered by the sluggish oxygen reduction reaction (ORR) kinetics especially when they are being operated at temperatures less than 100 °C [1,2]. For example, a 100 mV reduction in the overpotential towards ORR can increase the performance of PEMFCs significantly [3]. Carbon nanotubes (CNTs) with their unique electronic properties seem to offer a promising solution in many applications such as molecular wires, nano transistors, biomedical applications, and catalysis [4,5]. Indeed, CNTs tend to play a critical role in improving the performance of different components of PEMFCs such as electrolyte membrane, bipolar plate, catalyst support, gas diffusion layer and electrocatalyst. Further, the recent striking revelation of the nitrogen doped CNT's (N-CNTs) promising electrocatalytic activity towards ORR over commercial platinized carbon catalysts in alkaline medium has opened up new strategies to synthesize cost effective, environment friendly, robust catalyst systems based on functionalized CNTs [6]. Accordingly many metallic systems supported on CNTs have been studied systematically to prove the critical role played by CNTs in improving the key parameters such as exchange current density of a catalyst over carbon black or Vulcan XC supported systems [7]. However, the ability of CNTs alone to catalyze ORR in acidic medium is not well documented mainly due to the amount of impurities present and perhaps also due to variable distribution of dimensions from different source.

CNTs are generally believed to show ORR electrocatalytic activity through a two step peroxide pathway in alkaline medium while in acid medium it is expected to be inert [8]. However, only few reports are available demonstrating the role of

functional groups and metallic impurities as a source of electrocatalytic activity. For example, Alexeyeva *et al* has reported ORR activity for unmodified and pre-treated MWCNTs in acid media where, the onset potential for ORR is shifted by 250 mV towards more negative values for the pre-treated sample in comparison to that of the unmodified MWCNTs. This has been attributed to the presence of metal impurities (~1 %) in the unmodified MWCNTs that play a synergistic role in ORR [9]. However, the origin of ORR activity is not clear. Very recently, it has been further reiterated that the oxygen functionalities in MWCNTs tend to reduce the ORR activity of CNTs along with shifting the onset potentials towards more negative values [10]. However, semi-empirical AM1 (Austin Model 1) simulation studies on the role of oxygen as a hetero atom in CNTs reveal that ca. 4-6 % of oxygen provide the greatest electron donor ability to carbon [11]. This poses a contradiction of the understanding since the simulation suggests the presence of oxygen functionalities as the key for ORR while experimental studies suggest the other way. However, the CNTs in the above experiments had metallic impurities, which might have played a critical role in showing ORR activity. This is further supported by recent reviews, which emphasize the importance of using purified CNTs [12,13] for demonstrating electrocatalytic activity. In addition, CNTs without any surface functional group are reported to show a featureless cyclic voltammogram which reflects the need for a critical density of functional groups thus leaving lot of speculation about the ability of CNTs without nitrogen doping to show ORR activity [14].

Further, the role of ionomer binder in the catalyst layer is another critical parameter, which facilitates the mass transport of protons and oxygen inside the catalyst layer to reach Pt electrocatalyst sites. Also, it is well known that Nafion based

systems show higher proton conductivity and also better mass transport than that of the phosphoric acid doped PBI membranes [15]. Hence, it is essential to identify the role of these two ionomers in modifying the catalytic activity of the functionalized MWCNTs especially in sulphuric acid and phosphoric acid electrolytes. We chose these two electrolytes because of the structural similarities of sulphonic and phosphonic acid groups that are responsible for the proton conductivity of composite electrolytes with Nafion and PBI respectively.

In the previous chapter, we have studied the importance of optimizing MEA fabrication methodology for PBI based PEMFCs with different parameters such as ionomer binder in the catalyst layer and Pt catalyst loading. However, the superiority between Nafion and PBI as binder in the catalyst layer is not yet clarified. Also since functionalized MWCNTs are being used to make composite membranes it is imperative to understand the ORR catalytic activity of these functionalized MWCNTs for the final analysis. Hence, in this chapter, we study the ORR catalytic activity of MWCNTs with and without surface functional groups such as sulphonic acid and phosphonic acid with Nafion and PBI as binders in electrolytes such as 0.5 M sulphuric acid and phosphoric acid. We carried out pre functionalization of the CNTs intentionally under rigorous conditions to remove or minimize any metallic impurities and also to create a higher level of acid functional groups on the surface. This higher degree of functionalization has opened up another possibility of diagnosing the surface confinement behaviour of functional groups on the surface of CNTs along with the ORR activity. Most importantly, in sulphuric acid electrolyte, for sulphonated MWCNTs the number of electrons transferred in ORR as calculated by

Koutecky - Levich plots is shown to be 3.3 which is closer to the 4 electron reduction pathway of ORR.

## 3.2. Experimental Aspects

### 3.2.1. Purification of MWCNTs

MWCNTs with diameters ranging from 12-20 nm and with a purity of >90 % were obtained from Chemapol industries Pvt Ltd, Mumbai, India. The purification of MWCNTs was carried out as follows. MWCNTs (100 mg) were initially mixed with concentrated hydrochloric acid (HCl) (100 ml) and ultrasonicated for 1 h followed by refluxing at 120 °C for 5 h. The resulting mixture was filtered using a PTFE filter with a pore size of 200 nm in a filtration assembly and washed with DI water several times. Subsequently these MWCNTs were dried in an oven at 100 °C overnight and the resulting MWCNTs were further treated with conc.$HNO_3$ at 120 °C to remove any amorphous carbon present and also to induce some acid functional groups on its surface. The resulting mixture was filtered as mentioned above and dried in an oven at 100 °C overnight and stored in sample vials till further use.

### 3.2.2. Preparation of Sulphonated MWCNTs

#### 3.2.2.1. Normal Method

Sulphonated MWCNTs were prepared by mixing purified MWCNTs with a 1:1 mixture of concentrated $HNO_3$ and $H_2SO_4$ and ultrasonicating for 1 h. The resulting mixture was refluxed at 100 °C for 4 h and then allowed to cool to room temperature. Concentrated HCl was added to this mixture and refluxed further for 1 h and then filtered as described in the previous section. A schematic representation for the

preparation of functionalized MWCNTs from the $HNO_3$ purification step is presented in scheme 3.1.

### 3.2.2.2. Microwave Method

Acid treated MWCNTs (100 mg) were mixed with a 1:1 mixture of (50 ml each) $HNO_3$ and $H_2SO_4$ in a conical flask. The mixture was allowed to cool for 10 min followed by microwave treatment. A power of 640 W was used for 5 min with cooling steps after every one min. This mixture was further refluxed with conc. HCl for 1 h followed by filtration and washing as described in the previous section.

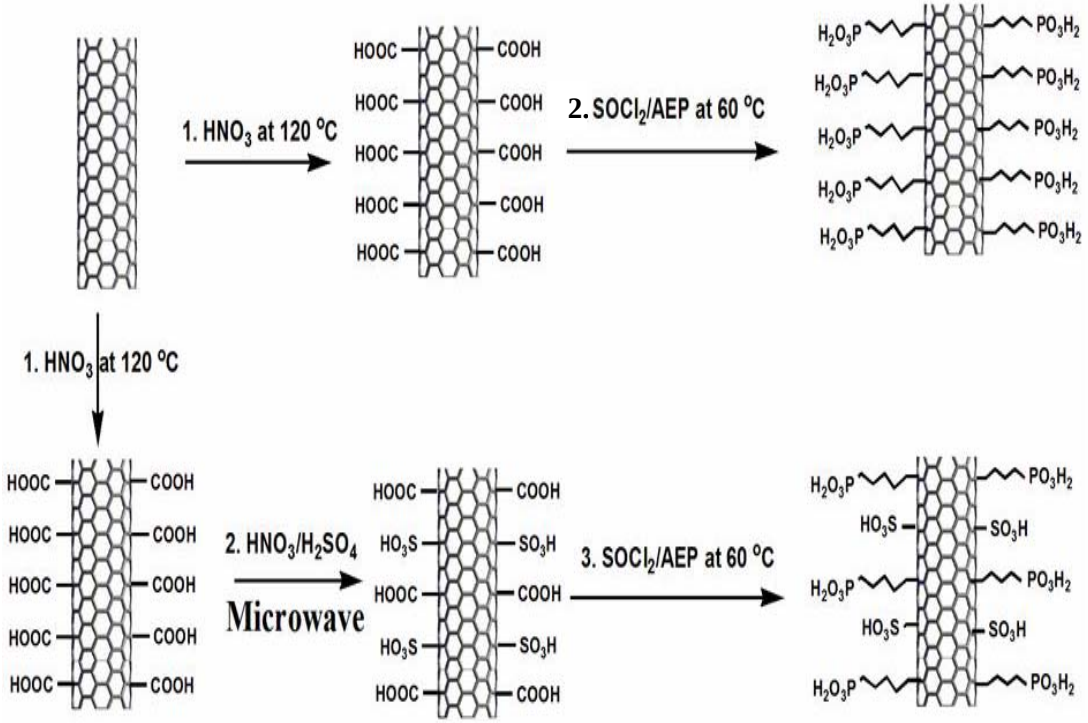


**Scheme 3.1.** Preparation of sulphonated and phosphonated MWCNTs under microwave and normal methods; in normal method, the mixture was heat treated at 100 °C for 5 h.

### 3.2.3. Preparation of Phosphonated MWCNTs

To prepare phosphonated MWCNTs (P-MWCNTs), 100 mg of S-MWCNTs was mixed with 100 mg of 2– amino ethyl phosphonic acid in a conical flask with a top.

To this physical mixture, a mixture of 99 ml of thionyl chloride and 1 ml of dimethyl formamide was added and refluxed at 60 °C for 5 h. The resulting mixture was filtered and washed with dry acetone several times and dried overnight and stored in sample vials till further use.

### 3.2.4. Preparation of MWCNT-Polymer Composite Electrodes

To carry out the cyclic voltammetry and linear sweep voltammetry measurements, 10 mg of functionalized MWCNT was mixed with 1 ml of 1 wt% Nafion and 4 ml of isopropyl alcohol and ultrasonicated for 30 min to prepare Nafion based composite electrodes. For PBI based composite electrodes, 1 ml of 1 wt% PBI in dimethyl acetamide and 4 ml of dimethyl acetamide were used. 30 μl of this mixture was used for drop casting the catalyst on a glassy carbon (GC) electrode and dried under a UV lamp.

### 3.2.5. Characterization of Functionalized MWCNTs

Scanning Electron Microscopy (SEM) and energy dispersive X-ray analysis (EDAX) were carried out on a Quanta 200 3D attached with an energy dispersive X-ray analyzer. X-ray photoelectron spectra (XPS) were recorded on a VG Microtech Multilab ESCA 3000 spectrometer that was equipped with an Mg Kα X-ray source ($h\nu$ = 1253.6 eV). Thermo gravimetric analysis (TGA) was carried out using a Mettler Toledo TGA/SDTA 851 with an oxygen flow rate at 20 ml $min^{-1}$ by keeping the temperature range from room temperature to 800 °C at a scan rate of 10 °C $min^{-1}$. Cyclic Voltammetry and Linear Sweep Voltammetry (LSV) were carried out on an Autolab PGSTAT 30 instrument. The rotation rate of the electrode was controlled by a Pine made rotating disk electrode (RDE) system. A large area Pt foil was used as the

counter electrode while a Pt wire was used as quasi reference electrode. $^{1}H$ and $^{31}P$ NMR of P-MWCNTs were taken in 400 MHz and 500 MHz Bruker instruments respectively using $D_2O$ as the solvent. FT-IR measurements of MWCNTs were taken in a Perkin instrument in the range of 400 to 4000 $cm^{-1}$.

## 3.3. Results and Discussion

### 3.3.1. SEM and EDAX Analysis

Since rigorous experimental conditions have been used to purify and functionalize MWCNTs, it is important to study the integrity of all samples as MWCNTs at least in

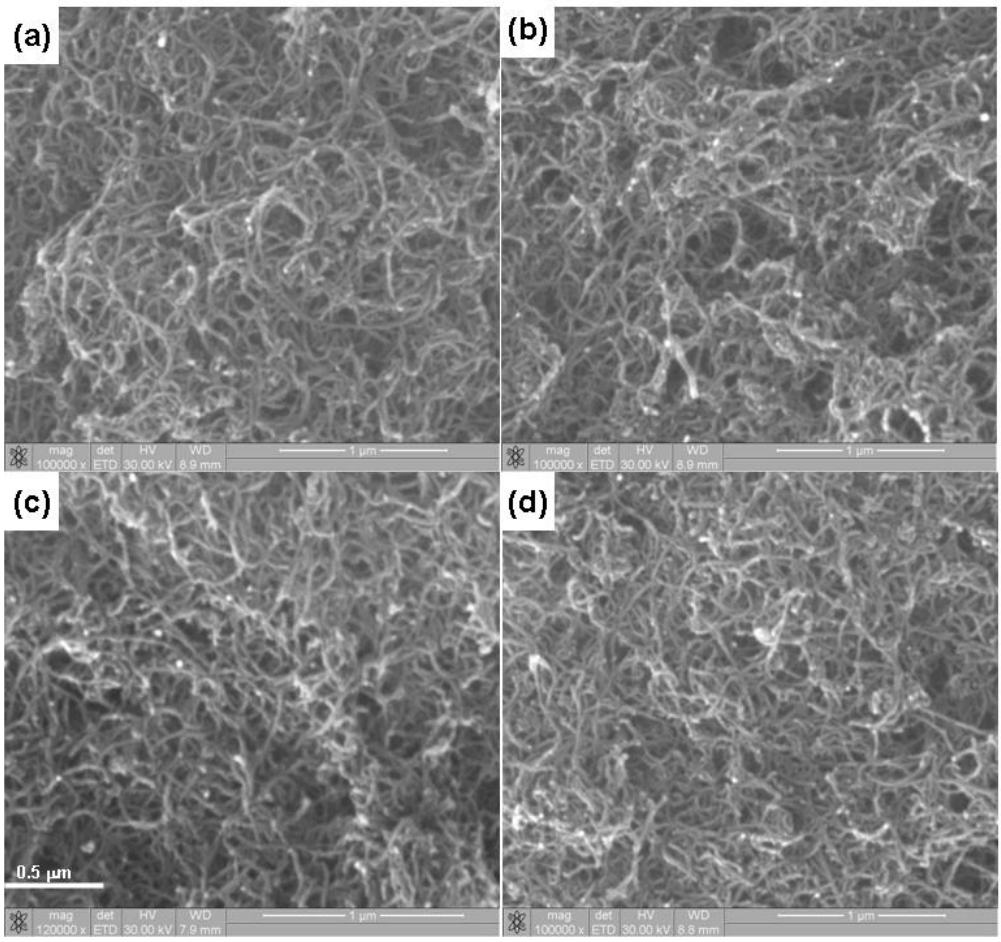


**Figure 3.1.** SEM images of pristine and functionalized MWCNTs obtained by dispersing the MWCNTs in isopropyl alcohol and coating on a copper grid followed by gold sputtering; (a) Pristine MWCNTs, (b) H-MWCNTs, (c) S-MWCNTs and (d) P-MWCNTs; the same scale bar is used for all the four images.

some cases are known to get chopped off by ultrasonication [16-19]. Figure 3.1 accordingly, displays the SEM images obtained with various functionalized MWCNTs, (a) pristine MWCNTs, (b) H-MWCNTs, (c) S-MWCNTs and (d) P-MWCNTs, which clearly demonstrates complete and intact MWCNTs for all functionalized MWCNTs with diameters mostly in the range of 14-20 nm. Further, the absence of any amorphous carbon impurity suggests their complete removal. The MWCNT morphology observed with the pristine and functionalized MWCNTs are very similar with no significant change.

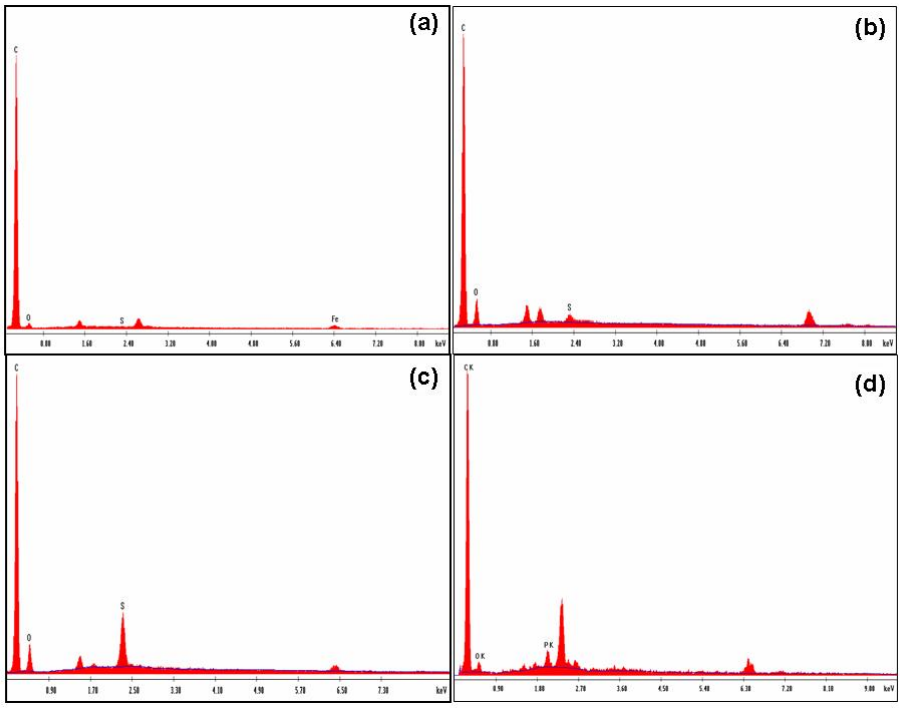


**Figure 3.2.** EDAX data of different functionalized MWCNTs; (a) Pristine MWCNTs, (b) H-MWCNTs, (c) S-MWCNTs and (d) P-MWCNTs; the elements arising from the substrate are left unlabeled.

Figure 3.2 shows EDAX data of different functionalized MWCNTs with S-MWCNT and H-MWCNTs, apparently suggesting the introduction of oxygen and sulphur groups in the functionalized MWCNT. The oxygen and sulphur content in S-MWCNT is 11.8 and 2.2 wt% respectively, while in H-MWCNT the oxygen content

is only 4 wt% which could be due to the hydroxyl groups attached on the tube ends of MWCNTs. In the case of P-MWCNTs, 1 wt% of phosphorous is observed in the EDAX measurements. This clearly indicates the higher level of defect sites present on the functionalized MWCNT surface and higher exposure of edge planes.

### 3.3.2. NMR of P-MWCNTs

While the sulphonic acid groups in S-MWCNTs are known to attach through the sulphur atom to the MWCNTs, the nature of bonding between MWCNT and amino ethyl phosphonic acid (AEP) is not clear since AEP can bind to acid functionalized MWCNTs either through the amide linkage or through the phosphonate group. Despite proving the presence of phosphorous atom in the P-MWCNTs, it is very

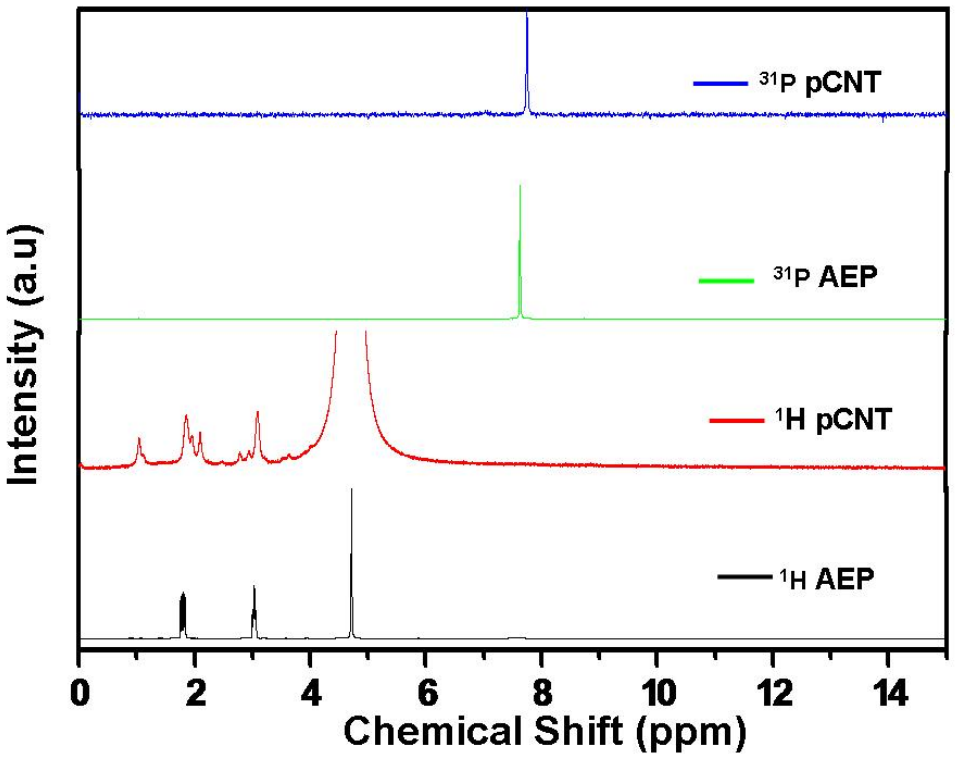


**Figure 3.3.** $^{1}H$ and $^{31}P$ NMR spectra obtained for the P-MWCNTs and AEP precursor using $D_2O$ as the solvent; the figure reveals a similar chemical environment for protons and phosphorous in AEP before and after attachment with the MWCNTs as no change in peak position is observed.

important to understand both the local chemical environment and the mode of attachment. We have confirmed the nature of bonding by $^{1}H$ and $^{31}P$ NMR studies where, $^{1}H$ NMR of AEP shows two peaks for the methylene protons at 2.9 and 1.8 ppm respectively which are consistent with its chemical structure (Figure 3.3). After the attachment of AEP with MWCNT, the peak near 3 ppm gets upfield shift to 3.1 ppm suggesting the formation of an amide link. Further, $^{31}P$ NMR also confirms this, as the peak position remains the same, suggesting that $–NH_2$ group is bonded to the carboxylic groups of CNTs, while phosphonate group remains free on the chain end (Figure 3.3).

### 3.3.3. FT- IR of Functionalized MWCNTs

Figure 3.4 shows a comparison of the FT-IR spectra for the various functionalized MWCNTs. We do not find any characteristic peak with pristine MWCNTs. However, in the case of S-MWCNTs, we clearly observe peaks corresponding to carboxylic

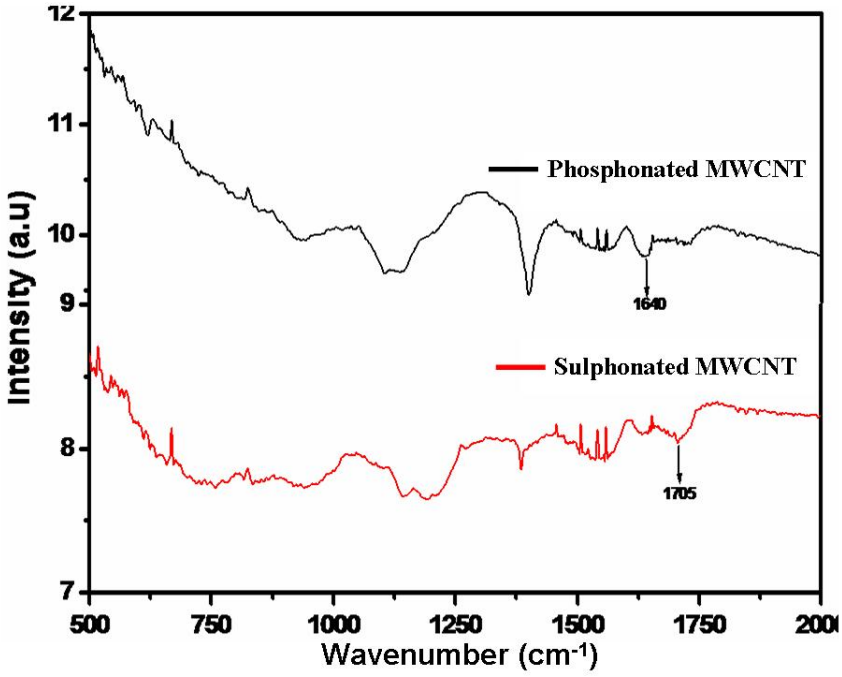


**Figure 3.4.** A comparison of the FT-IR spectra of phosphonate and sulphonate functionalized MWCNTs.

groups (1705 $cm^{-1}$) that form in the process of sulphonation. Also, further confirmation for the mode of attachment between P-MWCNT and AEP comes from the FT-IR of phosphonated CNT, where the C=O stretching peak of S-MWCNT at 1705 $cm^{-1}$ gets shifted to 1640 $cm^{-1}$ in the P-MWCNT corresponding to an amide link which also confirms the covalent nature of amine group on the CNT surface.

### 3.3.4. TGA of Functionalized MWCNTs

Figure 3.5 shows the TGA results obtained for the sulphonated and pristine MWCNTs in oxygen atmosphere. The heating rate of these experiments has been maintained as 10 °C per minute. The addition of functional groups on the sidewalls of carbon nanotubes results in reduced thermal stability in functionalized MWCNTs against that of pristine MWCNTs as S-MWCNTs tend to burn completely at 550 °C against that of 600 °C for the pristine sample. Further, a closer look at the thermograms shows a smaller onset near 380 °C for S-MWCNT. This can be easily

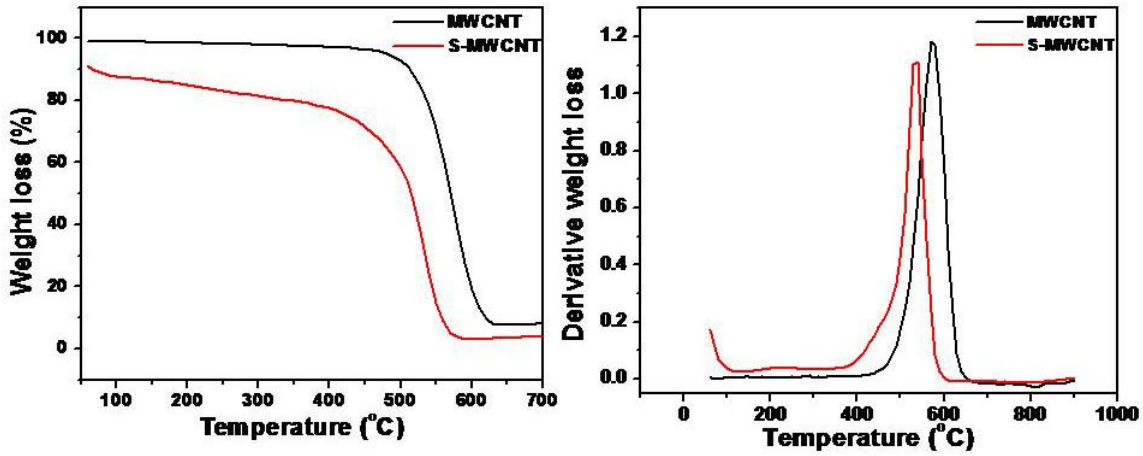


**Figure 3.5.** (a) Thermograms and (b) derivative of thermograms obtained with pristine and sulphonated MWCNTs (S-MWCNT) respectively in oxygen atmosphere at a heating ramp of 10 °C per minute; the plot clearly reveals the reduced thermal stability of S-MWCNTs due to the presence of functional groups on the CNT surface.

seen in the derivative plots shown in Figure 3.5 (b) suggesting the disintegration of functional groups (mainly sulphonic acid) that are attached on the sidewalls. Thus the surface functional groups on the sidewalls act as a catalyst for initiating the thermal decomposition of MWCNTs and overall a 50 °C drop in thermal stability is observed with the S-MWCNTs.

### 3.3.5. Cyclic Voltammetry of Functionalized MWCNTs in Sulphuric acid

A comparison of cyclic voltammograms of H-MWCNTs, S-MWCNTs and P-MWCNTs in 0.5 M $H_2SO_4$ at a scan rate of 5 mV $s^{-1}$ is shown in Figure 3.6. As with CNTs, a redox couple appear around -0.23 V corresponding to the functional groups present on the surface for S-MWCNT and P-MWCNT respectively. However, in the case of H-MWCNT this peak is not observed suggesting that this peak arises mainly

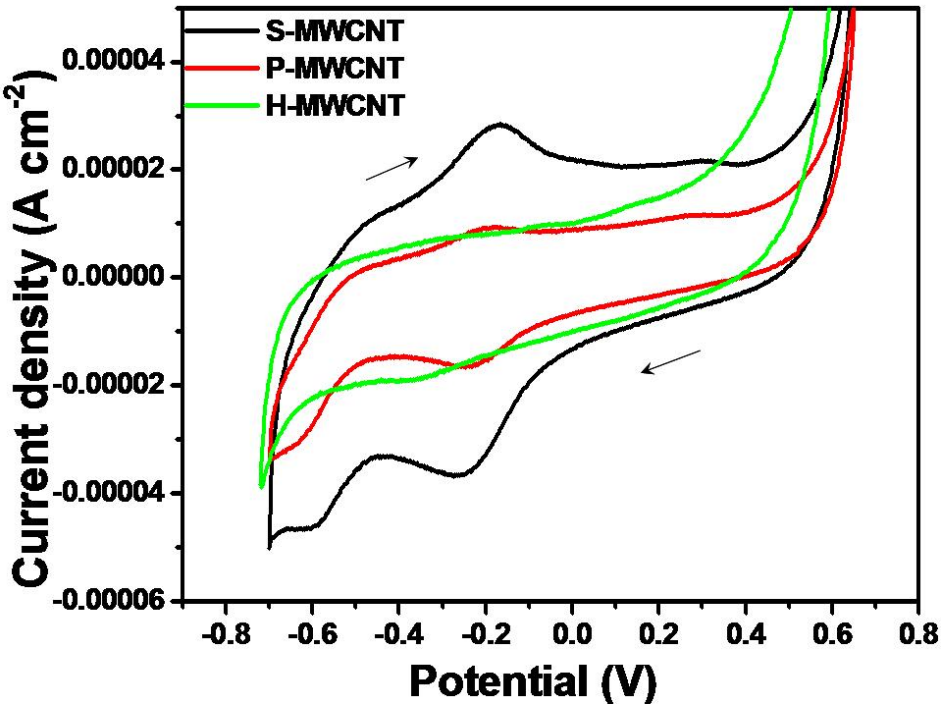


**Figure 3.6.** Cyclic voltammograms of various functionalized MWCNTs in 0.5 M sulphuric acid at a scan rate of 5 mV $s^{-1}$. S-MWCNT, P-MWCNT and H-MWCNT represents sulphonated, phosphonated and HCl treated MWCNTs respectively; the plots suggest significant ORR electrocatalytic activity for functionalized MWCNTs while H-MWCNTs show a featureless cyclic voltammogram.

from the oxidative acid treatment that induces phenolic, carboxylic and sulphonic acid groups on the side walls and at defect sites. This is in good agreement with other reports, where a featureless cyclic voltammogram is observed for MWCNT without oxygen functional groups based microelectrode bundle in an aqueous electrolyte [14]. Further, acid treatment enhances the number of defect sites on the CNT surface thereby increasing the edge plane like structure, which is one of the key factors for attaining ORR activity. Accordingly, another peak is observed at a potential of -0.6 V for S-MWCNTs that could be attributed to oxygen reduction. This is not observed with H-MWCNTs emphasizing the importance of defect sites towards ORR activity. For instance, CNTs with more edge planes have been reported to show higher ORR activity than CNTs with more basal planes [20]. Even with nitrogen doped CNTs, basal planes do not show significant ORR activity [21-25]. Thus the introduction of more defects and subsequently more edges in to the surface of CNTs helps in achieving enhanced electrocatalytic activity towards ORR.

In general, the redox peaks observed with the functionalized CNTs are attributed to the protonation and deprotonation of the surface functional groups such as quinone and hydroquinone especially when there is pH dependence [26,27]. In our case, we observe well resolved peaks for these oxygen functionalities on the CNT surface as we have intentionally increased the surface density of functional groups by means of rigorous oxidative conditions such as heating the MWCNTs at 100 °C in concentrated $HNO_3$:$H_2SO_4$ mixture for 5 h. The resulting MWCNTs have higher solubility in water and other polar solvents. Although these peaks arise from the surface functional groups they do not reveal signatures of surface confinement such as

1) ΔE close to zero; 2) the cathodic to anodic peak current ratio close to unity and 3) the peak current being directly proportional to the scan rate [28].

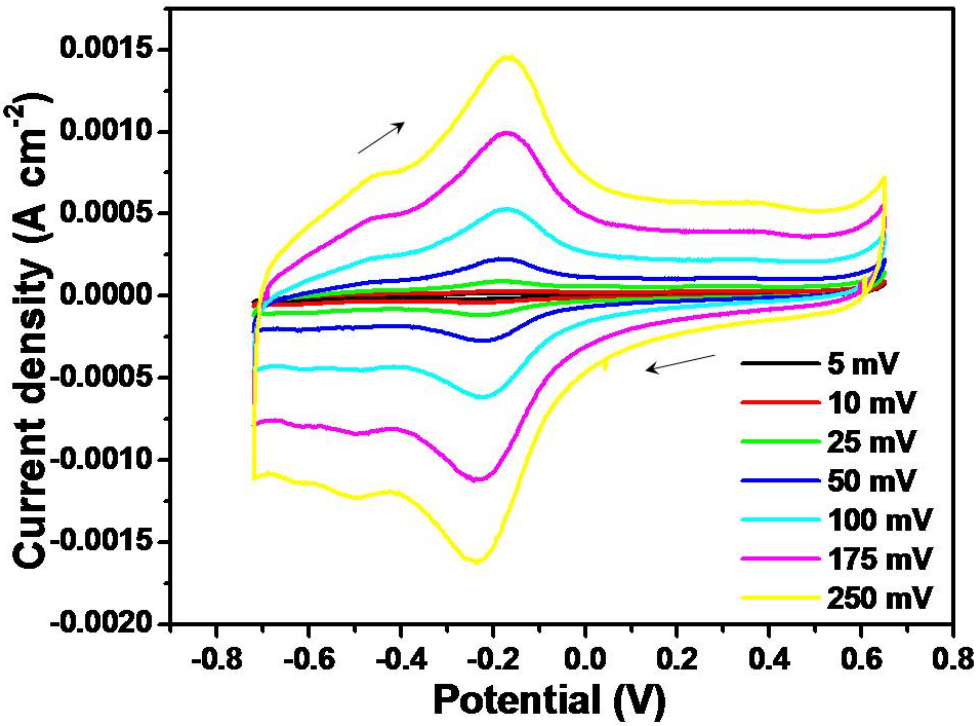


**Figure 3.7.** Cyclic voltammograms obtained for S-MWCNTs at various scan rates in 0.5 M sulphuric acid electrolyte suggesting the variation in peak potential with respect to scan rate.

It is clear from the cyclic voltammograms shown in Figure 3.7 that ΔE varies with scan rate and is not equal to zero. Further, the $i_{pa}/i_{pc}$ ratio varies from 0.5 to 0.9 depending on the scan rate, thus deviating from the expected surface confinement behaviour (Figure 3.8). Nevertheless, the scan rate dependence of peak current [for both anodic ($i_{pa}$) and cathodic peak currents ($i_{pc}$)] is nearly linear suggesting a direct proportionality (Figure 3.9). However, a similar behaviour is expected for double layer charging and hence, this alone is not sufficient to prove the possibility of surface confinement. Nevertheless, RDE techniques, which deal with the kinetics of electroactive species from the solution, can be a handy tool in confirming the surface

confinement of this peak as the peak current is not expected to increase with the rotation rate.

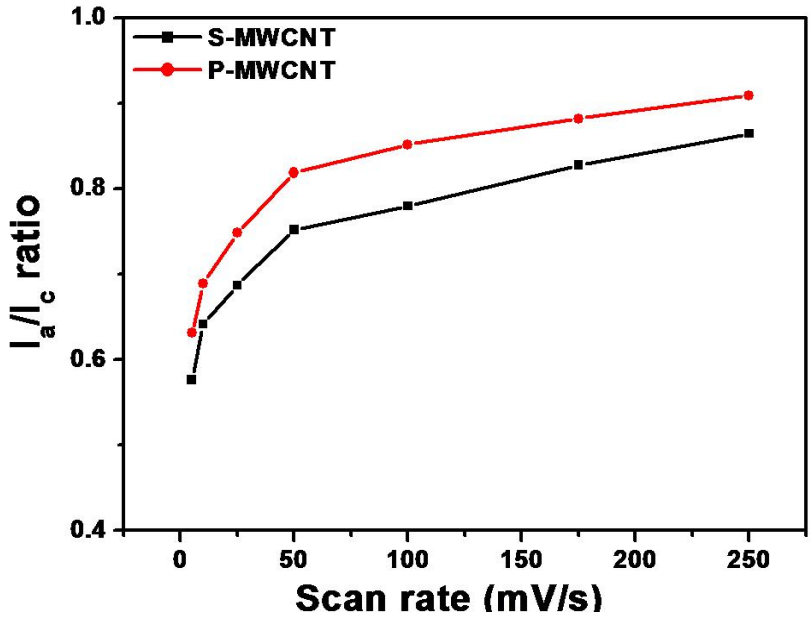


**Figure 3.8.** Variation of $i_{pa}/i_{pc}$ ratio for sulphonated and phosphonated MWCNTs obtained from the cyclic voltametry measurements with their respective scan rates; this indicates the variation of $i_{pa}/i_{pc}$ from 0.6 to 0.9 suggesting the deviation from ideal surface confinement feature.

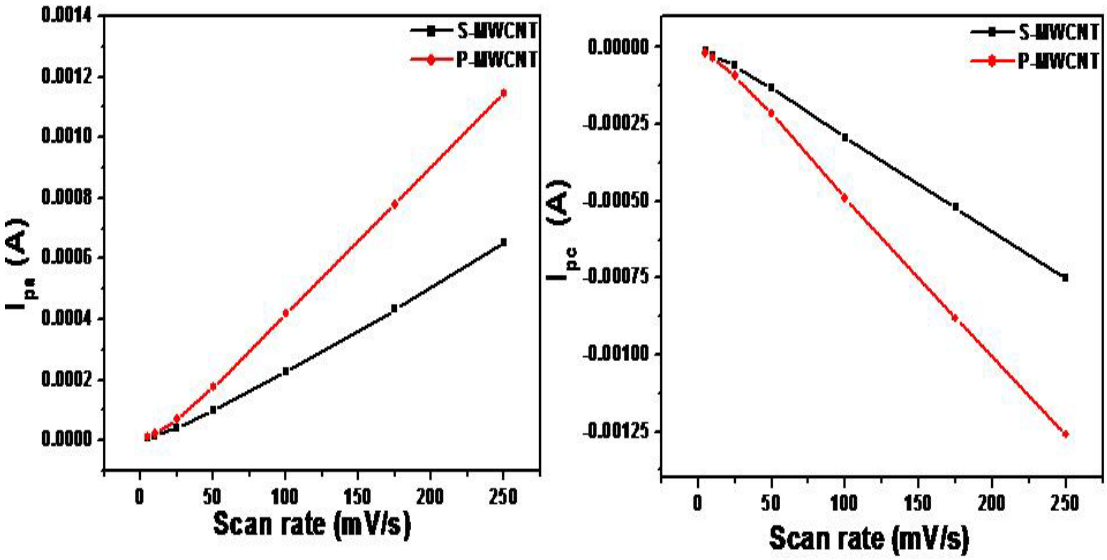


**Figure 3.9.** Variation of peak current (a) anodic, (b) cathodic with different scan rates suggesting a near straight line as expected for surface confinement for both P-MWCNTs and S-MWCNTs.

### 3.3.6. LSV Measurements of Functionalized MWCNTs

Figure 3.10 shows the results of LSV measurements for the S-MWCNT in different operating potential windows to identify the origin and a comparative evaluation of the reaction kinetics of different peaks observed in the cyclic voltammetry experiments. Figure 3.10a shows LSV experiments with a full operating potential window that includes the peak positions of both the reduction of surface functional groups and ORR at various rotation rates.

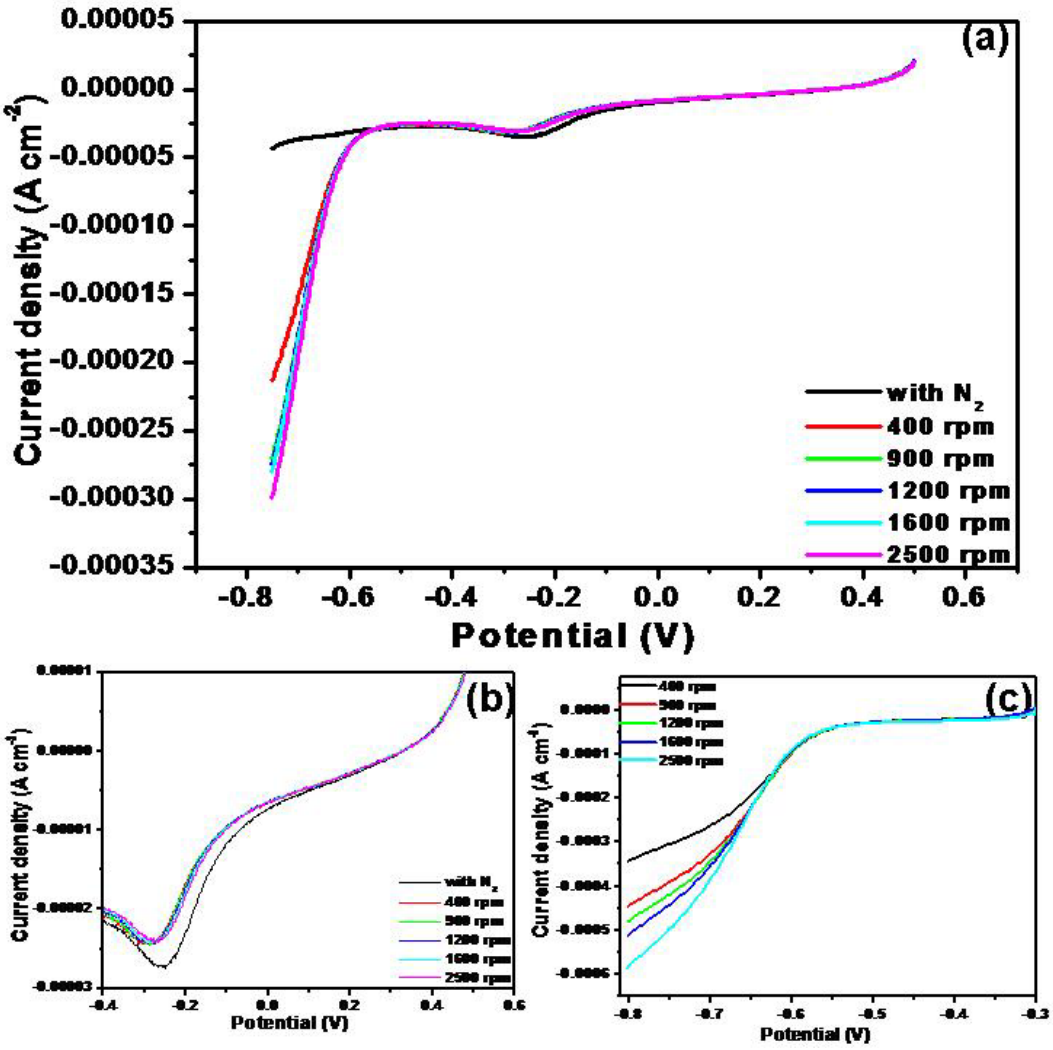


**Figure 3.10.** (a) LSV plots obtained for S-MWCNTs in the operating potential window comprising both the reduction of surface functional groups and ORR, (b) magnified view of surface functional groups redox region (c) ORR kinetics of S-MWCNTs at various scan rates.

Experiments carried out after purging of oxygen and nitrogen respectively on the electrolyte clearly specifies the peak corresponding to ORR and surface functional groups. The peak current corresponding to surface functional groups does not vary with the rotation rate (Figure 3.10b) (rotation rate per minute, rpm) since what matters is only the density of functional groups on the surface of the CNTs. While one can easily expect this, surprisingly no report is available on such an observation. This further emphasizes that this peak does not arise from the redox chemistry of the metallic impurities present on the CNTs as in which case the peak current would have varied with rotation rate. However, the peak corresponding to ORR does vary with rpm as with any catalytic process involving active species from the electrolyte. Accordingly, Figure 3.10c shows a comparison of the LSV curves at various rpm for the ORR activity of S-MWCNTs. The diffusion controlled nature of the process can easily be observed from the variation of peak current with rotation rates. After specifying the origin of two peaks and proving the surface confined nature of the redox peaks observed with functionalized MWCNTs our next objective is to compare the ORR activity of different functional group attached MWCNTs.

Accordingly, Figure 3.11 shows the LSV results of the various functionalized MWCNTs towards the ORR activity at 400 rpm. It is clear that H-MWCNTs do not show any clear activity for ORR and the peak for hydrogen evolution appears at around -0.75 V. However, with functionalized MWCNTs, ORR activity is observed with potentials much positive than that of the hydrogen evolution process and the kinetic limiting current is also achieved. While the onset potentials for ORR with functionalized CNTs are lower (~-0.55 and -0.6V) in comparison with Pt/C catalyst (-0.05V) it gives an important insight in to the ability of functionalized CNTs to

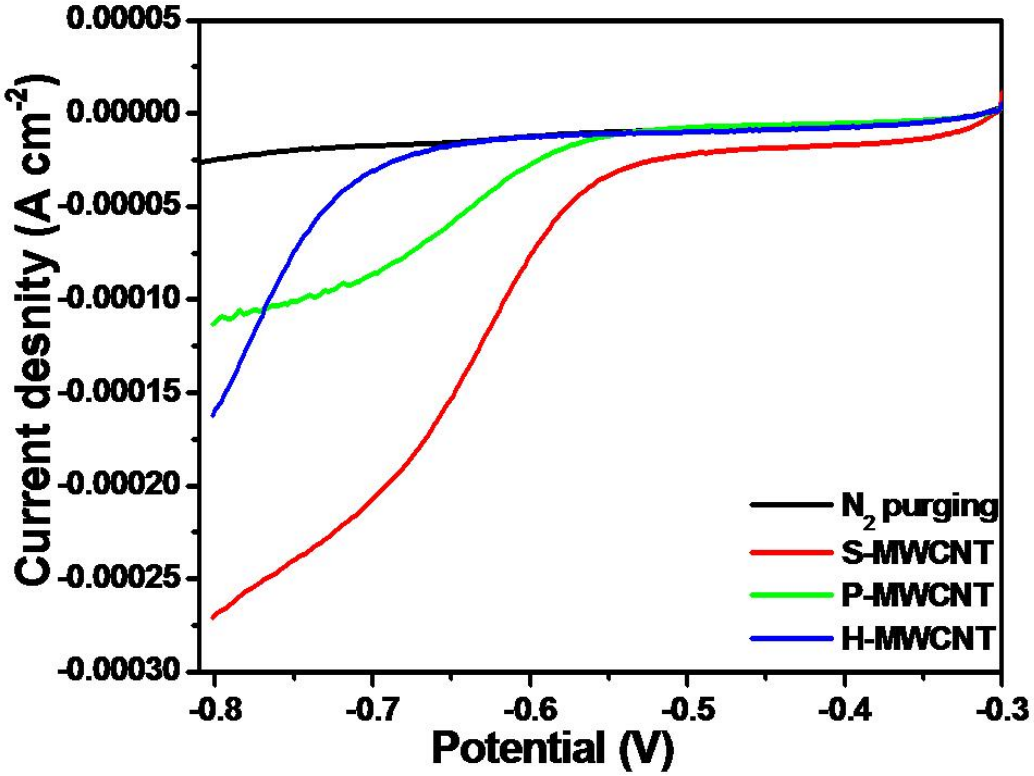


**Figure 3.11.** A comparison of LSV plots obtained with different functionalized MWCNTs in 0.5 M sulphuric acid at a rotation rate of 400 rpm and a scan rate of 10 mV $s^{-1}$; S-MWCNT, P-MWCNT and H-MWCNT represents sulphonated, phosphonated and HCl treated MWCNTs respectively; the plots suggest a significant ORR catalytic activity for functionalized MWCNTs while H-MWCNTs show negligible ORR activity with hydrogen evolution starting to appear at more negative potentials.

catalyze ORR by itself. The reason attributed for the ORR activity of N-CNTs is the formation of an impurity band near the Fermi level with the electrons donated by the nitrogen lone pair [29]. However, it is proved that functional groups such as hydroxy and carboxylic acid groups attached on the sidewalls of CNTs are capable of inducing an impurity band near the Fermi level that might have helped in achieving ORR activity for the acid functionalized MWCNTs [30]. Thus, we attribute the ORR catalytic activity observed for the functionalized MWCNTs to the possible formation of surface states or an impurity band near Fermi level due to the higher exposure of edge planes. Further, with different functional groups the onset potential for the ORR

reaction can also be tuned as observed in our case where, sulphonic acid group functionalized CNTs catalyze ORR at more positive potentials than that of P-MWCNTs.

ORR normally takes place through two different mechanisms in Pt based electrodes [31,32]: a four electron mechanism, where oxygen is directly converted in to water and a two electron mechanism where oxygen is converted to hydrogen peroxide (the peroxide route), which is further reduced to produce water as shown in equations 1,2 and 3.

$$O_2 + 4H^+ + 4e^- \rightarrow 2H_2O \qquad E^0 = 1.23\ V \quad \text{------- (1)}$$

$$O_2 + 2H^+ + 2e^- \rightarrow H_2O_{2(ads)} \qquad E^0 = 0.68\ V \quad \text{------- (2)}$$

$$H_2O_2 + 2H^+ + 2e^- \rightarrow 2H_2O \qquad E^0 = 1.77\ V \quad \text{------- (3)}$$

While the four-electron mechanism is known to be predominant at low current densities, at higher current densities hydrogen peroxide is always observed on the cathode side [33]. It has received further support from the observation of Pt-OH species on the cathode surface indicating the involvement of –OH species in the catalytic process [34]. The mechanism of ORR is very important, as electrodes that catalyze the ORR through a four electron pathway are known to be more stable than those that catalyze the ORR through the two electron pathway. However, in the case of CNT electrodes, the mechanism for ORR activity is not clear. On the other hand, one can estimate the number of electrons involved in the ORR through the Koutecky-Levich (K-L) plot through which a rough understanding of the mechanism for ORR can be obtained. The K-L plots displayed in Figure 3.12 for the S-MWCNT and P-MWCNTs show straight lines in 0.5 M sulphuric acid electrolyte. However, H-

MWCNTs do not show any such behaviour suggesting no or negligible ORR catalytic activity. Nevertheless, the 'n' values obtained from the K-L plot for S-MWCNT and P-MWCNT are 3.3 and 1.7 respectively, suggesting the possibility of both four and two electron pathways co-existing which, for undoped CNTs, has not been observed. The reason for the higher 'n' value observed with S-MWCNT is not clear although earlier reports show that higher exposure of edge plane would result in $H_2O$ as the product while with basal planes it is $H_2O_2$ [35]. Thus, the ORR activity of these functionalized MWCNTs could be presumably attributed to the higher level of functionalization and the positive effects created by the edge planes.

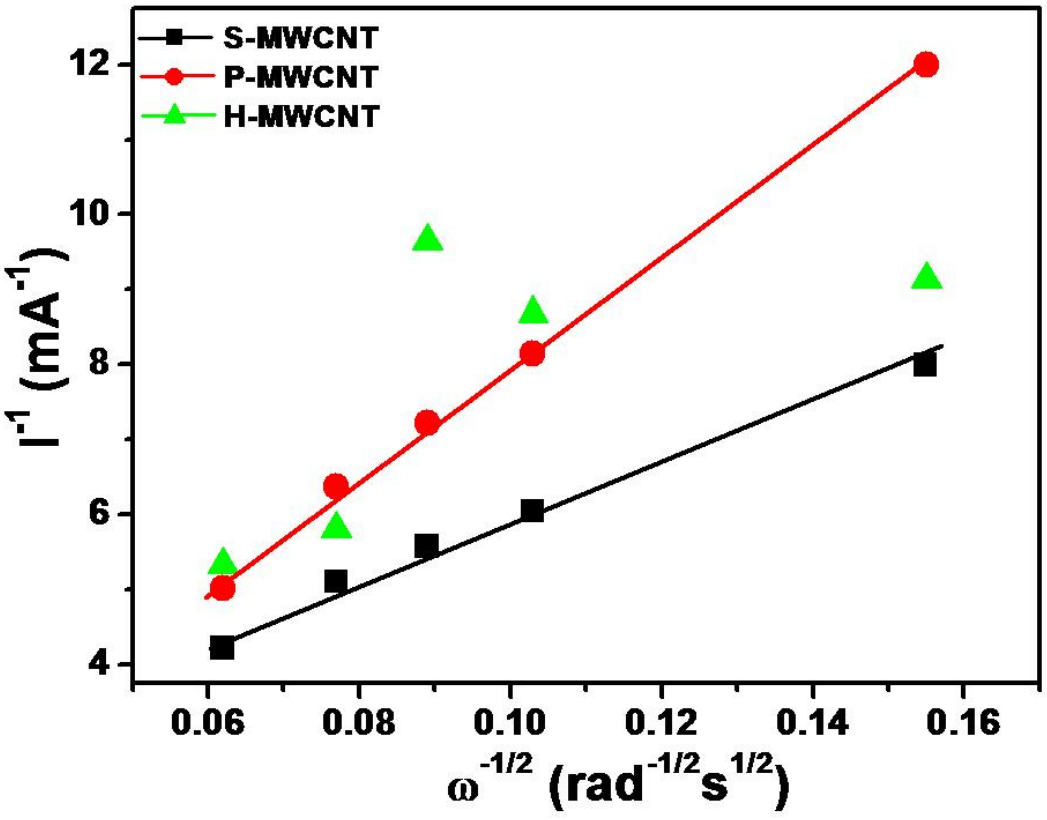


**Figure 3.12.** Koutecky-Levich (K-L) plots for electrochemical ORR on various functionalized MWCNTs. S-MWCNT, P-MWCNT and H-MWCNT represents sulphonated, phosphonated and HCl treated MWCNTs respectively; S-MWCNT and P-MWCNT show a straight line corresponding to 'n' values of 3.3 and 1.7 respectively while H-MWCNT do not show any catalytic activity towards ORR.

### 3.3.7. XPS Measurements on Functionalized MWCNTs

To unravel the reason behind the observed ORR activity, XPS measurements are very useful and the data taken on the H-MWCNTs and S-MWCNTs are shown in Figure 3.13. Accordingly, Figure 3.13 **(**a) shows the full scan window that clearly reveals the

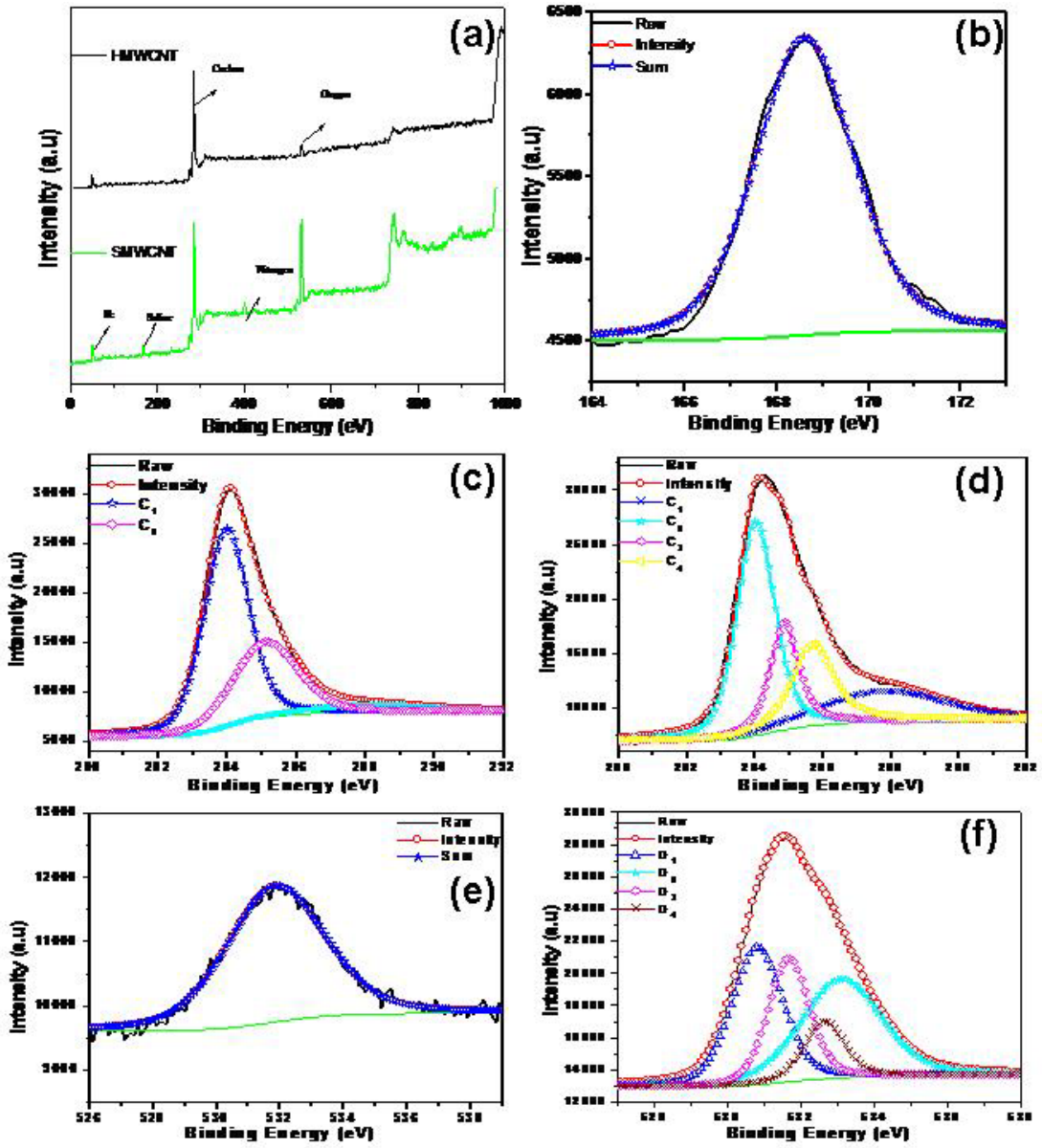


**Figure 3.13.** XP spectra of H-MWCNTs and S-MWCNTs. (a) full range survey scan, (b) $2p_{3/2}$ of sulphur for S-MWCNT, (c) and (d) C1s for H-MWCNTs and S-MWCNTs, (e) and (f) O1s spectra for H-MWCNTs and S-MWCNTs. The plot reveals the higher surface functional groups present in the S-MWCNTs in comparison with that of H-MWCNTs.

higher amount of functional groups incorporated in the functionalized MWCNTs as a significantly high peak is observed for oxygen in S-MWCNTs while a very small hump is seen for H-MWCNTs. More specifically, Figure 3.13 **(**b) shows the deconvoluted $2p_{3/2}$ spectrum of sulphur suggesting the presence of sulphonic acid groups on the sidewalls of S-MWCNTs. Figure 3.13 (c) and (d) shows the C1s deconvoluted spectrum of H-MWCNTs and S-MWCNTs. Two peaks observed with H-MWCNTs at 284 and 285.3 eV could be ascribed to the $sp^2$ carbon atoms with C-C and C-O bonding respectively. However, in the case of S-MWCNTs four peaks are observed at 284, 284.9, 285.8 and 287.8 eV, where 284 and 284.9 eV peaks are attributed to C-C and C-O bonds while 285.8 and 287.8 eV peaks could be ascribed to $C–SO_3$ and –COO satellite peaks, respectively [36]. Figure 3.13 (e) and (f) shows the O1s deconvoluted spectrum for H-MWCNTs and S-MWCNTs respectively. Again, while H-MWCNTs show only one peak, S-MWCNTs show four peaks all of which could be explained well. For example, the peak observed with H-MWCNTs is ascribed to the hydroxyl surface functional groups while for S-MWCNTs it could be accounted by –OH, -CO, $-SO_3H$ and –COOH. The aforementioned XPS results underline the higher level of functional groups present in S-MWCNTs and thus the creation of more defect sites and edge planes in the functionalized MWCNTs. MWCNTs with higher edge planes are known to be catalytically more active than the basal planes and introduction of functional groups provoke an impurity band near the Fermi level which induces the electron donating ability of CNTs. The involvement of surface states also could be another important reason which demands further detailed investigation. However, the reason for observing a four electron reduction mechanism

towards ORR is not clear and speculation on any specific role of sulphur in this needs further investigation.

### 3.3.8. Cyclic Voltammetry in Phosphoric acid

The scan rate dependant cyclic voltammograms of P-MWCNT-PBI composite electrodes in 0.5 M phosphoric acid are shown in Figure 3.14. The difference in $E_{pa}$-$E_{pc}$ ($\Delta$Ep) is comparatively higher in the case of phosphoric acid electrolyte in comparison with that of sulphuric acid. For example, the $\Delta E_p$ values for P-MWCNT-PBI composite electrode in sulphuric acid medium varies from 30 to 60 mV while that for P-MWCNT-PBI in phosphoric acid electrolyte varies from 40 to 260 mV, which is nearly four times higher (Figure 3.15). However, the reason for this is not

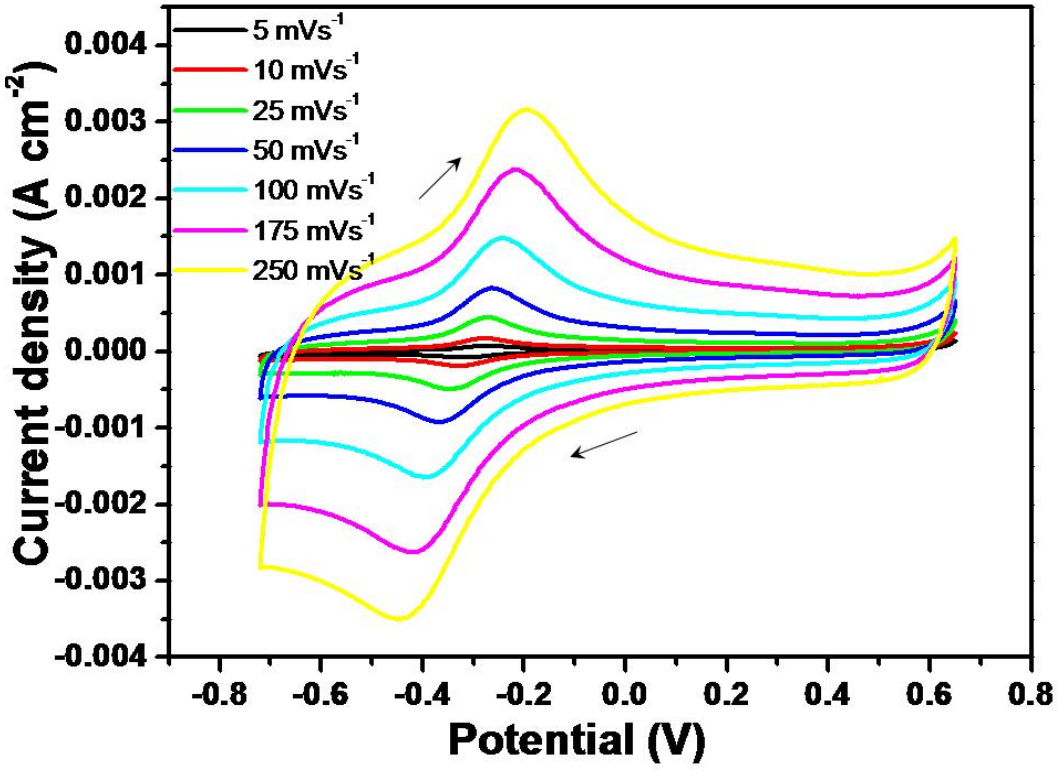


**Figure 3.14.** Scan rate dependant cyclic voltammetry of P-MWCNT\PBI composite electrodes in 0.5 M phosphoric acid clearly indicating the significant variation in the $\Delta$Ep for the surface functional groups with scan rate.

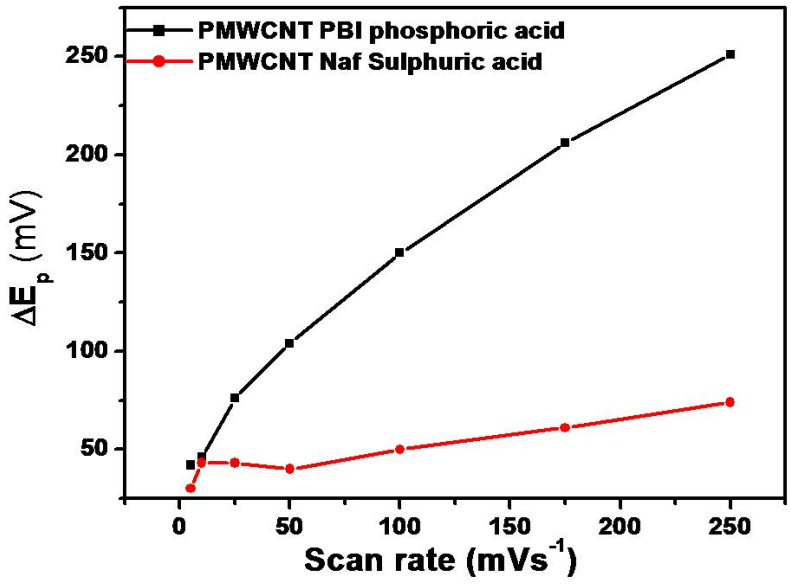


**Figure 3.15.** Comparison of $\Delta E_p$ Vs scan rate revealing the significant change in $\Delta Ep$ in phosphoric acid (60 to 250 mV); in case of sulphuric acid it is 30 to 60 mV.

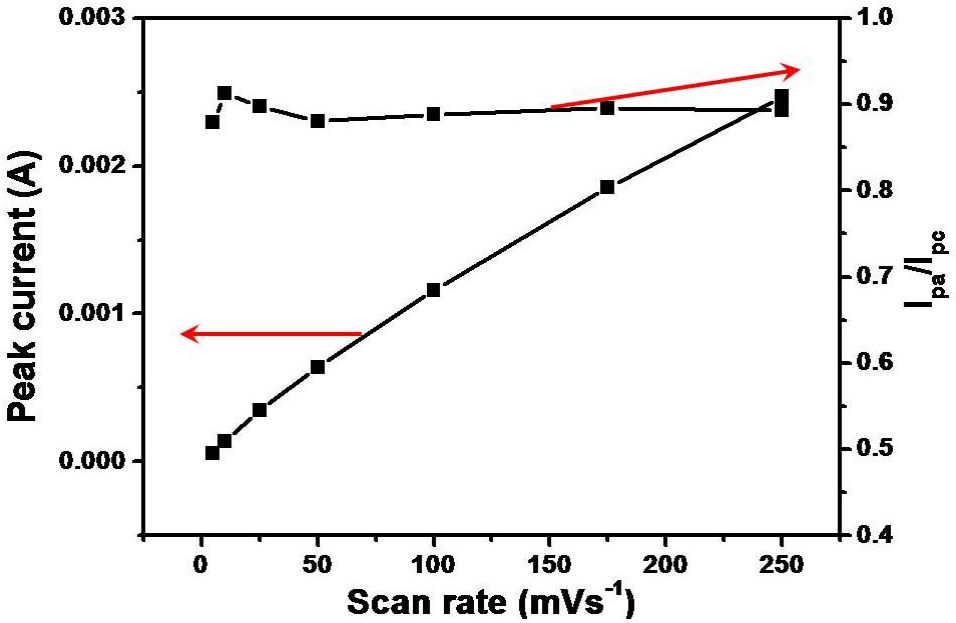


**Figure 3.16.** Scan rate dependence of peak current ($I_{pa}$) and variation of peak current ratio ($I_{pa}/I_{pc}$) with scan rate.

clear although it can be attributed to the higher viscosity of phosphoric acid and also lower conductivity that results in higher IR drop [37-39]. Further, the peak current variation with scan rate shows a near straight line suggesting the direct

proportionality while the $i_{pa}/i_{pc}$ ratio is very close to zero resembling with the features of surface confinement (Figure 3.16). Nevertheless, LSV measurements in phosphoric acid medium also reveal no change in peak current with rotation rate suggesting the surface confined nature of this peak.

### 3.3.9. LSV Measurements of Functionalized MWCNTs in Phosphoric Acid

Functionalized MWCNTs show good ORR catalytic activity in phosphoric acid medium, which could easily be understood from the LSV plots taken after purging with nitrogen and oxygen and also with various rotation rates as shown in Figure 3.17 (a) and (b). Even though the catalytic activity of P-MWCNTs towards ORR is clearly evident, the peak current does not increase linearly with the rotation rate. This can be attributed to the poor solubility of oxygen in phosphoric acid coupled with mass transport restriction across the ionomer binder in the composite electrode. Both PBI and Nafion based catalysts show similar behaviour in the LSV measurements. Thus, the 'n' value could not be derived from the above mentioned experiments due to the sluggish mass transport that prevents a proper K-L plot.

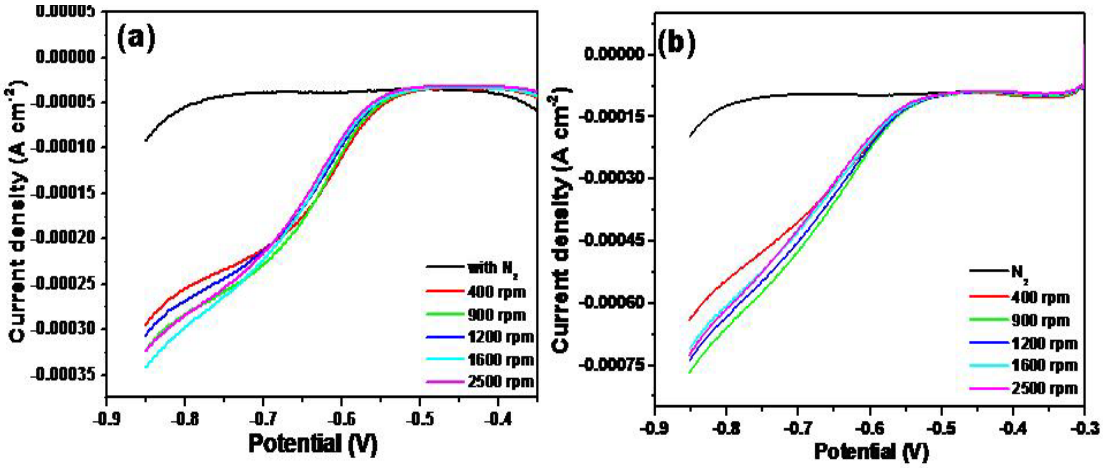


**Figure 3.17.** LSV plots of (a) P-MWCNT/PBI (b) P-MWCNT/Nafion composite electrodes obtained after purging of nitrogen and oxygen respectively and also with different rotation rates in 0.5 M phosphoric acid electrolyte.

This is in direct contrast with the results obtained in sulphuric acid electrolytes with similar electrodes. This can be attributed to the higher viscosity of phosphoric acid, which would reduce the mass transport of oxygen towards the electrode. For example, the diffusion coefficient of oxygen reported for 0.5 M sulphuric acid is 1.8 x $10^{-5}$ $cm^2$ $s^{-1}$ while for phosphoric acid it is 7.61 x $10^{-7}$ $cm^2$ $s^{-1}$ at 25 °C, suggesting two orders of magnitude lower diffusion coefficient values [41-43]. Further, the concentration of dissolved oxygen in sulphuric acid is 1.13 x $10^{-6}$ mol $cm^{-3}$ while in phosphoric acid it varies from 8.34 to 3.28x$10^{-7}$ mol $cm^{-3}$ in the temperature range of 75 °C to 150 °C revealing reduced dissolved oxygen concentration in phosphoric acid [43]. For comparison, in Nafion, the diffusion coefficients and solubility of oxygen are calculated to be 5.86 x$10^{-7}$ $cm^2$ $s^{-1}$ and 4.98 x $10^{-6}$ mol $cm^{-3}$ respectively indicating a lower diffusion coefficient but higher oxygen solubility than that of phosphoric acid [44]. Thus our observation is in excellent agreement with the literature reports that the reduced oxygen solubility and diffusion coefficient restricts the mass transport of oxygen towards the electrodes especially in the presence of Nafion and polybenzimidazole as the ionomer binders. For example, experiments with P-MWCNT\Nafion composite electrode in phosphoric acid electrolyte also yield similar results (Figure 3.17b) suggesting the significant role of phosphoric acid in determining the mass transport although for a similar catalyst/binder ratio, the electrode with Nafion binder shows higher peak current than that of PBI binder based electrode, probably due to its higher oxygen solubility.

To confirm the role of phosphoric acid in controlling the mass transport and to further rule out any specific role of MWCNTs in this particular observation, we have

also carried out similar experiments with commercial Pt/C based electrodes with and without the ionomer binder (PBI) in phosphoric acid medium. In the case of composite electrode, a similar mass transport restricted behaviour is obtained even for Pt/C catalyst system while without any binder in phosphoric acid it shows regular kinetic controlled linear increase in peak current with increasing rotation rate (Figure 3.18b). Thus in the case of ionomer binders, both Nafion and PBI binders face restricted mass transport in 0.5 M phosphoric acid medium while no such limitation was observed in sulphuric acid medium. However, in between these two ionomers, Nafion gives better mass transport as the limiting current obtained with Nafion based composite electrode is much higher than that of PBI based composite electrode.

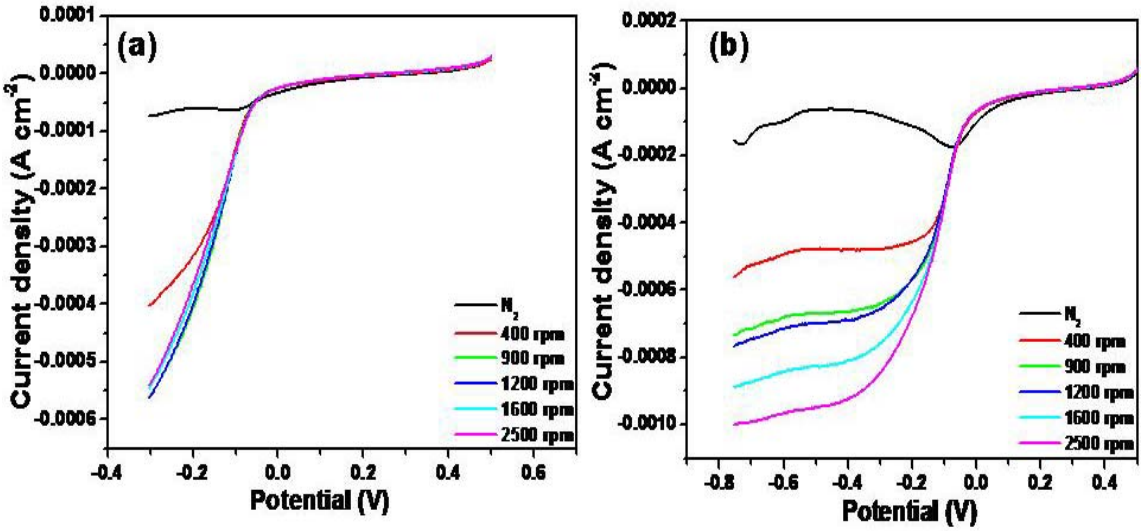


**Figure 3.17.** LSV plots of (a) PtC/PBI composite and (b) PtC electrodes obtained after purging with nitrogen and oxygen respectively and after various rotation rates in 0.5 M phosphoric acid electrolyte; the presence of PBI in the electrode restricts the mass-transport of oxygen with important consequences.

### 3.4. Conclusions

In this chapter, the ability of functionalized carbon nanotubes to catalyze the ORR is clearly demonstrated using sulphonated and phosphonated MWCNTs in the electrode

formulation. The activity towards ORR is expected to be arising mainly from the higher exposure of edge planes as observed from the use of S-MWCNT and P-MWCNTs for electrode preparation. This has been attributed to the formation of impurity band near the Fermi level, which can be tuned by varying the functional groups. Interestingly the 'n' value obtained with S-MWCNTs is 3.3 suggesting the validity of a four electron pathway. Also, the onset potential can be tuned by modifying the functional groups and the extent of functionalization. Hence, if carefully designed, CNTs can show better catalytic activity that is comparable to that of Pt based catalysts. While CNTs doped with nitrogen might help in shifting the onset potential towards more positive values, it is worth attempting other dopants or functional groups as the modification of electronic band structure and exposure of more edge planes hold the key for efficient ORR catalytic activity of CNT based cathodes.

### 3.5. References

**[1]** Steele, B. C. H.; Heinzel, A. *Nature* **2001,** 414, 345.

**[2]** Gewirth, A. A.; Thorum. M. S. *Inorg. Chem.* **2010,** 49, 3557.

**[3]** Chen, A.; Hindle, P. H. *Chem. Rev.* **2010,** 110, 3767.

**[4]** Eder, D. *Chem. Rev.* **2010,** 110, 1348.

**[5]** Kam, N.W.S.; Jessop, T.C.; Wender, P.A.; Dai, H. *J. Am. Chem. Soc.,* **2004,** 126 6850.

**[6]** Gong, K.; Du, F.; Xia, Z.; Durstock, M.; Dai, L. *Science* **2009,** 323, 760.

**[7]** Britto, P. J.; Santhanam, K. S. V.; Rubio, A.; Allonso, J. A.; Ajayan, P. M. *Adv. Mater,* **1999,** 11, 154.

**[8]** Yeager, E. *Electrochimica Acta,* **1984,** 29, 1527.

**[9]** Alexeyeva, N.; Tammeveski, K. *Electrochemical and Solid-State Letters,* **2007,** 10, F18.

**[10]** Matsubara, K.; Waki, K. *Electrochemical and Solid-State letters,* **2010,** 13, F7.

**[11]** Strelko, V. V.; Kartel, N. T.; Dukhno, I. N.; Kuts, V. S.; Clarkson, R. B.; Odintsov, B. M. *Surf. Sci.,* **2004,** 548, 281.

**[12]** Dumitrescu, I.; Unwin, P. R.; Macpherson, J. V. *Chem. Commun,* **2009,** 6886.

**[13]** Pumera, M. *Chem. Eur. J.* **2009,** 15, 4970.

**[14]** Kaempgen, M.; Roth, S. *Synth. Met,* **2005,** 152, 353.

**[15]** He, R.; Li, Q.; Xiao, G.; Bjerrum, N. J. *J. Membr. Sci.,* **2003,** 226, 169.

**[16]** Wang, Y.; Iqbal, Z.; Mitra, S. *J. Am. Chem. Soc.* **2006,** 128, 95.

**[17]** Kakade, B. A.; Pillai, V. K. *Appl. Sur, Sci.* **2008,**254, 4936.

**[18]** Kim, S. T.; Lim, J. Y.; Park, B. J.; Choi, H. J. *Macromol. Chem. Phys.* **2007,** 208, 514.

**[19]** Yuan, C.; Shen, L.; Li, D.; Zhang, F.; Lu, X.; Zhang, X. *Applied Surface Science* **2010,** 257, 440.

**[20]** Matter, P. H.; Wang, E.; Arias, M.; Biddinger, E. J.; Ozkan, U. S.; *J. Phys. Chem. B* **2006,** 110, 18374.

**[21]** Shao, Y.; Sui, J.; Yin, G.; Gao, Y. *Applied Catalysis B: Environmental,* **2008,** 79, 89.

**[22]** Lefevre, M.; Dodelet, J. P.; Bertrand, P. *J. Phys. Chem. B* **2002,** 106, 8705.

**[23]** Mu, T. C.; Huang, J.; Liu, Z. M.; Li, Z. H.; Han, B. X. *J. Mater. Res.* **2006,** 21, 1658.

**[24]** Maldonado, S.; Stevenson, K. J. *J. Phys. Chem. B* **2004,** 108, 11375.

**[25]** Matter, P. H.; Zhang, L.; Ozkan, U. S. *J. Catal.* **2006,** 239, 83.

**[26]** Barisci, J. N.; Wallace, G. G.; Baugmann, R. *J. Electroanal. Chem,* **2000,** 488, 92.

**[27]** Ye, J. S.; Liu, X.; Cui, H. F.; Zhang, W. D.; Sheu, F. S.; Lim, T. M. *Electrochem. Commun,* **2005,** 7, 249.

**[28]** Shanmugam, S.; Gedanken, A. *J. Phys. Chem. B.* **2006,** 110, 2037.

**[29]** Lim, S. H.; Li, R.; Ji, W.; Lin, J. *Phys. Rev. B.,* **2007,** 76, 195406.

**[30]** Zhao, J.; Park, H.; Han, J.; Lu, J. P. *J. Phys. Chem. B.* **2004,** 108, 4227.

**[31]** Markovic, N. M.; Schmidt, T. J.; Stamenkovic, V.; Ross, P. N. *Fuel Cells* **2001**, 1, 105.

**[32]** Walch, S.; Dhanda, A.; Aryanpour, M.; Pitsch, H. *J. Phys. Chem. C.* **2008,** 112, 8464.

**[33]** Sethuraman, V. A.; Weidner, J. W.; Haug, A. T.; Motupally, S.; Protsailo, L. V. *J. Electrochem. Soc.* **2008,** 155, B50.

**[34]** Li, X.; Heryadi, D.; Gewirth, A. A. *Langmuir,* **2005,** 21, 9251.

**[35]** Sidik, R. A.; Anderson, A. B.; Subramanian, N. P.; Kumaraguru, S. P.; Popov, B. N. *J. Phys. Chem. B* **2006,** 110, 1787.

**[36]** Maldonado, S.; Morin, S.; Stevenson, K. J. *Carbon,* **2006,** 44, 1429.

**[37]** Das, A.; Dev. S.; Shangliang, H.; Nonglait, K. L.; Ismail, K. *J. Phys. Chem. B.* **1997,** 101, 4166.

**[38]** Tsurko, E. N.; Neueder, R.; Barthel, J.; Apleblat, A. *Journal of Solution Chemistry,* **1999,** 28, 973.

**[39]** Chin, D. T.; Chang, H. H. *J. Appl. Electrochem.* **1989,** 19, 95.

**[40]** Ogrady, W. E.; Taylor, E.J.; Srinivasan, S. *J. Electroanal. Chem.,* **1982,** 132, 137.

**[41]** Jiang, J.; Yi, B. *J. Electroanal. Chem.* **2005,** 577, 107.

**[42]** Ayad, A.; Naimi, Y.; Bouet, J.; Fauvarque, J. F. *J. Power Sources* **2004,** 130, 50.

**[43]** Gang, X.; Hjuler, H. A.; Olsen, C.; Berg, R. W.; Bjerrum, N. J. *J. Electrochem. Soc.,* **1993,** 140, 896.

**[44]** Haug, A. T.; White, R. E. *J. Electrochem., Soc.* **2000,** 147, 980.

# Chapter 4

## Artificially Designed Membranes using Phosphonated Multiwalled Carbon Nanotube-Polybenzimidazole Composites for PEMFCs

This chapter demonstrates the ability of phosphonated carbon nanotubes to offer an unprecedented approach to tune both proton conductivity and mechanical stability of hybrid electrolytes based on polybenzimidazole (PBI) membrane for fuel cell applications. Incorporation of functionalized MWCNT increases the proton conductivity of membranes by forming a network structure which is well reflected in the fuel cell performance of composite membranes. The composite membrane with 1% P-MWCNT loading gives a power density of 780 mW $cm^{-2}$ while pristine PBI membranes show only 600 mW $cm^{-2}$ revealing a 35 % improvement in performance. The enhanced performance has been attributed to the formation of proton conducting networks with a domain size of 17 nm as estimated from the small angle X-ray scattering measurements. MEA impedance measurements reveal that the reduced ORR activation is the key for the improved performance along with enhanced proton conductivity. Further, the mechanical strength measurements reveal significant improvement in the yield strength and ultimate strength. For example, the ultimate strength determined for the composite and pristine membranes is 100 and 65 MPa respectively demonstrating the superiority of the composite electrolyte that suggests the synergistic role played by P-MWCNTs. This study opens up a new strategy to systematically tune the properties of polymer electrolytes for special applications by using appropriately functionalized CNTs.

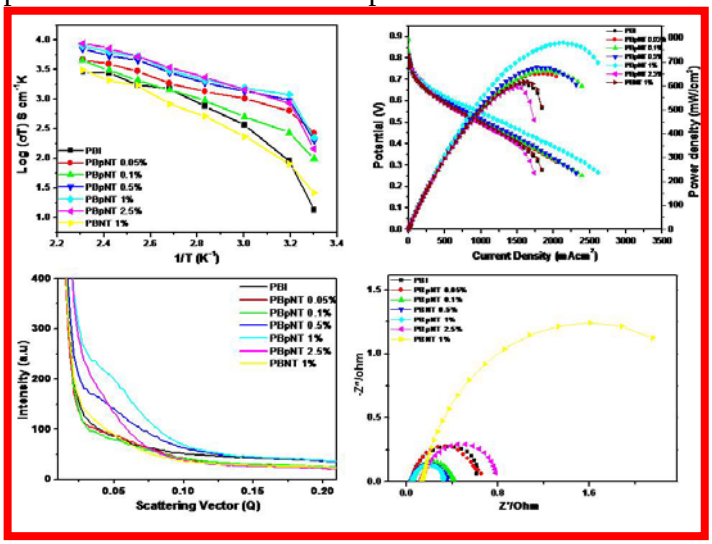


*A part of the work discussed in this chapter has been published in *J. Phys. Chem. Lett.* **2010,** 1, 2109.

## 4.1. Introduction

Although a large number of polymer electrolyte membranes (PEM) have been studied for PEMFC applications, most of them have many limitations and only limited success has been accomplished with few of them [1,2]. Among the different PEMs, perfluorosulfonic acid (PFSA) based membranes remain as the bench mark due to their high proton conductivity under humidified conditions and proven long term performance (over 60,000 h). However, its dependence on water for proton conductivity associated with low temperature operation has resulted in many limitations linked with (1) water management, (2) CO poisoning, (3) necessity for pure hydrogen, (4) fuel cross over (hydrogen and methanol) and thermal management (heat recovery). Many of the above mentioned drawbacks can be overcome if the PEMFCs can be made to work above 100 °C. Accordingly, an enormous amount of effort has been focused on PEM development for high temperature operations. A study on the suitability of different functionalities such as sulphonic acid, phosphonic acid and imidazole systems attached to aliphatic chain for high temperature and low humidity operations reveals that only phosphonic acid based systems show considerable proton conductivity (0.01 S $cm^{-1}$) in the temperature range of 100 – 200 °C while sulfonic acid based systems show higher proton conductivity under wet conditions [3]. In this respect, covalently phosphonated polymers can be an attractive option for the high temperature operation especially due to the strength of carbon phosphorus bond [4]. Further, due to the amphoteric nature of the phosphonic acid, these membranes can conduct protons through the structure by diffusion at low humidity while at higher humidity, water dynamics may help to conduct protons. However, phosphonic acid attachment to

polymers is difficult and more significantly a critical density of phosphonate group is required to achieve a significant proton conductivity [5].

Among the different polymer systems reported for high temperature PEMFC operation, phosphoric acid doped polybenzimidazole membranes are the most attractive candidates to work above 120 °C mainly owing to its higher thermal stability, good proton conductivity (when doped with phosphoric acid), zero water electro-osmotic drag, independent of water for proton conductivity (hence lesser balance of plant components) and better combined heat and power (CHP) generation that would boost the efficiency further with life time reported over 40,000 h [6-8]. PBI was developed by Vogel and Marvel in 1961 originally for flame retardant applications due to its very high thermal stability [9]. However, the ability to conduct protons when doped with phosphoric acid was first reported in 1995 by Wainright et al [10]. Phosphoric acid in PBI matrix presumably plays two roles, first as a proton donor and second, more importantly, as a proton conducting medium. Proton conductivity as high as 0.065 $Scm^{-1}$ has been reported for phosphoric acid doped PBI membranes at temperatures above 100 °C [11]. The proton conductivity under dry conditions follow a Grotthus mechanism involving the imide sites as well as the phosphoric acid groups since the distance between the two adjacent nitrogen atoms are too large to bridge without intermediate phosphoric acid molecules [12]. However, under wet conditions, vehicular mechanism can also be involved with water acting as the proton carrier [13]. Nevertheless, it's relatively low proton conductivity, acid leaching tendency, and inadequate mechanical stability under fuel cell operating conditions restrict their use as an electrolyte for PEMFC. Further, doping of phosphoric acid would increase the

proton conductivity but at the expense of mechanical stability and hence is not suitable for membrane electrode assembly (MEA) fabrication [14].

Efforts directed toward improving the proton conductivity are of two types; one by modifying the membrane to change its basicity (thereby increasing the acid base interaction) and level of localized (either covalently or ionically bound) phosphoric acid uptake,[15-17] and the second by adding inorganic and/or organic additives such as $SiO_2$, zirconium phosphate, phosphotungstic acid, silicotungstic acid and montmorillonites to increase the proton conductivity, but sacrificing mechanical strength [18-20]. For example, PBI with a pyridine moiety at the meta configuration is reported to have a localized phosphoric acid uptake level of 4 mol of phosphoric acid per repeat unit in comparison to that of 2 mol of phosphoric acid per repeat unit of unmodified PBI membranes [21]. Attempts to increase the mechanical stability involve cross linking the PBI membranes although other approaches have also been useful. Covalent cross linking attained by thermal treatment or through amide type linkage between the imidazole groups are helpful while external cross linkers such as p-xylene dichloride have also been used for increasing the mechanical stability [22-24]. Although carbon nanotube-PBI composites have also been reported to increase the mechanical stability, these efforts often result in a compromise on the proton conductivity [25-27].

In Chapter 3, we have demonstrated the ORR activity of functionalized MWCNTs as an electrode in different electrolytes although a detailed exploitation of their utility in the electrolyte to increase the proton conductivity has not been studied. However, such a study is highly important since the functional groups on the MWCNTs can synergistically interact with their counterpart in the polymer matrix thus improving their key aspects. Hence, in the present chapter, we focus on a strategy, involving P-

MWCNTs to prepare composite membranes of PBI with improved proton conductivity and mechanical stability (Scheme 4.1). The incorporation of phosphonate groups can increase the net phosphonic acid content thus helping to form a proton conducting network that effectively improves the proton conductivity, while MWCNTs can help to increase the mechanical strength. Further, the functional groups in the MWCNTs help to form a homogeneous composite membrane with uniform CNT distribution. The composite membranes have been tested for fuel cell electrolyte applications by making MEAs with Pt based standard electrode formulations. A maximum power density of 780 mW $cm^{-2}$ is achieved with the composite membranes while pristine membrane gives only 600 mW $cm^{-2}$ under similar conditions. The results have been supported by membrane conductivity through impedance, small angle X-ray scattering (SAXS), MEA impedance and solid-state cyclic voltammetry experiments. Mechanical strength of the membranes are analyzed through stress-strain plots to prove the superiority of the composite membranes. Six different compositions of P-MWCNT in PBI membranes (PBpNT) starting from 0.01 wt% to 2.5 wt% have been prepared to optimize the CNT

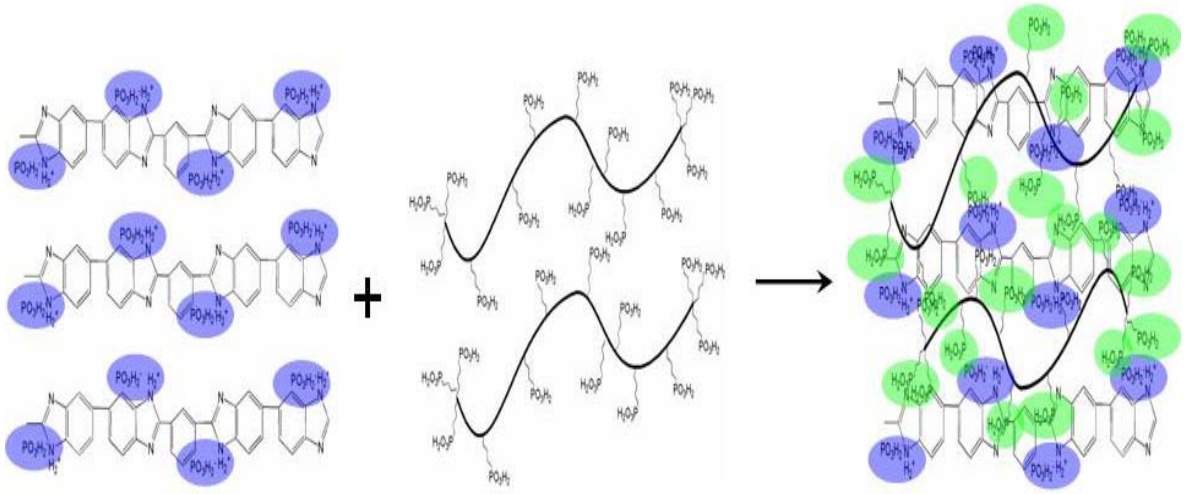

**Scheme 4.1.** Interaction of P-MWCNTs with phosphoric acid doped polybenzimidazole membranes resulting in the formation of localized networks for proton transport.

content and to compare their proton conductivity. Further, a composite with unfunctionalized MWCNT also ensures that the observed proton conductivity is due to the surface functional groups on the MWCNT and not due to the MWCNT itself.

## 4.2. Experimental Aspects

### 4.2.1. Preparation of PBI Membranes

In a three necked round bottom flask fitted with an overhead stirrer, 2000 g of polyphosphoric acid (PPA) was taken. It was purged with nitrogen through one side and other end was fixed with a guard to prevent moisture from entering the flask. PPA was heated to 120 °C after which 80 g of diaminobenzidine (DAB) was added slowly. The mixture was stirred at 120 °C for 90 min followed by the addition of isopthalic acid. The temperature of the solution was slowly increased to 170 °C and maintained for 5 h which was further increased to 210 °C and maintained for 14 h. The resulting hot mixture was slowly poured into deionised water with continuous stirring to prepare the fibrous PBI polymer. This fibrous material was cut into smaller pieces and crushed in to a fine powder followed by flushing overnight with water to remove the acid part. This was carried out by keeping the membrane in a spacer and allowing water to pass through it. The neutral polymer mixture obtained was placed in saturated $NaHCO_3$ solution overnight followed by washing with water again. The inherent viscosity of the resulting polymer was 1.2 dL $g^{-1}$ in conc. $H_2SO_4$ (concentration: 0.2 g $dL^{-1}$). The dense membrane was prepared by the solution casting method. Typically a 3 % PBI solution in N,N-dimethylacetamide was heated to 80–90 °C and kept for 16 h under dry conditions. The film was subsequently peeled off and dried under vacuum at 100 °C for 7 days before doping with phosphoric acid.

### 4.2.2. Preparation of PBpNT Composite Membranes

The composite membrane was prepared by mixing appropriate amount of P-MWCNT with a pre dissolved and filtered solution of 3 % PBI in dimethyl acetamide and probe ultrasonicated for 10 min on a 1 min on/off basis with a power utilization of 40 %. After ultrasonication, the composite solution was degassed for 5 min followed by casting on a glass tray at 80-90 °C for 16 h under dry conditions. The resulting membrane was peeled off and further dried at 100 °C under vacuum for one week. The resulting membrane was preserved for further experiments.

### 4.2.3. Doping of PBpNT Composite Membranes

Phosphoric acid doping was carried out by dipping the membranes in 88 % $H_3PO_4$ solution for 72 h followed by vacuum drying at 100 °C for 5 days. The $H_3PO_4$ uptake was estimated to be 12.9-13.5 mol per repeating unit for the 6 samples of pristine membrane, while for PBpNT membranes, it was around 11.5 – 12.3 mol per repeating unit for similar number of samples.

### 4.2.4. Characterization of PBpNT Composite Membranes

Proton conductivity of the membranes was measured by a two probe impedance setup using Autolab PG stat instrument coupled with a frequency response analyzer from room temperature to 160 °C. Temperature of the system was controlled by a home made heating set up with the variation in temperature < 2 °C. Thermo gravimetric analysis (TGA) was carried out using a Mettler Toledo TGA/SDTA 851 with a nitrogen flow rate at 20 ml $min^{-1}$ by keeping the temperature range from room temperature to 800 °C at a scan rate of 10 °C $min^{-1}$. The structure and morphology

were characterized using a scanning electron microscope using a Quanta 200 3D attached with an energy dispersive X-ray analyzer. Transmission electron microscopy (TEM) was performed on a FEI model TECNAI TS 30 instrument operated at an accelerating voltage of 300 kV; TEM samples were prepared by placing a drop of the dispersed solution onto a carbon-coated Cu grid (carbon coating 3-nm thick, deposited on a commercial copper grid for electron microscope), dried in air and loaded into the chamber.

Membrane electrode assemblies were prepared as follows. Gas diffusion layer (GDL) was prepared by coating a mixture of Vulcan XC-72 carbon and PTFE in cyclohexane on teflonized carbon paper after sonicating for 2 minutes on a 30 seconds on/off basis. The carbon loading was 1.5 mg $cm^{-2}$. Thus prepared GDL was pressed at 0.25 ton $cm^{-2}$ for 2 min followed by sintering at 350 °C for 30 min. The catalyst ink was made by mixing 20 wt% Pt/C (Arrora Matthey), Nafion and isopropyl alcohol at appropriate ratio and sonicating for 2 min. This ink was coated on the GDL to prepare the electrode with a Pt loading of 0.5 mg $cm^{-2}$, which was chosen in order to avoid variation in performance due to the catalyst layer. Thus prepared electrode was cut in to 2x2 $cm^2$ pieces and pressed uniaxially with phosphoric acid doped PBI membranes at 130 °C and a pressure of 0.5 ton $cm^{-2}$ for 3 min was applied to fabricate the MEA.

MEA impedance was measured by passing $H_2$ and $O_2$ gases (1 atm) in the anode and cathode respectively in the frequency range of 1 MHz to 0.1 Hz from room temperature to 140 °C. Solid-state cyclic voltammetry for the MEAs was measured by passing $H_2$ and $N_2$ gases to the anode and cathode respectively. $H_2$ electrode acted as the counter and reference electrode while the cathode acted as the working electrode.

### 4.2.5. Polarization Measurements of PBpNT Composite Membranes

Polarization measurements were carried out on an Arbin fuel cell test station (Model: Arbin-001 MITS Pro-FCTS 5.0-FCTS) under non-humidified conditions. Prior to the testing, the MEAs were conditioned by monitoring the open circuit potential (OCV) for 30 min to ensure its stability at constant temperature (140 $^{o}$C) and subsequently conditioned at 0.7 V for 30 min after which polarization measurements were carried out. A serpentine type flow field with an active area of 4 $cm^2$ was used for the testing and $H_2$ and $O_2$ flow rates were maintained constant at 1 slpm. The cells were operated at 140 $^{o}$C through a pair of external electrical heating elements.

### 4.2.6. Mechanical Strength Measurements of the Composite Membranes

All mechanical stability measurements were performed on a micro tensile meter (Linkam, using Linksys 32 model) at room temperature, and the measurements were repeated for six samples for reproducibility. The samples were cut into a dog bone using a strip cutter. The samples were kept between the holders and tightened up to 40 N cm. The membranes were pulled at a speed of 100 mm $s^{-1}$.

### 4.2.7. Small Angle X-ray Scattering Measurements

Small angle X-ray measurements (SAXS) were made using a Bruker Nanostar, with a rotating anode source (Cu K$\alpha$, l = 1.54 Å), 3 pinhole collimation and a two dimensional multiwire Histar® detector. The results are analyzed through a model independent porod analysis. The domain size was calculated using the relation $D=2\pi/q$, where q and D represents the scattering vector and domain size, respectively.

## 4.3. Results and Discussion

### 4.3.1. TEM and SEM of the Composite Membrane

TEM images obtained with the PBpNT composite membrane are shown in Figure 4.1. The P-MWCNTs are buried under the PBI polymer matrix and consequently clear observation of the CNT is difficult at lower resolution (Figure 4.1a). However, at high resolution, we can see a single P-MWCNT with a diameter of ca. 15 nm which is in accordance with the diameter observed for MWCNTs through SEM images (Figure 4.1.b). The TEM images clearly suggest the homogeneous distribution of P-MWCNTs in the PBI matrix. This is very important to exhibit higher mechanical strength as island like domains induce faster breaking of membranes than that in the homogeneous distribution. Further, it also suggests that the surface functional groups will have a better chance of interacting with the functional groups of the polymer matrix.

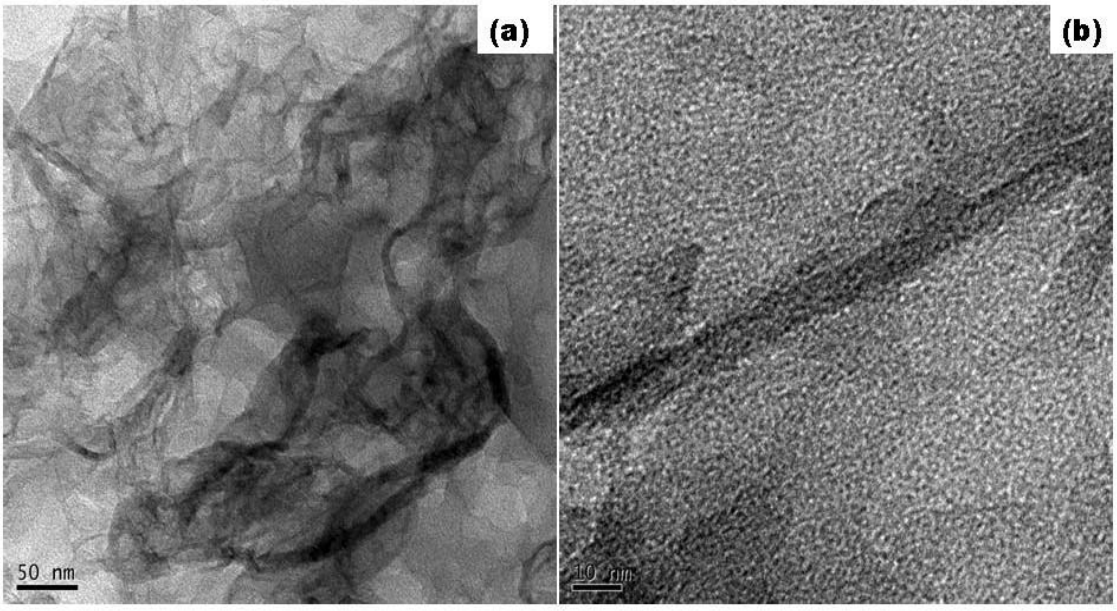


**Figure 4.1.** TEM images of the PBpNT composite membranes at different resolutions; (a) P-MWCNTs buried under the PBI matrix, (b) higher magnification reveals the 15 nm diameter P-MWCNT in the PBI matrix.

The SEM images (Figure 4.2) of the composite membrane, however do not reveal any characteristic change from the pristine membranes as very little CNT is expected to be at the surface of the composite membrane. Further, attempts for high resolution images resulted in pinholes due to the beam induced damages on the membrane. A similar trend is also observed with Nafion based membranes which will be discussed in the next chapter.

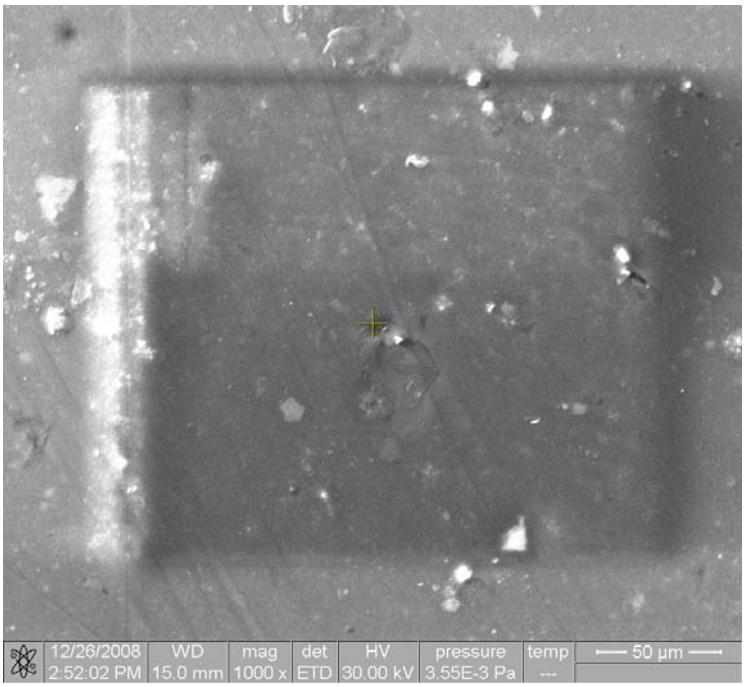


**Figure 4.2.** SEM images obtained with the PBpNT composite membrane after high energy beam exposure revealing the infringes created by the beam on the membrane sample.

### 4.3.2. TGA Measurements

A comparison of thermograms obtained with various PBpNT composite membranes in $N_2$ atmosphere from 50 to 800 °C is shown in Figure 4.3. Almost all the membranes reveal a similar pattern in the thermograms suggesting no significant change in the thermal stability by the addition of functionalized carbon nanotubes. The initial 10 %

weight loss observed with all the membranes till 150 °C can be ascribed to the loss of surface bound water from the PBI matrix. In sharp contrast, from 150 to 250 °C there is

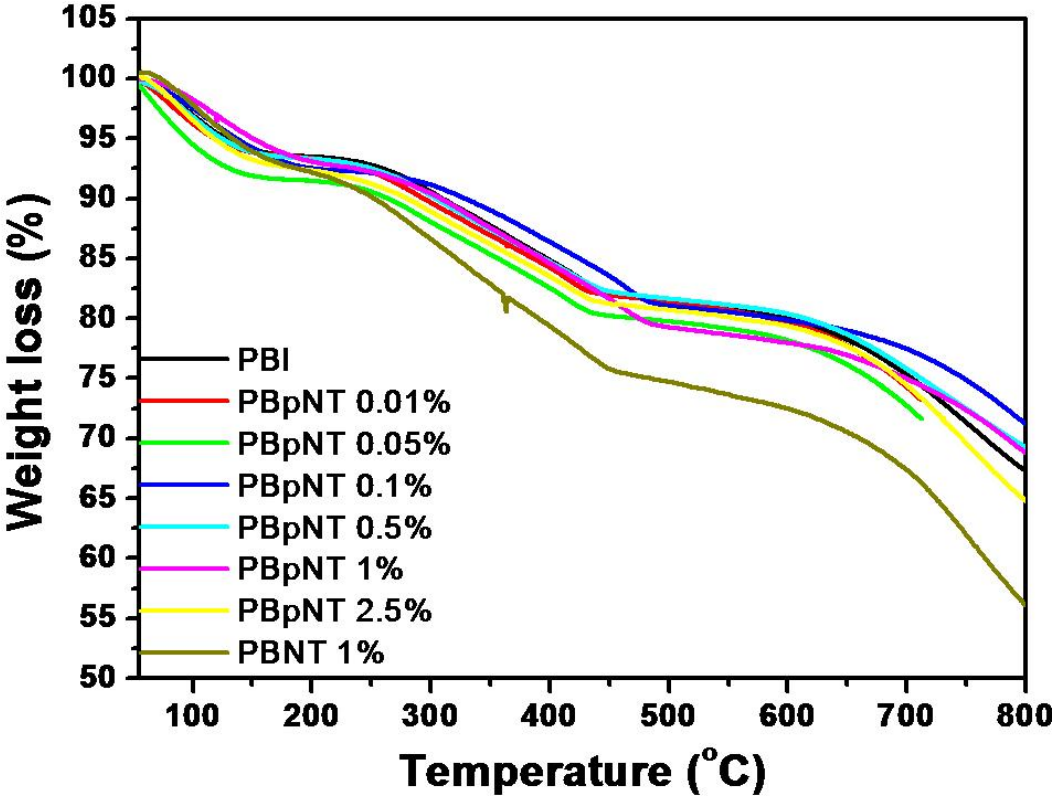


**Figure 4.3.** TGA of PBpNT membranes with various MWCNT concentrations measured at a temperature scan rate of 10 °C per min under nitrogen atmosphere. The plots reveal excellent thermal stability up to 600 °C. PBI, PBpNT and PBNT represents polybenzimidazole, polybenzimidazole-phosphonated MWCNT and polybenzimizole-pristine MWCNT composite membranes respectively.

hardly any weight loss, suggesting the thermal stability of all the membranes up to 250 °C, which is sufficiently higher than the operating temperature of PEMFCs. From 250 to 450°C an overall 10 % weight loss can be seen suggesting that the integrity of the membrane remains largely intact and could be ascribed to the loss of strongly bound water [28]. All the membranes show excellent thermal stability up to 650 °C which could be attributed to the combined effect of rigid aromatic ring backbone and intermolecular hydrogen bonding [29,30].

### 4.3.3. Membrane Conductivity

Figure 4.4 shows the temperature dependant proton conductivity of pristine PBI and composite membranes along with similar data taken for the unfunctionalized CNT/PBI (PBNT) composite for reference. All the composite membranes (PBpNT) show improved proton conductivity than that of the pristine membrane as anticipated with an exception of PBNT composite since it does not have any phosphonate group

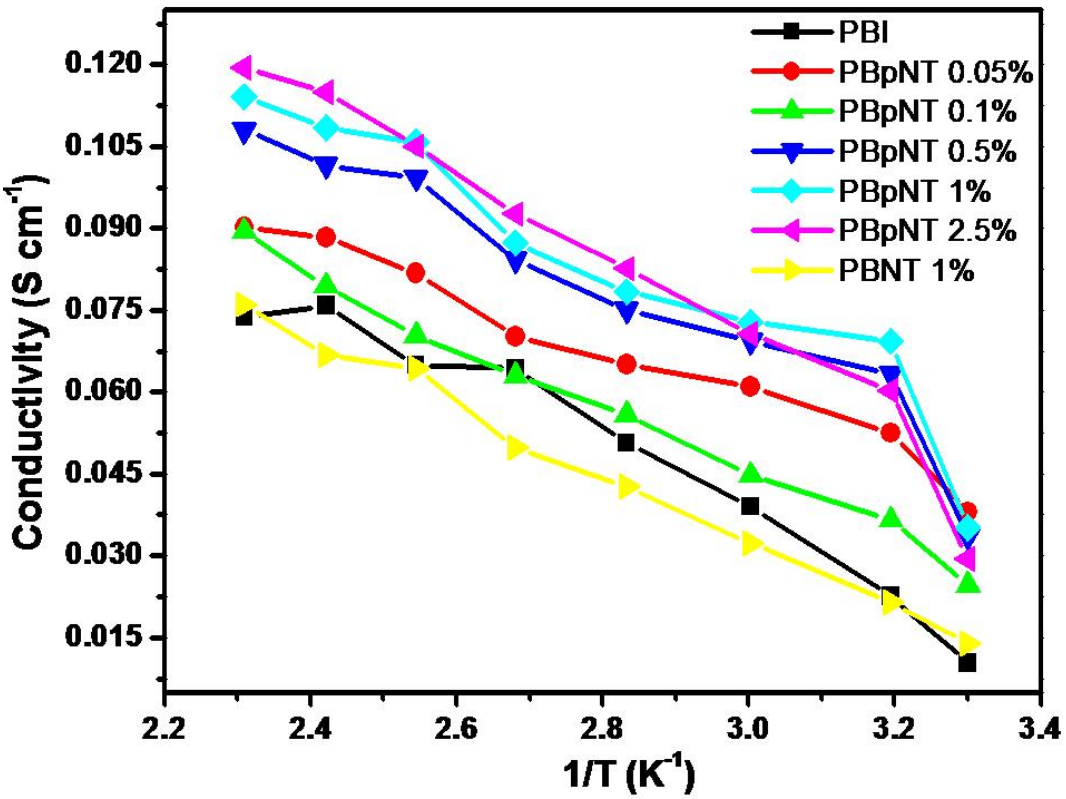


**Figure 4.4.** Temperature dependant proton conductivity of the composite membranes and pristine PBI membrane; PBI, PBpNT and PBNT represent polybenzimidazole, polybenzimidazole-phosphonated MWCNT and polybenzimizole-pristine MWCNT composites membranes respectively.

on the sidewalls to support proton transport. The improved proton conductivity of the PBpNT composite membranes could be attributed to the net increase in the phosphoric acid content while the lower proton conductivity in the PBNT case can also be understood similarly.

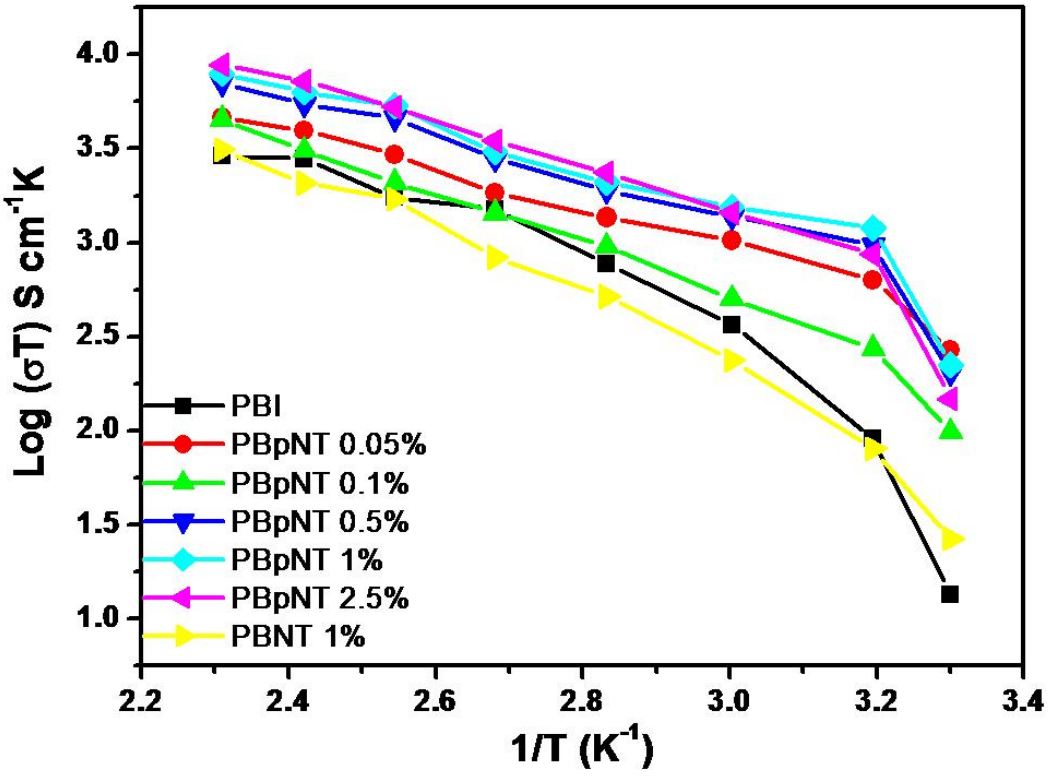


**Figure 4.5.** Arrhenius plots of different composite membranes measured in a two probe impedance measurement at temperatures ranging from 30 °C to 160 °C under humidified conditions; PBI, PBpNT and PBNT represents polybenzimidazole, polybenzimidazole-phosphonated MWCNT and polybenzimizole-pristine MWCNT composites membranes respectively.

Arrhenius plots (Figure 4.5) show a gradual decrease in the slope with the addition of P-MWCNTs emphasizing a change in the mode of proton transport. In phosphoric acid doped PBI membranes, proton transport is mainly through two modes; the rapid exchange of proton via hydrogen bonds between solvent molecules such as phosphate, water, N-heterocycles of PBI and through the self-diffusion of phosphate ions and water molecules [31]. Among the 13 mole per repeating unit of phosphoric acid in the PBI matrix only 2 mole per repeating unit are chemically bonded while the rest is attached by physisorption. It is the physisorbed phosphoric acid molecules that leach out which result in the membrane's poor durability. Efforts

to improve the chemically bonded phosphoric acid by increasing the basicity of the polymer has resulted up to 4 mol per repeat unit which has interestingly shown considerable proton conductivity even after washing [15,17,21]. A transference number of 0.02 and 0.98 measured for $H_2PO_4^-$ anion and for proton further advocates the need for localized phosphonate group networks that can assist

**Table 4.1.** Variation of phosphoric acid uptake and activation energy of PBI based composite membranes with increasing P-MWCNT content.

| Membrane | $H_3PO_4$ uptake (mol/repeat unit) | Activation energy (kJ/mol) |
|---|---|---|
| PBI | 13 | 40.9 |
| PBpNT 0.05% | 12.2 | 21.9 |
| PBpNT 0.1% | 11.4 | 29.4 |
| PBpNT 0.5% | 11.2 | 25.2 |
| PBpNT 1% | 12.4 | 25.1 |
| PBpNT 2.5% | 12.6 | 29.3 |
| PBNT 1% | 11.6 | 37.9 |

the hoping of protons better than increasing the free phosphoric acid that not only leaches out faster but also reduces the integrity of the membrane. These are in excellent agreement with our results where the phosphonic acid moieties immobilized on P-MWCNT help to form a network for proton conduction and thereby increasing the proton conductivity. Further, as shown in Table 4.1, a drop in activation energy from 40 kJ $mol^{-1}$ to 25 kJ $mol^{-1}$ (0.25 eV) is observed in the PBpNT 1% composite membrane. The small variation in the phosphoric acid uptake could not be accounted

for the change in activation energy since it is reported to have no influence on the activation energy [12]. However, in another report, the activation energy does vary with varying phosphoric acid uptake but only slightly after varying the phosphoric acid content significantly. Thus the variation in activation energy clearly reveals the synergistic role played by P-MWCNTs in facilitating the proton transport [14,32].

### 4.3.4. SAXS Study

The possible formation of network structure with the addition of P-MWCNTs in the PBI matrix has received further support in SAXS measurements. Figures 4.6 and 4.7 show the SAXS pattern of PBpNT composite membranes with and without doping of phosphoric acid with various compositions. The pristine PBI membrane does not show any peak corresponding to any domain like structure which is in accordance with literature [33]. However, with the addition of P-MWCNT beyond some critical value (0.5 wt%) the composite membranes start to reveal the formation of clustered networks whose intensity increases with increasing P-MWCNT content. The cluster size calculated using the relation $D=2\pi/Q$ for the composite membranes gives approximately ca. 17 nm and peak position is not affected by the increase in P-MWCNT loading until 1 %. This is close to the diameter of P-MWCNTs which might suggest that the phosphonic acid in the CNTs interact well with the PBI matrix and phosphoric acid to form a network of phosphoric acid along its sidewall. However, higher loading than this results in a change in peak position corresponding to higher cluster size which suggests that the CNTs may agglomerate in the polymer matrix. Further, unmodified CNT-PBI 1% composite (PBNT) does not reveal any cluster formation underlining the importance of functionalization for synergistic interaction.

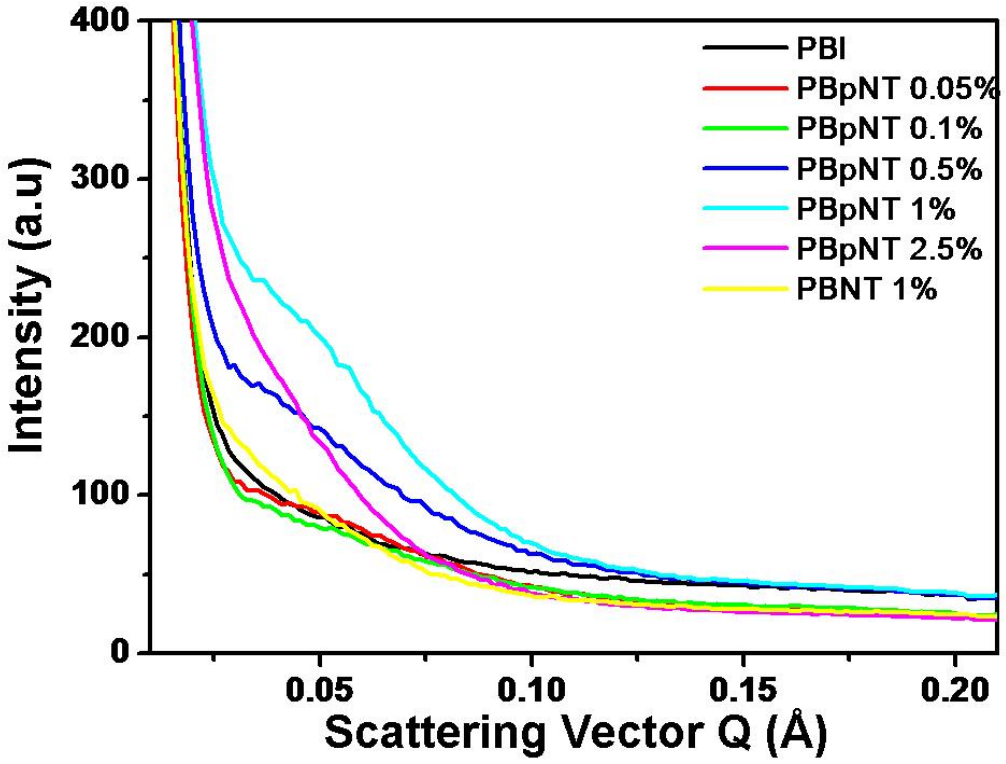


**Figure 4.6.** SAXS patterns obtained with different PBpNT compositions and PBI iso membrane after doping with phosphoric acid. PBI, PBpNT and PBNT represent polybenzimidazole, polybenzimidazole-phosphonated MWCNT and polybenzimizole-pristine MWCNT composites membranes respectively.

On the other hand, un-doped PBpNT and PBNT composite membranes do not show any peak suggesting the absence of any network structure formation due to the incorporation of P-MWCNTs in the PBI matrix (Figure 4.7). This further reiterates that, it is the interaction of phosphoric acid with the imidazole nitrogen and P-MWCNTs that is responsible for the domain formation. In the case of doped PBI membranes the normal reported doping levels range from 6 – 15 mole per repeating unit of PBI membrane and in that only 2 mole can bind chemically which is not sufficient to form networks for proton transport. Further, the vast excess of free phosphoric acid might bury any network structures, if at all it exists. However, due to the presence of phosphonate groups on the P-MWCNTs in the PBI matrix, now even

the physically adsorbed phosphoric acid could align themselves with CNTs resulting in a network formation in the PBpNT composites. This is further in line with the diameter of MWCNTs (13-19 nm) that is observed from the SEM and TEM images.

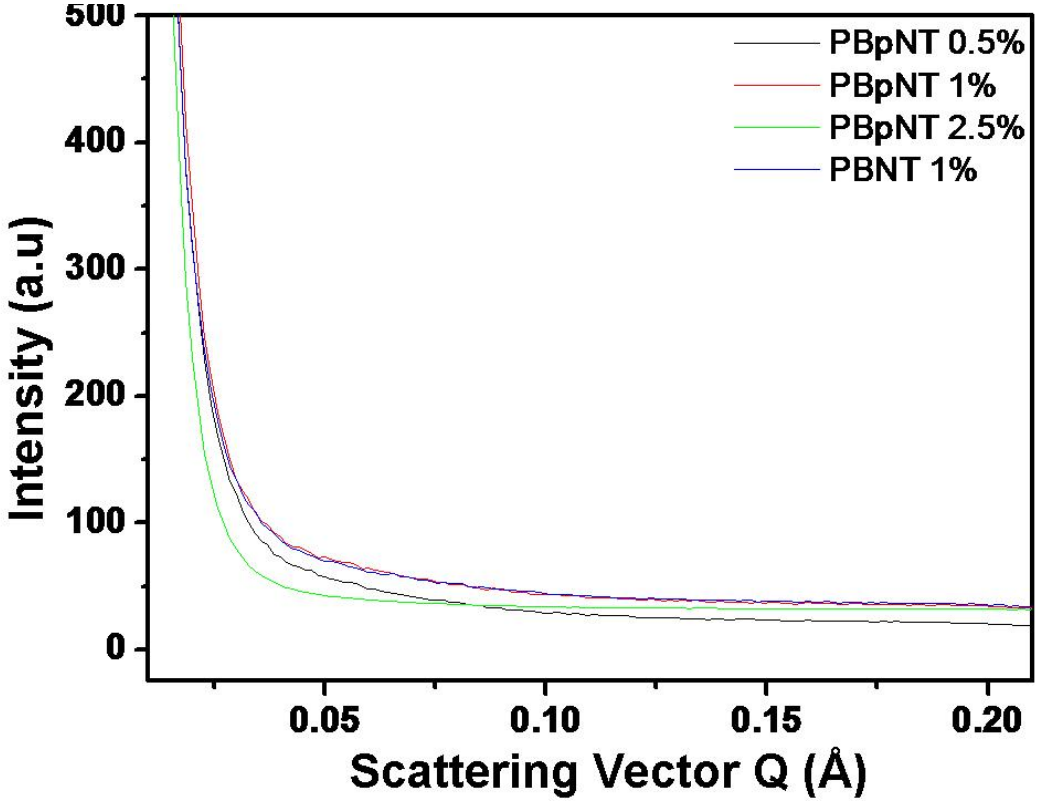


**Figure 4.7.** SAXS measurements obtained with different PBpNT compositions and PBI membrane before doping with phosphoric acid. PBI, PBpNT and PBNT represents polybenzimidazole, polybenzimidazole-phosphonated MWCNT and polybenzimizole-pristine MWCNT composites membranes respectively.

### 4.3.5. Polarization Measurements

Results of fuel cell polarization measurements obtained with the composite and pristine PBI membranes are shown in Figure 4.8. Pristine PBI membrane shows a maximum power density of 600 mW $cm^{-2}$ and the value increases with increasing P-MWCNT content to reach a maximum of 780 mW $cm^{-2}$ at P-MWCNT loading of 1 wt% and to a further diminished value of 600 mW $cm^{-2}$ at 2.5 wt%. We have not

attempted to make PBI membranes with P-MWCNT content higher than 2.5 wt% to avoid any possible electrical short circuiting that could arise from the incorporation of MWCNTs. This improved fuel cell performance is in accordance with the membrane conductivity data and Arrhenius plot where, a significant drop in activation energy

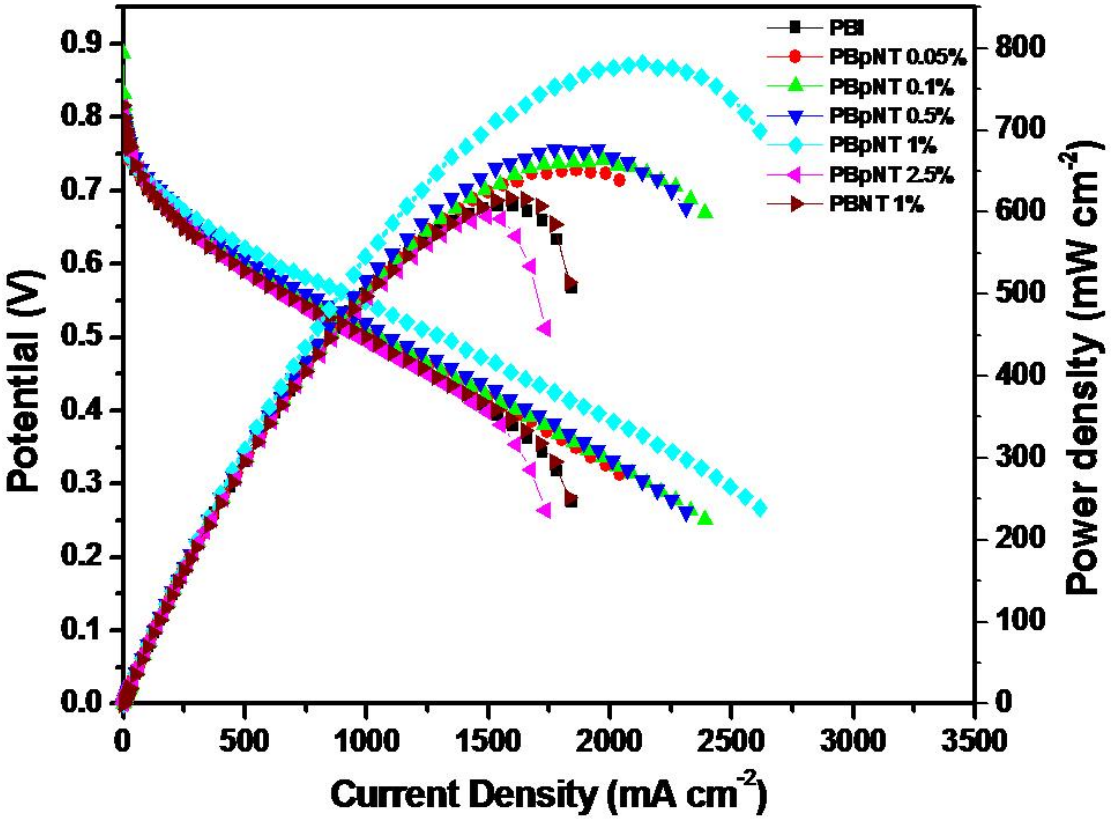


**Figure 4.8.** Fuel cell polarization data measured by passing ultra pure (dry) $H_2$ and $O_2$ with a flow rate of 0.2 slpm at 140 °C on the pristine PBI and composite membranes with different compositions; PBI, PBpNT and PBNT represent polybenzimidazole, polybenzimidazole-phosphonated MWCNT and polybenzimizole-pristine MWCNT composites membranes respectively.

has been observed for composite membranes. Accordingly a performance enhancement of 35 % in power density can be achieved with PBpNT 1% membrane. This can be attributed to better mass transport and reduced activation loss in the composite membrane. A minimum of 60 mV reduction in overpotential is achieved at all current densities and a maximum of 150 mV is observed at 2250 mA $cm^{-2}$ for PBpNT-1 %

composite corresponding to the mass transport limiting region of the polarization plot (Figure 4.9). Overall, all the membranes show similar open circuit potentials after which the composite membranes outperform the bare membrane in almost all three modes of resistive losses viz., activation, ohmic and mass transport losses. In particular, during the activation and mass transport region, the composite membrane shows minimal loss in potential than that of the pristine membrane.

The interface between electrolyte and electrocatalyst plays a significant role in the activation polarization and catalysts that are in intimate contact with CNTs are reported to have higher exchange current density than that of unsupported and those supported on carbon [34]. Hence the improved interface in the composite membrane between Pt catalysts and P-MWCNT-PBI presumably helps in achieving lower activation loss. Further, the slightly reduced activation energies obtained with composite membrane might also have played a role in decreasing the activation losses. Also, the increased sites for hoping in composite membrane means increased mass transport than that of the bare membrane as evidenced by the higher current density obtained with the composite membrane. However, the drop in performance in the case of PBpNT 2.5 wt% can be attributed to three dimensional constrains due to higher P-MWCNT presence that would restrict the swelling of PBI matrix during phosphoric acid uptake. Also as evidenced from the SAXS measurements, agglomeration of the P-MWCNTs might also have contributed to the reduced performance. For comparison the single cell performance of unmodified CNT- PBI composite membrane (PBNT-1%) is also shown in the Figure 4.8, which apparently reveals no improvement from that of the pristine PBI membrane. Since there are no

phosphonic acid groups on the side walls of unmodified MWCNTs, it doesn't seem to enhance the proton transport and hence the performance is not affected.

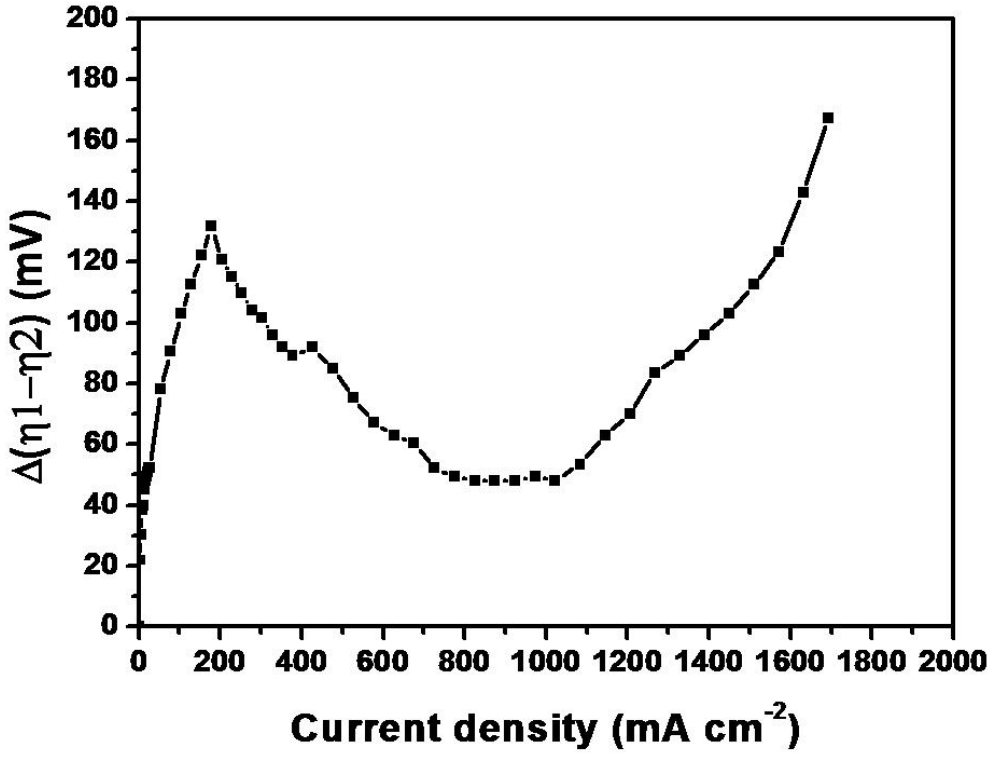


**Figure 4.9.** Comparison of the variation in overpotentials between PBI and PBpNT-1 % composite membranes with respect to current density revealing a minimum of 60 mV reduction in overpotential in the case of composite membranes.

### 4.3.6. MEA Impedance

To understand the reason for this improved fuel cell performance, we further carried out *in situ* impedance measurements on the MEAs of pristine and composite membrane. Figure 4.10 accordingly shows the Nyquist plot of MEA impedance measurements at different temperatures for pristine PBI and also at various overpotentials at 140 °C. The plots contain one semicircle in the high frequency region at low temperatures and with increasing temperature another semicircle in the low frequency range begins to appear. The high frequency semicircle corresponds to

the hydrogen oxidation reaction (HOR) while the low frequency region semicircle describes the oxygen reduction reaction (ORR) which has been verified by changing the rate of gas supply. The semicircle corresponding to hydrogen oxidation normally

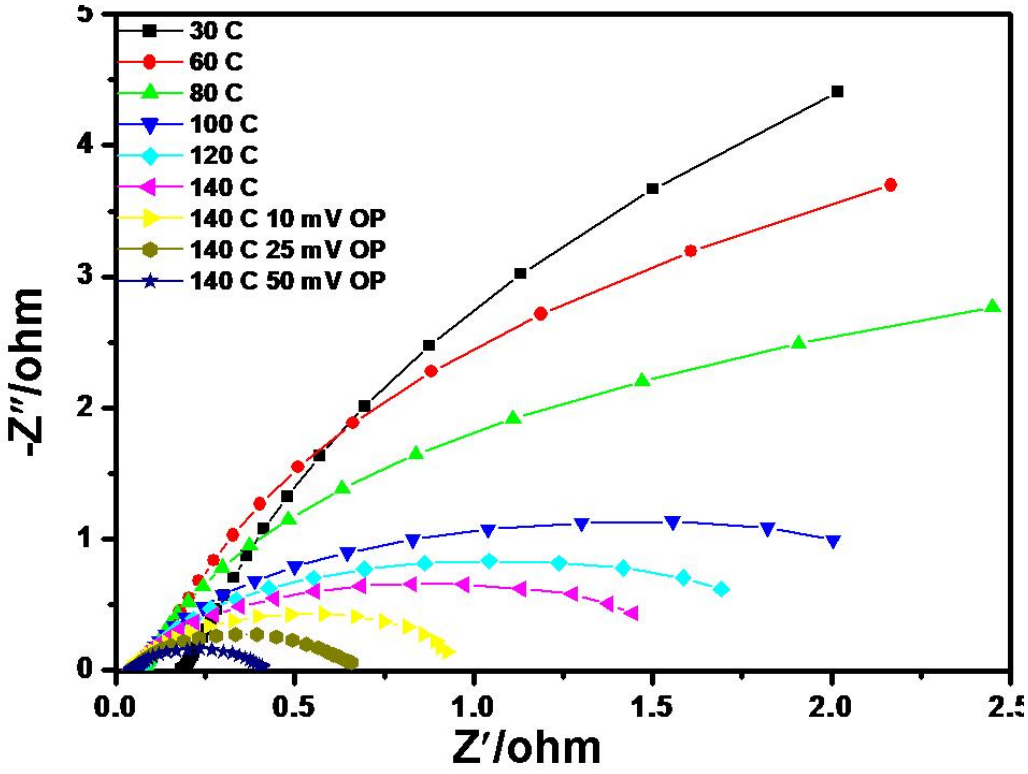


**Figure 4.10.** Impedance Nyquist plots obtained for pristine PBI membrane at various temperatures from 25 to 140 °C and at different overpotentials at 140 °C by passing hydrogen and oxygen to the anode and cathode respectively.

merges with that of the overlaying oxygen reduction reaction and is less significant considering the facile kinetics of HOR. However, the kinetics of ORR is very much sluggish and the effect of increasing temperature on improving the kinetics could be reflected in the dramatic fall in charge transfer resistance. Further, it is well-known that at low overpotentials (< 200 mV) the semicircle observed predominantly belongs to the charge transfer resistance of the cathode ORR while at higher overpotentials (> 200 mV), the impedance spectrum is complicated by processes related to the mass transport of oxygen and by the transport of product water. A detailed study of the

impact of operating potential, temperature, and flow rate on charge transfer resistance is helpful to understand all the relative contributions [35].

Accordingly, overpotentials up to 50 mV have been applied to measure the charge transfer resistance of ORR and the results obtained are shown in Figure 4.11. The charge transfer resistance for the ORR at 140 °C and at 50 mV overpotential, decreases with increasing P-MWCNT content although at very high P-MWCNT loading, the charge transfer resistance again increases, surprisingly to a higher value.

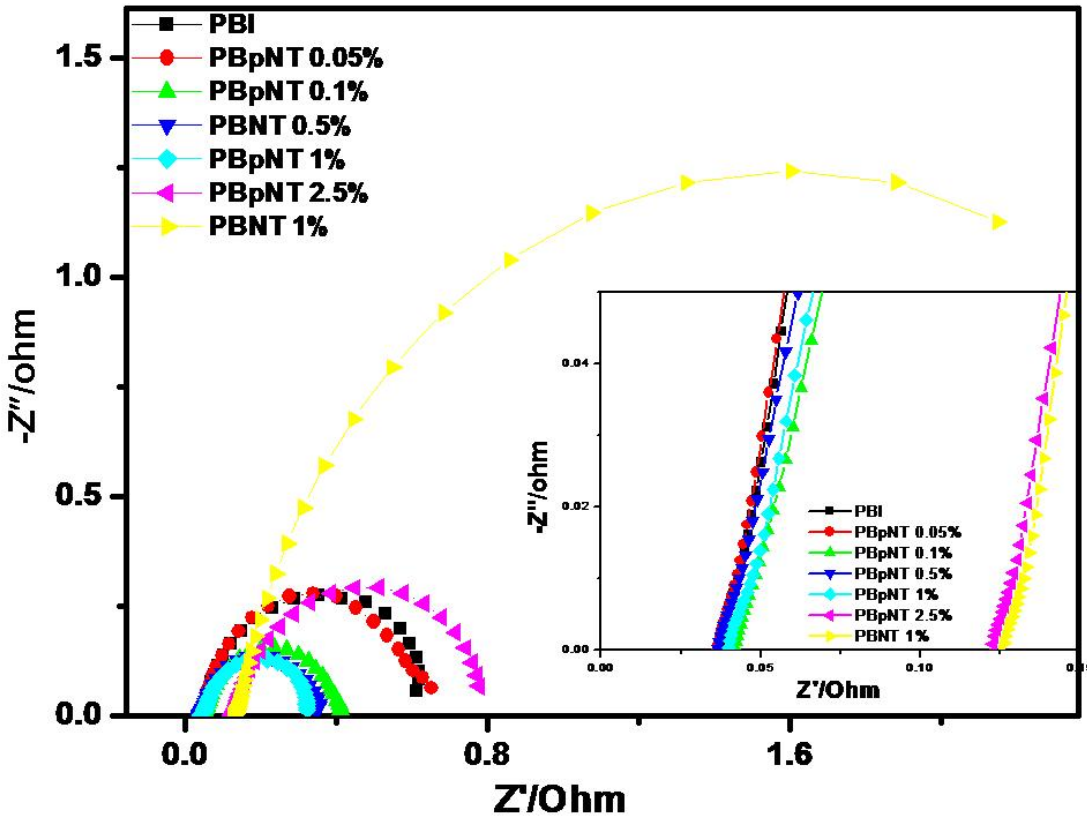


**Figure 4.11.** In-situ MEA impedance Nyquist plots observed for the pristine PBI and composite membranes at 140 °C with an overpotential of 50 mV from the open circuit potentials.

This could be explained on the basis of membrane conductivity and fuel cell performance. Despite showing a very high conductivity in the impedance measurement, PBpNT 2.5 % gives lesser performance than that of pristine membrane

which could be attributed to the rigidness of the membrane due to the higher loading of P-MWCNT. Further, SAXS measurements show increased domain sizes that could be attributed to the P-MWCNT agglomeration. Due to this, the mass transport is hindered across the membrane which could be easily seen from the drop in potential in the mass transport region of the polarization plots. Further, this increased rigidity affects the proper binding of electrodes to the membrane and in turn the MEA gets affected by the poor electrolyte-electrode interface. Hence an increased charge transfer resistance for the PBpNT-2.5 wt% composite membrane is seen despite the higher P-MWCNT loading. It also reduces the membrane conductivity as inferred from the MEA impedance and this collectively results in poor fuel cell performance. This further validates our decision of not going beyond 2.5 wt% for composite making.

### 4.3.7. Solid-State Cyclic Voltammetry of Composite MEAs

Solid-state cyclic voltammograms of PBI and composite membranes based MEAs, obtained by passing $H_2$ and $N_2$ to the anode and cathode, respectively reveal an almost similar hydrogen desorption peak area suggesting an equivalent level of electrochemically active Pt (Figure 4.12). We have intentionally chosen a high level of Pt loading (0.5 mg $cm^{-2}$) in order to avoid any contribution from Pt to the variation in fuel cell performance. This further proves that the improved fuel cell performance is achieved by the enhanced proton conductivity of membrane alone and other parameters such as ionomer binder loading, carbon support and Teflon binder in the gas diffusion layer are identical and does not contribute significantly.

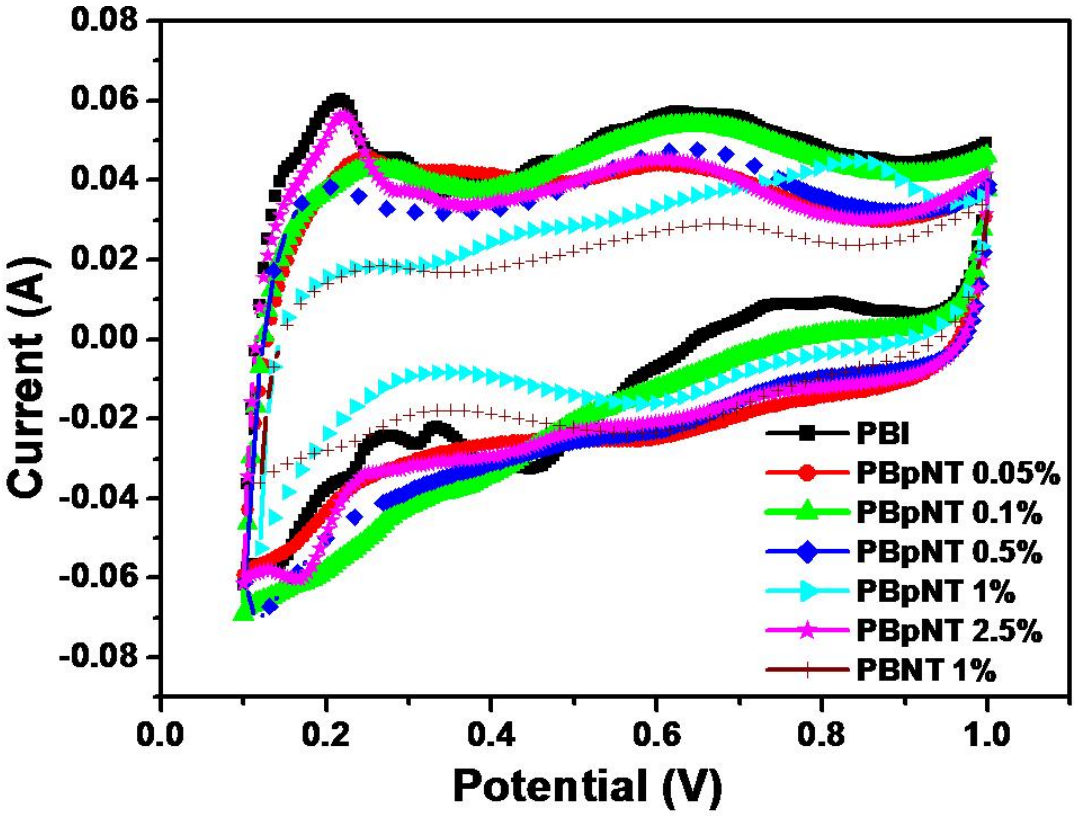


**Figure 4.12.** Solid-state cyclic voltammograms obtained with PBI, PBpNT and PBNT composite membranes by passing $H_2$ and $N_2$ to the anode and cathode respectively; the working electrode in this experiment is the cathode while the anode acts as counter and reference electrode.

### 4.3.8. Mechanical Stability Measurements

The stress strain plots measured for the P-MWCNT composite and pristine PBI membranes are shown in Figure 4.13. Composite membranes demonstrate improved mechanical stability over pristine membrane in almost all the characteristic regions of stress-strain plot. For example, the yield strength of PBI membrane is 62 MPa while that of the PBpNT-1% composite membrane is 80 MPa suggesting the synergistic role of P-MWCNTs in increasing the mechanical strength. Similarly, the ultimate strength of the composite membranes is much higher than that of the pristine PBI membrane as a maximum of 95 MPa is observed with PBpNT-1 % membrane while PBI shows only 60 MPa. A similar trend in stress at rupture (the point where the membrane

breaks completely) is observed although in terms of strain, the breaking point varies drastically.

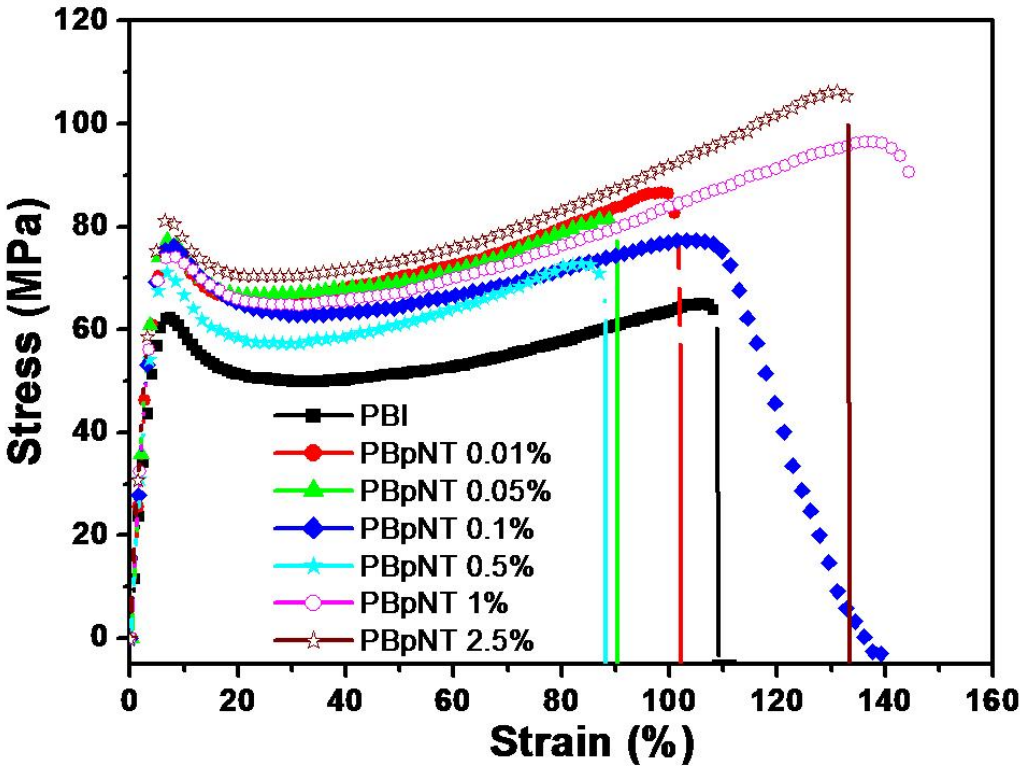


**Figure 4.13.** Stress-strain plots of the pristine PBI and P-MWCNT/PBI composite membranes at room temperature.

The incorporation of functionalized MWCNTs in polybenzimidazole matrix has resulted in significant improvement in proton conductivity as well as the mechanical stability of the resulting composite membranes. However, one of the key challenges with phosphoric acid doped PBI membranes is the leaching out of phosphoric acid from the polymer matrix that results in the loss of proton conductivity and hence a consequent deterioration in fuel cell performance. In this regard, the incorporation of P-MWCNTs can increase the integrity of the PBI membrane as inferred from the mechanical stability facilitating improved performance since it could reduce the phosphoric acid leaching. Further experiments are desired to test the

long term performance of the composite membrane in providing sustained performance.

### 4.4. Conclusions

In this chapter, we have prepared composite membranes based on PBI and phosphonated MWCNTs demonstrating enhanced proton conductivity and fuel cell performance. The optimum level of P-MWCNT doping is 1 wt% as observed collectively from membrane conductivity and polarization studies. Further, SAXS measurements reveal a network formation for proton conductivity in the composite membrane which could be associated to its improved performance. The incorporation of functionalized MWCNTs improves both the mechanical stability and proton conductivity and hence this work would make a significant impact in the fuel cell technology. For example, a maximum power density of 780 mW $cm^{-2}$ is attained with PBpNT-1 % composite membrane while only 600 mW $cm^{-2}$ is observed with the pristine PBI membranes. Further, the composite membranes with its improved integrity, thanks to the incorporation of P-MWCNTs, might reduce the acid leaching from the polymer matrix at least partly to achieve increased durability.

## 4.5. References

**[1]** Metha, V.; Cooper, J. S. *J. Power Sources*, **2003,** 114, 32.

**[2]** Li, Q, He, R.; Jensen, J. O.; Bjerrum, N. J. *Chem. Mater.* **2003,** 15, 4896.

**[3]** Schuster, M.; Rager, T.; Noda, A.; Kreuer, K. D. Maier, J. *Fuel Cells,* **2005,** 5, 355.

**[4]** Huang, J. M.; Chen, R. Y. *Heteroat. Chem.* **2000,** 11, 480.

**[5]** Zhao, T. S.; Kreuer, K. D.; Nguyen, T. V. Advances in fuel cells, Elsevier, **2007,** Volume 1, Chapter 3.

**[6]** Savinell, R. F.; Wainright, J. S.; Litt, M. *Proceedings of the 2nd Symposium on Proton Conducting membrane Fuel Cells*, **1998,** p.81.

**[7]** Zhao, T. S.; Kreuer, K. D.; Nguyen, T. V. Advances in fuel cells, Elsevier, **2007,** Volume 1, Chapter 5.

**[8]** http://www.osti.gov/bridge/servlets/purl/936594-1t8iYb/936594.pdf accessed on **20th September, 2010.**

**[9]** http://itech.dickinson.edu/chemistry/?cat=100 accessed on 20th September, 2010.

**[10]** Wainright, J. S.; Wang, J. T.; Weng, D.; Savinel, R. F.; Litt, M. *J. Elelctrochem. Soc.*, **1995,** 142, L121.

**[11]** Wainright, J. S.; Litt, M. H.; Savinell, R. F.; Vielstich, W.; Lamn, A.; Gasteiger, H. A. Hand Book of Fuel Cells – Fundamentals, Technology and Applications, Vol. 3, John Wiley and Sons, **2003,** Ch. 34. Chichester, UK.

**[12]** Bouchet, R.; Siebert, E. *Solid State Ionics.*, **1999,** 118, 287.

**[13]** Li, Q.; He, R.; Jensen, J. O.; Bjerrum, N. J. *Fuel Cells,* **2004,** 4, 147.

**[14]** Li, Q.; Hjuler, H.; A. Bjerrum, N. J. *J. App. Electrochem.*, **2001,** *31*, 773-779.

**[15]** Yu.S.; Zhang. H.; Xiao. L.; Choe. E.W. Benicewicz. B.C. *Fuel Cells* **2009,** 09, 318.

**[16]** Carollo, A.; Quartarone, E.; Tomasi, C.; Mustarelli, P.; Belotti, F.; Magistris, A.; Maestroni, F.; Parachini, M.; Garlaschelli, L.; Righetti, P. P. *J. Power Sources* **2006,** 160, 175.

**[17]** Mustarelli. P. Quartarone. E.; Grandi. S.; Carollo. A.; Magistris. A. *Adv. Mater.* 20, 1339-1343, 2008.

**[18]** Quartarone. E.; Mustarelli. P.; Carollo. A.; Grandi. S.; Magistris. A.; Gerbaldi. C. *Fuel Cells* **2009,** 09, 231.

**[19]** He. R.; Li. Q.; Xiao. G.; Bjerrum. N.J. *J. Membr. Sci.* **2003,** 226, 169.

**[20]** Chuang. S.W.; Hsu. L.C.; Hsu. C.L. *J. Power Sources* **2007,** 168, 172.

**[21]** Carollo, A.; Quartarone, E.; Tomasi, C.; Mustarelli, P.; Belotti, F.; Magistris, A.; Maestroni, F.; Parachini, M.; Garlaschelli, L.; Righetti, P. P. *J. Power Sources,* **2006,** 160, 175.

**[22]** Gillham, J. K. *Science* **1963,** 139, 494.

**[23]** Jorgensen, B. S.; Young, J. S.; Espinoza, B. F. *US patent* 6, 946, 015 (**2005**).

**[24]** Li, Q.; Pan, C.; Jensen, J. O.; Noye, P.; Bjerrum, N. J. *Chem. Mater.* **2007,** 19, 350.

**[25]** Lu, Y.; Chen, J.; Cui, H.; Zhou, H. *Composite Science and Technology,* **2008,** 68, 3278.

**[26]** Fujigaya, T.; Okamoto, M.; Nakashima, N. *Carbon,* **2009,** 47, 3227.

**[27]** Li, N.; Zhang, F.; Wang, J.; Li, S.; Zhang, S. *Polymer,* **2009,** 50, 3600.

**[28]** Knowlton, G. D.; White, T. R.; McKague, H. L *Clays and Clay minerals,* **1981,** 29, 403.

**[29]** Xu, H.; Chen, K.; Guo, X.; Fang, J.; Yin, J. *J. Membr. Sci.* **2007,** 288, 255.

**[30]** Kumbharkar, S. C.; Islam, Md. N.; Potrekar, R. A.; Kharul, U. K. *Polymer,* **2009,** 50, 1403.

**[31]** Pu, H., Meyer, W. H.; Wegner, G. *J. Polym. Sci., Part B: Polym. Phys.* **2002,** 40, 663.

**[32]** He, R.; Che, Q.; Sun. B. *Fibers and Polymers,* **2008,** 9, 679.

**[33]** Zhang, H.; Li, X.; Zhao, C.; Fu, T.; Shi, Y.; Na, H. *J. Membr. Sci.* **2008,** 308, 66.

**[34]** Britto, P.J.; Santhanam, K. S. V.; Rubio, A.; Allonso, J. A.; Ajayan, P. M. *Adv. Mater.,* **1999,** 11, 154.

**[35]** Ciureanu, M.; Roberge, R. *J. Phys. Chem. B* **2001,** 105, 3531.

# Chapter 5

## Sulphonated Carbon Nanotubes and Their Composites with Perfluoro Sulphonic Acid Membranes for PEMFC Applications

In this chapter, the application of sulphonic acid-functionalized multiwalled (S-MWNT) carbon nanotubes to manipulate the hydrophilic domain size of Nafion membranes is explored as an option for tuning the proton conductivity of polymer electrolyte membranes for hydrogen-oxygen fuel cells. Electrochemical impedance experiments provide preliminary evidence for increased proton conductivity, while small-angle X-ray scattering measurements line out enhanced ionic cluster domain size in these composite membranes as the central reason for higher conductivity (70 Å as the optimum size for the composite membrane *Vs* 50 Å for Nafion 115) values. Scanning electrochemical microscopy studies indicate synergistic interactions between the sulphonic acid functional groups present in the Nafion membrane and those on the nanotube surface. More interestingly, the nanotube-tailored Nafion membranes enhance the performance of fuel cells as confirmed by measurements at a single-cell level, which reveal a maximum power density of 380 mW $cm^{-2}$, which is higher than those for Nafion 115 (250 $mWcm^{-2}$) and recast Nafion (230 $mWcm^{-2}$) membranes. Thus, in addition to providing an elegant means of controlling the ionic cluster size, the strategic approach of using CNT both as an anchoring backbone for $-SO_3H$ groups to enrich proton conductivity and as a blending agent to improve the mechanical characteristics of the Nafion phase help in alleviating many critical problems associated with the use of commercial Nafion membranes.

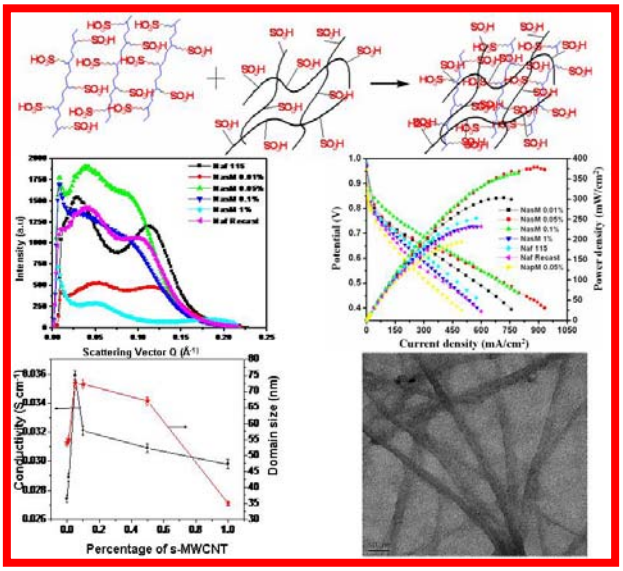


* A part of the work discussed in this chapter has been published in *Angew. Chem.* **2008,** 120, 2693 and *Langmuir* **2009,** 25, 8299.

## 5.1. Introduction

One of the most important components limiting the overall performance of a PEMFC is the proton exchange membrane (PEM). Critical characteristics of a good PEM include fast proton conduction, good water transport, low electro-osmotic drag, thermal/mechanical stability and sustained durability under operation [1-3]. Commonly used PEMs, namely Nafion membranes are composed of a hydrophobic polytetrafluoroethylene backbone and hydrophilic perflouorinated pendant side chains ending with sulphonic acid moieties. These sulphonic acid moieties, when exposed to water, form hydrophilic domains of approximately 40 Å in size [4,5]. It is this domain structure that controls the transport properties of almost all amphiphilic polyelectrolytes in general. However, it is important to note that the 'existence' of hydrophilic and hydrophobic domains is only a necessary condition, but not a sufficient condition for 'high' proton conductivity. For example, while perflouorinated sulphonic acid PEMs exhibit proton conductivities of about $1x10^{-1}$ S $cm^{-1}$ at 80 °C, those with hydrocarbon backbones at similar temperatures display only $1x10^{-3}$ S $cm^{-1}$ [6,7]. Similarly, the reduced proton conductivity for sulphonated poly(ether ketones) has been attributed to the less pronounced separation of the hydrophilic and hydrophobic domains [8]. Further, significant differences in proton conductivity within the perfluorinated class of PEMs have also been reported with changes in factors like equivalent weight, degree of sulphonation and processing procedures [9-12]. These observations clearly indicate that in addition to the 'presence' of domains, their number, ordering and distribution, (collectively denoted as the 'microstructure' of the PEM) are the determining factors of their performance. On the other hand, the effect of the 'size' of the hydrophilic domains can be

appreciated by reports on enhanced proton conductivity by increasing the number of sulphonic acid groups per domain either while synthesizing the PEM or by introducing sulphonic acid containing additives into the polymer matrix.

Recently, additives with sulphonic acid groups have attracted the attention for making composites with Nafion since this would help to increase the net sulphonic acid content, which otherwise would be reduced [13-20]. For instance, sulphated β-cyclodextrin, sulphonated organic montmorillonites and super acid species like inorganic sulphated zirconia have been utilized as an additive to increase the proton conductivity by increasing the water uptake and binding the water more rigidly even at high temperatures [13-15]. Similarly, sulphonated poly(phenylmethyl silsesquioxane) has been incorporated with Nafion to improve its proton conductivity concomitantly reducing the permeability of liquid fuels [16]. Similarly, aromatic polymers with increased sulphonic acid content have also been reported for PEM fuel cell applications with proton conductivity comparable to that of Nafion membranes [19]. However, attempts to increase the water retention ability of the PEM by increasing the hydrophilic domain size by incorporating hygroscopic materials like $SiO_2$, $ZrO_2$, $TiO_2$, zirconium phosphate and zeolites have often reduced its proton conductivity because of the decrease in the number of sulphonate groups per unit volume of the domain [21-25]. On the contrary, increasing the sulphonic acid content and hydrophilic domain size beyond a certain limit has led to adverse behaviors like swelling and related dimensional changes of the membranes. These observations insist the necessity to control the domain sizes without affecting water management. Although the unprecedented influence of domain sizes in Nafion membrane has been realized in many studies, deliberate attempts to manipulate them have not been very

successful probably due to the lack of proper control over the interactions of the additives and the PEM domains.

In chapter 4, we studied the importance of incorporating functionalized MWCNTs with tailor made groups (phosphonic acid) to increase simultaneously the proton conductivity and mechanical strength of PBI membranes. Further, we could also see a network formation for proton transport. In this regard, sulphonated MWCNTs might help to increase the proton conductivity of Nafion membranes as both have sulphonic acid in common whose presence plays a crucial role on domain size control and in turn proton conductivity (Scheme 1). Consequently we, in this chapter, demonstrate a novel strategy of deliberate manipulation of hydrophilic domain sizes in Nafion by gradually introducing sulphonated multiwalled carbon nanotubes (S-MWCNT) into the matrix. A systematic analysis of the critical changes in the domain sizes as estimated from small angle X-ray scattering and its effect on the proton conductivity of the composite membranes has helped to correlate the enhancement in fuel cell performance with results obtained from electrochemical techniques like cyclic voltammetry, steady state polarization studies and scanning electrochemical microscopy.

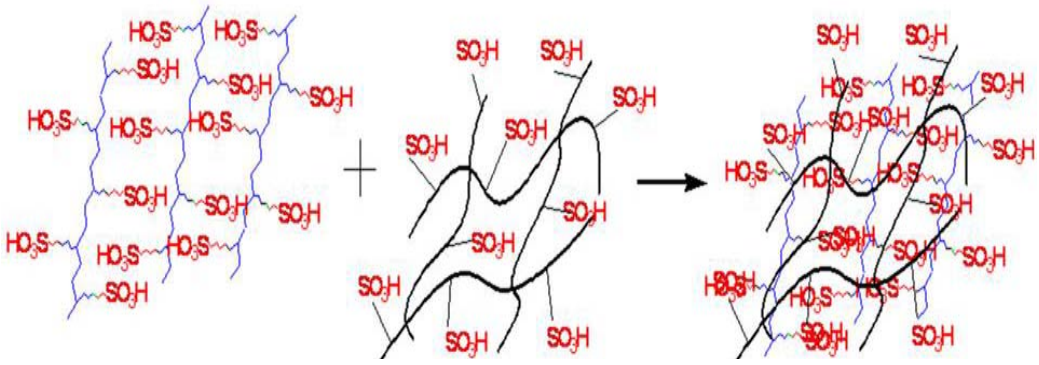

**Scheme 5.1.** Interaction of sulphonic acid groups on the S-MWCNTs with that on the Nafion matrix; the sulphonic acid domains in the Nafion matrix can be bulged by the presence of sulphonic acid groups on the S-MWCNTs.

## 5.2. Experimental Aspects

### 5.2.1. Preparation of NasM Composite Membranes

570 mg of precast Nafion membrane (5% Nafion solution, Electrochem Inc.,) was dissolved in dimethylacetamide (15 mL) and mixed with a solution of S-MWCNTs in dimethylacetamide (20 mg in 100 mL in appropriate amount). The mixture was stirred for 4 h at 70 °C followed by a 45 min ultrasonication before being cast in an oven at 90 °C. These membranes were further annealed at 150 °C for 2 h in a vacuum oven. The resulting membrane (≈120-130 μm thickness) was pre-treated by boiling for 1 h in 3 % $H_2O_2$ to remove any impurities followed by boiling in water to remove excess $H_2O_2$. The resulting membrane was finally boiled in 0.5 M $H_2SO_4$ for 1 h to acidify the membrane followed by boiling in water to remove any excess of acid. These membranes were kept in de-ionized water until further use.

### 5.2.2. Characterization of the Composite Membranes

The temperature-dependent ionic conductivity of the composite membranes was measured by a homemade, two-probe cell with a built-in heating facility. Thermal gravimetric analysis (TGA) was conducted using a Mettler Toledo TGA/SDTA 851 under oxygen atmosphere with a heating rate of 10 °C per min in the temperature range of 50 to 700 °C. FT-IR experiments were measured on a PerkinElmer instrument.

### 5.2.3. Polarization Measurements

Gas diffusion layers (GDL) were prepared by applying a slurry of Vulcan XC-72, PTFE, water, and cyclohexane on teflonized carbon cloth. The slurry was brushed

until a carbon coating of 4 mg $cm^{-2}$ was achieved. The GDL was heat-treated at 350 °C for 30 min before the application of the catalyst ink. The electrodes were prepared by brushing the catalyst ink on the GDL. The ink was prepared by mixing 20 wt% Pt/C, Nafion, water, and isopropyl alcohol using a homogenizer (Cole Parmer, model CV33) for 2 min on a 20 s on-off basis. The amounts of Pt and Nafion loading were 0.5 and 0.6 mg $cm^{-2}$, respectively, for both electrodes. Finally, a thin layer of Nafion was applied on the electrode surface before it was uni-axially pressed with the membrane at 120 °C and a pressure of 0.25 ton $cm^{-2}$ for 3 min to prepare the membrane electrode assembly (MEA). Single-cell fuel cell experiments with these MEAs were tested on an Arbin fuel cell test station (model Arbin-001 MITS Pro-FCTS 5.0-FCTS) at 70 °C. The single cell had an apparent area of 5 $cm^2$ with serpentine flow fields (Electrochem ink). Prior to the testing, the MEA was conditioned at 0.2 V for 30 min, after which the polarization measurements were conducted with a flow of 0.2 slpm using both humidified Hydrogen and Oxygen. MEA impedance measurements were conducted on an Autolab PGSTAT30 (Ecochemie) instrument by passing humidified hydrogen and oxygen at room temperature using a root-mean-square amplitude of 10 mV between 100 kHz and 0.1 Hz, while solid-state cyclic voltammetric measurements were taken by passing humidified hydrogen and nitrogen to the anode and cathode sides respectively.

### 5.2.4. Scanning Electrochemical Microscopy (SECM) Measurements

Scanning electrochemical microscope (SECM) experiments were conducted using a CHI 900 series instrument on feedback mode using 0.1 mM $[Ru(NH_3)_6]^{3+}$ as the redox mediator in 1 mM $KNO_3$ with a 1 μm Pt tip as the probe. A Pt wire served as the

counter electrode, while Ag/AgCl-saturated KCl was used as the reference electrode. SECM imaging was conducted 1 μm above the substrate by keeping the tip potential at -0.15 V using a typical scan area of 500 $\mu m^2$. The bias potential of the tip was determined by cyclic voltammetric measurements while the distance between the substrate and tip was estimated by probe approach curves. Prior to imaging, the SECM tip was characterized by cyclic voltammetry to ensure that the electrode exhibited reasonable current amplitude, low capacitive current, and steady state behavior. The cyclic voltammograms were recorded in 0.1 M KCl containing 1 mM ferrocenemethanol, with an Ag/AgCl saturated KCl reference electrode and a Pt counter electrode from which the steady state current was measured. From this steady state current, the tip diameter was calculated to be ~1 μm.

### 5.2.5. Mechanical Stability Measurements

All mechanical stability measurements were performed on a micro tensile meter (Linkam, using Linksys 32 model) at room temperature, and the measurements were repeated for six samples for reproducibility. The samples were cut into a dog bone using a strip cutter. The samples were kept between the holders and tightened up to 40 N cm. The membranes were pulled at a speed of 100 mm $s^{-1}$.

### 5.2.6. SAXS Measurements

Small angle X-ray measurements (SAXS) were made using a Bruker Nanostar, with a rotating anode source (Cu Kα, l = 1.54 Å), 3 pinhole collimation and a two dimensional multiwire Histar® detector. The results were analyzed through a model independent porod analysis. The domain size was calculated using the relation $D=2\pi/q$, where q and D represents the scattering vector domain size respectively.

## 5.3. Results and Discussion

### 5.3.1. SEM and TEM Studies

SEM images of the composite membranes are shown in Figure 5.1 before and after the analysis since higher resolution requires high beam energy which sometimes could damage the membrane. Figure 5.1 (a) reveals the uniform morphology of the composite membranes on its surface with no observable carbon nanotubes on its surface. This emphasizes that, the composite membranes are homogeneous and CNTs are not distributed randomly. However, we could not see the MWCNTs inside the Nafion matrix as beam induced damages on the polymer matrix (Figure 5.1. b) occur to produce pin holes as seen in Figure 5.1. (c).

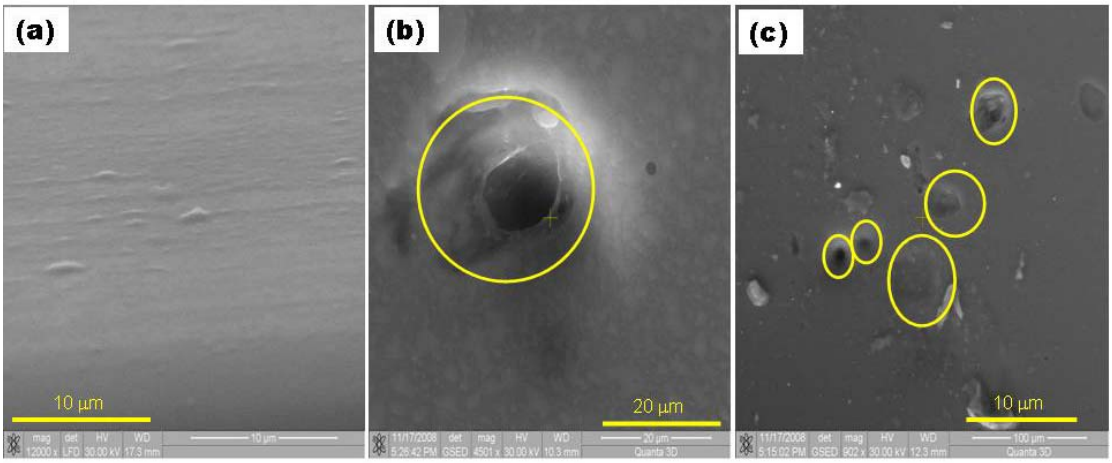


**Figure 5.1.** SEM images of NasM composite membranes at different magnifications; (a) before attempting high resolution images, (b) creation of pin hole by high energy beam and (c) pin holes and infringes created by the high energy beam on the polymer matrix.

TEM image of the composite membrane is shown in Figure 5.2, revealing the homogeneous distribution of S-MWCNTs inside the Nafion matrix as the CNTs are observed under the polymer matrix. This is well in accordance with the SEM analysis

and more interestingly the diameters observed in the TEM analysis are in the range of 12-20 nm. This further reveals the individual distribution of CNTs as no bundled structure is observed which is in order with the diameters of MWCNTs. This can be explained by the interaction between the functional groups present on the S-MWCNT surface with the sulphonic acid groups of the polymer matrix thus ensuring homogeneous distribution.

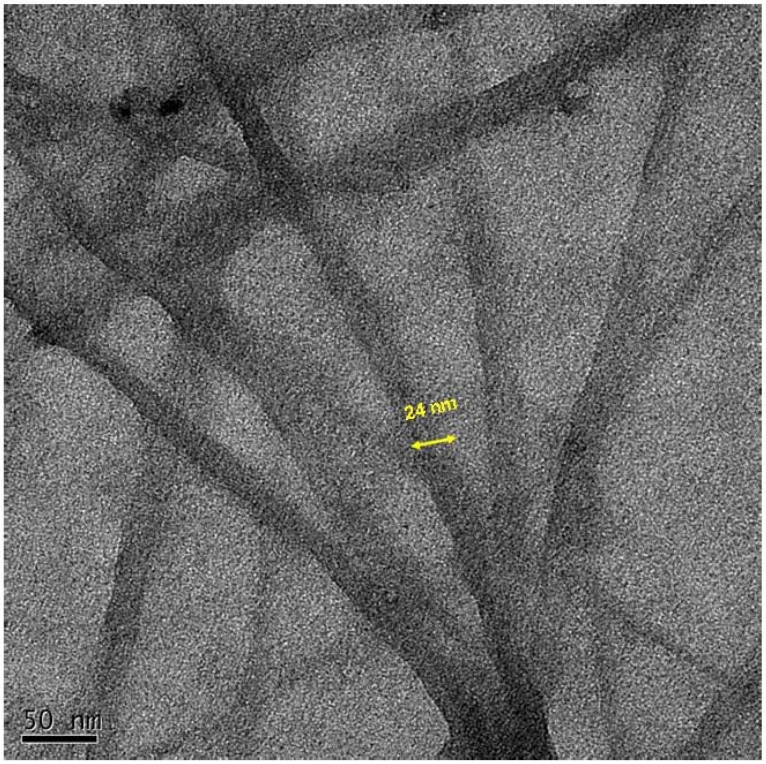


**Figure 5.2.** TEM image of NasM composite membrane clearly revealing the distribution of S-MWCNTs on the Nafion matrix.

### 5.3.2. FT - IR

The FT-IR spectra of Nafion 115, re-casted Nafion and NasM 0.05 % membranes are shown in Figure 5.3. We could not observe any significant FT-IR spectra for composites with more than 0.05 wt% of S-MWCNTs as the transparency of the composite membrane reduces drastically. All the three membranes show the

characteristic peaks of Nafion membranes and no significant change in the spectra is observed. This can be attributed to the homogeneous distribution of S-MWCNTs in the matrix and also due to the presence of similar functional groups between them such as sulphonic acid groups [26,27]. The peaks observed at 1051, 968, 1143 $cm^{-1}$ could be attributed to the symmetric stretching frequency ($\nu_s$) of SO, COC and $CF_2$ respectively.

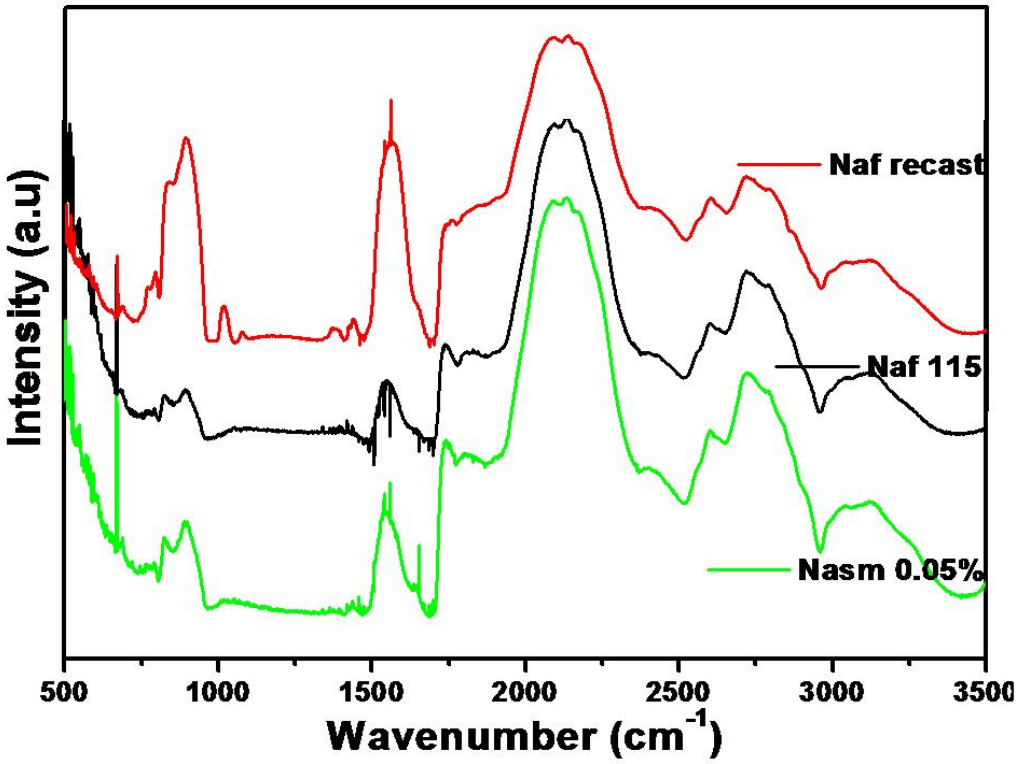


**Figure 5.3.** FT-IR spectra obtained for Nafion 115, Nafion recast and NasM composite membranes; clearly demonstrating the chemical similarity of the environment in all three membranes.

### 5.3.3. Thermo Gravimetric Analysis

A comparison of the thermograms for the composite membrane and Nafion 115 is given in Figure 5.4. Up to 300 °C, only a small fraction of weight loss (ca. 5%) is observed for both membranes, which could be attributed to the loss of water.

However, all the membranes disintegrate completely by 600 °C, which suggests that the incorporation S-MWCNTs does not increase the thermal stability of Nafion. Indeed, S-MWCNTs might act as a catalyst for the decomposition of the Nafion/S-SWCNT membrane because its disintegration takes places about 20 °C lower than that of Nafion 115. The smaller onset around 300 to 350 °C in the Nafion membrane corresponds to the degradation of sulphonic acid groups in the side chains [28,29]. In

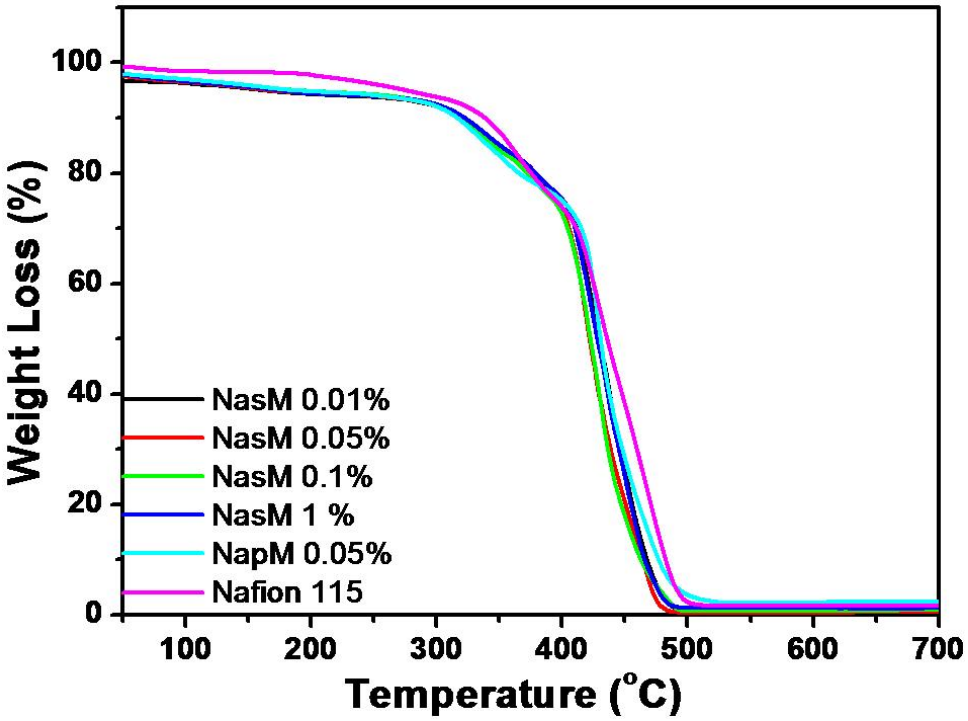


**Figure 5.4.** Thermograms obtained for different Nafion sulphonated MWCNT composite membranes under $O_2$ atmosphere at a heating rate of 10 °C per minute revealing almost similar thermal stability for all the membranes.

our composite membranes, two such onsets are observed in this region, which indicate perhaps the separate disintegration of sulphonic acid groups of the Nafion membrane and S- MWCNTs respectively. These onsets can be clearly seen in the derivative plots (Figure 5.5) which show a doublet corresponding to the two onsets at around 300 to 350 °C. Furthermore, the two-stage disintegration of the Nafion and its composite

membranes beyond 400 °C can be explained by the decomposition of polyether side chains and the PTFE backbone. However, the two-stage disintegration of Nafion 115 membrane is not observed in composite membranes since the disintegration of S-MWCNTs at the same temperature region might induce further disintegration thus restricting the observation of two stage decomposition.

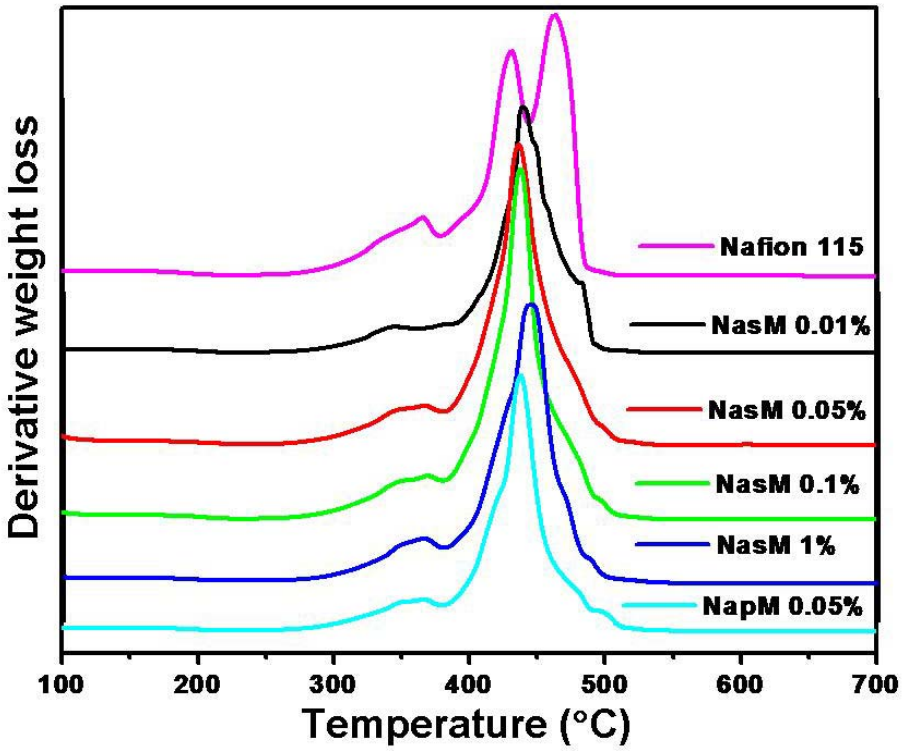


**Figure 5.5.** First derivative of the thermograms obtained for different Nafion composite membranes under $O_2$ atmosphere at a heating rate of 10 °C per minute.

### 5.3.4. Proton Conductivity

Figure 5.6 shows temperature dependent proton conductivity of Nafion 115 and NasM composite membranes under fully humidified conditions. The composite membranes exhibit higher proton conductivities than that of pristine Nafion membrane at all temperatures (0 to 120 °C). A closer observation of the figure reveals that the NasM 0.05 % membrane exhibits higher proton conductivity than that of composite

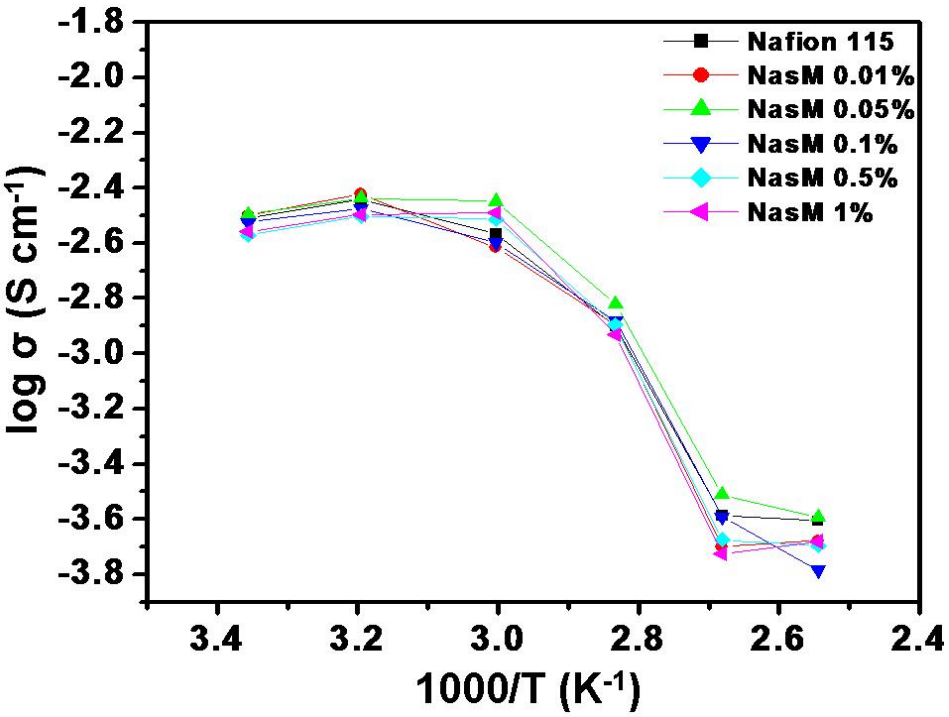


**Figure 5.6.** Temperature-dependant proton conductivity of Nafion and composite membranes with varying s-MWCNT content; the experiments have been carried out at fully humidified conditions in a two probe set up.

**Table 5.1.** Yield strength of the composite membranes along with that of Nafion 115 and recast Nafion membrane along with water content of all the membranes. The tensile strength experiments have been carried out by pulling the sample placed in between two holders at a speed of 100 μm $s^{-1}$.

| Membrane | Yield strength (Mpa) | Water content# |
|---|---|---|
| Nafion 115 | 2.68 | 29.1 |
| Recast Nafion | 2.4 | 42.4 |
| NasM 0.01% | 2.5 | 39.6 |
| NasM 0.05% | 2.62 | 33.5 |
| NasM 0.1% | 2.67 | 30.5 |
| NasM 1% | 4.3 | 27.3 |

# - water content is measured from the dry weight and wet weight of the membranes

membranes of all the other compositions at 60 °C, which is the optimum operating temperature of Nafion based PEMFCs. Moreover, the similarity in the slopes of the Arrhenius plots indicates that the activation energy (0.26 eV) and hence probably the mechanism of proton transport does not vary significantly because of the introduction of S-MWCNTs. This is especially interesting as it implies that the sulphonated MWCNTs are able to enhance the proton conductivity of Nafion without affecting its microphase-separated morphology. The enhancement in proton conductivity could be explained by the increased sulphonic acid content of the membrane due to the addition of S-MWCNTs, which could possibly increase the number of micro-channels available for proton transport by interconnecting some of the hydrophilic domains. On the other hand, the proton conductivity of the composite membranes decreases after a loading of S-MWCNTs higher than 0.05 %. Such a peak shaped variation of proton conductivity passing through a maximum value at an optimum concentration of the incorporated species in composites of amphiphilic proton conducting polymers like Nafion is often attributed to the micellar nature of the hydrophilic pools dispersed in the hydrophobic domains, which is disrupted at non-optimum concentrations of the fillers [30]. By a similar argument, the trend observed in proton conductivity could be attributed to the increased stiffness of the Nafion membranes, which results in reduced water uptake, thereby adversely affecting the proton conductivity (Table 5.1). However, this problem could be overcome simply by increasing the sulphonic acid content per nanotube to achieve higher and higher proton conductivity, instead of sacrificing membrane stiffness and water uptake, by increasing the nanotube loading. This observation is in contradiction to earlier reports wherein, increasing the sulphonic acid content increases water uptake finally leading to over-swelling and

mechanical breakdown of the membranes [1]. Surprisingly, this contradiction positively indicates that a combination of very high proton conductivity with good mechanical strength can be achieved by optimizing the balance between the amount of nanotube fillers in the membrane and the degree of sulphonation per nanotube.

### 5.3.5. SAXS Studies

Following our preliminary observation of the trends in proton conductivity and hints on possible manipulation of domain sizes while conserving the phase separation, the next objective is to verify the effect of nanotubes on the size of the hydrophilic clusters of Nafion. We have chosen Small angle X-ray scattering (SAXS) for this purpose, as it provides a unique means of understanding local ordering in semi-crystalline materials in a non-destructive manner and is being increasingly used to study the nanostructure of phase-separated polymers [5, 30, 31-32]. Accordingly,

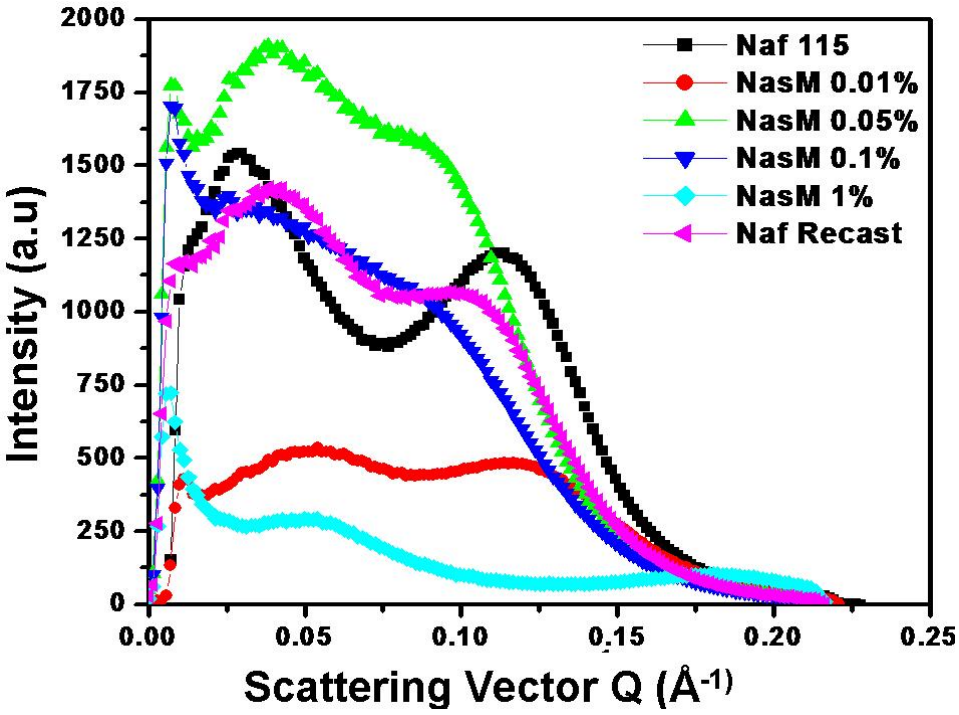


**Figure 5.7.** Small angle X-ray scattering patterns of the Nafion 115, Nafion recast and composite membranes after background and transmission correction; NasM represent S-MWCNT-Nafion composite membranes.

SAXS measurements on composite membranes along with that on commercial and recast Nafion membranes coupled with a model independent porod analysis provide the domain size of the membrane through the relation $D=2\pi/q$ where D is the domain size and q is the scattering vector [5]. The SAXS pattern of Nafion membrane is known to consist of two peaks, one in the low q region (0.025 to 0.035) and other in the high q region (0.11 to 0.25), respectively[21,32]. The latter ionomer peak is generally ascribed to the distribution of ionic clusters in the membrane while the low q peak is ascribed to the long-range crystalline domains of a lamellar structure in the matrix [4,5].

Figure 5.7 shows a comparison of the SAXS patterns of the commercial Nafion 115 and composite membranes along with that of recast Nafion membrane revealing a remarkable shift in the ionomer peak towards lower q values with increasing S-MWCNT content till NasM 0.05 %, becomes constant followed by a decrease at nanotube loading higher than 0.1 %. Since we have carried out our experiments on a semi quantitative manner with a model-independent porod analysis, we did not attempt the complex peak intensity calculations, instead compared the results based on peak positions. Interestingly, the hydrophilic domain size remarkably increases with increasing S-MWCNT content ranging from a value of 65 Å for the lowest CNT loading (0.01 %) and reaches a maximum at 0.05 % loading of S-MWCNT to 72 Å and decreases further to 35 Å at a nanotube loading of 1 %. More significantly, a comparison of variation in domain sizes with the variation in proton conductivity reveals a striking evidence for the effect of domain size manipulation on

the proton conductivity of the composite membranes (Figure 5.8). We believe that the sulphonic

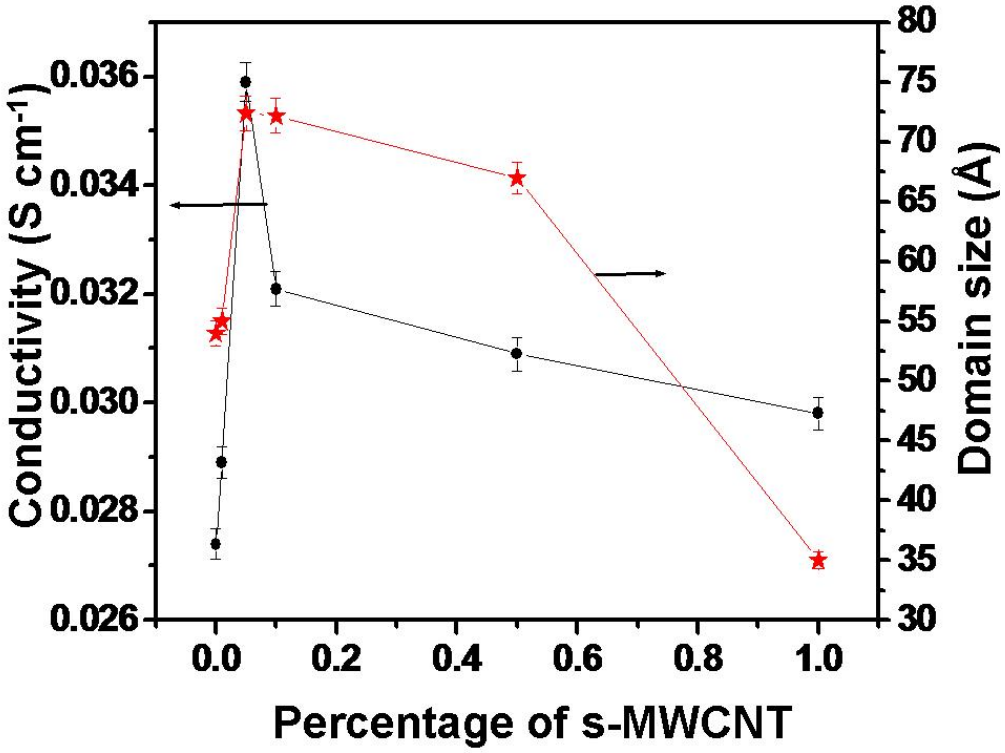


**Figure 5.8.** Correlation of proton conductivity and domain size from small angle X-ray scattering on the percentage of s-MWCNT content in the NasM composite membranes.

acid groups on Nafion interact electrostatically with the sulphonated groups on CNT surface mediated by water molecules and this provides channels for easy proton transport through hydrophilic domains. Consequently the cylindrical domains might undergo a distortion in shape as reflected in the low q peak in the SAXS data. The impact of change in hydrophilic cluster size on proton conductivity has long been anticipated by theoretical models of Nafion [21]. This observation could be compared with a recent report by Wang *et al* dealing with tuning the hydrophilic domain size of high molecular weight polysulphones from 10 to 25 nm by increasing the degree of sulphonation [33]. However, because of the higher domain sizes, the polysulphone

membranes could be highly permeable to methanol and hydrogen at least in some cases. On the other hand, with in our knowledge, not many experimental attempts to tune the domain sizes while maintaining the membrane integrity have been successfully demonstrated so far. All the composite membranes and re-cast Nafion membranes show reduced long-range crystallinity which is understandable as our preparative conditions are not comparable with that of the commercially extruded Nafion membranes. Nafion 115 shows a crystalline domain size of 220 Å while the composite membranes and recast Nafion show only approximately 160 Å. However, this could also be due to the increased ionic cluster domain size and topology as the increased water content may have a negative impact on the crystallinity of the polymer matrix.

### 5.3.6. SECM Studies

The above investigation indicates the combined effect of hydrophilic cluster size and water content on the proton conductivity of the composite membranes. At this stage, it is also important to verify whether there is any synergistic interaction between the sulphonic acid functional groups present in the Nafion membrane and those on the nanotube surface. This is achieved by analyzing the composite membranes using Scanning Electrochemical Microscopy (SECM). This technique involves the recording of the current of an ultra-microelectrode (UME) tip, rastered over a substrate by virtue of a faradaic process between the two. Exploiting the ability of CNTs to catalyze the oxidation of $[Ru(NH_3)_6]^{2+}$, the composite membrane has been analyzed using the SECM in its feedback mode [34]. The feedback imaging principle in this study involves the reduction of $[Ru(NH_3)_6]^{3+}$ dissolved in the electrolyte at the

UME tip to produce $[Ru(NH_3)_6]^{2+}$ which will be re-oxidized to $[Ru(NH_3)_6]^{3+}$, when the tip is held in close proximity to the substrate. Only representative results of NasM 1 % composite membrane and Nafion 115 membrane are presented here for simplicity. Also for comparison, a small amount of S-MWCNT after filtration through PTFE membrane (PTFEsM) has been dried, pressed and used as a substrate to compare the results obtained with the composite membrane.

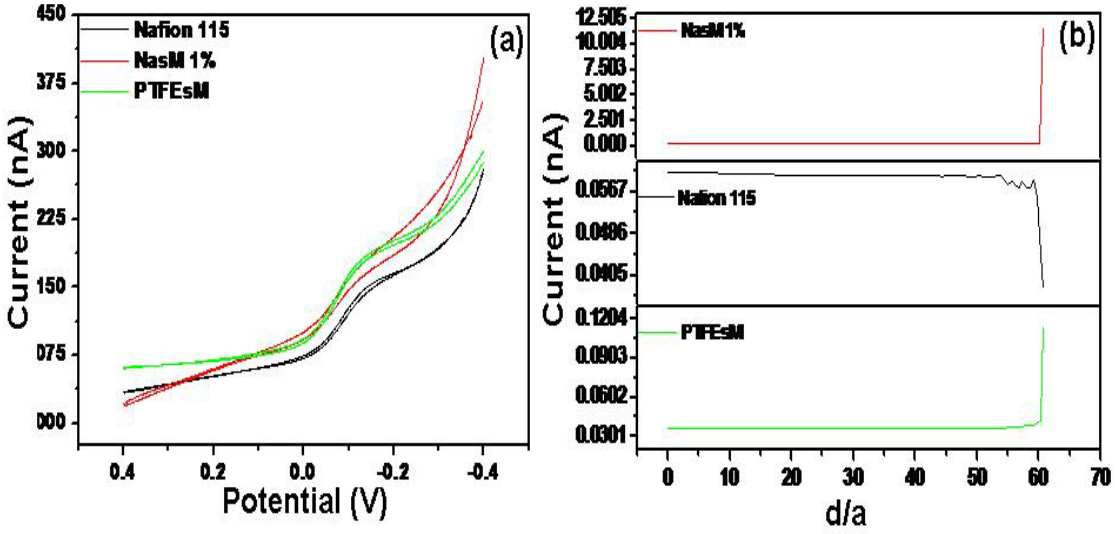


**Figure 5.9.** (a) Cyclic voltammograms in 0.1 mM $[Ru(NH_3)_6]^{3+}$ in 1 mM $KNO_3$ using 1µm Pt tip as the working electrode, Pt wire as the counter electrode and Ag/AgCl as the reference electrode in a Teflon cell at a scan rate of 50 mV $s^{-1}$. (b) Probe approach curves are obtained by keeping the tip potential at –0.15 V and moving the tip at 50 µm $s^{-1}$.

Accordingly, Figure 5.9.a shows the cyclic voltammograms of 0.1 mM $[Ru(NH_3)_6]^{3+}$ in 1 mM $KNO_3$ using a 1 µm Pt tip as the working electrode, Pt wire as the counter electrode and Ag/AgCl, satd. KCl, as the reference electrode in a Teflon cell specially made for SECM measurements. The membranes, which served as substrates, have been fixed in a cell holder with its surface perpendicular to the UME tip and kept immersed in the electrolyte solution. Cyclic voltammograms have been taken at an infinite distance from the substrate to avoid any contributions from the

substrate. A sigmoid curve, characteristic of steady state response at UMEs is observed with the redox reaction taking place at –0.15 V, where the current is almost the same in all the three cases as any contribution from the substrate membrane is negligible. Then the tip-substrate separation is determined by recording the tip current held at –0.15 V as a function of distance from the substrate until a change in bulk current ($I_{T,\infty}$) is observed either positively or negatively. These probe approach curves (Figure 5.9.b) indicate a positive feedback both for the composite membranes and PTFEsM, while for Nafion 115 membrane, a negative feedback is observed. Interestingly, the higher current observed in the case of NasM 1 % membrane compared to that for a bare CNT surface (PTFEsM membrane) probably implies synergistic effects offered by the sulphonate groups present in the Nafion membrane. More specifically, the Nafion matrix probably improves the accessibility of the cationic redox species to the sulphonate functionalized nanotube surface. By a similar argument, the S-MWCNTs are also expected to augment the proton conductivity of the Nafion membrane. Although the specific nature of interaction between the sulphonate groups in the Nafion matrix and those on the nanotubes is not clearly understood, there could be hydrogen bonding between the two which can obviously expand the water channels.

Figure 5.10 shows a comparison of the SECM images at a tip-substrate separation of 1 μm obtained with the composite NasM 1 % (a) and Nafion 115 membranes (b), by rastering an area of 500 x 500 $\mu m^2$ over the substrate surface by keeping the tip potential at –0.15 V while (c) shows similar image of S-MWCNT filtered through a PTFE membrane. There are distinct domains with increased current densities in the composite membrane due to the presence of S-MWCNTs and from

this it is clear that S-MWCNTs are spanned over the polymer membrane almost homogeneously. However, Nafion membranes do not show such variations in current density as there is no site to catalyze the redox reaction (Figure 5.10.b) to reveal a near-uniform current distribution all over the substrate. Further, the current values in the composite NasM 1 % membranes are much higher than the corresponding currents observed with the Nafion membranes and PTFEsM (Figure 5.10.c) respectively. This is not surprising as the local concentration of the redox mediator near S-MWCNTs is more in the case of NasM 1 % membrane compared to that of PTFE filtered membrane. The current variation in Figure 5.10.c clearly reveals the catalytic activity of S-MWCNTs towards the oxidation of $[Ru(NH_3)_6]^{2+}$. However, the current magnitude is not as high as in the case of composite membranes, where the penetration of redox species in the polymer matrix results in enhanced local concentration, in turn increasing the current to a much higher value. Thus these results are in excellent agreement with the earlier results where MWCNTs improve the proton conductivity along with reducing the activation loss by improving the interface.

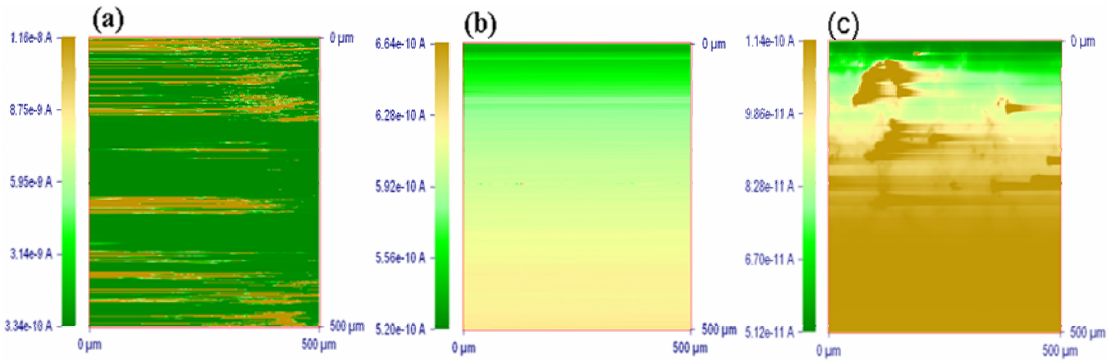


**Figure 5.10.** (a) SECM image obtained with NasM 1 % composite membrane over 500 x 500 $\mu m^2$ area of the membrane; 1 µm Pt tip has been held at -0.15 V and rastered over the substrate at a speed of 0.3 µm $s^{-1}$ at a tip-substrate separation of 0.5 µm. (b) SECM image of commercial Nafion 115 membrane under identical conditions and (c) image obtained with PTFEsM substrate.

### 5.3.7. Mechanical Strength

In an amphiphilic proton exchange membrane like Nafion, the dimensions and shape of the hydrophilic clusters are determined by the equilibrium between the internal osmotic pressure of the clusters and the counteracting elasticity of the organic

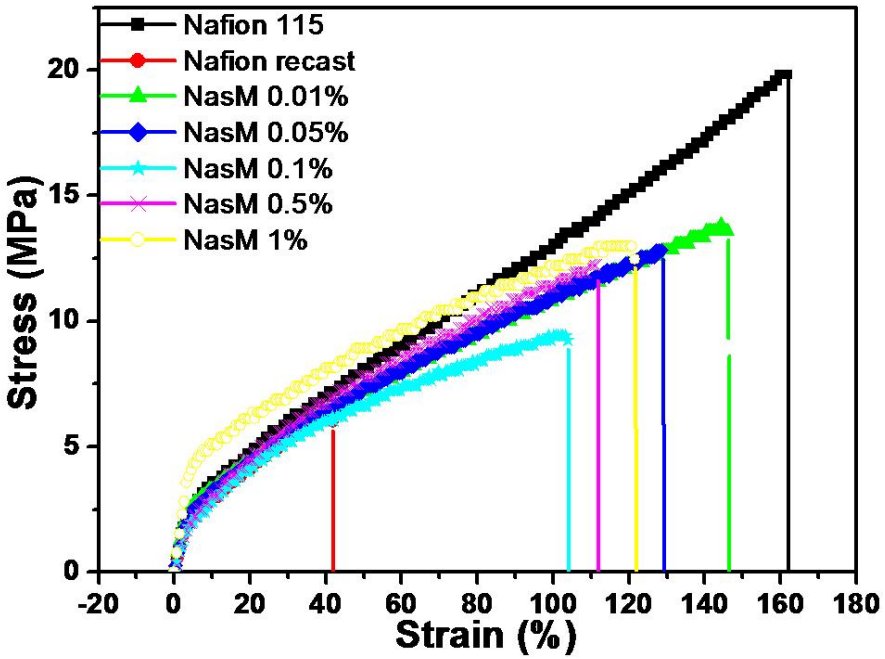


**Figure 5.11.** A comparison of the stress-strain plots obtained with the different composite membranes, Nafion 115 and Nafion recast membranes; the plot reveals the increased yield strength obtained with NasM 1 % composite than that of Nafion 115.

Matrix [35,36]. In this context, it is appropriate to investigate and compare the mechanical properties of the composite membranes with increasing S-MWCNT content, and accordingly, the results of tensile strength measurements on our composite membranes are shown in Table 5.1 and Figure 5.11, which reveal an increase in yield strength with increasing S-MWCNT content compared to that of the recast Nafion membranes. However, the addition of 1 % S-MWCNT results in a significant enhancement of the yield strength, even more than that of commercial Nafion 115. The stress-at-rupture is improved considerably with the addition of S-

MWCNTs in comparison with that of the recast Nafion membrane (Figure 5.11). However, rupture takes place at comparatively lower stress values than that of Nafion 115, where the membranes are industrially extruded and are supposed to have higher mechanical stability in comparison with the solution cast membranes [37,38]. The increased mechanical stability compared to that of recast Nafion membranes could be ascribed to the presence of S-MWCNTs, which would reinforce interfacially well with the polymer matrix to form mechanically more robust membranes. This is in accordance with available reports, where, the incorporation of CNTs and functionalized CNTs in to the Nafion matrix has resulted in increased mechanical stability [39-41].

### 5.3.8. Polarization Studies

Having analyzed the effect of introducing S-MWCNTs on the proton conductivity, hydrophilic domain size and mechanical properties of Nafion membranes, the next objective is to verify whether the change in these fundamental properties affects the performance when these composite membranes are used as the electrolyte in a fuel cell environment. Accordingly, Figure 5.12 shows the single cell polarization plots obtained with MEAs from commercial Nafion, Nafion recast and composite membranes at 70 °C by passing humidified $H_2$ and $O_2$ at a flow rate 0.2 slpm along with that of 0.05 % Nafion composite with unfunctionalized pristine MWCNT (NapM 0.05 %) for comparison. Other than NasM 1 %, where the S-MWCNT content is high, all other composite membranes show enhanced fuel cell current and power densities than that of Nafion 115 and Nafion recast membranes. Nafion 115 is selected as the benchmark since its thickness is of the order of our composite membranes (≈ 120 to 130 μm).

Further, it also confirms that NasM 0.05 % has the optimum S-MWCNT content as it gives the maximum power density of 380 mW $cm^{-2}$ against the 250 mW $cm^{-2}$ and 230 mW $cm^{-2}$ for commercial Nafion 115 and Nafion recast membrane respectively. These results are in accordance with that of proton conductivity and cluster size data obtained in earlier experiments. For example, the 0.05 % NasM composite membrane shows the maximum proton conductivity coupled with peak cluster size. This further justifies the increased power density in fuel cell experiments

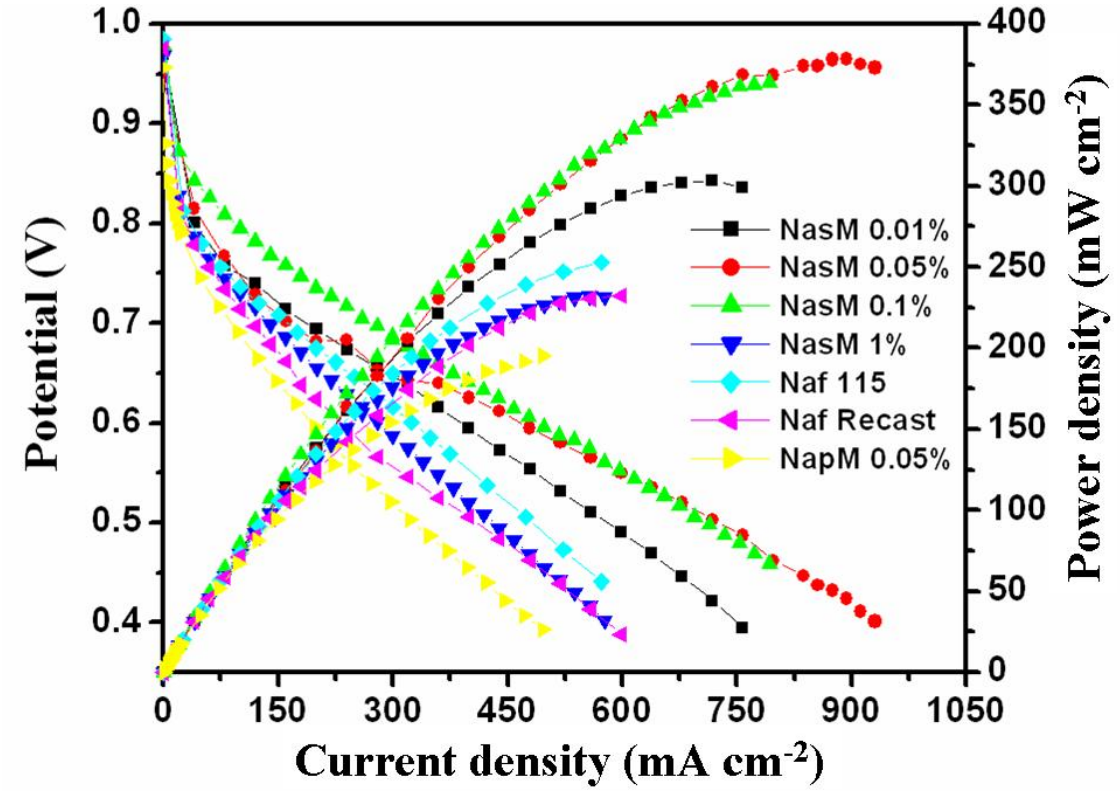


**Figure 5.12.** Fuel cell single cell polarization plots of MEAs with nafion and composite membranes at 70 °C. $H_2$ and $O_2$ were passed at a rate of 0.2 slpm after humidification at 80 °C. The cells were conditioned at 0.2 V for 30 minutes before taking the polarization measurements.

and the reason can be identified easily due to composite with optimum S-MWCNT concentration. In comparison, NasM 0.1 % composite membrane shows similar cluster size comparable to that of NasM 0.05 %, while its proton conductivity is

significantly less than that of NasM 0.05 %. Interestingly, it gives an almost similar fuel cell performance (power density 350 mW $cm^{-2}$ against 380 mW $cm^{-2}$) to that of NasM 0.05 %. This could be explained by the water content presented in Table 5.1. The addition of S-MWCNTs more than the optimum content seems to increase the stiffness of the membrane which subsequently reduces the water uptake. Even though the cluster size is almost similar for both 0.1 % and 0.05 % cases, the reduction in water content disrupts the channels, which eventually reduces the proton conductivity. However, in actual fuel cell conditions, water is being produced during the operation as well as fed to the membrane via humidified gases ($H_2$ and $O_2$). This *in situ* water generation keeps the membrane rich in water content and helps in achieving improved power density as it already has higher ionic clusters. However, as expected, the pristine MWCNT composite NapM 0.05 % give only 200 mW $cm^{-2}$ as it has only very few functional groups to facilitate the proton conduction. Further the unfunctionalized MWCNTs could act as a barrier for proton conduction as it could block some channels**.** These results signify the importance of sulphonic acid functionalized MWCNT for composite polymer electrolyte using CNT as a reinforcement, although the open circuit potential for all the membranes are almost the same. Further, the lifetime of the membranes, which is equally a prominent factor in commercializing the fuel cells, is also expected to be more for these composite membranes since their mechanical integrity is expected to be more.

### 5.3.9. MEA Impedance Measurements

Figure 5.13 shows the results of impedance (Nyquist) measurement for Nafion 115 membrane at different potentials carried out by purging humidified $H_2$ and $O_2$ at room temperature in between 100 kHz to 0.1 Hz. It is well known that at low overpotentials

(≤ 200 mV), the semicircle observed predominantly belongs to the charge transfer resistance for the cathode oxygen reduction reaction while at higher over potentials (≥ 200 mV) the impedance spectrum is complicated by processes related to the mass transport of oxygen and product water. A detailed study of the impact of operating potential, humidification temperature, flow rate on the charge transfer (CT) resistance is made by Ciureanu et al. We report the change in $R_{CT}$ with the incorporation of S-MWCNTs at an overpotential of 150 mV since the OCV is 0.98 V for almost all the membranes [42].

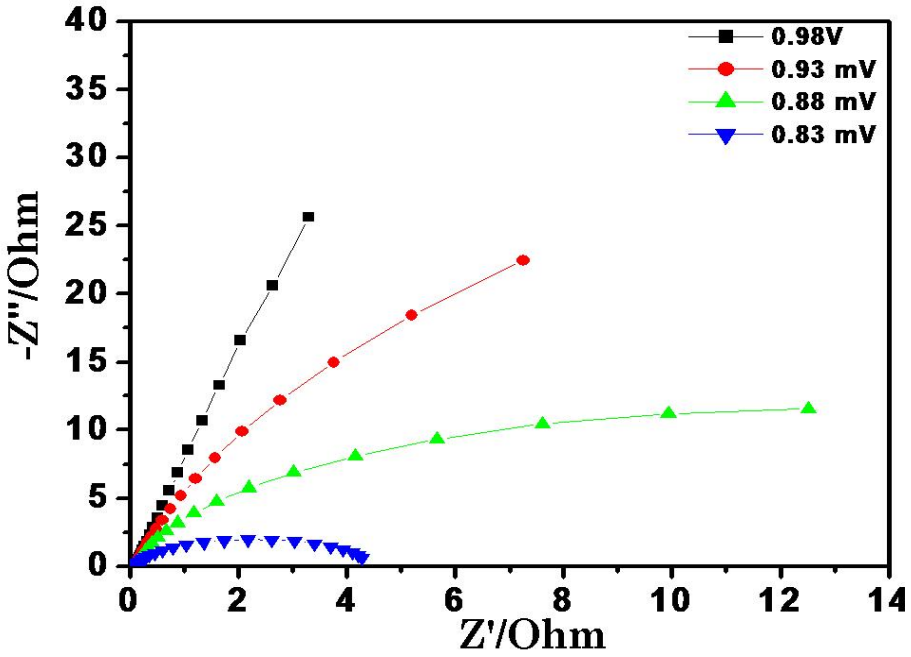


**Figure 5.13.** Potential-dependent impedance (Nyquist) plot of Nafion 115 membrane at room temperature by passing humidified $H_2$ and $O_2$ obtained at different overpotential values; 0.98 V was the open circuit potential of the cell.

Figure 5.14 shows the Nyquist plots measured for the composite MEAs at an overpotential of 150 mV. The figure clearly reveals that the CT resistance decreases with the increase in the S-MWCNT content and reaches a minimum and then again starts increasing. However, the minimum occurs at NasM 0.1 %, with NasM 0.05 %

showing a slightly higher value. In addition, in agreement with the earlier discussed measurements, the ionic conductivity of the membranes is found to increase with increasing CNT content until a loading of 0.1 % after which, it starts to decrease with the further addition of CNTs. This fact explains the mutual importance of increased cluster size and water content of composite membranes on fuel cell performance. The increased ionic cluster size without enough water results in reduced ionic conductivity

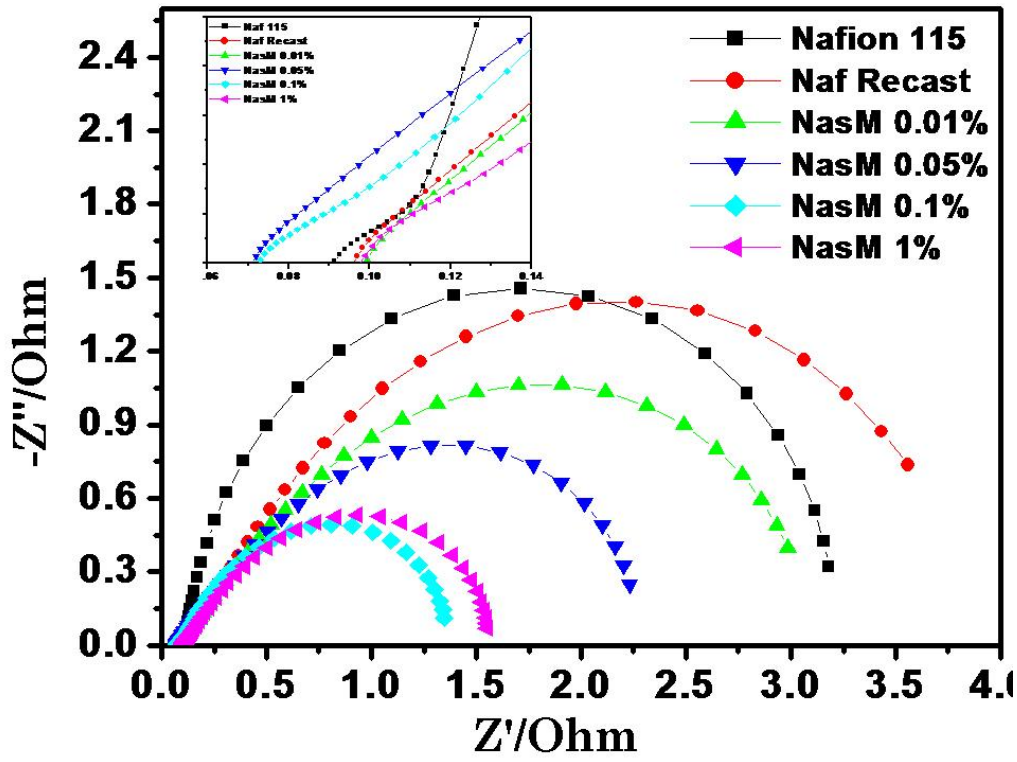


**Figure 5.14.** Nyquist plot for the composite membranes measured at an overpotential of 150 mV. (Inset: magnified view of high frequency range to show the change in the ohmic resistance)

while the supply of sufficient water either by means of humidification or *in situ* generation as product gives much enhanced fuel cell performance and ionic conductivity values as reflected in these MEA impedance measurements. Moreover, the decrease in conductivity at very high CNT loading indicates the absence of

significant electronic conductivity effects in which case the conductivity of the composite membranes would have been increasing continuously with increasing CNT content at least till the expected percolation threshold.

### 5.3.10. Solid-State Cyclic Voltammetry

To prove further that the improved performance is due to membrane alone, Figure 5.15 shows solid-state cyclic voltammograms of the MEAs while passing humidified hydrogen and nitrogen at room temperature. Typical hydrogen adsorption/desorption

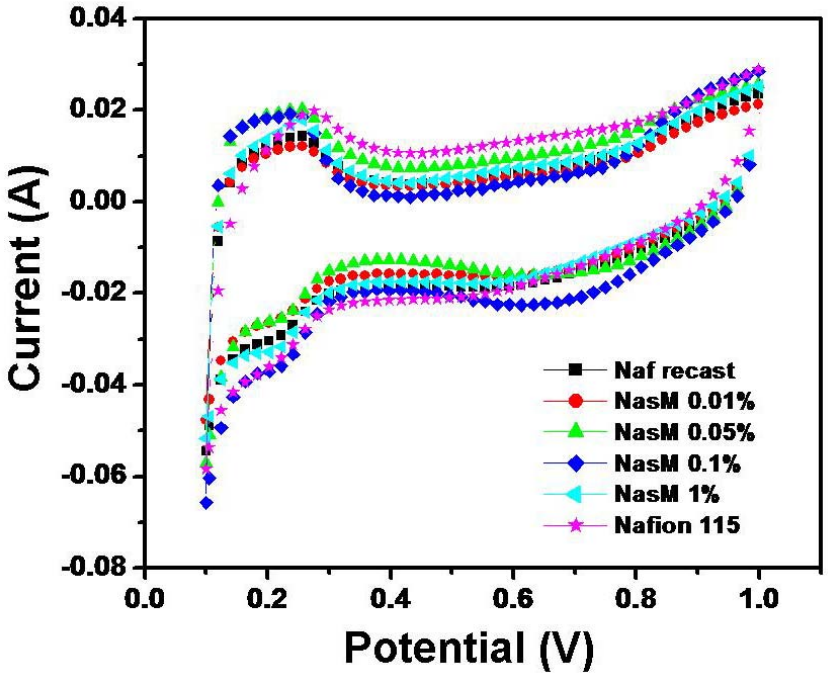


**Figure 5.15.** Solid-state cyclic voltammograms measured at room temperature for the MEAs with Nafion and composite membrane electrolytes; these experiments have been carried out after fuel cell single cell study by passing $H_2$ and $N_2$ on the anode and cathode side respectively.

peaks are observed in the 0.1 to 0.3 V region, the areas of which are a measure of active electrochemical surface area (ECSA) of Pt availability in the MEA. It can be seen from the SSCVs that almost all the MEAs show nearly equal values of ECSA for the Pt. This further clears the fact that the performance enhancement we observed is

solely due to the composite membrane and is not related to variations in Pt loading in the catalyst layer.

However, before the benefits of this finding can be used for commercialization, several challenges such as the durability and chemical stability of these composite membranes in actual fuel cell operating conditions need to be evaluated rigorously. Nevertheless, this investigation creates enormous interest in the Nafion/S-MWCNT composite membranes to be considered as an alternative to avoid some of the limitations of Nafion membranes during the fabrication of PEMFCs. In addition, this would also allow operation with better efficiency that would also help to have a simplified balance of plant in PEM stack fabrication.

## 5.4. Conclusions

Controlled manipulation of the ionic domain size of Nafion by incorporating sulphonated multiwalled carbon nanotubes and its remarkable influence on a number of fundamental properties of the membrane as well as the overall fuel cell performance has been systematically demonstrated in this chapter. Key evidence for the increase in the ionic cluster size is obtained from SAXS measurements of the composite membranes. Associated increase in proton conductivity is understood from the resultant decrease in charge transfer resistance for oxygen reduction from electrochemical impedance analysis. Temperature-dependent proton conductivity measurements clearly reveal that the CNTs do not disrupt the phase-separated morphology or the proton conduction mechanism of the PEM, which is also supported by the results of the SECM investigations. Most surprisingly, studies on mechanical stability reveal for the first time that this is a good strategy to increase the sulphonic

acid content of the membrane without adversely affecting its swelling and mechanical strength. Above all of these improvements in the fundamental properties, the increased ionic cluster size provides a remarkable enhancement in fuel cell performance with a peak power density of 380 mW $cm^{-2}$ for the NasM 0.05 % membrane, while Nafion 115 and Nafion recast membranes reveal only 250 and 230 mW $cm^{-2}$ respectively. Thus these results would be of much impact as it would help to bring down the *per se* cost and size per kW considerably.

## 5.5. References

**[1]** Steele, B. C. H.; Heinzel. A. *Nature* **2001,** 414, 345.

**[2]** Jacobson, Z.; Colella, W. G.; Golden, D. M. *Science* **2005,** 308, 1901.

**[3]** Haile, S. M.; Boysen, D. A.; Chisholm, C. R. I.; Merle, R. B. *Nature* **2001,** 410, 910

**[4]** Mauritz, K. A.; Moore, R. B. *Chem. Rev* **2004,** 104, 4535.

**[5]** Haubold, H. G.; Vad, T.; Jungbluth, H.; Hiller. P. *Electrochim. Acta* **2001,** 46, 1559.

**[6]** Li, Q.; He, R.; Jensen, J. O.; Bjerrum, N. J. *Chem. Mater* **2003,** 15 4896.

**[7]** Einsla, M. L.; Kim, Y. S.; Hawley, M.; Lee, H. S.; Mcgrath, J. E.; Liu, B.; Guiver, M. D.; Pivovar, B. S. *Chem. Mater.* **2008,** *20,* 5636.

**[8]** Wang, F.; Hickner, M.; Kim, Y. S.; Zawodzinski, T. A.; Mcgrath, J. E. *J. Membr. Sci.* **2002,** 197, 231.

**[9]** Kreuer, K. D. *J. Membr. Sci.* **2001,** 185, 29.

**[10]** Choi, P.; Jalani, N. H.; Datta, R.; *J. Electrochem. Soc,* **2005,** 152, E123.

**[11]** Kreuer, K. D.; Schuster, M.; Obliers, B.; Diat, O.; Traub, U.; Fuchs, A.; Klock, U.; Paddison, S. J.; Maier, J. *J. Power Sources* **2008,** 178, 499.

**[12]** Moilanen, D. E.; Spry, D. B.; Fayer, M. D. *Langmuir* **2008,** 24, 3690.

**[13]** Jeon, J. D.; Kwak S. Y. *J. Power Sources* **2008,** 185, 49.

**[14]** Zhai, Y.; Zhang, H.; Hu, J.; Yi, B. *J. Membr. Sci.* **2006,** 280, 148.

**[15]** Rhee, C. H.; Kim, H. K.; Chang, H.; Lee, J. S. *Chem. Mater*. **2005,** 17 1691.

**[16]** Nam, S. E.; Kim, S. O.; Kang, Y.; Lee, J. W.; Lee, K. H. *J. Membr. Sci.* **2008,** 322, 466.

**[17]** Bae, B.; Ha, H. Y.; Kim, D. *J. Membr. Sci* **2006,** 276 51.

**[18]** Rena, S.; Suna, G.; Li, C.; Songa, S.; Xin Q.; Yang, X. *J. Power Sources* **2006,** 157 724.

**[19]** Lafitte, B.; Jannasch, P. *Adv. Funct. Mater.* **2007,** *17*, 2823.

**[20]** Elabd, Y. A.; Napadensky, E. *Polymer* **2004,** 45, 3037.

**[21]** Watanabe, M.; Uchida, H.; Emori, M. *J. Phys. Chem. B* **1998,** 102 3129.

**[22]** Tang, H. L.; Pan, M. *J. Phys. Chem. C* **2008,** 112 11556.

**[23]** Sahu, A. K.; Selvarani, G.; Pitchumani, S.; Sridhar, P.; Shukla, A. K. *J. Electrochem. Soc.* **2007,** 154, B123.

**[24]** Silva, R. F.; Passerini, S.; Pozio, A. *Electrochim. Acta* **2005,** 50 2639.

**[25]** Zhang, W.; Li, M. K. S.; Yue, P.L.; Gao, P. *Langmuir* **2008,** 24 2663.

**[26]** Liang, Z.; Chen, W.; Liu, J.; Wang, S.; Zhou, Z.; Li, W.; Sun, G.; Xin, Q. *J. Membr. Sci.* **2004,** 233, 39.

**[27]** Lavorgna, M.; Mascia, L.; Mensitieri, G.; Gilbert, M.; Scherillo, G.; Palomba, B. *J. Membr. Sci.,* **2007,** 294, 159.

**[28]** deAlmeida, S. H.; Kawano, Y. *J. Therm. Anal. Calorim.* 1999, 58, 569.

**[29]** Deng, Q.; Wilkie, C. A.; Moore, R. B.; Mauritz, K. A. *Polymer* 1998, 39, 5961.

**[30]** Rohr, K. S.; Chen, Q. *Nature Materials* **2008,** 7, 75

**[31]** Hsu, W. Y.; Gierke, T. D. *J. Membr Sci.* **2008,** 13, 307.

**[32]** Tsao, C. S.; Chang, H. L.; Jeng, U. S.; Lin, J. M.; Lin T. L. *Polymer* **2005,** 46, 8430.

**[33]** Wang, F.; Hickner, M.; Kim, Y. S.; Zawodzinski, T. A.; Mcgrath, J. E. *J. Membr. Sci.* **2002,** 197, 231.

**[34]** Wilson, N. R.; Guille, M.; Dumitrescu, I.; Fernandez, V. R.; Rudd, N. C.; Williams, C. G.; Unwin, P. R.; Macpherson, J. V. *Anal. Chem.* **2006,** 78 7006.

**[35]** Bath, B. D.; Lee, R. D.; White, H. S. *Anal. Chem*. **1998,** 70, 1047.

**[36]** Hashimoto, T.; Fujimura, M.; Kawai, H. In Perfluorinated Ionomer Membranes; American Chemical Society: Washington, DC, **1982;** pp 217-248.

**[37]** DuPontTM Nafion® perfluorinated polymer products, NAE302 (September 1998), http://www.dupont.com.

**[38]** Silva, R. F.; Francesco, A. P. *Electrochim. Acta* **2004,** 49, 3211

**[39]** Liu, Y. L.; Su, Y. H.; Chang, C. M.; Suryani, Wang, D. M.; Lai, J. Y. *J. Mater. Chem.,* **2010,** 20, 4409.

**[40]** Liu, Y. H.; Yi, B.; Shao, Z. G.; Wang, L.; Xing, D.; Zhang, H. *J. Power Sources* **2007,** 163, 807.

**[41]** Thomassin, J. M.; Kollar, J.; Caldarela, G.; Germain, A.; Jérôme, R.; Detrembleur, C. *J. Membr. Sci.* **2007,** 303, 252.

**[42]** Ciureanu, M.; Roberge, R. *J. Phys. Chem. B* **2001,** 105, 3531.

# Chapter 6

## Functionalized MWCNT - Polymer Composite Membranes as Solid Polymer Electrolyte in "All Solid-State" Supercapacitors

In this chapter, the ability of specifically functionalized carbon nanotubes to enhance proton transport in Nafion and polybenzimidazole membranes leading to improvement in the specific capacitance of an all solid-state supercapacitor is demonstrated. Cyclic Voltammetry experiments reveal a 25% improvement (185 and 150 F per gram of $RuO_2$ for composite and Nafion membranes respectively) in capacitance by a meager 0.05 wt% addition of sulfonated MWCNTs in Nafion membranes. On the other hand, an addition of 1 % phosphonated MWCNTs results in ~ 60 % improvement in PBI based composites (from 160 to 260 F $g^{-1}$). Further, composite membranes based on functionalized MWCNTs show increased cycle life, which is attributed to the presence of electrostatically linked network structures due to functional moieties on the side walls of carbon nanotubes that increase the integrity of the membrane. The equivalent series resistance for the PBI and PBI phosphonated MWCNT (PBpNT) membranes are 470 and 89 mΩ, respectively. Charge discharge measurements reveal a capacitance value of 500 $Fg^{-1}$ for PBpNT membrane based supercapacitors even after 1000 cycles of operation. The use of such nanocomposite membranes is expected to dramatically improve the life time as well as performance of supercapacitors which in turn, would facilitate different applications such as hybrid electric vehicles.

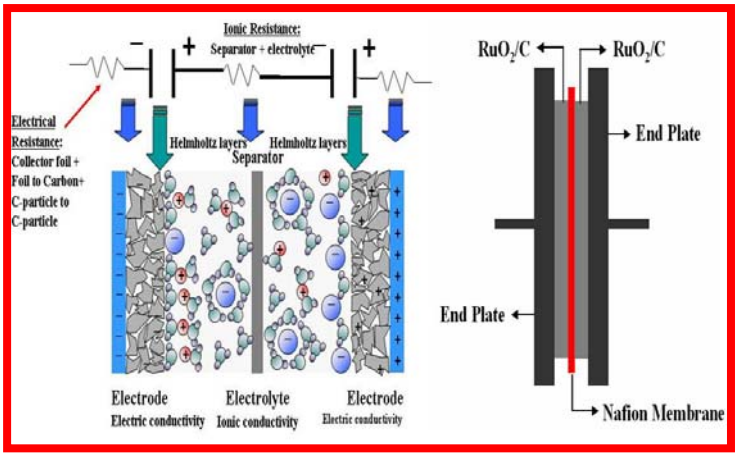


* A part of the work discussed in this chapter has been communicated to *Journal of Nano Energy and Power Research.*

## 6.1. Introduction

Fuel cells and batteries are electrochemical power sources which are very good for storing/retrieving energy by means of electrochemical faradaic reactions. However, both of them fail miserably when repeated bursts of power are desired as they have very poor power density despite having a large energy density. Supercapacitors on the other hand, are also electrochemical power sources which can become especially useful for these situations and coupling of a supercapacitor with a fuel cell or battery can give many characteristics of a desirable power source. Supercapactiors have become increasingly important due to their high power density and better cycle life and is used in many critical applications involving pulsed and bridged power requirements like hybrid electric vehicles, medical devices and computer memory back-up [1-3]. The possibility of opportunity charging, where supercapacitors can recharge themselves during the process, such as a downhill driving or during breaking (regenerative breaking), makes them ideally suited for electric and hybrid electric vehicle applications [4].

Supercapacitors are mainly classified in to two catagories: electrical double layer capacitors and pseudocapacitors. The performance of both types depend strongly on the nature of electrode-electrolyte interface [5]. Most of the present supercapacitors use liquid electrolytes like aqueous sulphuric acid, potassium hydroxide, disodium sulphate or certain organic liquids with dissolved salts like tetrabutylammonium tetrafluoroborate, $LiClO_4$ and more recently ionic liquids such as ethyl-methylimmidazolium-bis(trifluoromethane-sulfonyl)imide [6-11]. However, the use of a majority of these electrolytes results in serious limitations like the leakage of liquid electrolyte during storage/operation, flammability, toxicity and poor oxidative

stability in addition to having a low potential window of operation (except perhaps for ionic liquids). The use of solid polymer electrolytes with high ionic conductivity can alleviate many of these shortcomings in addition to providing valuable benefits like thin film forming ability, hermetic sealing and flexibility [12-15].

In order to exploit the advantages of a solid polymer electrolyte over conventional liquid electrolytes, intense research has been carried out in recent years using a variety of approaches including hybrid nanocomposite electrolytes [6-11, 16-19]. For example, Sampath *et al.,* demonstrated a supercapacitor with hydrogel electrolytes as the separator while Nafion based membranes and sulfonated poly (ether ether ketone) membranes coupled with high surface area carbon, have been utilized as an electrolyte to show a specific capacitance value of 90 -120 F $g^{-1}$ in an electrical double layer type capacitor (EDLC). The utility of phosphoric acid doped polybenzimidazole as a polymer electrolyte membrane in redox supercapacitors with excellent specific capacitance (290 F $g^{-1}$), especially suitable for high temperature operations (> 100 °C) has been demonstrated recently [20]. In all these work, one of the key aspect is the enhanced ionic conductivity of the polymeric membrane which is an essential prerequisite for faster charge transport that indeed helps in achieving improved performance and durability, with Nafion based membranes as the bench mark for proton conductivity. Despite this, the efforts are directed mainly to improve the electrode characteristics by modifying the electrodes and the prospect of altering the membrane conductivity remains largely unexplored.

In chapters 4 and 5 we have demonstrated a methodology to increase the proton conductivity of Nafion and phosphoric acid doped PBI membranes by incorporating sulfonated and phosphonated MWCNTs respectively, where the

functional groups on the sidewalls of MWCNTs help in achieving better proton transport. We have demonstrated their application in fuel cells where, they show improved performance in terms of energy and power density. Similarly, due to the improved proton conductivity coupled with the presence of MWCNTs, these composite electrolyte membranes are expected to show enhanced capacitance in addition to better mechanical integrity and durability. Accordingly, in this chapter we analyze the improved specific capacitance in an "all solid-state supercapacitor" by employing composite membranes based on both Nafion/sulfonated MWCNT (NasM) and PBI/phosphonated MWCNT (PBpNT) composite membranes respectively as polymer electrolytes over conventional Nafion and PBI membranes using 30 % $RuO_2$/C as the standard electrode material. We chose $RuO_2$ as the electrode material due to its unique characteristics, such as metallic conductivity, high chemical and thermal stability and electrochemical redox properties, which makes this as a standard electrode material due to its facile $Ru^{3+/}Ru^{2+}$ redox charge [21-23].

## 6.2. Experimental Aspects

### 6.2.1. Preparation of Electrode and Electrolyte

PBpNT and NasM composite membranes were prepared as explained in chapter 4 and 5 respectively while $RuO_2$/C (30 wt%) composite was prepared by physical mixing of $RuO_2$ and Vulcan XC-72 followed by homogenizing for 2 min in isopropyl alcohol (on 30 seconds on-off basis). Carbon support layers (CSL) were prepared by brushing a slurry of carbon, PTFE and cyclohexane on carbon paper until a loading of 1.5 mg $cm^{-2}$ was achieved. These CSLs were cold pressed at 0.5 ton $cm^{-2}$ compaction load for 1 min and dried at 350 °C. The electrode was prepared by brushing a slurry of 30 %

$RuO_2$/C, Nafion and isopropyl alcohol that was obtained through homogenization for 2 min, on the above prepared CSLs. $RuO_2$ loading on the CSL was 0.1 mg $cm^{-2}$ and these electrodes were uni-axially pressed with the electrolyte membranes at 130 °C for 3 minutes to prepare the membrane electrode assembly (MEA).

### 6.2.2. Electrochemical Evaluation

Electrochemical experiments were carried out on an Autolab PGSTAT 30 instrument. Cyclic voltammetric experiments were conducted at different scan rates in the potential window of 0 – 1 V for PBI and 0 – 1.2 V for Nafion based MEAs respectively. Impedance measurements were carried out to unravel the changes that occur at the electrode-electrolyte interface in the case of pristine and composite membrane based MEAs. Charge-discharge experiments were carried out in the potential window of 0.1 – 1.1 V at a charge-discharge rate of 2.5 mA $cm^{-2}$ in a Solartran 1250 instrument. Electrochemical experiments for Nafion based system were carried out at room temperature while for PBI based systems these were measured at room temperature and at 140 °C, respectively.

## 6.3. Results and Discussion

### 6.3.1. Cyclic Voltammetry Using Nafion based MEAs

Figure 6.1 shows a comparison of cyclic voltammograms of supercapacitor MEA modules with commercial Nafion 115 at different scan rates. The plot clearly reveals capacitive behaviour of the MEAs and a maximum capacitance of 150 F $g^{-1}$ is obtained nearly at all the scan rates although a small variation is observed at lower scan rates. The capacitance arises due to the following electrochemical process inside the electrode-electrolyte interface [24,25].

$$RuO_2 + H^+ + e^- \leftrightarrow RuO(OH) \quad \text{-----} \quad (1)$$

Thus an electrolyte with higher proton concentration or conductivity is expected to help storing higher charge inside the electrode than that of an electrolyte with poor proton conductivity. Hence, composite electrolytes are expected to show an increased capacitance than that of pristine membranes.

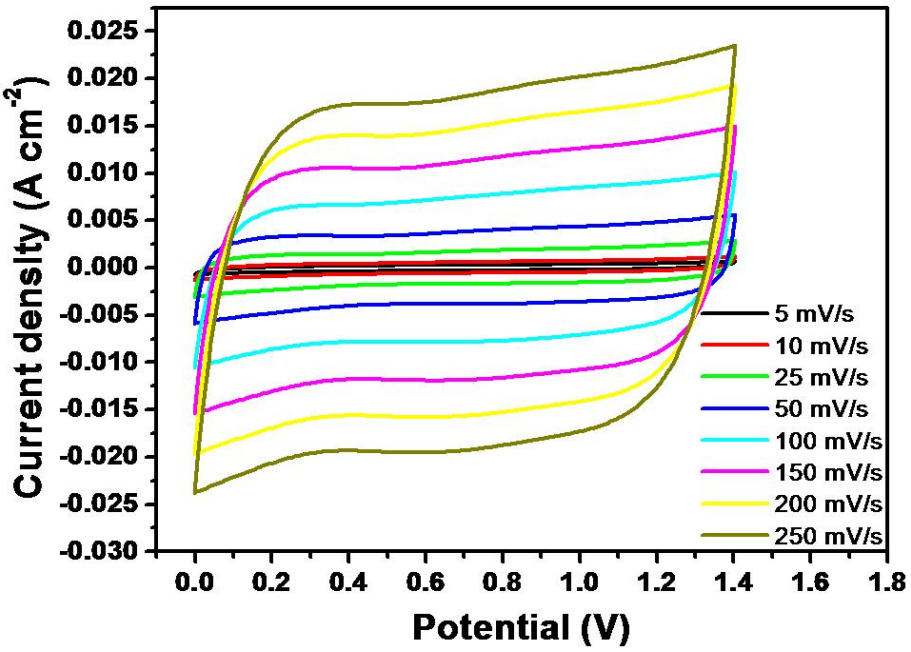


**Figure 6.1.** Cyclic voltammograms of MEAs using Nafion 115 membrane electrolyte at different scan rates and $RuO_2$/C as the standard electrode formulation obtained at room temperature (25 °C); the plot clearly reveals a capacitive behaviour.

Accordingly, a comparison of cyclic voltamograms obtained with Nafion 115 and NasM composite membranes respectively at a scan rate of 100 mV $s^{-1}$ is shown in Figure 6.2. The capacitive behavior of both the membranes with $RuO_2$/C is clearly revealed by the near rectangular shape of both curves and accordingly a capacitance of 185 F $g^{-1}$ could be estimated for the composite membrane while that for the MEA with commercial Nafion 115 membrane is only 150 F $g^{-1}$. Thus the MEA with the composite membrane shows an almost 25 % enhancement in capacitance by the mere

addition of 0.05 wt% sulfonated MWCNTs that might be attributed to the enhanced proton conductivity. We have analyzed only NasM 0.05 wt% composite membrane

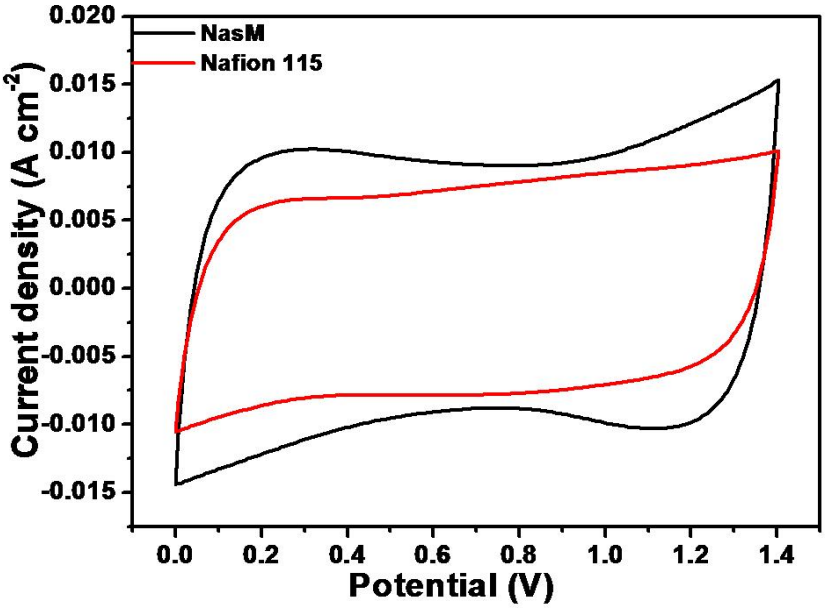


**Figure 6.2.** Comparison of cyclic voltammograms for MEAs based on Nafion 115 and NasM 0.05 % composite membrane electrolytes with 30 % $RuO_2$/C electrode at a scan rate of 100 mV $s^{-1}$ and at 25 °C; the plot clearly reveals the higher capacitance of NasM composite membrane over that of commercial Nafion 115 membranes.

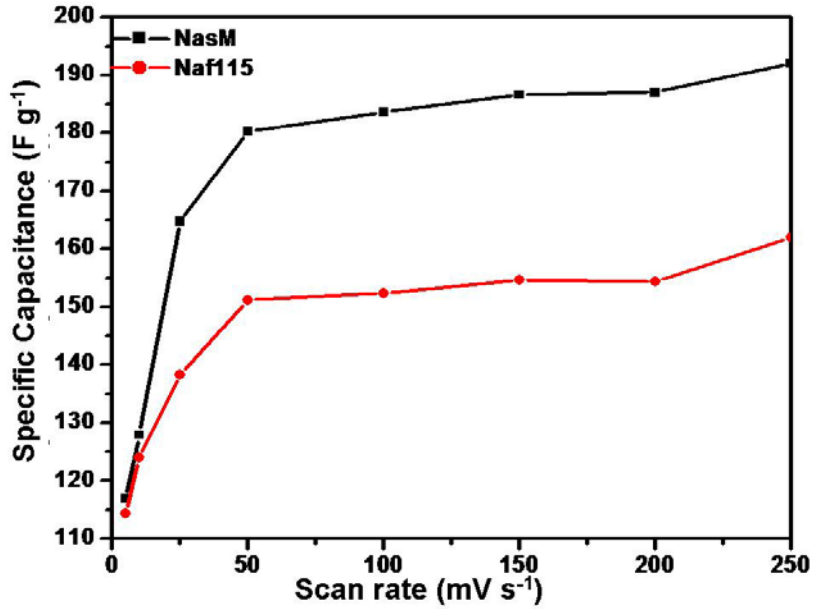


**Figure 6.3.** Comparison of specific capacitance obtained with Nafion and NasM composite membrane based MEAs at various scan rates revealing the increased capacitance for MEAs with composite membranes; 30 % $RuO_2$/C has been used as the electrode.

for supercapacitor electrolyte applications as this composite gives the maximum proton conductivity. Further, a plot of specific capacitance against the scan rate for the MEAs based on both the membranes reveal almost a straight line suggesting a scan rate independent capacitance as expected for electronic capacitors although a small variation is observed at very low scan rates (Figure 6.3). This clearly indicates that both the membranes are capable of faster charging and discharging at much higher rate without any significant drop in the capacitance. This is especially important since supercapacitors are expected to fulfill the energy requirements as a secondary power supply where it is required to deliver the energy at much higher power densities than that of batteries and fuel cells.

### 6.3.2. Charge-Discharge Measurements

After successfully demonstrating the improved specific capacitance for NasM based composite membranes in cyclic voltammetry measurements, Figure 6.4 reveals the charge-discharge curves obtained with MEAs based on Nafion 115 and NasM composite membranes with a charging current of 2.5 mA $cm^{-2}$. NasM composite membrane gives a specific capacitance of 220 F $g^{-1}$ while Nafion 115 membrane gives only 200 F $g^{-1}$. The capacitance measurements for 1000 cycles (inset: Figure 6.4a) show that after an initial drop in the capacitance, both the membranes display an almost stable capacitance. For example, after 1000 cycles of charge-discharge, the composite and Nafion 115 membranes show a specific capacitance of 195 and 175 F $g^{-1}$ respectively suggesting a capacitance drop of 11 and 12.5 %. More significantly, NasM membranes show more stable cycle life characteristics while comparing with Nafion 115 membranes. This could be attributed to the presence of MWCNTs which

helps in keeping the integrity of the membrane by reducing the problems associated with swelling and drying. Further, the time constants calculated from charge discharge plots for NasM and Nafion 115 are 5.7 and 7.0, respectively which again reinforces that NasM membrane based supercapacitors can charge and discharge at faster rates than that of Nafion 115.

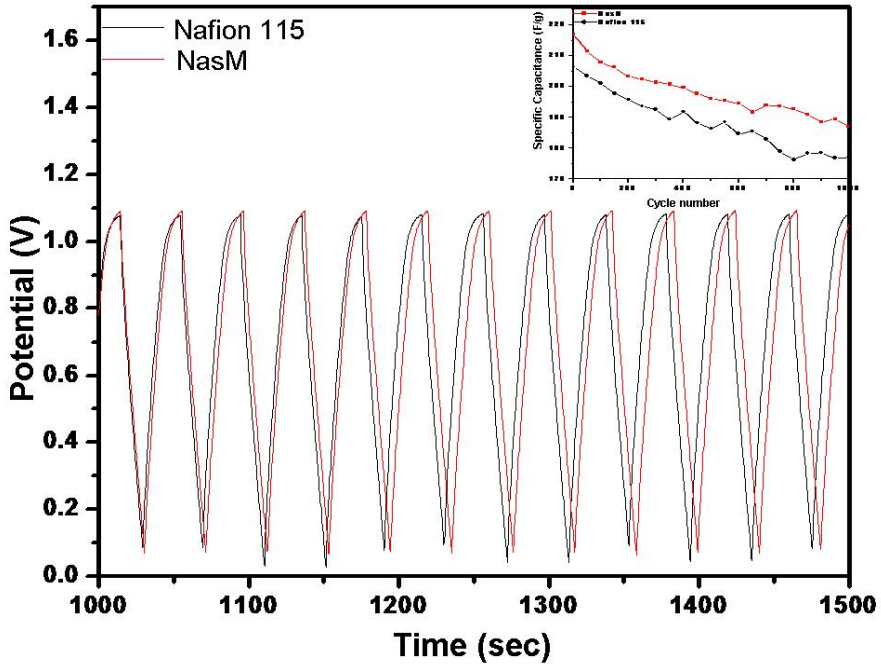


**Figure 6.4.** Charge-discharge plots with Nafion 115 and NasM composite membranes coupled with $RuO_2$/C electrode with a charging rate of 2.5 mA $cm^{-2}$; the plot clearly reveals the improved capacitance obtained with composite membranes at 25 °C; inset: variation of specific capacitance with cycle numer for both the MEAs.

### 6.3.3. Impedance Measurements on Nafion based MEAs

Impedance plots for the composite and Nafion 115 membrane based MEAs respectively in the frequency range of 0.01 Hz to 1 MHz with an amplitude of 10 mV rms are shown in Figure 6.5. The impedance plots are analyzed using a standard Randles equivalent circuit (inset: Figure 6.5a). In the case of MEAs based on Nafion and its composite membranes, NasM shows lesser equivalent series resistance (ESR of 2.05 Ω than that of commercial Nafion 115 membrane 2.25 Ω), corresponding to a

ohmic resistance drop of ~180 mΩ, as expected due to the higher proton conductivity of the composite membrane. Further, the charge transfer resistance estimated from the complex nonlinear square fitting (CNLS) at very high frequencies, (inset: Figure 6.5b) indicates the ease of ionic charge separation inside the MEA and the charge transfer resistance for the redox reaction of $RuO_2$ as mentioned in equation 1, is considerably less than that of Nafion 115 membrane based MEA (~200 mΩ drop in charge transfer resistance). At intermediate frequencies, both the MEAs show frequency independent straight lines, which are expected behavior of a capacitor. Thus, the improved capacitance in the case of composite membrane is attributed to the increased proton conductivity and better electrode-electrolyte interface provided by the MWCNTs present in the composite membrane.

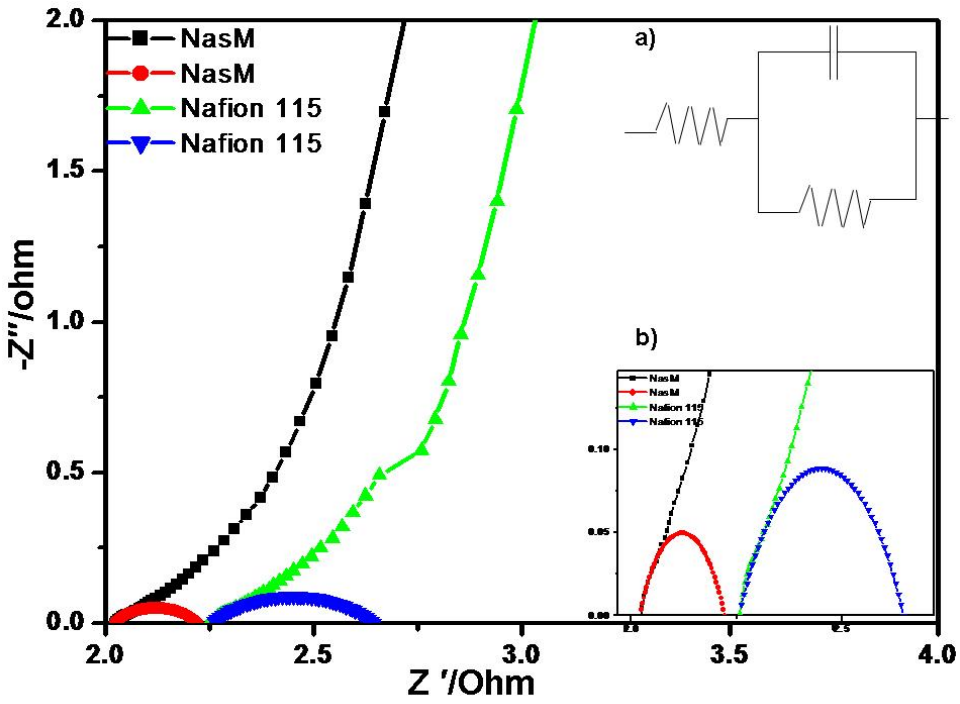


**Figure 6.5.** Impedance (Nyquist) plots of Nafion 115 and NasM composite membranes with $RuO_2$/C electrode in the frequency range of 1 M Hz to 0.1 Hz; inset: (a) Randles equivalent circuit used for the analysis of the impedance data, (b) magnified view of the high frequency part revealing the reduced membrane resistance and improved charge transfer in the composite membrane based MEA.

### 6.3.4. Solid State Cyclic Voltammetry

After demonstrating the higher capacitance and better durability of composite membranes over their pristine counterpart, we carried out solid-state cyclic volttametry in Nafion based system (Nafion and NasM composite membrane) with $RuO_2$ as the working electrode, Pt wire as the counter electrode and Ag wire as the quasi reference electrode to unravel the reason behind the improvements in the capacitance of the composite systems [26]. Accordingly, cyclic voltammograms obtained are shown in Figure 6.6. The composite membrane shows much higher capacitance than that of Nafion 115 membrane and this could be attributed to the presence of S-MWCNTs and increased conductivity, which is inferred from the impedance measurements of the composite membranes. Further, in the case of NasM

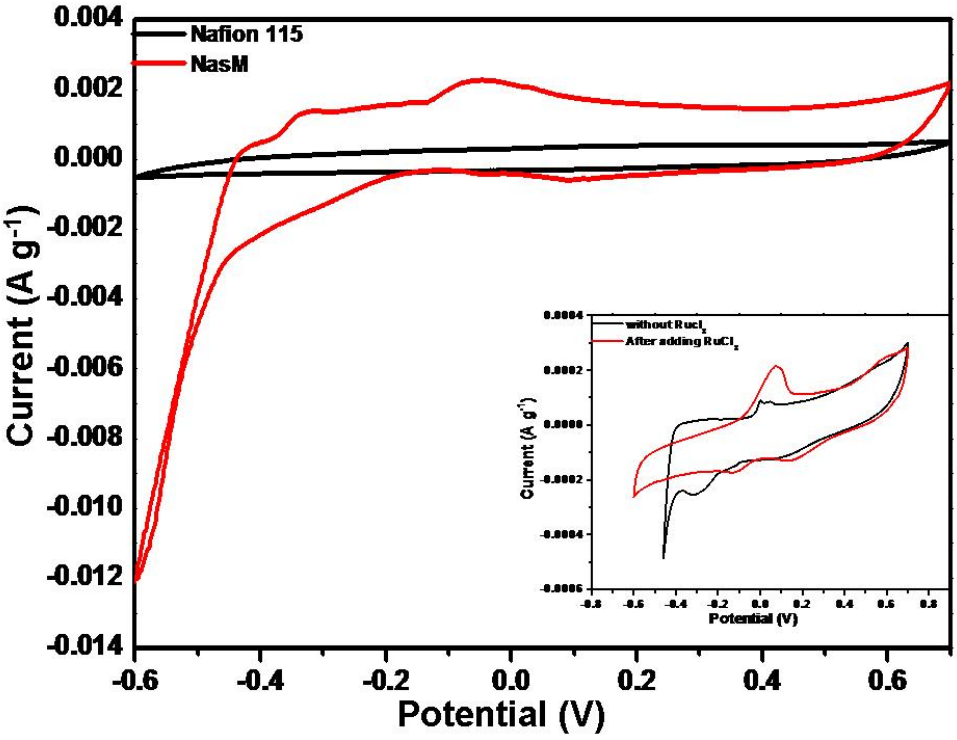


**Figure 6.6.** Solid state cyclic voltammograms of Nafion 115 and Nasm 0.05 % membranes using $RuO_2$ as the working electrode, Ag as the quasi reference electrode and Pt wire as the counter electrode at a scan rate of 20 mV $s^{-1}$. Inset: change in cyclic voltammogram before and after putting $RuCl_3$ on the membrane.

composite membranes, a peak due to Ru redox process is observed while with Nafion 115, only a rectangular cyclic voltammogram with no characteristic redox peak is observed**.** The origin of this peak in the composite membrane is further confirmed separately by adding a little amount of $RuCl_3$ in to the NasM matrix which results in an increase in the peak current that could be attributed to the redox peak of $Ru^{3+/2+}$(Inset Figure 6.6). This is an indication of the autocatalytic behaviour of MWCNTs to catalyze the $Ru^{3+/2+}$ system coupled with the increased conductivity of composite membranes.[27]

### 6.3.5. Cyclic Voltammetry on PBI based MEAs

Cyclic voltammograms obtained with PBpNT composite and PBI membranes respectively after coupling with $RuO_2$/C are shown in Figure 6.7. As expected, the composite membrane shows much higher specific capacitance than their pristine couterpart with an almost 60 % increment in specific capacitance by the incorporation of 1 wt% P-MWCNT. Pristine PBI membrane based MEA shows a specific capacitance value of 150 F $g^{-1}$ while that based on PBpNT membrane shows about 260 F $g^{-1}$ at 140 °C. The capacitance values observed at room temperature (30 °C) also follows a similar trend with a maximum specific capacitance of 190 F $g^{-1}$ for $RuO_2$ in PBpNT based MEAs. Further, the capacitance does not vary significantly with the scan rate ranging from 50 mV to 250 mV per second as depicted in the inset of Figure 6.7, similar to the observation with Nafion membrane based MEAs. This again demonstrates the ability of solid polymer electrolyte towards faster charging and discharging at much higher rate without any significant drop in the capacitance.

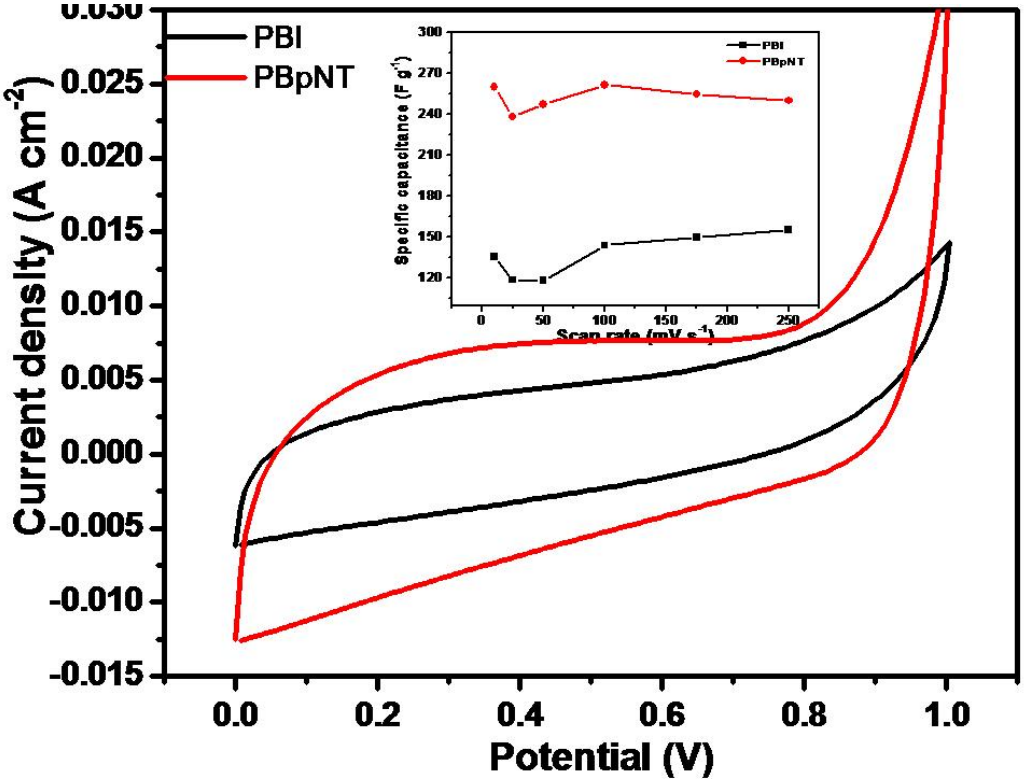


**Figure 6.7.** A comparison of cyclic voltammograms with PBI and PBpNT composite membrane based MEAs at 140 °C using $RuO_2$/C based standard electrode formulations; the plot clearly reveals the higher capacitance observed with PBpNT composite membranes. Inset: variation of specific capacitance with scan rate ranging from 5 mV to 250 mV $s^{-1}$ revealing the ability of both membranes towards faster charging.

### 6.3.6. Charge – Discharge Measurements on PBI based MEAs

Figures 6.8 (a) and (b) show the charge-discharge behaviours obtained with PBI and PBpNT composite membrane based MEAs, respectively at room temperature along with variation of specific capacitance with cycle life. A specific capacitance of 40 and 60 F $g^{-1}$ is observed for PBI and PBpNT membrane based MEAs respectively after 300 cycles while their capacitance value prior to cycling is 80 and 120 F $g^{-1}$. Phosphoric acid doped PBI membranes are known to have lesser proton conductivity at temperatures less than 80 °C and the observed low specific capacitance values are in line with this fact. However, charge discharge measurements at 140 °C reveal

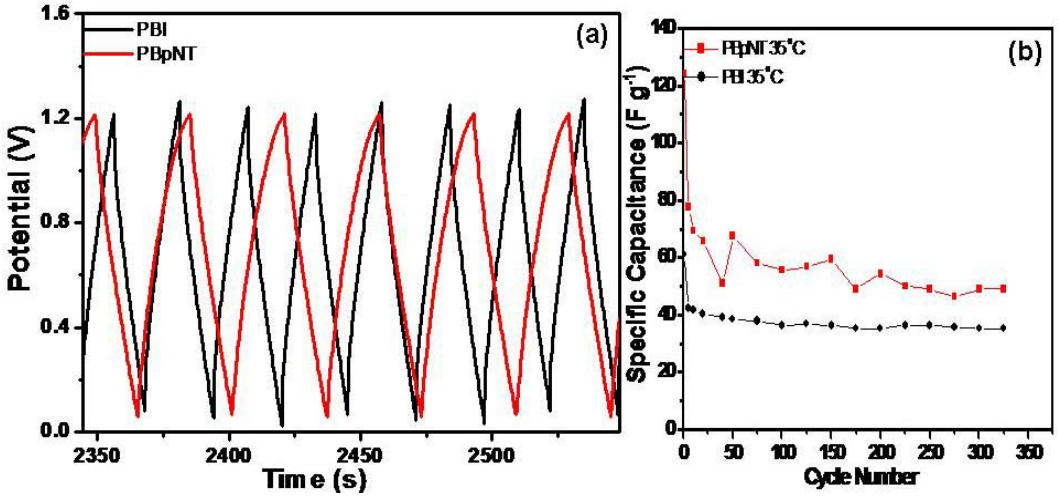


**Figure 6.8.** (a) Charge-discharge curves obtained with PBI and PBpNT composite membrane based MEAs with $RuO_2$/C electrode at room temperature with a charging current of 2.5 mA $cm^{-2}$, (b) Variation of specific capacitance with cycle number for PBI and PBpNT membrane based MEAs; the plots reveal the higher specific capacitance for PBpNT based MEAs.

much higher specific capacitance even after 1000 cycles of operation (Figure 6.9). For example, we observed specific capacitance values of 500 and 650 F $g^{-1}$ for PBI and PBpNT membranes, respectively. This capacitance value drops initially after which a stable performance is observed for both the membranes. The final capacitance values observed with PBpNT membrane is 500 F $g^{-1}$ while PBI membrane gives only 225 F $g^{-1}$ at 140 °C using standard $RuO_2$ electrodes. The trend is in accordance with the cyclic voltammetry data eventhough the capacitance values in the charge discharge experiments are much higher. On the other hand, room tempeature specific capacitance observed with PBpNT and pristine PBI are 60 and 33 F $g^{-1}$ respectively which are much lower than that of room temperature capacitance values observed through cyclic voltammograms. This trend is in accordance with the reported proton conductivity behaviour of PBI based membranes where, below 80 °C PBI membranes show very poor proton conductivity.

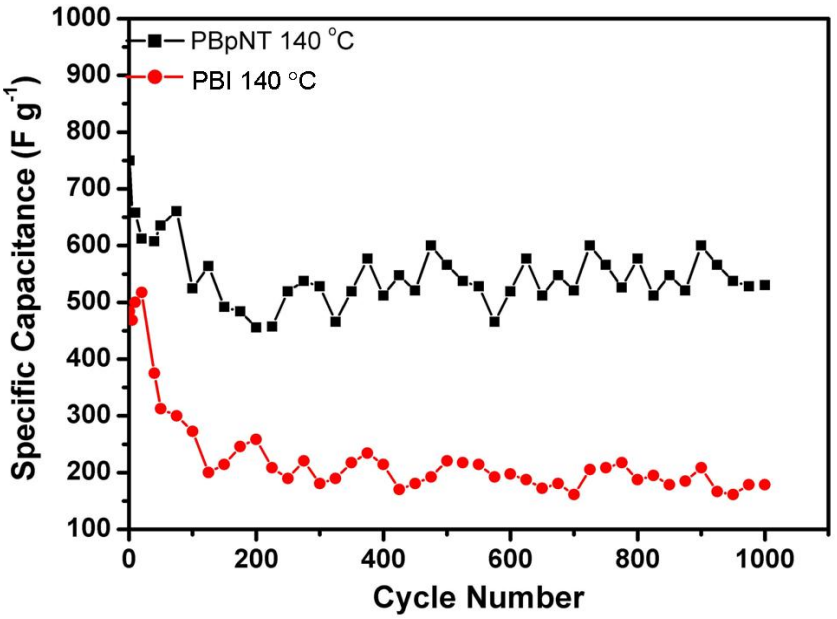


**Figure 6.9.** A comparison of variation in specific capacitance with cycle number for PBI and PBpNT composite membranes with $RuO_2$/C electrode at 140 °C with a charge discharge current of 2.5 mA $cm^{-2}$.

This fact further emphasizes the need for improving the proton conductivity of polymer electrolytes to achieve higher specific capacitance. The reason for such a high value of specific capacitance is not clearly known although the improved proton conductivity and a possible role of P-MWCNTs that are present in the composite membranes along with improved interface between the electrode and electrolyte could be attributed as plausible reasons.

### 6.3.7. Impedance Measurements on PBI based MEAs

Figure 6.10 shows impedance (Nyquist) plots obtained for PBI and PBpNT membrane based MEAs at 140 °C. A similar trend to that observed for Nafion based MEAs is observed in the impedance behaviour of the PBpNT composite membranes also (an ESR of 80 and 470 mΩ for composite and pristine membranes respectively)

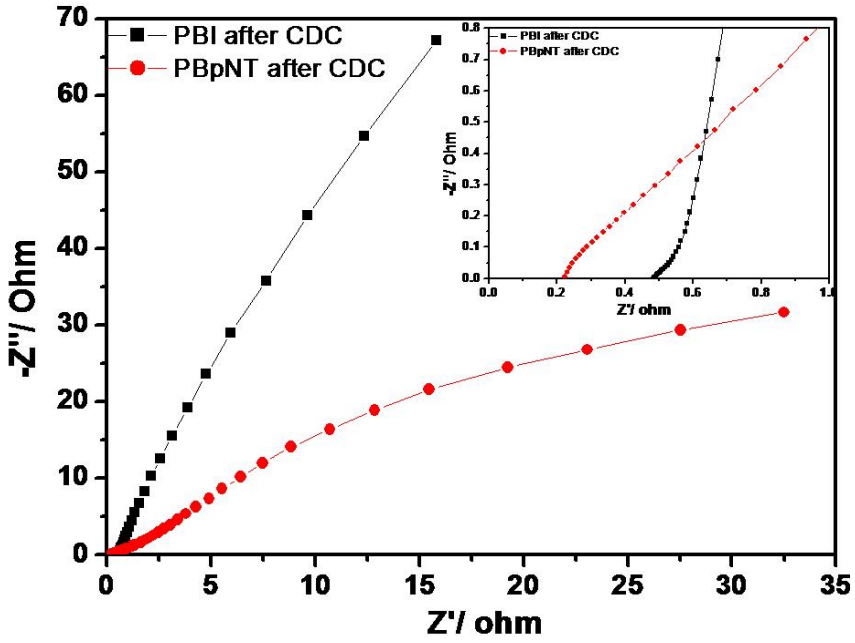


**Figure 6.10.** Impedance Nyqusit plots after 1000 cycles of charge discharge with PBI and PBpNT composite membrane based MEAs in the frequency range of 1 MHz to 0.1 Hz with an amplitude of 10 mV.

suggesting the importance of P-MWCNTs in improving the proton conductivity and in turn the specific capacitance. Further, this reiterates the significant role of proton conducitivity on the specific capacitance of any electrode. The improved specific capacitance with the PBI based MEAs at higher temperature can be attributed to the increased proton conductivity of the reinforced membrane as also room temperature impedance measurements show higher resistance for both PBI and PBpNT composite membranes.

The above results underline the utility of functionalized MWCNTs in increasing the proton conductivity of composite electrolytes and thereby increasing the specific capacitance of an electrode material. For example, in NasM composite membranes, the incorporation of sulphonated MWCNTs increases the specific capacitance of $RuO_2$/C electrodes. Further, the synergistic role played by S-MWCNT

is further confirmed by the solid state cyclic voltammetry experiments where the autocatalytic activity of MWCNTs towards the $Ru^{3+/2+}$ redox reaction is utilized. However, such a characterization study is not possible with PBI based systems where the phosphoric acid leaching out due to the addition of aqueous $RuCl_3$ and environmental moisture content restricts the effectiveness of the results. While the formation of network structure in both the composite membranes help in higher charge storage in the electrolyte, the MWCNTs present in the polymer matrix help in improving the electrode-electrolyte interface thereby enhancing the effective charge transport near the interface. Further, the amount of sulfonic acid groups on the MWCNTs is calculated to be ~2.5 wt% and a mere addition of 0.05 wt% means an increase in sulfonic acid content by only 0.001 %. A sulfonation level of up to 15 % has been reported for MWCNTs which would increase the sulfonic acid content to 0.007 %, a six fold increment that might improve the conductivity of Nafion further with out increasing the MWCNT content [19]. Similarly the phosphonic acid content of the P-MWCNTs can also be tuned by varying the reaction medium, temperature, time and concentration. Thus, reinforcement of Nafion and PBI membranes with functionalized MWCNTs offer significant advantages to solid polymer electrolytes for supercapacitor applications as illustrated below;

- The increased proton condutivitiy helps in the accumulation of higher charge on the electrode surface thereby increasing the specific capacitance.
- Improved electrode-electrolyte interface due to the presence of functionalized MWCNTs on the electrolyte that might synergistically

- Increased durability due to higher mechanical stability provided by the MWCNTs present in the composite polymer matrix and decreased ESR of the resulting supercapacitor.
- The possibility to tune the degree of functionalization helps to increase the proton conductivity without actually increasing the MWCNT loading.

Thus, these results underline the possibility to tune the proton conductivity of Nafion and phosphoric acid doped PBI membranes above that of their pristine counterparts and hence to fabricate better electrolytes for supercapacitors.

## 6.4. Conclusions

We have demonstrated a strategy to increase the capacitance of an all solid-state supercapcitor in this chapter by employing nanocomposite electrolytes using functionalized MWCNTs with tailor made functional groups on their surface for reinforcement. Nafion and $H_3PO_4$ doped PBI membranes have been chosen as the candidate membranes respectively to demonstrate the utility of this strategy. The incorporation of MWCNTs with functional groups helps in improving the proton conductivity than that of their pristine counterpart and thus assisting in achieving enhanced specific capacitance. A maximum capacitance of 220 F $g^{-1}$ is achieved with NasM composite membranes agaisnt 200 F $g^{-1}$ for the Nafion 115 membranes. PBpNT and PBI membranes show maximum specific capacitance of 500 and 225 F $g^{-1}$ after 1000 charge discharge cycles suggesting a 100 % improvement in the perforamance. Further, the enhanced mechanical integrity arising from the presence of

MWCNTs helps to increase the durability of the composite membranes. We believe that the possibility to tune the sulphonic acid and phosphonic acid content of the MWCNTs also helps specially to tune the storage capacity and time constant which are crucial factors for many hybrid electric vehicle applications based on supercapacitors.

## 6.5. References

**[1]** Jeong, H. K.; Jin, M.; Ra, E. J.; Sheem, K. Y.; Han, G. H.; Arepalli, S.; Lee, Y. H. *ACS Nano,* **2010,** 4, 1162**.**

**[2]** Miller, J. R. ; Simon, P. *Science* **2008,** 321, 651**.**

**[3]** Kalinathan, K.; DesRoches, D. P.; Liu, X.; Pickup, P. G. *J. Power Sources* **2008,** 181, 182**.**

**[4]** Shukla, A. K.; Sampath, S.; Vijayamohanan, K. C*urrent Science* **2000,** 79, 1656.

**[5]** Liu, C.; Li, F.; Ma, L.P.; Cheng, H.M. *Adv. Mater*, **2010,** 22, E28**.**

**[6]** Du, X.; Wang, C.; Chen, M.; Jiao, Y.; Wang, J. *J. Phys. Chem. C* **2009,** 113, 2643**.**

**[7]** Athouël, L.; Moser, F.; Dugas, R.; Crosnier, O.; Be´langer, D.; Brousse, T. *J. Phys. Chem. C* **2008,** 112, 7270**.**

**[8]** Placin, F.; Desvergne, J. P.; Lasse`gues, J. C. *Chem. Mater.* **2001,** 13, 117**.**

**[9]** Largeot, C.; Portet, C.; Chmiola, J.; Taberna, P. L.; Gogotsi, Y.; Simon, P. *J. Am. Chem. Soc.* **2008,** 130, 2730**.**

**[10]** Frackowiak, E.; Lota, G.; Pernak, J. *Appl. Phys. Lett.* **2005,** 86, 164104**.**

**[11]** Lufrano, F.; Staiti, P. *Electrochim. Acta,* **2004,** 49, 2683**.**

**[12]** Park, K. W.; Ahn, H. J.; Sung, Y. E. *J. Power Sources* **2002,** 109, 500**.**

**[13]** Ma, L.; Yang, Y. *Appl. Phys. Lett.* **2005,** 87, 123503**.**

**[14]** Suppes, G. M.; Deore, B. A.; Freund, M. S. *Langmuir* **2008,** 24, 1064**.**

**[15]** Sivaraman, P.; Hande, V. R.; Mishra, V. S.; Rao, C. S.; Samui, A. B. *J. Power Sources,* **2003,** 124, 351**.**

**[16]** Sampath, S.; Choudhury, N. A.; Shukla, A. K. *J. Chem. Sci.,* **2009,** 121, 727.

**[17]** Osaka, T.; Liu, X.; Nojima, M.; Momma, T. *J. Electrochem. Soc.* **1999,** 146, 1724**.**

**[18]** Gogotsi, Y.; Dash, R. K.; Yushin, G.; Yildirim, T.; Laudisio, G.; Fischer, J. E. *J. Am. Chem. Soc.* **2005,** 27, 16006**.**

**[19]** Peng, F.; Zhang, L.; Wang, H.; Lv, P.; Yu, H. *Carbon*, **2005,** 43, 2405**.**

**[20]** Rathod, D. G.; Vijay, M. P.; Islam, N. M.; Kannan, R.; Kurungot, S.; Kharul, U. K.; Pillai, V. K. *J. Appl. Electrochem,* **2009,** 39, 1097**.**

**[21]** Liu, X.; Pickup, P. G. *J. Power Sources,* **2008,** 176, 410**.**

**[22]** Chang, K. H.; Hu, C. C. *Appl. Phys. Lett.* **2006**, *88*, 193102.

**[23]** Trasatti, S. *Electrochim. Acta* **1991**, *36*, 225.

**[24]** Hu, C. C.; Chang, K. H.; Lin, M. C.; Wu, Y. T. *Nano Letters*, **2006,** 6, 2690.

**[25]** Dmowski, W.; Egami, T.; Swider-Lyons, K. E.; Love, C. T.; Rolison, D. R. *J. Phys. Chem. B* **2002**, *106*, 12677.

**[26]** Parthasarathy, M.; Gopinath, C. S.; Pillai, V. K. *Chem. Mater.* **2006,** 18, 5244

**[27]** Wilson, N. R.; Guille, M.; Dumitrescu, I.; Fernandez, V. R.; Rudd, N. C.; Williams, C. G.; Unwin, R. R.; Macpherson, J. V. *Anal. Chem.* **2009,** 78, 7006**.**

# Chapter 7

## Conclusions and Future Prospects

This last chapter deals with significant conclusions of the present study on functionalized MWCNT polymer composite electrolytes for PEMFC applications. It also outlines several limitations of polymer nano-composites in comparison with other reinforced polymer electrolyte membranes. Related promising developments and daunting challenges in this area are also discussed to extend the applications of these fascinating CNT polymer composites in view of the fundamental and technological interest in several fields. Finally some of the future prospects and precautions in using functionalized carbon nanotubes for polymer electrolyte fuel cells are also explained with in the broad perspective of nanotechnology and its social impact.

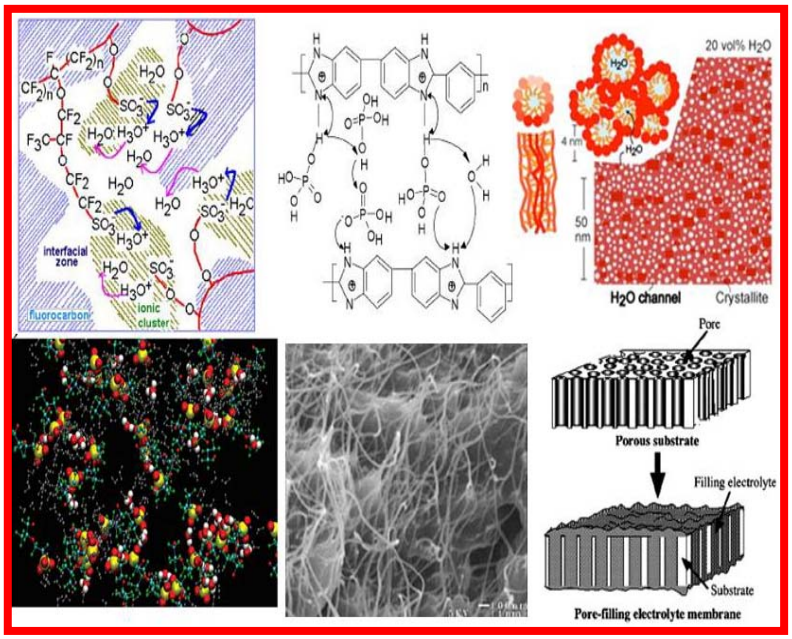

Polymer electrolyte membrane fuel cells offer clean and efficient technology from renewable resources to fulfil the future energy needs. However, currently the technology is too expensive and also faces many material and process related challenges. The use of less expensive components and fewer processing steps might facilitate prospects for more wide-spread practical applications. In this respect, carbon nanotubes offer great promise due to their unique electronic and electrical properties as it plays a critical role in almost all subcomponents of PEMFCs. Recently, there have been some breakthroughs using CNT and graphene based electrocatalysts as possible replacements for Pt as an electrocatalyst for oxygen reduction reaction and more ground-breaking research in materials is needed to reduce the cost and enhance the efficiency. The utility of CNTs in improving the characteristic features of different PEMFC components such as catalyst supports, catalysts, fillers in bipolar plates and electrolyte membranes have been discussed in Chapter 1, revealing the critical role of CNTs with special emphasize on electrolyte part using Nafion and polybenzimidazole as the candidate membranes. Further, the requirements for using functionalizing CNTs and their possible efficacy as a reinforcing material associated with many advantages such as homogeneous membrane formation have been outlined along with different strategies for sidewall and tip functionalization. Major advantages and limitations associated with Nafion and polybenzimidazole membranes are analyzed due to their promise for PEMFC electrolyte applications and the necessary steps to improve their proton conductivity and mechanical stability to take the technology a step further towards commercialization have also been delineated.

However, before studying the performance of composite membranes based on functionalized MWCNT with Nafion and polybenzimidazole membranes, it is important to optimize the MEA fabrication procedure for PBI based fuel cell stacks due to its high temperature operation, and this has been discussed in chapter 2 along with the use of a $2^{7-3}$ fractional factorial design to optimize the MEA fabrication parameters such as catalyst loading, binder loading etc,. Further, the possible role of functionalized MWCNTs in demonstrating catalytic activity towards oxygen reduction reaction has been examined in chapter 3, coupled with the probable effects of different aqueous and polymer electrolytes in determining the mass transport of oxygen towards the electrode-electrolyte interface.

The role of phosphonated MWCNTs in improving the proton conductivity and mechanical stability along with superior fuel cell performance has been discussed in chapter 4. The Formation of network structures in the polymer matrix by the incorporation of P-MWCNT is lined out as the major cause for enhanced functioning of PBpNT composite membranes. The possibility of tuning the hydrophilic domain size in Nafion membrane by the incorporation of sulphonated MWCNTs is analyzed in chapter 5. It has been found that a maximum domain size of 72 Å has been achieved for the composite membrane against the 40 Å of Nafion 115 membranes, explaining the influence of increased domain size in improving the proton conductivity and fuel cell performance. The use of these functionalized MWCNT polymer composites in enhancing the specific capacitance of an electrode in an all-solid-state supercapacitor has been demonstrated in chapter 6 for both Nafion and polybenzimidazole membranes at room temperature and 140 °C respectively.

Thus the main results of this thesis unravel some of the critical issues associated with solid polymer electrolytes such as Nafion and phosphoric acid doped polybenzimidazole membranes in fuel cells. In the entire thesis, we have focused mainly on functionalizing MWCNTs and their role in improving the proton conductivity and mechanical stability of the membranes simultaneously. We have explored the advantages of using functionalized carbon nanotubes as filler materials for composites over their pristine counterpart, which due to the surface functional groups could provide increased sites for proton hoping. More importantly, we have also analyzed the ability of functionalized MWCNTs to show ORR activity and possible synergy in forming an improved electrode-electrolyte interface. Also the fabrication parameters of MEA for PBI based fuel cell stacks have been studied to illustrate their central role.

Thus the major accomplishments of the present investigations could be summarized as follows-

- Factorial optimization of the membrane electrode assembly and subsequent fabrication of polybenzimidazole based fuel cells.
- Synthesis of surface functionalized MWCNTs with tailor made groups such as sulfonic acid and phosphonic acid.
- Improved oxygen reduction kinetics of functionalized MWCNTs over pristine MWCNTs as electrocatalysts.
- Fabrication of polybenzimidazole - phosphonated MWCNT composite membranes with improved fuel cell performance at high temperatures along with enhanced mechanical stability.

- ❖ Characterization of network structure in the polybenzimidazole - phosphonated MWCNT composite membranes.
- ❖ Systematic manipulation of the hydrophilic domain size in the Nafion membranes using sulphonated MWCNTs and subsequent fabrication of MEAs with composite membranes to demonstrate increased proton conductivity and mechanical stability.
- ❖ Demonstration of these functionalized polymer composites in improving the specific capacitance of electrode materials for supercapacitor applications.

However, there are several unresolved issues that remain to be urgently addressed before these materials could be explored commercially. For example, durability data for both reinforced membranes with respect to acid leaching is one of the critical aspects necessitating urgent studies. Although, this strategic approach of using appropriately functionalized CNTs with polymer electrolytes helps in improving the proton conductivity through well-connected network formation, life-time of these membranes under sustained operation (such as 1000 h and 5000 h) has to be rigorously evaluated. Similarly, the mode of bonding between aminoethyl phosphonic acid and acid functionalized MWCNTs has been confirmed by $^{1}H$ and $^{31}P$ NMR results, yet molecular simulation and modelling studies of the local chemical environment inside the polymer matrix are badly needed despite SAXS measurements directly indicating the network formation. More importantly, any variation in the degree of functionalization of carbon nanotubes can directly affect the formation of network for proton hopping. As a result, much more efforts are essential to resolve these issues before finally realizing the complete control over the outcome of

composite electrolytes. In addition, several existing gaps in our understanding need to be filled by important investigations focusing on the nature of domains formed in the polymer matrix. For example, several models are currently available for the hydrophilic and hydrophobic domains distribution in the Nafion matrix although we have used a simple model. There are several daunting tasks like addressing the environmental concern and societal impact of these materials as the toxicity data of carbon nanotubes upon long term processing is not yet clear. Hence, experiments dealing with advantages or limitations of functionalization involving concentrated acids and other carcinogenic agents such as thionyl chloride are need to evolve safe and precaution measures in handling these chemicals.

Our approach of using CNTs with tailor-made functional groups offers an unprecedented opportunity for the simultaneous improvement of proton conductivity and mechanical stability of polymer electrolyte membrane for fuel cells, obviating many limitations of currently employed polymer electrolyte membranes. However, several limitations of this investigation need to be kept in mind before taking these results to the next level.

- Since carbon nanotubes are rigorously treated to induce the specific functional groups on its sidewalls and tips, its chemical stability might get adversely affected and specific efforts are required to optimize the durability of these carbon nanotubes in the highly acidic (pH ~ 1) operating conditions of fuel cells.
- Phosphoric acid leaching of PBI membranes during sustained operation at high current densities needs to be rigorously investigated so that durability issues and degradation modes are sorted out.

- ❖ Safety, health and environmental issues arising from the application of functionalized MWCNTs need to be understood.

Since some of these disadvantages restrict the full potential of commercial applications of functionalized CNT - polymer composites, further work is desired to alleviate these problems. Despite these limitations, the present approach offers enough scope to design different CNT - polymer composite electrolytes with enhanced performance parameters. More significantly, this strategy offers an ideal route to tune the proton conductivity and mechanical stability by varying the degree of functionalization and amount of CNT loading in the polymer matrix thus providing one possible route to improve the fuel cell performance. Due to this and several other material innovations, there is every reason to believe that the efficiency of polymer electrolyte fuel cells will continue to improve along with cost reduction causing significant advances in this field. Further, this would help to reduce cost per kW of the fuel cell stack thus taking the technology a step closer to commercialization in the coming years.

# List of Publications

1. Polymer Electrolyte Fuel Cells Using Nafion-Based Composite Membranes with Functionalized Carbon Nanotubes **R. Kannan,** B. A. Kakade, V. K. Pillai, *Angew. Chem.* **2008,** 120, 2693-2696.
2. Synthesis of Platinum Y-Junction Nanostructures Using Hierarchically Designed Alumina Templates and Their Enhanced Electrocatalytic Activity for Fuel-Cell Applications S. Mahima, **R. Kannan,** I. Komath, M. Aslam, V. K. Pillai, *Chem. Mater.* **2008,** 20, 601-603.
3. Comparative Study of the Shape-Dependent Electrocatalytic Activity of Platinum Multipods, Discs, and Hexagons: Applications for Fuel Cells S. Mahima, **R. Kannan,** V. K. Pillai, *Langmir*, **2008,** 24, 3576-3583.
4. A 27-3 fractional factorial optimization of polybenzimidazole based membrane electrode assemblies for H2/O2 fuel cells **R. Kannan,** Md. N. Islam, D. Rathod, M. Vijay, U. K. Kharul, P. C. Ghosh, K. Vijayamohanan, *J. Appl. Electrochem.* **2008,** 38, 583-590.
5. Domain Size Manipulation of Perflouorinated Polymer Electrolytes by Sulfonic Acid-Functionalized MWCNTs To Enhance Fuel Cell Performance **R. Kannan,** M. Parthasarathy, S. U. Maraveedu, S. Kurungot, V. K. Pillai, *Langmuir*, **2009,** 25, 8299-8305.
6. Y-junction nanostructures of palladium: Enhanced electrocatalytic properties for fuel cell reactions S. Mahima, **R. Kannan,** M. Aslam, V. K. Pillai, *J. Electroanalytical Chemistry* **2009,** 629, 58-62.

7. Applications of carbon nanotubes in polymer electrolyte membrane fuel cells **R. Kannan**, V. K. Pillai, *Journal of the Indian Institute of Science* **2009,** 89, 4
8. Design of an ‘‘all solid-state’’ supercapacitor based on phosphoric acid doped polybenzimidazole (PBI) electrolyte D. Rathod, M. Vijay, Md. N. Islam, **R. Kannan,** U. K. Kharul, S. Kurungot, V.K. Pillai, *J. Appl. Electrochem.* **2009,** 39, 1097-1103.
9. Artificially Designed Membranes Using Phosphonated Multiwall Carbon Nanotube-Polybenzimidazole Composites for Polymer Electrolyte Fuel Cells **R. Kannan,** P. P. Aher, T. Palaniselvam, S. Kurungot, U. K. Kharul, V. K. Pillai, *J. Phys. Chem. Lett.* **2010,** 1, 2109.
10. Bio-Inspired Catalyst Compositions for Enhanced Oxygen Reduction using Nanostructured Pt Electrocatalysts in Polymer Electrolyte Fuel Cells P. Meera, **R. Kannan**, K. Sreekumar, K. Vijayamohanan, *Journal of Materials Chemistry,* **2010,** 20, 9651**.**
11. Enhanced charge storage of sulfonate functionalized carbon nanotube-Nafion composite electrolyte in all solid-state supercapacitors **R. Kannan**, R. Vellacheri, N. Pardeshi, S. Kurungot, V. K Pillai **submitted to “Journal of Nano Energy and Power Research”**.
12. Enhanced electrocatalytic performance of functionalized carbon nanotube electrodes for oxygen reduction in proton exchange membrane fuel cells **R. Kannan,** K. Sreekumar, V.K. Pillai, **submitted to *J. Phys. Chem. C***.
13. Charge transport in functionalized multi-wall carbon nanotube-polymer composite C.S. Suchand Sangeeth**, R. Kannan,** Vijayamohanan K. Pillai, and Reghu Menon, **submitted to Journal of Applied Physics**.

14. Enhanced performance of porous $Co_3O_4$ nanorods as anode material in rechargeable Li–ion batteries S. Vijayanand, **R. Kannan,** Vijayamohanan K. Pillai, Hari S. Potdar, Pattayil A. Joy **submitted to J. Mater. Chem**.
15. Facile construction of Non Precious Iron nitride doped Carbon Nanofibers as cathode electrocatalysts in Proton Exchange Membrane Fuel Cells T. Palaniselvam, **R. Kannan,** S. Kurungot, **submitted to ChemComm** on 20th October.
16. Phosphonated carbon nanotube-polybenzimidazole composites for electrolyte applications in polymer electrolyte membrane fuel cells with improved characteristics **R. Kannan,** K. Sreekumar, U. K. Kharul, V. K. Pillai, manuscript under preparation.

# Erratum